Faculteit Wetenschappen

Departement Fysica

Ligand binding in globins of *Caenorhabditis elegans* and *Methanosarcina acetivorans*: from over-expression to spectroscopic characterization

Proefschrift voorgelegd tot het behalen van de graad van Doctor in de wetenschappen: Fysica aan de Universiteit Antwerpen

te verdedigen door
Niels Van Brempt

Promotoren:
Prof. dr. Sabine Van Doorslaer
Prof. dr. Sylvia Dewilde†
Prof. dr. em. Luc Moens

Antwerpen, 2023

Acknowledgements

This thesis in its final form is not the work of an individual, but the result of a close collaboration, supported by a network of colleagues and friends inside and outside the University of Antwerp. It is therefore also appropriate to express my sincere thanks to everyone who played an important role in this process.

Allereerst wil ik mijn dank uitspreken aan mijn **promotoren**, Prof. dr. Sabine Van Doorslaer en Prof. dr. Sylvia Dewilde, en later Prof. dr. em. Luc Moens. Zij hebben mij een tweede kans geboden om een frisse start te maken. Ik herinner me nog goed ons Skype-gesprek ergens in een afgelegen lokaal, dat de bal aan het rollen bracht en uiteindelijk leidde tot mijn aanstelling bij zowel de PPES als TSM^2 onderzoeksgroepen.

Sabine, ik wil je bedanken voor de inspirerende gesprekken, het vertrouwen dat je in mij hebt gehad en de feedback en kritiek op mijn werk, vanaf mijn bachelorscriptie tot aan mijn doctoraatsthesis. Ook wil ik je danken voor de vrijheid die je me hebt gegeven om mijn eigen weg in het onderzoek te vinden. Jouw toewijding die je in onze papers hebt gestoken, is van onschatbare waarde gebleken. Het was altijd interessant om na een gesprek van enkele uren en na het doornemen van enkele papers die je zonder enige twijfel uit een diep verscholen map tevoorschijn toverde, enigszins verward maar met tal van nieuwe ideeën jouw bureau buiten te stappen. Ook de momenten in het lab achter de gepulste EPR-spectrometer zullen me nog lang bijblijven.

Sylvia, ook al ben je niet meer bij ons, wil ik je bedanken voor het warme welkom binnen de PPES-groep en de nauwe opvolging. Ik ben er absoluut van overtuigd dat ons onderzoek naar de *C. elegans* globines veel verder zou zijn gekomen als we vaker hadden kunnen discussiëren en richting konden geven aan het werk. Jouw expertise is onvervangbaar. Ik koester warme herinneringen aan de O2-BiP conferentie in Barcelona, waar we naast wetenschap ook tijd hadden voor gezellige gesprekken en avonden met de onderzoeksgroep. We missen jouw aanwezigheid nog elke dag!

My sincere gratitude goes out as well to all the **members of my committee**, chair Prof. dr. Sandra Van Aert, Prof. dr. Alessandra Pesce, Prof. dr. Stéphane Grimaldi, Prof. dr. Alain Labro and Prof. dr. Christian Johannessen. Thank you for going in detail through the work, asking interesting questions and making valuable suggestions and edits.

Scientifically, **my peers** dr. Zainab Hafiddenine and dr. Roberta Sgammato. I lost track of the hours we spent together in the lab, planning experiments and organizing measurements for and with each other. It was a real pleasure to work with you! Also, dr. Vincent Hue Ching, you made sure I had the opportunity to learn about W-band and spin-trapping experiments, and even visit the impressive HiPER spectrometer. Thank you for being always so optimistic and cheerful; your excitement for science was contagious. Herald Berghmans also played a crucial role in the PhD trajectory. He taught me the arts, crafts, and wizardry of globin over-expression and purification. Thanks a lot for teaching me; these skills will come in very handy, if not in a future lab, definitely in the kitchen where I am learning to clean up after myself better. I even weigh out my coffee grounds and water these days. I would also like to express my gratitude to dr. Dietmar Hammerschmid and dr. Sander Neukermans for their support with the experiments.

At a border-line scientific level or not scientific at all, my **desk buddies**. A shout out to my friends at the N-building: Miguel, thanks for blasting your hardcore EDM so loudly through your headphones that I could vibe too, and for the lunch-break runs together. Momo, we started more or less at the same time; we grew together from students, who did not know much, to PhD holders, who know slightly more. Sometimes we got really stressed, but luckily, Andrea was in the office to always set a chill mood and share a meme. Andrea, I wish you the best with finalizing your PhD. Also Joeri, we did not overlap much, but it was nice to have you nearby too! Thank you guys!

Op de vierde verdieping van het S-gebouw was het ook altijd fijn werken. Naast Herald, voor wie nooit iets te veel was gevraagd, was er ook Joey. Joey, ik begrijp niet hoe je er altijd zo ontspannen bij liep en toch uitstekende wetenschappelijke resultaten behaalde. Ik bewonder hoe soepel je met alle PhD-verantwoordelijkheden en stress wist om te gaan; daar kan ik van leren. Karen en Eva, soms in de bureau, soms in het practicum. Ook een grote dank aan jullie twee; jullie waren geweldige collega's. Allen samen hebben we Sylvia gekend in zowel goede als slechte tijden, en tijdens de rouwperiode daarna. Ondanks de moeilijke sfeer heb ik veel aan jullie gehad en hebben we er op een humane manier mee om kunnen gaan.

Evi, An, Zoë en Stijn, jullie waren de ervaren rotten toen ik begon en druk bezig, en misschien een tikkeltje "klaar" met het doctoraat, maar dat hoort bij "the cycle of the PhD life". Bedankt voor de tips en trucs en fijne gesprekken.

Ook buiten de acht muren van mijn twee kantoren zijn er **tal van personen** die ik graag nog wil bedanken. Kevin, vanaf de master zijn we samen in de EPR-wereld beland. Ik ben zo blij dat ik je heb leren kennen. Zowel tijdens, maar vooral nadat ik het labo heb verlaten, was je een enorme steun en uitlaatklep. Bedankt voor de peptalks en interessante artikelen die ervoor hebben gezorgd dat ik niet heb opgegeven en mijn mentale gezondheid min of meer heb kunnen behouden. Zainab, ook hier nogmaals bedankt voor de extra tijd die je in het welzijn van de groep hebt gestoken. Je was die collega die iedereen goed gestemd kreeg, wat er ook gebeurde, en daarnaast wist je samen me Kevin de CW-EPR te temmen en stabiel te krijgen, ongezien. Ivan, altijd druk in de weer met lange intensieve experimenten, onze paden kruisten ook al sinds de masteropleiding, het was fijn om jou in onze groep te hebben. Melissa, ik waardeer je vrolijke, zij het soms licht melancholische kijk op de dingen, maar ook jouw competenties als wetenschapper.

Illenia, we delved into this nitrite interaction together; it was wonderful to exchange thoughts, simulations, and witness your development as a scientist, excelling in your intensive Paracat trajectory. The same goes for the other "Paracatters" who entered and left the lab. Finally, I want to extend **honourable mentions** to Salome, Maksiem, Ania, Miles, Marina, Dimitry, Wouter, Alexander, Ivan, Federico, Sofie, and Etienne for the engaging conversations during the numerous coffee breaks. I believe these discussions were essential in maintaining a pleasant atmosphere within the building.

Special thanks to Ruben the jokester, Emilie, the "Claudei": Claudio, Claudina, and Claudia, and of course, gracias a Julio también, for the enjoyable lunches and office parties we shared.

The final stages, during and after the pandemic were most definitely the hardest,

especially when I was not physically in Antwerp. Muchas gracias a Santi, Agustín, Mitcheell, Aida, Joaquín, José y a todo **el equipo de Mestrelab** por haberme apoyado tanto y haberme permitido dedicar tiempo de trabajo a mi tesis doctoral; creo que nunca la hubiera terminado sin esta posibilidad. Estoy muy agradecido por haber tenido la libertad de hacerlo.

Mijn **dierbaarste vrienden**, die keer op keer mijn excuses hebben aangehoord waarom mijn thesis nog niet is ingeleverd, bedankt dat jullie geïnteresseerd zijn gebleven en begrip hebben getoond voor mijn afwezigheid bij verschillende gelegenheden. Dank aan mijn ouders en naaste familie voor hun onvoorwaardelijke steun en het bieden van financiële en mentale ondersteuning gedurende mijn studie, waardoor ik naast mijn universitaire verplichtingen ook tijd kon vinden voor sport, ontspanning en vrije tijd.

En ten slotte, en "hands down" de belangrijkste factor. **Sibylle**, ik weet niet eens waar ik moet beginnen. Je hebt me gemotiveerd en geinspireerd om beter te presteren, om door te zetten. Op de moeilijkste momenten was je daar, met lachen en tranen, en nog meer tranen tot aan het punt van wanhoop waarop het woord "thesis" als taboe werd gezworen. Academische uitdagingen hebben ons beiden getest, maar we zijn er steevast voor elkaar. Dank je met heel mijn hart om aan mijn zijde te staan.

Bedankt iedereen, nu kan ik met eindelijk met trots terugbliken op de meest intense en leerzame periode in mijn leven, tot dusver.

Contents

List of Abbreviations

Acronyms

AA	amino acid
Abs	absorbance
Al	*Aplysia limacina*
Ap	*Aeropyrum pernix*
BV	biliverdin
CCD	charge-coupled device
CCP	cytochrome c peroxidase
Ce	*Caenorhabditis elegans, C. elegans*
Cgb	cytoglobin
CH	chimeric
CID	collision-induced dissociation
CNG	cyclic nucleotide-gated
CT	charge-transfer
CW	continuous-wave
dq	double quantum
DTT	Dithiothreitol
EC	electron coherence
ECD	electronic circular dichroism
E. coli	*Escherichia coli*
EDTA	ethylenediaminetetraacetic acid
EM	electromagnetic
ENDOR	electron nuclear double resonance
EPR	electron paramagnetic resonance
EPRI	EPR imaging
ESE	electron-spin-echo
ESEEM	electron spin echo envelope modulation
ESI	electrospray ionisation
EZE	electron Zeeman effect
FAD	flavin adenine dinucleotide
Fe(III)	ferric
Fe(II)	ferrous
Fe(IV)	ferryl

FHbs	flavohemoglobins
FRET	fluorescence resonance energy transfer
FT	Fourier transform
gbs	globins
GC	guanylate cyclase
GCS	globin-coupled sensor
GD	globin domain
GFP	green fluorescent protein
GPCR	G protein-coupled receptor
Hb	hemoglobin
hh	horse heart
HI	hyperfine interaction
HOMO	highest occupied molecular orbital
HPLC	high-performance liquid chromatography
HRP	horse radish peroxidase
HS	high-spin
hs	horse skeletal muscle
IPTG	Isopropyl β-d-1-thiogalactopyranoside
IR	infrared
KHD	Kramer Heisenberg Dirac
Lp	*Lucina pectinata*
LS	low-spin
LUCA	last universal common ancestor
LUMO	lowest unoccupied molecular orbital
Ma	*Methanosarcina acetivorans*
Mb	myoglobin
MCD	magnetic circular dichroism
MM	molecular mechanics
MRI	magnetic resonance imaging
MS	mass spectrometry
MTS	mitochondrial targeting site
NAD	nicotinamide adenine dinucleotide
NC	nuclear coherence
Ngb	neuroglobin
NiR	nitrite reductase
NMR	nuclear magnetic resonance
NP	nitrophorin
NQI	nuclear quadrupole interaction
NZE	nuclear Zeeman effect
PCR	Polymerase Chain Reaction
Pgb	protoglobin
PPES	Proteinchemistry Proteomics and Epigenetic Signalling
QM	quantum mechanical
QS	quantum-mechanically mixed state

RNS reactive nitrogen species
ROA Raman optical activity
ROS reactive oxygen species
rRaman resonance Raman
SD single-domain
SDS-PAGE sodium dodecyl sulfate–polyacrylamide gel electrophoresis
SOD superoxide dismutase
sq single quantum
sw sperm whale
Tf *Thermobifida fusca*
TM transmembrane
TMA-PTIO 2-(4-trimethylammonio)phenyl-4,4,5,5-tetramethylimidazoline-1-oxyl 3-oxide
Tr truncated
TSM^2 Theory and Spectroscopy of Molecules and Materials
UV ultraviolet
WT wild-type
XRD X-ray diffraction
ZFI zero-field interaction

†*This thesis is written in dedication to the memory of my dear co-supervisor, Prof. dr. Sylvia Dewilde, who passed away at the age of 47 during the course of the PhD program. Unfortunately, this work forms one of the last collaborative projects between TSM^2 and PPES due to her unexpected and unfortunate loss. Nevertheless, we look back with gratitude on the fruitful and long-standing research collaboration between the supervisors and the high-quality research that was done over the past 25 years. Dear Sylvia, your kindness, intelligence, and generosity will always remain in our hearts. Your legacy will continue to inspire us in our own pursuits, and we are forever grateful for the time we had with you.*

Preface

This work was jointly carried out at the cluster groups of Prof. Sabine Van Doorslaer (Previously, BIMEF at the start of the PhD, now Theory and Spectroscopy of Molecules and Materials, TSM^2) and Prof. Sylvia Dewilde (Protein chemistry, Proteomics and Epigenetic Signalling, PPES) at the University of Antwerp. The molecular biophysics and spectroscopy unit led by Prof. Van Doorslaer is continuously improving and testing existing and new electron paramagnetic resonance techniques on the most diverse organic and inorganic systems covering photovoltaics, electrochemical catalysis, and hybrid materials. On the other hand, the protein chemistry unit led by Prof. Dewilde within PPES has years of experience with the over-expression and purification of globins and has an overall research goal to understand the structural and biochemical properties of recombinantly-expressed globins from all kinds of different organisms.

This thesis aims to elucidate the structure-function relationship of recently discovered globins in the nematode *Caenorhabditis elegans* and the protoglobin from *Methanosarcina acetivorans*. Special focus was brought on the nitrite-binding properties and subsequent reactions. Furthermore, I wanted to explore new strategies to study these reactions using electron paramagnetic resonance techniques. Additionally, the intense collaboration with dr. Roberta Sgammato, who was part of the group led by Prof. Christian Johannessen and Prof. Wouter Herrebout (previously MolSpec, nowadays part of TSM^2), complemented the results with electronic circular dichroism spectroscopy and resonance Raman.

The thesis chapter outline is as follows: Chapter 1 contains an overall introduction to globins, from structure to evolution and function. Moreover, the globin-nitrite interaction will be introduced and discussed there. Chapter 2 gives the state-of-the-art of the globins that were of particular interest in this thesis. Accordingly, the specific research objectives and how they are part of the greater research lines of the groups are stated there as well. Chapter 3 gives a brief theoretical overview of the various methods that were used to carry out the biochemical and biophysical characterization of the globins introduced in Chapter 2. Chapters 4 until 7 contain the main results. In detail, chapter 4 and 5 are related to globin number 33 from *C. elegans*. First, its interaction with nitrite studied at various pH values using a plethora of complementary spectroscopies was done, second, the in-depth EPR study on the hydroxide-ligated globin domain is presented. In the following chapter 6, the collaborative project with Molspec on the ferric protoglobin from *Methanosarcina acetivorans* and its reaction with nitrite and NO is covered. The final results chapter 7 contains my contributions to a first characterization study on the cysteine-rich GLB-3 from *C. elegans*, together with a description of the experimental optimization that was done in order to determine the redox potential of this peculiar globin. Finally, as the conclusive chapter, a brief summary, together with a future outlook, is formulated.

Part I

Introduction

Chapter 1

A general introduction to globins

1.1 Background

Globins (gbs) are small heme-containing α-helical proteins widespread throughout the kingdoms of life [1, 2, 3] and are best known for their capacity to reversibly bind O_2 and other small gasses such as NO, CO and H_2S, anions such as CN^-, OH^-, $NO_2{}^-$ and small molecules such as imidazole, at the distal side of the heme. Gbs have attracted researchers' attention since long which eventually led to the first protein structures ever that were determined using X-ray crystallography: the elucidation of the molecular structure of myoglobin (Mb) and hemoglobin (Hb), for which J. C Kendrew and M. Perutz received the Nobel prize in 1962 [4], a milestone in structural biology. In the following decades, many other globin (and other protein) structures followed, which led to meaningful insights in heme-protein function and porphyrin chemistry. Moreover, interdisciplinary research effort was focused on understanding the structure-function relationship of gbs, with a special interest in mammalian Hb. To date, due to the wealth of knowledge, mammalian gbs remain great model systems and references to test new methodologies in protein science. Furthermore, the advances in genome sequencing starting in the end of the of 20th century led to the discovery of many new members of the globin family with far less clear functions, such as vertebrate neuroglobin (Ngb), and cytoglobin (Cgb), which sparked renewed interest in this ancient protein family [5, 6].

1.2 Globin structure

On a primary structural level, typical gbs consist of roughly 150 amino acids (AA) which are, on a secondary structural level, folded into a number of *alpha* helices, usually eight labelled A-H. A rigid three-on-three helical sandwich structure is created by helices A-G-H and B-E-F, connected by a more flexible CD region (see Fig. 1.1 (A)). This tertiary structure organization of two layers of helices is also indicated as the three-over-three helical fold (3/3). Variation in this structure mainly occurs by N- and C-terminal extension and variation in length of the inter-helical segments. Next to the 3/3 globin

fold, the two-over-two globin fold (2/2) is recognized as a sandwich of the B-E and G-H helices. The 2/2 gbs are normally shorter than the 3/3 gbs (20-40 residues) and therefore referred to as truncated Hbs. In both globin folds, a hydrophobic crevice, the heme pocket, is formed in which an iron containing protoporphyrin (see §1.2.1 and Fig. 1.2) is embedded that acts as the active catalytic center.

At the level of quaternary structural organization, gbs can be either monomeric, dimeric, tetrameric or of a higher-order multimerization. Mb (Fig. 1.1 (A)), one of the best-studied gbs found in muscle tissue, is a monomeric protein of O_2 storage, whereas human Hb, essential for O_2 transport in blood, is a tetrameric globin[1]. Next to the formation of heteromultimers, chimeric gbs exist, such as the flavohemoglobins (FHbs) and the globin-coupled sensor (GCS).

The wide variety of globin structures is reflected on a primary level as remarkable amino-acid sequence diversity, originating from the long evolutionary history of the globin family. Nevertheless, key AAs are highly conserved, with position F8 always occupied by a His residue and E7 mostly occupied by histidine, especially in mammalian globins, but not exclusively in all globins. The E10 residue plays an important role in some globins as a stabilizer and is usually occupied by a positively charged residue in truncated Hbs, capable of forming salt bridges involving the heme propionates [7]. In other (bacterial) globins, E10 or E11 are involved in the hexacoordination of the heme [8, 9]. Finally, residue B10 (often Leu) plays an important role in ligand binding as well, and deviations from all of the above-mentioned have a high impact on the globin's O_2 and overall ligand binding properties. CD1 (Phe) is another strongly conserved position essential for maintaining the globin structure by supporting the heme.

1.2.1 The heme group

The heme group (Fig. 1.2) is a naturally occurring compound and can be considered as the active center of a globin and gives the protein a typical brilliant red to brown color. It consists of a tetrapyrrole or porphyrin (four pyrrole rings linked by four methine bridges) with an iron atom centrally located. The substituents of the porphyrin ring are four methyl groups, two vinyl groups and two proprionate side chains. Depending on the presence, position or deviation of the specific vinyl or methyl side groups, hemes are classified with an alphabetic letter. Heme types *a*, *b*, *c* and *o* are biologically the most relevant with type *b* being the most abundant, see Fig. 1.2. All gbs, but also other heme proteins such as horse radish peroxidase (HRP), chlorite dismutase and cytochrome P450 and many more, are heme-*b* bearing proteins. Examples of other heme-type containing proteins are cytochrome c oxidase (heme *a*), the cytochrome c_1 (heme *c*) that is part of bc_1 electron transfer complex and some bacterial terminal oxidases (heme-*o*) [10]. Other examples of heme derivatives include heme *I, m, D* and *S*.

Due to its substitution, the heme-*b* group has a hydrophilic (proprionates) and a hydrophobic edge. In gbs, it is held into its place by hydrophilic and hydrophobic interactions with surrounding amino acid (AA)s, and *via* a covalent bond between its central

[1] A tetrameric organization is essential for mammalian Hb to exert its function as an O_2 carrier. O_2 acts as a positive allosteric modulator which upon binding, enhances the affinity for O_2 of the other subunits. *Vice versa*, O_2 release causes a decrease in O_2 affinity allowing efficient delivery to the tissue.

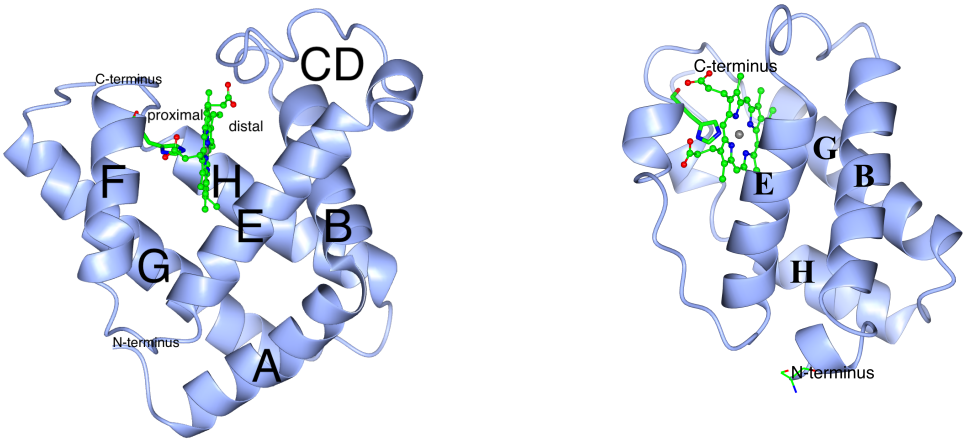

(A) (B)

FIGURE 1.1: The three-dimensional structural organisation of globins: (A) the 3-over-3 α-helical sandich (A-H) structure of horse heart Mb (pdb:1WLA). (B) Structure of the 2-over-2 fold of TrHb from the *Mycobacterium tuberculosis* (pdb:1S56).

iron atom and a nitrogen atom from F8His. The central heme iron has another four bonds with the pyrrole nitrogens of the protoporphyrin. The central iron atom and the 4 pyrrole nitrogens determine the heme plane with the 5th and 6th binding places perpendicular to it. This heme plane divides the heme pocket in a proximal side with the F8His (5th) and a distal side bearing the ligand-binding place (6th). The ligand-binding positions, can be occupied by an external ligand (O_2, CO, NO) or by an internal ligand being mainly the E7 side chain.

When the coordination number is six, these gbs are referred to as hexacoordinated. If the distal ligand is E7His, these gbs are called bis-His coordinated gbs. If the six^{th} ligand position is vacant, we call them pentacoordinated gbs. The heme iron in gbs can either be in the reduced ferrous (Fe(II)), the oxidized ferric (Fe(III)), or even the ferryl (Fe(IV)) oxidation state. Only when Fe(II), most gbs are able to reversibly bind O_2, but the Fe(III) and Fe(II) states are observed in many reaction intermediates. The ferryl state is a transient state that is formed during catalase or peroxidase reactions involving gbs, resulting in a Fe(IV)-porphyrin cation radical also known as compound I ($Por^{\bullet}$-Fe(IV)=O) and follow-up products.

1.3 Globin evolution and classification

Gbs can be classified based on their fold (3/3 and 2/2), or evolutionary-wise, based on their lineage: *F-family (3/3), T-family (2/2) and S-family (3/3).*

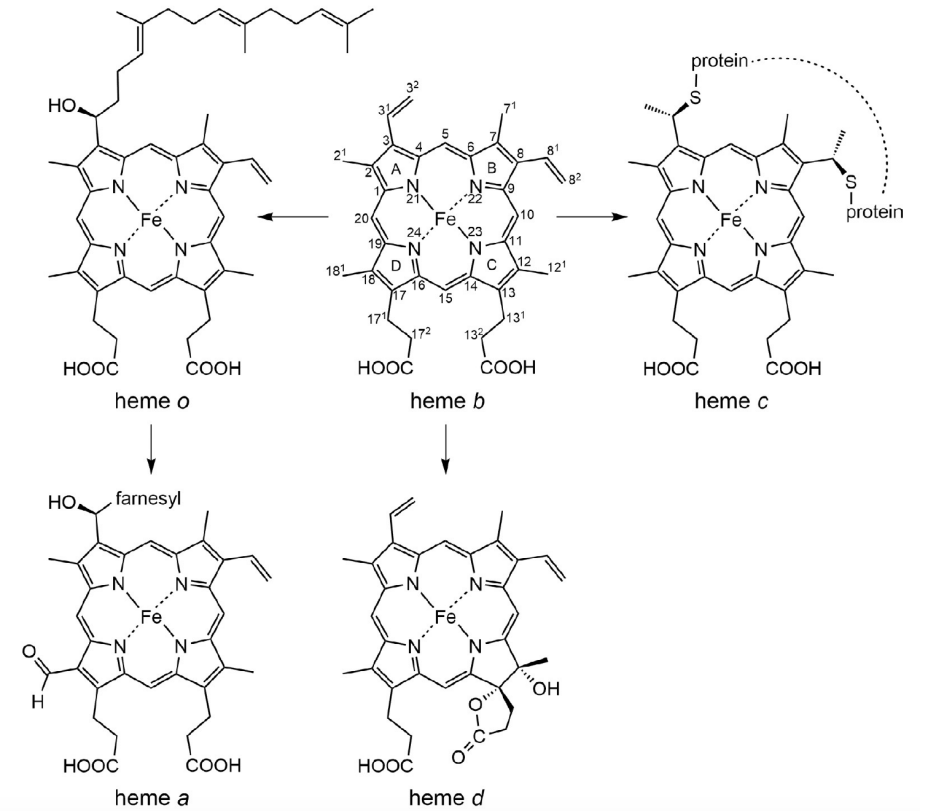

FIGURE 1.2: Some of the most common heme types: structures of hemes *a*, *b*, *c*, *d* and *o*. The biosynthetic relationship is indicated by arrows. IUPAC numbering is shown for heme *b*. This figure was taken from [11].

First, let us focus on the structural level. The classical three-over-three gbs, such as Mb, and the truncated two-over-two gbs, such as the truncated (Tr)Hbs, are single-domain (SD)gbs. Furthermore, chimeric (CH) gbs can be either FHbs, which consist of an N-terminal globin domain and a C-terminal ferredoxin reductase-like nicotinamide adenine dinucleotide (NAD)/flavin adenine dinucleotide (FAD)-binding domain [12, 13] or GCSs, which have an N-terminal globin-like domain and a C-terminal domain with a variety of activities (aerotactic, diguanylate cyclase, histidine kinase activity) [14, 15]. The *M*-, *S*- and *T-families* all have SD and CH representatives.

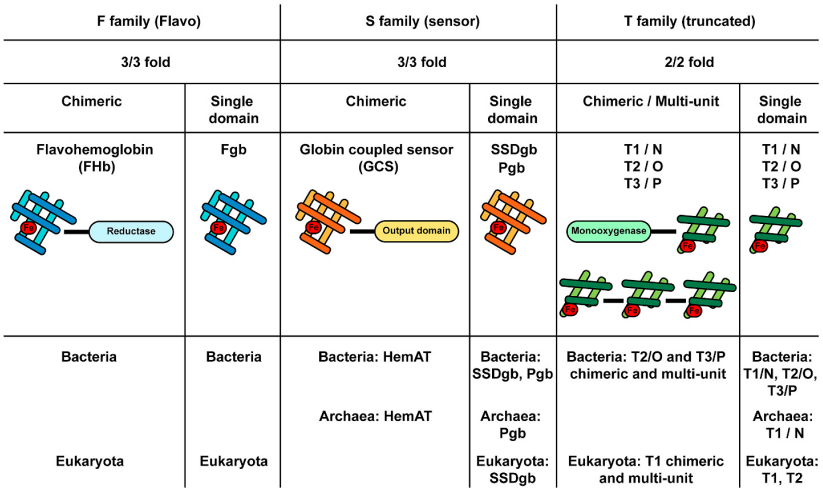

FIGURE 1.3: The three globin families. The F (or M) (Flavo) family, the S (Sensor) family and the T (Truncated) family can all be found in a chimeric or in a SD configuration. Figure taken from [16].

Evolutionary-wise, the Hbs, Mbs, and other SDgbs are related to the CH FHbs and are grouped together in the *M-family*, which stands for "Mb-like" (sometimes also referred as the *F-Family.*, Fig. 1.3). Chimeric (FHb) and SD (Fgb) F globins are found in bacteria and eukaryotes, but absent in archaea, and are numerically preponderant. The second separate *T-family* stands for "truncated", and thus contains the SD and CH 2/2 TrHbs. T family globins exist in three structural subfamilies, T1, T2 and T3, which, in bacteria, are also termed N, O and P, respectively. Chimeric and multi-unit T globins can be found in bacteria (T2/O and T3/P) and eukaryotes (T1), whereas SD T globins appear in bacteria (T1/N, T2/O and T3/P), in archaea (T1/N) and eukaryotes (T1 and T2) [16]. The third lineage or the "sensor" *S-family* contains the CH GCSs and SDprotoglobin (Pgb)s. These *S-family* gbs are thought to be closely related to the ancestral globin in the last universal common ancestor (LUCA), however evolutionary issues are still under debate. S family globins include CH GCS proteins which carry a C-terminal output domain (including HemAT for aerotactic heme sensor), and sensor SD globins (SSDgb) and their shorter version the Pgbs. HemAT is found in bacteria and archaea, SSDgbs are found in bacteria and eukaryotes, and Pgb in bacteria and archaea.

All three lineages are unequally distributed in the three kingdoms of life as revealed by an extensive genomic study of Vinogradov *et al.* [17] (see Fig. 1.4). Chimeric gbs have only been found in invertebrates, prokaryotes and yeasts, whereas the M-, and T-family are widespread over the different kingdoms. Interestingly, the 2/2 Hbs (T-family) are represented in all kingdoms.

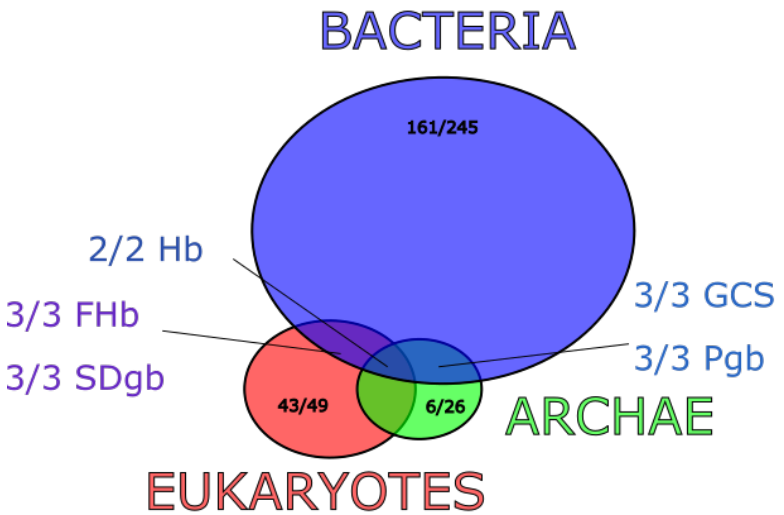

FIGURE 1.4: Venn-diagram adapted from [18]: in which globin sequences in 245 bacterial, 26 archaeal and 49 eukaryote genomes were searched and analysed. The diagram shows the three globin lineages represented unequally over the three kingdoms of life. The fraction represents the number of globin sequences identified in the total number of analysed genomes.

1.3.1 Prokaryote globins

The spread of the respiratory proteins known as (hemo)globins throughout all kingdoms of life[2] is no coincidence, as specialized O_2 transport and O_2 storage mechanisms in which gbs fulfill an important role are crucial throughout evolution. However, gbs occur so far in only about 62% of bacterial genomes according to [17]. Although the specific percentage may be considered outdated, the overall consensus in current research is that the majority of bacterial genomes harbor globins [16]. GCSs and Pgb are found in archae and bacteria, but some bacterial globin families and subfamilies such as the FHbs, TrHbs and SDgbs are found in eukaryotes as well. Nevertheless, gbs are present in each of the major bacterial groups and therefore it is likely that a globin originated in a bacterial ancestor that dates back from the LUCA of all living organisms [18]. Considering that the LUCA lived in an anaerobic environment, a respiratory function of this ancestor protein is unlikely, but other functions are not excluded like reactive oxygen species (ROS)- and reactive nitrogen species (RNS) detoxification functions, or redox functions that are observed for other prokaryote gbs [19].

1.3.2 Invertebrate globins

The invertebrates (non-chordate metazoans) comprises soft tissue animals lacking a vertebral column. Over ninety percent of animals belong to this overall very diverse class,

[2]Gbs are found in eukaryotes (vertebrate and invertebrates animals, fungi, plants and protists) and prokaryotes (archae and bacteria). [15, 1].

including worms, arthropods, cnidarians, echinoderms, mollusks and sponges, which span a wide diversity in morphology. Being far less complex than vertebrates, often without a profound vascular network, invertebrate organisms have to rely on O_2 delivery by diffusion, regulated by specialized proteins such as gbs. Not surprisingly, the common ancestral globin evolved in structural diverse gbs among those species as well. The class of invertebrate gbs did not receive as much attention compared to the vertebrate globin family and is therefore less extensively studied, but nevertheless, not less interesting [20, 21, 22, 23, 24, 25]. This implies that O_2-binding protein diversity is likely underestimated across this subkingdom. For example, a (3.5 million Da) Hb built up by 144 separate globin chains is found in Arthropods [26]. Such large globin complexes are unprecedented in other phyla. Furthermore, extracellular gbs are common in invertebrates [27]. Interestingly, the nematode *Caenorhabditis elegans, C. elegans* (*Ce*) is known to express up to 34 different gbs with large structural and functional diversity[3], which will be introduced and reviewed in Chapter 2, §2.2.

1.3.3 Vertebrate globins

Even though this work is focused on nematode[4] and archaeal gbs and not on vertebrate gbs, a small part on vertebrate gbs is in its place. With the emergence of larger animals, O_2 delivery by diffusion was insufficient and specialized structures, such as specific respiratory organs and circulatory systems emerged. Simultaneously, respiratory proteins, such as the ancestral globin, evolved in what we now know as the vertebrate globin family. The family consists of 8 different members including the well-known mammalian Mb and Hb. Additionally, in the past decades six other gbs were discovered in respective order: Ngb [6], Cgb [28, 5, 29], globin X[5], Y and E [30, 31, 32, 33, 34, 35] and androglobin [36]. A detailed overview on vertebrate gbs can be found in [37, 38, 39, 40, 16].

1.4 Globin function

1.4.1 Versatile functions of globins

A tremendous amount of research on vertebrate Mb and Hb resulted in the definition of a very clear function: Hb is an essential O_2 carrier capable of binding and delivering O_2. Mb is a muscle-specific globin that extracts O_2 from the blood and delivers it to the mitochondria. However, the story does not end there. Mb has affinity towards CO, NO, H_2O_2 and $ONOO^-$ suggesting that it potentially fulfills other physiological roles in cellular regulation and oxidative damage control [41]. More generally, given the large structural diversity within the globin family, many alternative functions have been associated with and suggested for gbs. *In vitro* they are found to act as O_2, HS^- and NO carriers and sensors, but also enzymatic functions such as superoxide ($O_2{}^-$) dismutase

[3] Related nematodes harboring orthologs to many Caenorhabditis gbs.

[4] Nematodes are evolutionary-wise separated from the vertebrates since the emergence of the Coelomates about 600 to 580 million years ago.

[5] Restricted to fish and amphibians

activity, NO dioxygenase, reductase activity and peroxidase activity, are observed for gbs [42]. Although many questions are still open, some of these functions are already found to be biologically relevant.

Through heme pocket mutations in the course of evolution, the O_2-binding kinetics were fine-tuned matching the specific needs of an organism. In some cases, such as the Hb of the parasitic nematode *Ascaris suum*, the affinity for O_2 has been found to be extraordinary high due to stabilization of the bound O_2 by H-bonds from the E7 and B10 residues, and therefore, efficient O_2 delivery is not the main function. Low O_2 affinity on the other hand is observed in genetic disorders associated with human Hb-specific single AA mutations and for the clam *Lucina pectinata* Hb, that instead has a very high affinity for H_2S [43, 44].

Ngb is the first discovered vertebrate globin that displays bis-His hexacoordination [6, 45], a coordination state that was already observed in plant (phytoglobins) and bacterial gbs [46, 47]. The distally coordinated HisE7 residue in Ngb can make place for O_2 or other ligands allowing reversible binding and, therefore, Ngb is in principle capable of having a function involving O_2 binding. However, this bis-His coordination state can be very strong in some gbs and hence, one can raise the question whether bis-His coordinated gbs are involved in other functions than ligand binding. Ngb was for instance found to be capable of electron transfer to cytochrome *c* [48], potentially playing a role in preventing hypoxia-induced apoptosis [49]. Until now, the exact role of many bis-His coordinated gbs is not clear.

1.4.2 Globins and reactive nitrogen species

Structure, biosynthesis and function of nitric oxide RNS, which stands for a collection of nitrogen and oxygen-containing small molecules, play an important role in globin-ligand interactions [50]. One of the most important RNS is nitric oxide (NO), because many reactive products are derived from it. NO is a gaseous molecule with an unpaired electron (radical) occupying the antibonding π^* orbital, which makes it chemically reactive. NO can be oxidised to form nitrogen dioxide (NO_2) and in aerobic environment, nitrite (NO_2^-) and nitrate (NO_3^-). Reversely, the reduction of NO leads to nitroxyl, hydroxylamine and ammonia.

Nitric oxide became a hot topic in biology [50], especially in the beginning of the 21st century as this simple molecule has proven to be important in many regulatory mechanisms and signalling pathways covering cardiovascular function [51], memory [52], and anti-tumor responses [53]. NO regulates biofilm formation in different bacteria [54, 55]. Also gut bacteria and parasites have developed clever mechanisms that exploit NO [56]. Many of these pathways involve NO binding to heme proteins, such as cytochrome *c* oxidases, catalases, nitrophorins and many more including gbs [57, 58, 59, 60]. Furthermore, NO can modify thiol groups of cysteines (for example in cyclic nucleotide-gated (CNG) channels) and other amino-acid residues, altering protein function [61]

Almost every species is able to foresee in its own NO production *via* specialized enzymes, as depicted in Fig. 1.5, that shows the most important sources of NO. The pathway involving NOS, which is a heme-containing enzyme, is of great importance. For example, in the mammalian bloodvessels, NO is synthesized in the endothelial cells that

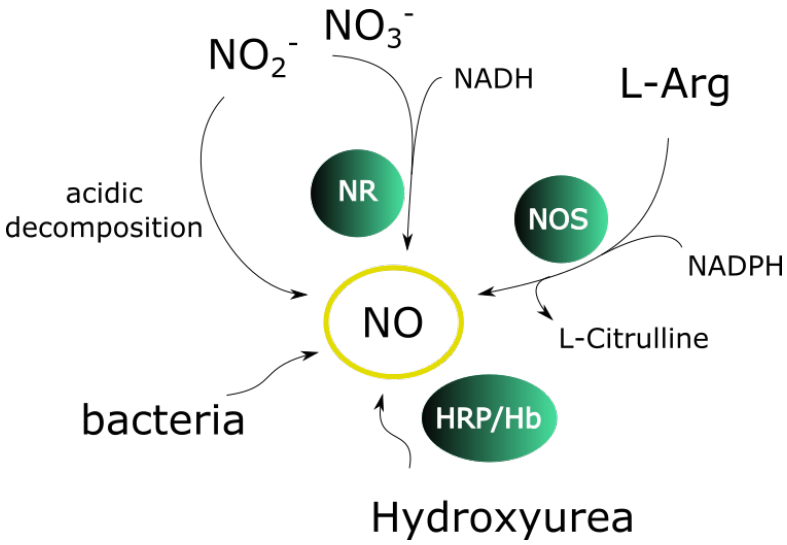

FIGURE 1.5: Nitric oxide (bio)synthesis: nitric oxide can be converted from nitrite and nitrate by proteins (green) such as nitrate reductases (NRs) or is formed *via* the L-arginine-dependent NOS [62, 63]. Direct uptake of NO produced by bacteria (via previous mechanisms) can be another source of NO [64]. Hydroxyurea is a clinically used compound that can be a viable source of NO when catalyzed by Hb [65] or even by other enzymes found in plants e.g. HRP [66].

line the blood vessel. The L-arginine metabolism involves the interaction with endothelial NOS in a complex reaction pathway together with O_2 to form NO and citrulline. The effort to obtain the structure and function of NOSs is fascinating and many aspects of the reaction mechanism are still under investigation [67, 68]. L-arginine is furthermore involved in the synthesis of $NO_3{}^-$, $NO_2{}^-$ and NO is created as an intermediate product. The nematode *Ce*, however, approaches a different strategy to obtain NO because it lacks its own NOS and therefore relies on environmental NO produced by bacteria [64]. In plants, the mechanism for NO production is more complex, involving the reduction of nitrate to nitrite to NO and an arginine-dependent mechanism as well [69]. Finally, therapeutic agents enhancing NOS activity (statins), or hydroxyurea used to treat sickle cell disease cause nitric oxide release.

Studies addressing the physiological role of NO, often mention its role in vascular regulation and the homeostasis in *vascular smooth muscle relaxation* (SMR) in mammals [70, 51]. Notably, gbs fulfill a crucial role in that process. The specific mechanism involves the activation of guanylate cyclase (GC) by NO[6]. Deoxygenated globins are able to reduce nitrite to NO, and thus contribute to this NO signalled activation pathway during ischemia. Additionally, gbs contribute to the activation and regulation of GC [73, 74].

[6]a heme-containing enzyme essential for the conversion of GTP to cGMP. cGMP on its turn activates protein kinase G which will activate a Ca^{2+} transporter causing an extracellular Ca^{2+} increase driving the muscle regulation mechanism. cGMP activates MLC phosphatase as well, again stimulating SMR. Recent reviews on the topic can be found here [71, 72].

This is a great example of a well-studied process, but the interplay between oxygen, NO, nitrite and in general RNS and globins extends far beyond blood flow regulation and oxygen delivery to tissues. We end the chapter with a brief overview of relevant globin reactions in the context of RNS. We will demonstrate this for mammalian Hb, but the same reactions can be described for Mb (which are generally faster due to the lack of allosteric effects [75]) and other gbs [76, 77, 60].

Hb removes bioactive NO Gbs fulfil a crucial role in the NO metabolism and their reactivity strongly depends on the oxygenation level and pH of the environment in which they reside. First we have a look at oxygenated Hb. The O_2-bound state in gbs can undergo various reactions including the following one with NO:

$$\mathrm{HbFe(II)}{-}\mathrm{O_2} + 4\,\mathrm{NO} \longrightarrow \mathrm{(met)HbFe(III)} + 4\,\mathrm{NO_3}^{-}. \tag{1.1}$$

This reaction is known as the dioxygenation reaction in which the globin is oxidized and $NO_3{}^-$ is created. Note that the reaction stoichiometry is 4-fold, as Hb bears 4 heme groups.

On the other hand, NO can react again with the Fe(II) deoxy state as well according to

$$\mathrm{HbFe(II)} + 4\,\mathrm{NO} \longrightarrow \mathrm{HbFe(II)}{-}\mathrm{NO}, \tag{1.2}$$

in which NO ends up a tightly bound, nitrosyl complex, a state which function is not immediately clear, but it can be regarded as a feedback mechanism in stabilizing the R-state[7] in Hb. Nitrosylation does not permanently eliminate NO as the dioxygenation reaction does, but the dissociation rate constant of NO is both slow for T and R states.

The reduction of $NO_2{}^-$ to NO: nitrite reductase activity Nitrite is less reactive than NO, and mammalian globins (Hb, Mb, Ngb and Cgb) are all known for their ability to reduce nitrite to NO, strongly indicating a physiological relevance of the reaction. In order to do so, nitrite must enter the heme pocket and bind the heme. The reaction, and thus the NO formation is regulated by a globin-dependent control mechanism, which is strongly controlled by oxygen levels.

Under *hypoxic* conditions, NO is created during the nitrite reductase (NiR) reaction in which the Fe(II) deoxygenated (penta-coordinated) Hb interacts with nitrite. An oxygen atom removal ruptures the N−O bond in $NO_2{}^-$ and a reduction should follow next. The NiR reaction can be expressed as follows:

$$4\,\mathrm{NO_2}^{-} + 8\,\mathrm{H}^{+} + \mathrm{HbFe(II)} \longrightarrow \mathrm{HbFe(III)} + 4\,\mathrm{NO} + 4\,\mathrm{H_2O}, \tag{1.3}$$

On the other hand, nitrite can also react with the globin under *normoxic* conditions, forming nitrate. This oxidation reaction occurs when nitrite reacts with $\mathrm{HbFe(II)}{-}\mathrm{O_2}$

[7] Mammalian Hb can be either in the closed T-state or open R-state. The R-state promotes O_2 binding, whereas the T-state is formed once O_2 is released from a critical number of sites in the liganded tetramer. This allosteric interplay between T- and R-state is crucial for efficient O_2 uptake and delivery.

via a more complex mechanism that involves various reaction pathways and reactive intermediates such as H_2O_2 and Fe(IV) Hb [78, 79, 80, 81] resulting in the net reaction:

$$\mathrm{HbFe(II)}{-}\mathrm{O_2} + 4\,\mathrm{NO_2}^- + 4\,\mathrm{H}^+ \longrightarrow \mathrm{HbFe(III)} + 4\,\mathrm{NO_3}^- + \mathrm{O_2} + 2\,\mathrm{H_2O}. \tag{1.4}$$

This reaction takes place in the bloodstream creating $NO_3{}^-$ and (met)HbFe(III) and explains why $NO_3{}^-$ and not $NO_2{}^-$ is the predominant metabolite of NO *in vivo* [82, 83, 84, 79]. Moreover, the reaction prevents the nitrite accumulation *in vivo* under normoxic conditions and is among other reaction pathways, responsible for the NO lifetime control [50].

Nitro versus nitrito binding In the NiR mechanism, nitrite binds the heme and the subsequent reaction can occur *via* two (or more) mechanisms involving H^+ which is either originating from H_2O in the heme pocket or donated by e.g. the distally located protonated HisE7. It is known that the binding mode of nitrite at the heme plays a crucial role in the choice between the two pathways. One distinguishes the O-bound *nitrito* or the N-bound *nitro* binding mode (see Fig. 1.6) [85, 86, 87, 88, 89].

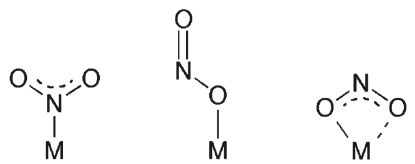

FIGURE 1.6: The three common binding modes of nitrite: From left to right, the N-bound *nitro*, the O-bound *nitrito* and the O, O-*bidentate* binding mode.

In the *nitro* mode, a formal double protonation of the O-atom precedes the release of a water molecule and generation of an Fe(III) – NO species which then dissociates. The Fe(III) – NO intermediate will eventually be in equilibrium with Fe(III)Hb releasing NO:

$$\mathrm{Fe(II)}{-}\mathrm{nitro} + 2\,\mathrm{H}^+ \longrightarrow \mathrm{HbFe(III)}{-}\mathrm{NO} + \mathrm{H_2O} \tag{1.5}$$

$$\mathrm{Fe(III)}{-}\mathrm{NO} \longrightarrow \mathrm{Fe(III)} + 4\,\mathrm{NO}. \tag{1.6}$$

The $\mathrm{Fe(II)}{-}\mathrm{NO} \longleftrightarrow \mathrm{Fe(III)}{-}\mathrm{NO}^+$ resonance structure can for example either release NO, which can nitrosylate a Fe(II) heme in soluble GC resulting in vasodilation. NO can also bind the Fe(II) heme of the globin, if present, as shown in eq. 1.9. Alternatively, it can also reduce the heme in what we call *reductive nitrosylation* [90]. This is the opposite of NiR activity, which is mediated by the presence of OH^-:

$$\mathrm{Fe(III)}{-}\mathrm{NO} + \mathrm{OH}^- \longrightarrow \mathrm{Fe(II)} + \mathrm{HNO_2} \tag{1.7}$$

$$\mathrm{HNO_2} + \mathrm{OH}^- \longleftrightarrow \mathrm{NO_2}^- + \mathrm{HNO_2}. \tag{1.8}$$

Interestingly, the formed HbFe(III) in Eq. 1.6 and NO can react with NO_2^- according to:

$$\mathrm{Fe(III)-NO_2^- + NO \longrightarrow HbFe(II) + N_2O_3.} \tag{1.9}$$

The formed N_2O_3 could serve a role in preventing formation of damaging superoxide in the mitochondria, or disproportionate again in nitrite and NO.

In the O-linked *nitrito* mode, NO is released through an ON−O bond homolysis after protonation of the O-bound nitrito ligand, resulting in a Fe(III) hydroxo species [91].

$$\mathrm{Fe(II)-nitrito + H^+ \longrightarrow Fe(III)-OH^- + NO} \tag{1.10}$$

$$\mathrm{Fe(III)-OH^- \longleftrightarrow Fe(III) + OH^-.} \tag{1.11}$$

This latter can be converted to the Fe(III) met state or a ferric-NO intermediate.

Overall, by highlighting a few relevant interactions between Hb and nitric oxide and nitrite, we showed that the chemical mechanisms involved are complex but crucial for maintaining proper cellular function and facilitating a wide range of physiological processes in various life forms. These RNS-globin interactions are also highly dependent on the globin structure, and consequently have many implications on the cells and organisms in which the globins are expressed and reside. Part of these interactions are investigated in this thesis for a specific set of globins. Especially, we focussed on the interaction of nitrite with ferric globins and investigate the above-mentioned binding modes, but also the nitrosylated forms and ferric-NO bound states will be addressed and discussed.

Chapter 2

Research objectives and motivation

In recent years, the knowledge on the structure and function of gbs increased tremendously due to advancements in genome sequencing and biochemical characterization methods. The creation of various databases containing genomic and structural information on proteins (such as Uniprot and the Protein Data Bank) made this information readily available to the scientific community and general public. Decades of research lead to a detailed insight in the molecular function of vertebrate Hb and Mb, however, the augmentation of numerous gbs to the family with a wide structural and functional diversity, expression pattern and appearance resulted in a non-adequate description of the current functionality. Until today, new gbs are being discovered and novel functions are associated with them. With this information explosion, the need increased for enhanced characterization methods, ranging from computational methods to whole three-dimensional structure determination methods and advanced spectroscopy.

2.1 Advanced methods to study the globin-nitrite interaction

The research group of Prof. Van Doorslaer, Theory and Spectroscopy of Molecules and Materials (TSM^2), addresses the growing need for new and better methods and developments to characterize gbs and metalloproteins in general by the application and exploration of existing electron paramagnetic resonance (EPR)-based strategies on heme proteins. Moreover, it has a long-standing collaboration with the research group of Prof. Dewilde *et. al.*, Proteinchemistry Proteomics and Epigenetic Signalling (PPES), and expertise in the study of gbs with advanced pulsed EPR methods which has led to a better understanding of the electronic structure of ligand binding in gbs [92, 93, 94, 95]. In addition to conventional methods, including ultraviolet (UV)-vis and resonance Raman spectroscopy, which give us a general idea about the coordination and spin-state of the heme protein complex under investigation, the choice of EPR as the main characterization tool is valid because the paramagnetic nature of many globin states. Standard CW

EPR can be combined with more advanced pulsed hyperfine methods to provide structural information on the heme pocket and on the electronic structure of the coordination bonds that the heme iron forms with interacting ligands [96]. A detailed introduction and description of the various EPR methods used in this work can be found in Chapter 3.

2.1.1 Towards a better understanding of the globin-nitrite interaction

In this thesis, I investigate a selected set of gbs from *Ce* and the protoglobin of *Ma*, with a special focus on the globin-nitrite interaction. Advanced EPR methods, complemented by a multi-spectroscopic approach including electronic circular dichroism (ECD) and resonance Raman (rRaman) spectroscopy, are used. A detailed overview of the characteristics of these gbs follows below.

From a biological point of view, the study of the globin-nitrite interaction is highly relevant because next to O_2 binding and transport functions, gbs fulfill a crucial role in the nitrogen metabolism in many organisms in which they may carry out a nitrite reductase function. In Chapter 1, the reaction mechanism of the NiR reaction in globins is introduced in general; however, the detailed mechanism of this reaction in vertebrate Hb is not well understood and is highly dependent on the heme pocket structure and subsequent stabilization of nitrite at the heme. Furthermore, the globin-nitrite interaction is very complex with intermediate states, that in some cases lead reactions creating heme modifications or inducing partial heme loss [97, 98, 99, 100, 101]. Overall, open questions remain about the globin reaction with nitrite, derivatives and other small ligands, in particular concerning the following:

The nitrite isomer state at the heme From a more methodological point of view, the study of the globin-nitrite interaction is highly relevant. The nitrite binding mode to heme proteins, including Mb, Ngb, cytochrome c peroxidase (CCP)s, nitrophorin (NP)s, and many more, has recently received a lot of attention because this binding mode (N-nitro vs O-nitrito) has implications for the subsequent NiR mechanism [102, 103]. Currently there is some discussion about the isomer state in nitrite-bound complexes. Ambiguity exists between experimentally observed linkage isomers and quantum mechanics and or molecular mechanics calculations [104, 105, 106, 86]. The experimentally observed linkage isomer is frequently determined with X-ray crystallography in which the protein needs to be in a crystalline state [107, 108, 109], which is often a bottle neck. Moreover, the crystal packing may force the protein to take a certain conformation, which might not be biologically relevant. Therefore, EPR methods were explored as a tool for the determination of the isomer state, as EPR does not require a crystalline state and therefore lies closer to the actual conformation *in vivo*.

In particular hyperfine spectroscopy, CW-EPR and ECD spectroscopy was used in this work, because they are proven to be very powerful tools. However, the interpretation of the data obtained by these methods on heme proteins is not always well understood. Overall, this work aims at demonstrating the strength of EPR and other spectroscopic

techniques, and identifies the current pitfalls and limitations of these techniques, stimulating future methodological developments.

2.2 Globins in *C. elegans*

Besides the more general goal of getting more insight in the Fe(III) globin-nitrite interaction, we also aim to better understand the role and explore novel functions of gbs found in the nematode *Ce*. The PPES group was closely involved in the discovery of the numerous gbs found in *Ce* and their research efforts over the past 15 years, has resulted in many renewed insights in globin function [110, 111, 112, 113, 114, 115, 116, 117, 118, 119]. This was mainly accomplished by over-expression, purification and the subsequent biochemical characterization and analysis. PPES has a large in-house library of *Ce* globin constructs, readily expressible, allowing to study gbs on a protein level.

2.2.1 The model system *C. elegans*: why do we study worms?

The nematode *Ce* is a popular model organism and was first proposed by the Nobelprize laureates in Physiology or Medicine of 2002, Brenner, Sulston and Horvitz [120, 121]. Another two Nobel prizes were awarded to *Ce* researchers: Fire and Mello in 2006 for their discovery of RNA interference and Chalfie in 2008 for the discovery and development of green fluorescent protein (GFP) [122, 123], which is demonstrative of the major impact studies of the nematode have had on biomedical research of today.

A model organism can be defined as a well studied, easy to maintain, life-form that has specific features to describe certain biological phenomenons such as cellular processes, organ development, aging, pathology, *etc.* Popular model organisms in order of complexity from low to high are the bacterium *Escherichia coli*, baker's yeast *Saccharomyces cerevisiae*, the nematode *Ce* which will be the model of interest in this thesis, the fruitfly *Drosophila melanogaster* and to give an example of a vertebrate: the mouse *Mus musculus*.

Ce is a free living nematode that is widespread worldwide. It has a rapid life-cycle of three days, feeds on bacteria and lives on rotting organic matter, such as vegetable waste [124]. It is relatively small in size (adult 1 mm), has a smooth exterior and is transparent to visible light. The nematode population mainly consists of self-fertilizing hermaphrodites with a small percentage (0.2 %) of males. After hatching from the egg, the development goes through 4 larval stages (L1-L4). Under stressful conditions such as depletion of nutrition, stage L2 larvae are able to form *Dauer* larvae which are able to survive for months and continue their life cycle as slightly altered L4 larvae when conditions are restored (See Fig. 2.1).

Its fixed number of somatic cells (959 in the adult hermaphrodite, 1031 in the adult male), makes it a popular organism for genetic studies, but also its fixed number of neurons (302) has allowed to completely map the wiring network over 25 years ago [125, 126]. *Ce* is an ideal model organism, since it is relatively large and the rapid life cycle makes it easy to cultivate and grow the organism under laboratory conditions. Because it is self-fertilizing, it is easy to propagate genetic strains and design genetic

crosses. The easy genetic manipulability, maintenance and the fact that *Ce* is viable even after being frozen makes it possible to study the phenotype of genetically modified strains [120]. Its transparent nature allows studying the nematode under a microscope *in vivo*, e.g. in behavioural assays or in studies to track protein expression by labelling it with a fluorescent marker [122]. The *Ce* genome was the first eukaryotic genome ever sequenced, and with this, a whole new era in modern biological science was entered [127]. This means that all building blocks that make up the nematode are known, but far from completely understood. By now, many genomes including the human genome are completely sequenced and by comparative genetic studies, we can start to unravel the code, study newly discovered proteins and link them to various diseases [128].

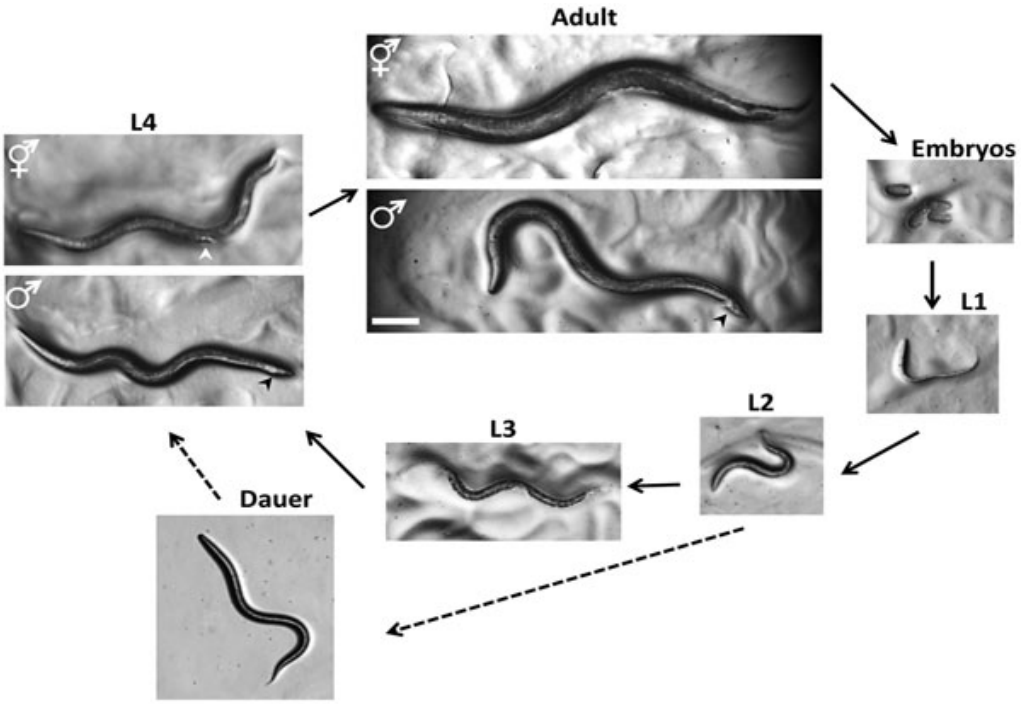

(A)

FIGURE 2.1: Life Cycle of *C. elegans*. After hatching from the egg, the development goes through 4 larval stages (L1-L4). Figure obtained from WormAtlas [129]

2.2.2 State of the art of the 34 *C. elegans* globins

Discovery Already in the 19th century it was recognized that nematodes have gbs, or at least oxygen carriers, according to a review paper of Blaxter [130, 131] and were given the name "nemoglobins". Later on, it was indeed biochemically and spectroscopically clear that these carriers were globins as we know them today. For example, a red pigment in the nematode *Mermis nigrescens* has been shown spectro-photometrically to be a globin

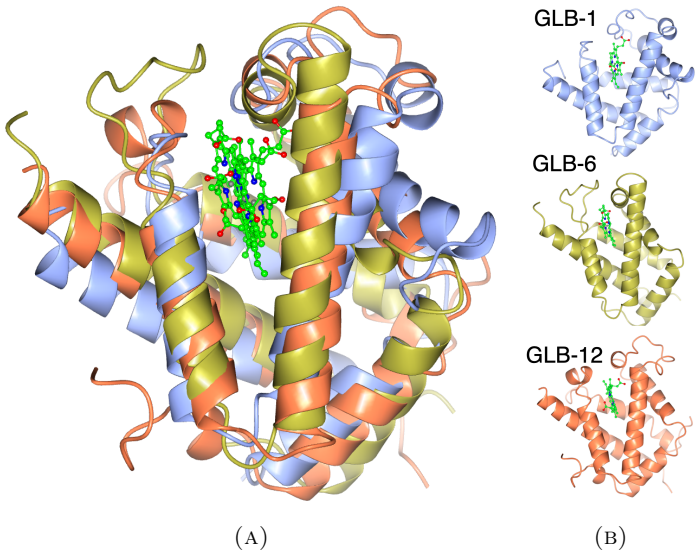

FIGURE 2.2: Crystal structures of GLB-1 (pdb:2WTG, color ice), a GLB-6 construct (pdb:3MVC, color gold) and GLB-12 (pdb:4BJA, color coral). The structures are shown as monomers.

[132]. Only a few dozen gbs across different Nematoda were known in the mid-nineties, most of them in parasitic worms. The globin of *Ascaris suum* received particular attention because of its 25×10^4 times higher O_2 binding affinity than human Hb [133, 134]. Its function remains debated, but a potential O_2 detoxification role driven by nitric oxide is proposed [135, 136]. The first globin detected in *Ce*, was discovered in an early stage in the genome sequencing of *Ce* [137] by chance on chromosome III (gene ZK637.13). Today, this globin goes by the name "globin number 1" (GLB-1), and the fact that it was given a number already reveals that many more would be identified in the following years. Indeed, almost two decades ago, Hoogewijs *et al.* showed that 33 and more recently [138], 34 gbs are transcribed and expressed in distinct cell types [110]. The availability of the full genome of *Ce* and other nematodes allowed in-silico searches for matching globin motifs based on the alignment with more than 700 gbs [139]. The large number of globin genes is surprising, but the finding is not unique since *Ce* accounts for 37 potential insulins [140] and 40 genes of metalloproteases [141]. Also some other metaozoans contain large number of globin genes [16] such as the 40 globin genes of the insect *Chironomus* [142], the multiple globins of the acorn worm [143] and echinoderm [144].

Structural and functional characterization Three years later in a follow-up study [112], it was confirmed that 33 widely diverse putative globin genes were expressed. Some of them in chemosensory neurons supporting behavior and motor functions. Indeed, among the 33 discovered gbs, some gbs showed specific up-regulation as a consequence of O_2 deprivation [112]. More specifically the URX and BAG neurons in *Ce* are responsible

for O_2 and CO_2 sensing, resulting in social and feeding behavior [145, 146, 147]. The low expression and huge sequence diversity may point out that the gbs evolved into very specialized cell-specific proteins [111, 112]. Additionally, the lack of evidence for recent gene duplication events points out a long evolutionary history.

At the start of my PhD, seven globins were partially characterized biochemically: GLB-1, GLB-5, GLB-6, GLB-12, GLB-13, GLB-26, and GLB-33 (the latter only containing the globin domain). These globins were also localized *in vivo*, and putative functions were ascribed to them [114, 74, 145, 148, 149, 119]. The research groups of my supervisors (PPES and TSM[2]) were involved in many of those studies. To date, only the crystal structure of GLB-1, GLB-6 and GLB-12 have been determined, see Fig. 2.2. A concise overview is given in the Table. 2.1, but for the detailed specifications I refer to the original papers and for more specifications on the (globin) genes of *Ce*, I suggest to access `https://wormbase.org/` [150]. Since GLB-33 and GLB-3 were investigated in this work, a more detailed description follows below in which the current knowledge gaps we aim to address in this work are formulated.

2.2.3 *C. elegans* globins studied in this work

GLB-33 Globin number 33 (GLB-33, gene: Y75B7AL.1, Chromosome V) is expressed in the motor neurons or interneurons in the head, tail and the nerve cord [112], but it was not until 2015, that a first biochemical characterization and the *in vivo* localization was published by Tilleman *et al.* [118]. The authors confirmed the membrane localization via transfection of GFP-tagged GLB-33GD in human neuroblastoma SH-SY5Y cells. With its 542 AAs, GLB-33 is the largest of its kind and has a 372 AAs long N-terminal extension that consists of a G protein-coupled receptor (GPCR) domain with 7 transmembrane (TM) helices and a C-terminal GLB-33 globin domain (GD) (see Fig. 2.3 for model)[1]. Furthermore, the GD has by definition the conserved F8His but CD1Phe and E7His/Gln are replaced by CD1Val and E7Ile. The spectral characterization was limited to the GD and showed that the over-expressed Fe(III) form coordinates to OH^- in two distinguishable low-spin hexacoordinated (LS/6c) Fe(III) forms. When reduced with sodium dithionite, it becomes fully pentacoordinated (5c). GLB-33GD shows a high affinity for O_2, a high auto-oxidation rate and is capable of reducing nitrite to nitric oxide faster than any other reported globin [118, 114]. From homology modelling, it is plausible that ligand binding can induce a conformational change allowing allosteric regulations between the 7TM and the GD.

[1]Other CH heme proteins besides GLB-33 are known in *Ce* namely the CH O_2 sensor guanylate cyclase [146, 151]

	Gene	nr. AAs	Localization	Putative function	Spin-state	Coordination	Redox pot. [V]	Ligand binding	multi-merization	Ref.
GLB-1	ZK637.13	159	VC neuron, germ line, head muscle, head neurons, tail neurons	role in O_2 metabolism	High-spin	His/H_2O	n.d.	O_2, CO, NO	homodimer	[114]
GLB-5	C18C4.1	397	PQR, head neurons, intestine, pharynx, somatic nervous system	O_2 sensor	n.d.	Bis-His	n.d.	O_2	n.d.	[74]
GLB-6	C18C4.9	389	neurons, somatic nervous system	redox sensor	Low-spin	Bis-His	-0.193	None	n.d.	[148]
GLB-12	C52A11.2	266	gonad, neurons, vulva	electron transfer	Low-spin	Bis-His	-0.244	O_2, CO, CN^-	n.d.	[119]
GLB-13	F19H6.2	282	head, somatic nervous system and tail neurons	neuroglobin-like, ROS signalling	n.d.	n.d.	n.d.	n.d.	n.d.	[149]
GLB-26	T22C1.2	183	membrane localized, nuclear lamina, anal depressor muscle, head mesodermal cell, intestinal muscle	electron transfer	Low-spin	Bis-His	n.d.	CO	monomer, homodimer	[114]
GLB-33GD	Y75B7AL.1	546 (462)	neurons, somatic nervous system	O_2 sensor	Low-spin	His/OH^-	n.d.	O_2, CO, NO	monomer	[118]

TABLE 2.1: Physicochemical characteristics of over-expressed globin genes of *Ce* as known at the start of my research.

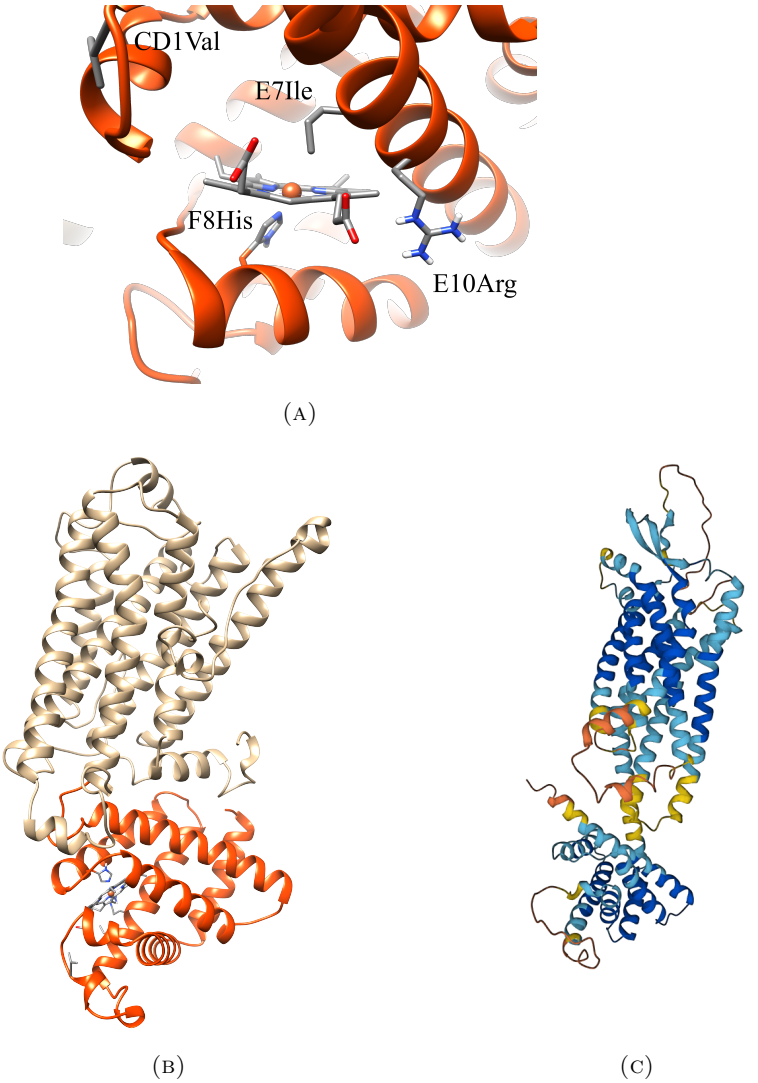

FIGURE 2.3: I-TASSER [152] (A) model of GLB-33 as published in [118]. The heme pocket structure of *Ce* GLB-33GD, with key residues highlighted in a sticks representation. (B) Docking of the globin domain (orange) with the N-terminal 7TM domain (beige). (C) full-length GLB-33 model generated by Alphafold [153, 154].

The limited functional information we know was found by Hoogewijs *et al.* in which the authors found that GLB-33 was mildly induced by anoxia, and required hif-1 activity[2] which is unprecedented. Based on the CH nature and similarities with an *Ascaris suum* FMRF-amide receptor (24% identity and 44% similarity) a similar role as a neuropeptide

[2]hif-1 activates transcription of genes whose protein products function to regulate O_2 availability. [155].

receptor for GLB-33 is currently proposed, in which its activity might be influenced by O_2 or NO levels, but the exact mechanism remains until now elusive. The closest related human receptor with known structure is the β_2 adrenergic G-protein-coupled receptor (41% sequence similarity to 7TM domain), which may indicate that a G-protein-coupled receptor function is plausible.

Within the *Ce* globin scope, one of the aims of this thesis is to better understand the origin and purpose of the OH^--ligation in the as-expressed form of the GD. The origin of the two low-spins is unclear and a better understanding of the heme pocket structure is needed. Next, the extremely fast nitrite reductase activity, combined with a very hydrophobic heme-pocket raises many questions about the underlying mechanism of this NiR reaction. For that purpose, the Fe(III) nitrite (NO_2^-) bound state and the Fe(II) NO-bound nitrosyl state of the globin domain of GLB-33 was investigated in more detail, in line with the first objective (Chapters 4 and 5).

GLB-3 GLB-3 (gene: C06H2.5, Chromosome V) is another *Ce* globin which is far less known compared to the globins listed in Table. 2.1. Again, from Hoogewijs *et al.* [110, 111, 112] we know that it is mainly expressed in 20 to 30 neurons in the head, tail and the nerve cord and in the somatic gonad. It is predicted that GLB-3 is spliced into two isoforms of 210 and 282 AAs long, respectively. Remarkably, the glb-isoforms are coding for a large number of cystein residues: 9 Cys in GLB-3a and 12 in GLB-3b. Cysteines are sulfer-containing AAs that, when located in the proximity of each other, are able to form disulfide bonds either inter- or intramolecularly. Cys is the least abundant AA in proteins and often plays a role in functionally active sites, especially in redox processes [156].

The gene structures of these isoforms are given in Fig. 2.4, which shows that glb-3a differs from glb-3b as it lacks a myristoylation site precedenting a (masked, glb-3b only) mitochondrial targeting sequence at the N-terminal (Fig. 2.4). Both isoforms are likely targeted to mitochondria and anchored via palmitolylation in combination with myristoylation (glb-3b only). Preliminary data of our group, furthermore, points out that GLB-3 is a mitochondrial protein[3]. This might be the first evidence to our knowledge of a mitochondrial globin in invertebrates. Knock-out of the gene coding for *Ce* GLB-3, gives a clear phenotype, namely sterility. Its role in reproduction and how this relates to the large number of Cys AAs, is yet to be understood.

Clearly, further research is needed to unravel the structure-function relationship. Therefore, the second aim in this thesis is focused on the discovery of potential functions of GLB-3, which is part of the FWO project GDC3518N, I was jointly working on with dr. Zainab Hafideddine.

[3]Upregulation of GLB-3 was observed upon RNA1 knockdown of the mitochondrial complex III subunit cyc-120 and the treatment with resveratrol.

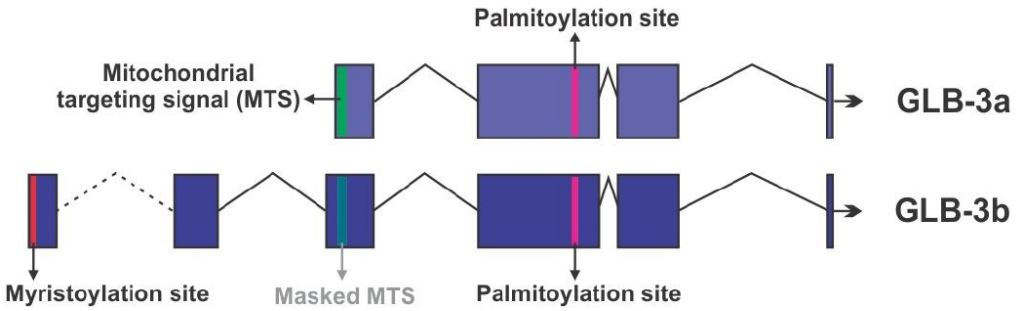

(A)

FIGURE 2.4: Gene structure of *Ce* glb-3. Figure taken with permission from FWO project GDC3518N application of the supervisors

2.3 The protoglobin of *Methanosercina acetivorans*

Methanosarcina acetivorans is a metabolically diverse, methane-producing species of methanogenic archaea that lives in oil wells, sewage lagoons, trash dumps, decaying leaves, stream sediments, and the stomach of cows, among other places. (Fig. 2.5). It is a strictly anaerobic methane-producing, and is used as a model organism for the understanding of methanogenesis [157, 158].

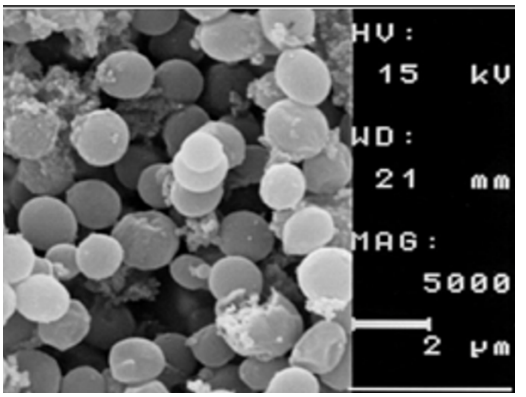

FIGURE 2.5: Scanning electron microscope image of *Ma*Pgb. image taken from [159]

Besides the versatile gbs in *Ce*, part of this thesis is focused on *Ma*Pgb. The unique structural properties of *Ma*Pgb has been puzzling researchers for almost two decades and still many questions remain unresolved about its special nature and function. Until now, limited attention was paid to the NO_2^--binding of *Ma*Pgb. Nevertheless, a role in detoxification as an RNS/ROS scavenger (and its associated enzymatic activity) is still

the most commonly suggested function, since this might facilitate the conversion of CO to methane, a vital process within *Ma*.

2.3.1 The archaeal globin

Heme proteins in the form of CH heme sensors were already present in early prokaryotic life forms [160]. They are predominantly globin based and we refer to them as the globin-coupled sensors (GSC)s, see chapter 1§1. It was postulated by Freitas *et al.* [160] that, based on phylogenetic analysis, an ancestral hemoglobin is to be found in archae and that this ancestor should be a globin-only progenitor. However, it could have disappeared throughout evolution. A year later, two so-called Pgbs were discovered: one in the strictly anaerobic methanogen *Ma* and one in the obligately aerobic hyperthermophile *Aeropyrum pernix* (*Ap*) [161, 162]. These were initially thought to be the closest related to a bacterial common globin ancestor, but based on phylogenetic analysis, it is nowadays accepted that these single-domain Pgbs, are part of the GCSs lineage comprising the two-domain globin- coupled sensors and single-domain sensor gbs [18]. Since their discovery, more than two dozen papers were published mentioning protoglobin and discussing its properties and role in evolution. In the following, we briefly review the current knowledge on this extraordinary globin. A more extended review can be found elsewhere [163], and the latest findings are reported here [164, 165, 166, 167].

2.3.2 The unusual structure of Protoglobin

We now know that both protogbs contain 195 AAs, and after overexpression in *E. coli* its ligand-binding characteristics were defined [161]. Protoglobin oxidises rapidly, possibly suggesting an O_2 detoxification role by promoting electron transfer to O_2. From homology modeling and site-directed mutagenesis, F8His was found to be crucial for heme binding and Cys-45 at the A-B helical junction and Cys-102 are in the proximity to form disulphide bridges, potentially increasing the thermostability of the protein.

Later on, the crystal structure of *Ma*Pgb [168, 169] revealed an extraordinary structure compared with other known gbs. The protein fold is consisting of nine main helices Z, A, B, C, E, F, G, H, and H' (instead of A-H for Mb) and contains the heme group which is very deeply embedded in the protein matrix by the CE and FG loops and covered by the 20 AA long N-terminal extension. Removal of this extension, which lies closely to the heme propionate groups, has shown to affect the heme pocket but does not alter the overall fold [170, 171]. Depletion of the Z-helix together with the 20 AA N-terminal extension is associated with loss of α-helical content [171]. The heme itself, shows a high distortion from planarity, with out-of-plane deviations of ($\pm[0.5-0.6]$Å) of the four heme pyrrole rings (Fig. 2.6 (D)). Two apolar, orthogonal ligand tunnels located at the B/G and B/E helix interfaces, allow small ligands to access the heme (Fig. 2.6 (A-C)).

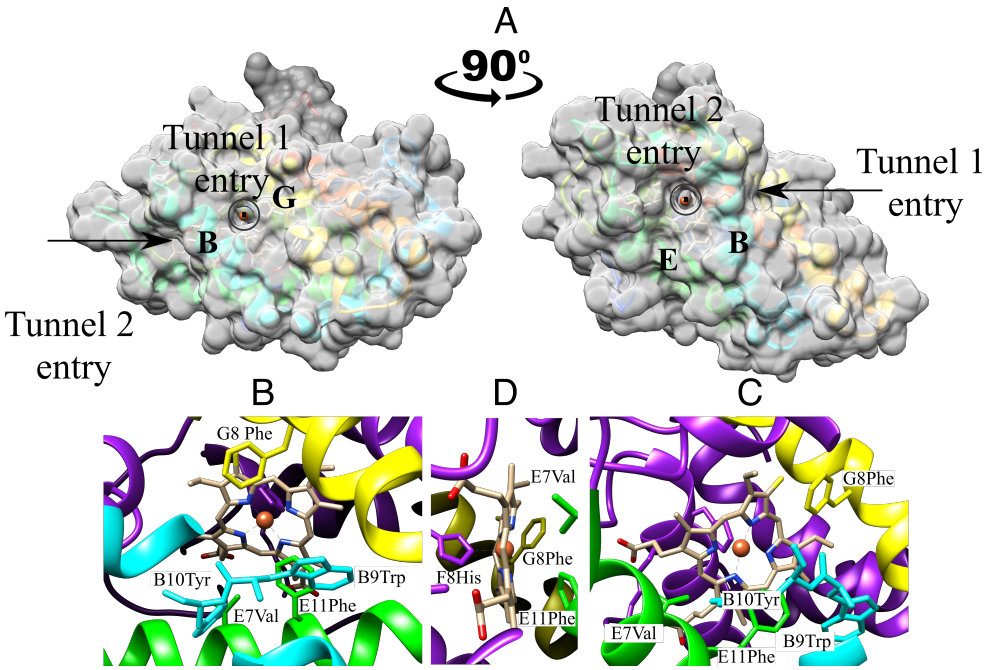

FIGURE 2.6: Monomer view of the 1.3 Å *Ma*Pgb crystal structure (PDB:2VEE): (A) A surface representation (1.3 Å cutoff) is shown in grey, with a semitransparent color in order to reveal the underlying ribbon structure of the α-helices. The orthogonal ligand tunnels are annotated with an arrow. This figure was recreated after [169]. Zoom of the heme-pocket structure looking into tunnel 1 (B) and tunnel 2 (C) with key AAs highlighted in a stick representation. The deviation of planarity of the ruffled heme is shown in (D).

Heme ruffling Whereas it is long clear that the ligand-binding properties of gbs are largely affected by the surrounding heme-pocket AAs, it is still quite unclear how a distortion from planarity of the heme impacts the structure-function relationship. To unravel this effect, and the overall effect of distortions from planarity on the electronic structure of the heme, *Ma*Pgb was investigated. Calculations such as quantum mechanical (QM) and hybrid QM-molecular mechanics (MM)) were employed, especially to study the effect of in- and out-of-plane distortions [172]. It was generally concluded that heme distortions decrease O_2 affinity, except for some positive in-plane distortions. Overall, it was shown that heme ruffling is a non-negligible factor and a potential modulating mechanism in fine-tuning ligand binding. Electron paramagnetic resonance spectroscopy is particularly suited to study heme ruffling because it reveals the electronic structure of the heme moiety (see also *Ch.* 3) [173, 170]. The EPR data of Fe(III) cyanide-ligated *Ma*Pgb could be correlated to an altered admixing of the different *d* orbitals in the molecular orbital that contains the unpaired electron when compared to cyanide-ligated Mb [170]. This effect was best pronounced in the *Ma*PgbF(G8)145W mutant, confirming previous findings that the G8 site fulfills a crucial role (Ref. 2.6) [174].

Ligand tunnels and binding kinetics The question arose how the observed orthogonal tunnels relate to the structure-function relationship. For Mb it was shown that ligands access the heme via the E7 gate [175], but for Pgb the access to the heme is completely different. A study of the protein structure and dynamics found that one of the two ligand tunnels ((Fig. 2.6)) can be closed and the interplay between an open and closed state is dependent on either the formation of a protoglobin dimer or the presence of a heme-bound ligand itself [174]. Moreover, Phe(93)E11 and Phe(145)G8 play a crucial role in this interplay (see Fig. 2.6 (B, C)) [174, 170].

Due to these two tunnels and the ruffled heme, the ligand binding in *Ma*Pgb is shown to be complex. Multiple CO-bound forms are observed in the CO-rebinding kinetics and resonance Raman spectra of CO-ligated *Ma*Pgb. The heterogeneous carbonylation kinetics results from a ligation-dependent equilibrium between a fast and a slow-rebinding conformation with ligation favouring the former [176]. *Ma*Pgb is known to have many ligand binding partners: besides O_2 other ligands such as CO, NO, cyanide, azide, and bulkier ligands (*i.e.* imidazole and nicotineamide) are all able to bind the heme [177, 164]. The crystal structure of these *Ma*Pgb complexes lead to the insight that a PheE11 side chain rotation occurs and that it plays a role in ligand sensing. TrpB9 and TyrB10 are H-bond donors in ligand stabilization. Upon ligand binding, TrpB9 relocated towards the heme, sealing tunnel 1 [177]. This, together with the fact that there are two H-bonded AAs, might be the reason for the earlier found carbonylation heterogeneity. A different H-bond stabilization might be the underlying reason for the observed two low-spin imidazole-ligated *Ma*Pgb complexes. Whereas the crystal structure only revealed one conformation, EPR results clearly show the presence of two low-spin species that can be linked to two distinct distal imidazole plane conformations [165].

2.3.3 Protoglobin and reactive nitrogen species

One spectroscopic study showed the interaction of *Ma*Pgb with NO and revealed that *Ma*Pgb is able to bind NO in the Fe(III) state and the Fe(II) state. Interestingly, over time, Fe(III) *Ma*Pgb-NO may reduce to *Ma*Pgb(II)-NO [178]. This reductive nitrosylation is reported to be irreversible and is biphasic. This shows again that *Ma*Pgb, has not only an O_2 scavenging, but a reactive nitrogen scavenging/enzymatic function. Later, a follow-up study investigated in more detail the NiR activity by mixing Fe(II) *Ma*Pgb with NO_2^- [164]. Ferrous *Ma*Pgb is able to convert NO_2^- to NO, only when it is in an unligated state prior to NO_2^- binding. When CO is ligated, the reductase activity is not reported. Also here, NiR activity is a biphasic process and requires one H^+ for the NO and OH^- formation. The rebinding of NO with *Ma*Pgb-Fe(II) is on its turn a fast monophasic process. Finally, peroxynitrite isomerisation is catalyzed by *Ma*Pgb and is monophasic a process as well [164].

In this thesis, we focus on extending the state-of-the-art by investigating nitrite-binding in ferric *Ma*Pgb, an area that has not received much attention in current literature. This objective is in line with my other goal of investigating the nitrite binding mode in globins using spectroscopy. Interestingly, the nitrite binding in ferric *Ma*Pgb is atypical, as is evident from the ferric as-purified spectra, which already reveal atypical features as well. Therefore, a more detailed spectroscopic investigation is needed.

Chapter 3

Relevant biochemical and biophysical techniques for globin research

Spectroscopy is the study of the interaction of electromagnetic (EM) radiation with matter, as a function of the energy of the EM radiation. The energy of the EM radiation can range from radiowaves in the order of 1×10^{-7} eV or smaller to gamma radiation which is of the order of MeV. By careful analyses of the interaction of the matter under investigation with EM radiation, information about its molecular and electronic structure can be obtained. The prosthetic group (heme) in gbs make them interesting as a subject to many different kinds of spectroscopic techniques. Next to the conventional techniques[1] such as UV-vis absorption, ECD, more specialized techniques such as rRaman, Raman optical activity (ROA), and EPR were employed in this thesis to obtain structural and functional properties. These techniques are complementary and allow obtaining a complete picture of the protein structure and heme product region. Although strictly not a spectroscopic technique, mass spectrometry (MS) is a popular technique used for the detection of post-translational modifications, multimerization and interactive studies, and was used in this work mainly to do protein stability controls. With this plethora of available techniques, the challenge arises to choose the right methods to answer specific research questions. In this chapter, the different biochemical and biophysical techniques are briefly explained.

[1] Other conventional and less conventional techniques to obtain structural info on proteins include: whole three-dimensional protein structures are typically obtained with nuclear magnetic resonance (NMR) methods or X-ray crystallographic studies. The latter requires the protein to be in a crystalline state, which is often a bottleneck. Small-angle X-ray scattering is therefore used in solution, however has limited resolution and gives an idea of the overall shape of the protein. Cryo-electron microscopy is nowadays more and more used for high-resolution structure determination and performs well for large molecular weight proteins, but struggles with low-molecular weight proteins, however recent developments are promising [179]. Lastly, and very recently, neural networks and artificial intelligence-driven computational studies of protein folding are promising to do *ab-initio* structure prediction [180]. Fluorescence spectroscopy, fluorescence resonance energy transfer (FRET), Fourier transform (FT) (and transient) infrared (IR) spectroscopy, X-ray absorption and magnetic circular dichroism (MCD) are other examples of techniques that are often used in metalloprotein research.

3.1 Cloning, expressing and purification

3.1.1 Choosing the correct overexpression system

High-purity and in some cases, large quantities of protein is needed for spectroscopic investigations. Unfortunately, many proteins are expressed in low quantity by the organism. Other obstacles preventing to obtain high amounts of protein from the organism are: the organisms are too tiny (< 1 mm, bacteria, ...), are unavailable to the researcher, are a protected species or there exist general ethical reasons that prohibit the direct extraction out of the cells and tissue (human proteins for example). Therefore, overexpression systems were developed that exploit bacteria, yeast, or higher eukaryotic cells to produce the protein of interest. In this thesis we used *E. coli* (BL21PlySs(DE3) Competent Cells) for the overexpression of recombinant gbs, for its easy accessibility and high protein yield. An overview of the expression protocol is given in Fig. 3.1

3.1.2 His-tagged globin expression protocol

Construction of the recombinant expression vectors The cDNA coding for a selected set of *Caenorhabditis elegans* gbs and for the protoglobin of *Methanosarcina acetivorans* were cloned into the recombinant expression vector pET23a with a C-terminal His-tag (Novagen). The gbs of interest were already available in pET3a vectors and were Polymerase Chain Reaction (PCR) amplified for further cloning. In-house design of primers containing restriction sites (NdeI and XhoI (Biolabs)) was done. Standard restriction enzyme cloning methods were used to obtain the final construct in the pET23a vector. Specific point-mutations were made using the Quickchange^{TM} site-directed mutagenesis method (Stratagene).

Expression in *Escherichia coli* After growing BL21(DE3)PlysS with coding cDNA in Terrific Broth (TB) medium containing the antibiotics ampicilin and chloramphenicol, and the heme precursor 5-aminolevulinic acid, cells were resuspended (50 mM Tris pH 7.5, 300 mM NaCl) followed by repeated freeze-thaw cycles and sonication to lyse the cells. After centrifugation (10 min, 10000 g, 4 °C), the supernatant was loaded onto a Ni Sepharose High Performance column (GE Healthcare), pre-equilibrated with an equilibration buffer (50 mM Tris-HCl pH 7.5, 300 mM NaCl, 20 mM imidazole) and eluted (50 mM Tris pH 7.5, 250 mM imidazole). The eluate was dialyzed (50 mM Tris pH 7.5, 0.5 mM ethylenediaminetetraacetic acid (EDTA), 150 mM NaCl), concentrated and loaded onto a Superdex G75 self-packed gelfiltration column as a final purification step. In some cases, additional ion-exchange chromatography steps were used to get rid of unwanted proteins that have a similar column retention time.

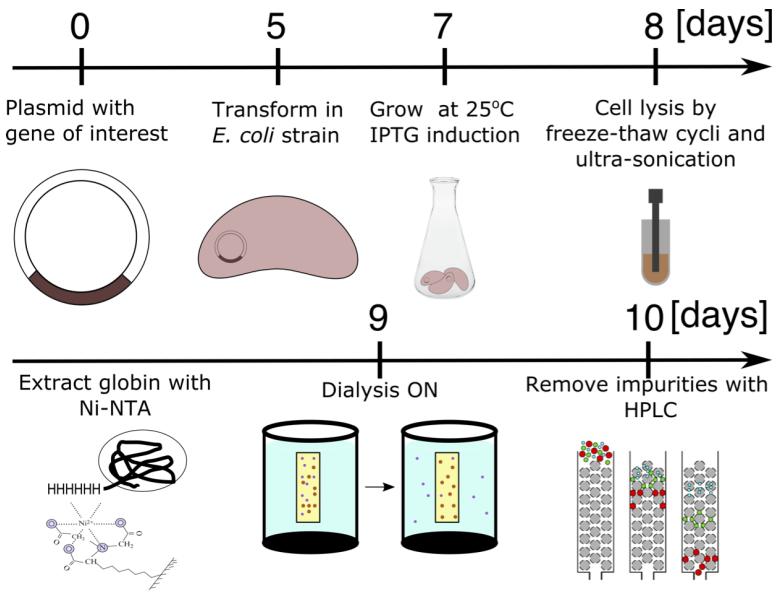

FIGURE 3.1: Protein overexpression scheme: containing the essential steps during globin expression and purification. A globin encoded shuttle molecule (pET-23a vector) containing a 6× His-tag is transformed into the *E. coli* bacterial strain, that after addition of an inducer molecule IPTG, will be transcribed and translated yielding a - hopefully - correctly folded protein. After cell lysis, the protein of interest is thereafter extracted. Subsequent (ultra) centrifugation, NiAC, dialysis and a final preparative liquid chromatography step are performed to isolate the protein of interest from other biomolecules, undesired cell debris and small molecules.

3.2 UV-visible spectroscopy

3.2.1 Absorption spectroscopy

Basic principles Absorption spectroscopy measures the absorption of EM radiation by atoms and molecules. The absorbed energy by the system results from the excitation of an electronic ground state to an excited state. The Bouguer-Lambert-Beer law

$$\log\left(\frac{I_0}{I}\right) = A(\lambda) = \epsilon(\lambda)bc \tag{3.1}$$

is a fundamental law describing the logarithm of the ratio of the incident to the transmitted light at a specific wavelength which is proportional to the path length b in cm and concentration c in $\mathrm{mol\,L^{-1}}$ of the sample. The proportionality constant ϵ ($\mathrm{L\,mol^{-1}\,cm^{-1}}$) is the molar extinction coefficient which is wavelength dependent, unique for each molecule system and can be used to determine the concentration of an unknown analyte solution.

Experimental setup Two setups are commonly used, being a single- and a double-beam setup. In the single-beam setup a reference sample is measured *a priori* whereas in the double-beam setup, both the sample and the reference sample are measured simultaneously. On one side a lamp (Halogen/Deuterium) emits photons, with a characteristic wavelength distribution depending on the operating voltage. These photons pass through a monochromator (wavelength selection) and the monochromatic light passes via a slit directly (or via a beamsplitter) the protein sample (and reference) contained in UV-vis transparent cuvettes. The non-absorbed light will be detected using a photomultiplier or charge-coupled device (CCD) detector and $A(\lambda)$ is measured. Some UV-visible spectra in this work were recorded on a single-beam Varian Cary 5E UV-vis near IR spectrometer. Others on a ChirascanTM-Plus spectrophotometer equipped with an LAAPD solid-state detector (Applied Photophysics, Leatherhead, Surrey, UK). The instrument was continuously flushed with N_2 (4 L/ min flow rate). The final spectra were subtracted by the buffer used for the respective measurement for solvent correction. All spectra were collected at room temperature with a protein concentration between 1-5 µM contained in SUPRASIL® (Hellma BeNeLux, Kruibeke, BE) quartz sample cells with a pathlength of 1 cm.

Optical spectroscopy of porphyrin-containing systems Proteins absorb EM radiation in the near UV (200-380 nm) and are therefore colorless. Especially the aromatic side chains of tryptophan (288 nm), tyrosine (273 nm) and phenylalanine (255 nm) are the main chromophores contributing to the absorption spectrum. Heme, on the other hand, when embedded in the protein matrix has absorption bands in the visible region with a so-called Soret (or B) band around 408-435 nm – violet to blue – and Q-bands in the range of 500-580 nm – green to yellow – which gives heme proteins their typical brown to brilliant red color. The highly conjugated π-electron system of the heme group gives rise to its characteristic spectrum. The theoretical basis of this phenomenon was first described in the four-orbital model of Martin Gouterman and others [181, 182, 183, 184]. This model describes the absorption spectrum of a porphyrin, starting from the transitions between two π highest occupied molecular orbital (HOMO)s to two π^* lowest unoccupied molecular orbital (LUMO)s (see Fig. 3.2 (B) adapted from [185]). Initially, the two LUMOs are degenerate, but due to orbital mixing, two energy levels are created. The excitation from the HOMOs ($S_0 \rightarrow S_2$) to the highest energy LUMO gives rise to the Soret band and the one to the lower LUMO ($S_0 \rightarrow S_1$), to the Q-bands. The Q-band region reflects the (symmetry breaking of) C_{4v} symmetry[2]. Other regions where the (plane polarized) transitions $S_0 \rightarrow S_1$ and $S_0 \rightarrow S_2$ occur are the bands N: [300-350] nm; L: [250-320] nm).

Porphyrin has four Q-bands labeled (IV-I), but when Fe is bound to the porphyrin to form heme, the Q-bands reduce to two bands labeled α and β. The relative ratio between the α and β bands reflects spatial organization and stability of the metal iron in the heme plane. If $A(\beta) < A(\alpha)$, the heme Fe is well-aligned in the heme plane which is the case for (Fe(II)) hexacoordinated gbs. *Vice versa*, when the heme iron is slightly out of the heme plane, the Q-band intensities rearrange ($A(\beta) > A(\alpha)$) which is the

[2]Note that S_0, S_1 and S_2 are not indicated in Fig. 3.2.

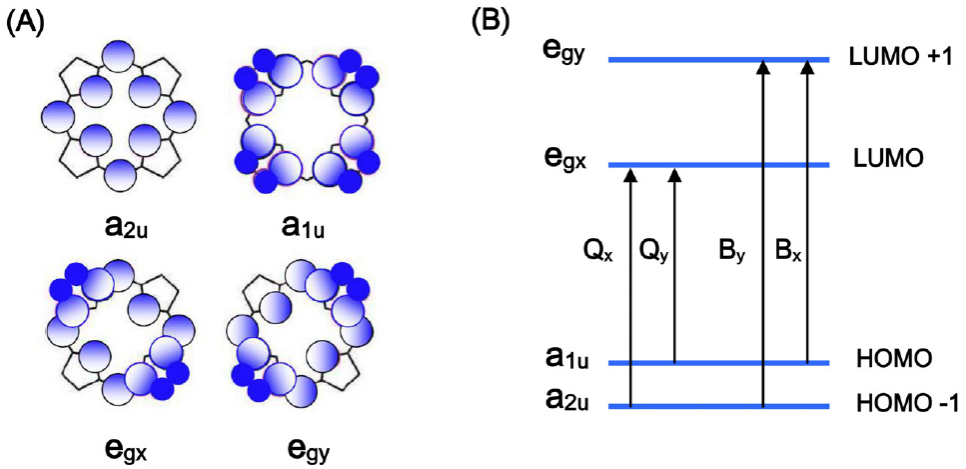

FIGURE 3.2: Porphyrin HOMOs and LUMOs: (A) Representation of the four Gouterman orbitals in porphyrins. (B) Drawing of the energy levels of the four Gouterman orbitals upon symmetry lowering from D_4h to C_2v. The excitation to the e_g orbitals gives rise to Q and B bands. Figure taken from [186].

case for pentacoordinated gbs. As already indicated in brackets, this Q-band structure is influenced by the spin and oxidation state of the iron. Therefore, by comparison with well-known cases, this information can thus be extracted from the UV-vis spectrum.

3.2.2 Electronic circular dichroism spectroscopy

Basic principles ECD is related to absorption spectroscopy with the main difference that ECD measures the differential absorption between left-handed and right-handed polarized light. Chiral molecules absorb left-handed and right-handed light differently. When linearly polarized light propagates through a solution (or crystal) containing a chiral molecule, it will become elliptically polarized, with the main axes tilted versus the original polarization plane. The ECD spectrum is simply $\phi(\lambda)$ with the ellipticity ϕ in radians the magnitude of this effect defined as

$$\phi = \frac{\pi}{\lambda(\eta_l - \eta_r)}, \tag{3.2}$$

with λ the wavelength, η_l and η_r the absorption indices of left and right-handed polarized light.

Proteins are chiral molecules and typically, the far-UV region is collected which will contain information on aromatic AAs, disulfide bonds and the secondary structure of the protein. Therefore, ECD is routinely applied to check the secondary and tertiary structure of proteins. Electronic transitions in the backbone of a peptide bond occur at 190 nm and 220 nm. Furthermore, exciton splitting causes an electronic transition at 208 nm and this together with the 220 nm transition is polarized [187]. Depending on the

structural motif of the protein, characteristic ECD spectra are observed with a positive and negative feature at 190 nm and 220 nm for α-helices, 195 nm and 215 nm for β-sheets, respectively and a minimum at 200 nm for random coils (Fig. 3.3 (A)).

Experimental setup UV-visible Abs/ECD spectra were recorded at the Chira-scan^{TM}-Plus spectrophotometer (by Applied Photophysics, Leatherhead, Surrey, UK). The instrument was continuously flushed with nitrogen ($4\,\mathrm{L\,min^{-1}}$ flow rate), and the measurements were carried out at 20 °C. For all the recorded spectra, 0.2 cm path length SUPRASIL quartz sample cells (Hellma BeNeLux, Kruibeke, BE) were used. The final spectra were subtracted by the solvent baseline for the respective measurement. The ECD experiments shown in this thesis were recorded and interpreted by dr. Roberta Sgammato (TSM^2, Dept. of Chemistry).

ECD on heme proteins The heme group itself is only chirally active when embedded in a protein matrix and additional information, besides the secondary structure, can be obtained in the four main regions where the plane polarized transitions $S_0 \rightarrow S_1$ and $S_0 \rightarrow S_2$ occur (Q: [470-600] nm; B or Soret: [380-450] nm; N: [300-350] nm; L: [250-320] nm). The Q-band region reflects the (symmetry breaking of D2h or D4h to) C_{4v}-C_1) symmetry. The Soret region on the other hand is typically positive for Fe(III) hemeproteins and negative for deoxygenated and O_2-bound hemes or a combination of both positive and negative ellipticity. The heme orientation in the heme pocket will be reflected in that region as well [192]. Ligand binding at the heme can induce changes in ellipticity in contrast to sometimes limited changes in the absorption spectrum (Fig. 3.3 (B)). The N and L- bands ([300-350] nm and [250-320] nm, respectively), which are of limited interest in the absorption spectra, reflect a resonant interaction between the electronic transition dipole moment vectors of aromatic residues [193]. In addition, in the near-UV region [250-350 nm], an ECD signal appears from mainly the aromatic AAs and disulfide bonds (Fig. 3.3 (C)). Overall, ECD is a valuable complementary spectroscopic technique, which reveals a lot of additional information to the absorption spectrum, with the advantage that the latter is obtained simultaneously.

3.3 Resonance Raman spectroscopy

3.3.1 Basic principles

Raman spectroscopy classifies as vibrational spectroscopy since it is able to detect atomic vibrations with well-defined frequencies in the EM spectrum[3]. In Raman spectroscopy, the energy difference between two vibrational states is not obtained by simply the absorption of a vibrational quantum[4]. In contrast, it makes use of a coherent EM radiation (laser light) and detects the light scattered from the molecule. When this event occurs, there is a small (1 in a millionth) probability that the incident light excites the ground

[3]Section based on Chapter 3 from [194].

[4]Such as in IR absorption spectroscopy. In Raman spectroscopy, the wavelength of the incident beam does not have to match the difference between the vibrational ground and excited states.

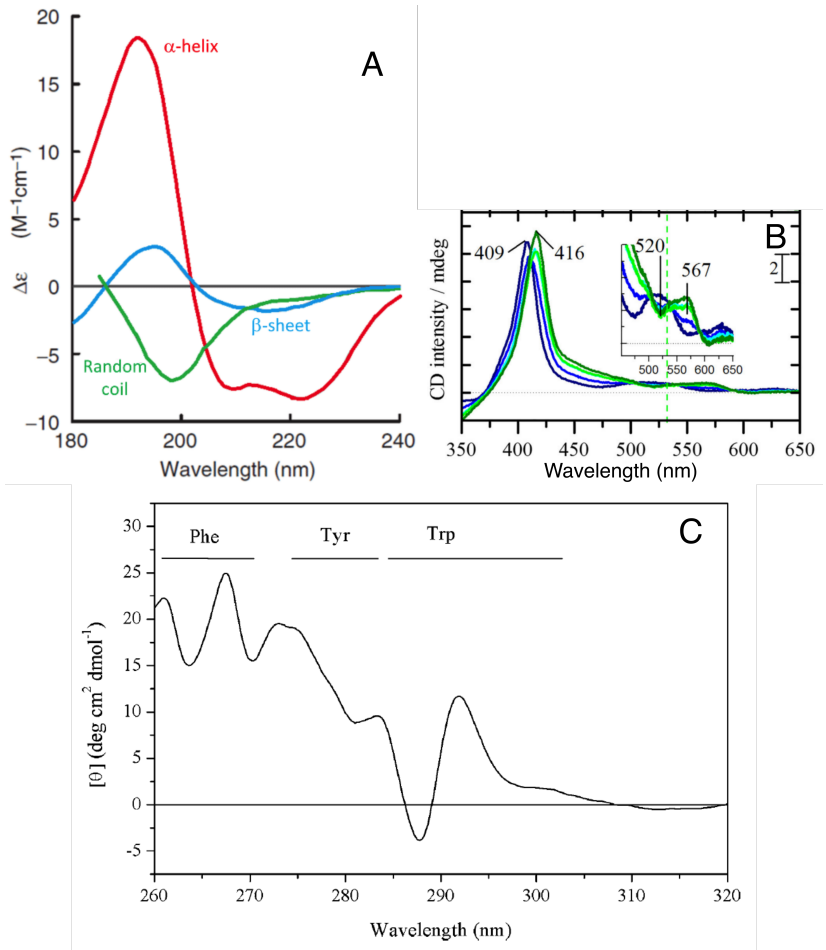

FIGURE 3.3: Typical regions for which ECD spectra are collected: (A) The far-UV ECD spectra of proteins is used to gain information on the secondary structure. It shows typical ECD spectral features of α-helical structural elements (red), β-sheets (blue) and random coils (green). Figure taken from: [188]. (B) The UV-vis ECD spectrum for Mb with increasing concentrations of imidazole illustrates the sensitivity of ECD for changes in heme ligation (Figure taken from [189]).(C) The near-UV ECD spectrum for type II dehydroquinase from *Streptomyces coelicolor* (Figure taken from [190], containing adapted data from [191]).

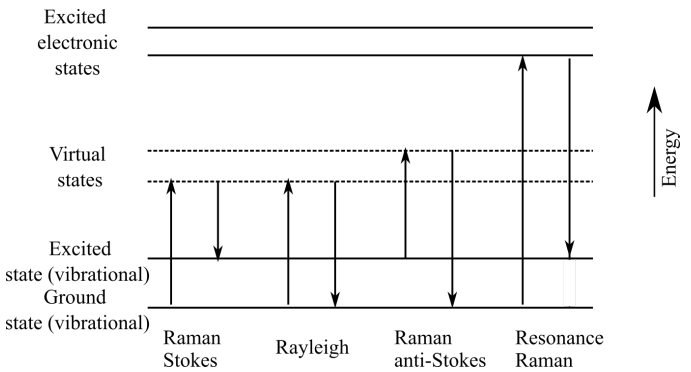

FIGURE 3.4: Absorption and scattering processes.

state to a virtual state (e.g. not an eigenstate), which can be understood as a short-lived distortion of the electron cloud, which quickly relaxes to an excited vibrational state (Stokes scattering) and thereby losing a vibrational quantum instead of scattering elastically (Rayleigh scattering) in which no energy transfer occurs. A second inelastic scattering event can take place in which the opposite happens and we differentiate between so-called Stokes and anti-stokes Raman scattering (Fig. 3.4).

Most of the molecules in an ensemble are in the ground state and therefore the intensity of Stokes scattering will be larger than the anti-Stokes scattered photons. The intensity difference will be governed by a Boltzmann equation

$$\frac{N_n}{N_m} = \frac{\gamma_n}{\gamma_m} \exp\left(\frac{E_m - E_n}{k_B T}\right) \tag{3.3}$$

with N the number of molecules in the excited vibrational energy level n or ground state m, with energy $E_n > E_m$) . The factor γ denotes the degeneracy of the energy levels n and m and k_B is Boltzmann's constant (1.3807×10^{-23} J K^{-1}).

Each electronic state in a molecule consists of several vibrational states which energies are quantized according to a Morse curve. Several overtone absorptions can occur, but in most cases, only the first excited state is of importance (selection rule). For a diatomic molecule, the frequency is approximately

$$\nu = \frac{1}{2\pi c}\sqrt{\frac{K}{\mu}}, \tag{3.4}$$

where c is the velocity of light, K is the force constant of the bond between A and B and is a measure of bond strength and μ is the reduced mass of atoms A and B. This simple approximation illustrates that the lighter the atoms, the higher the frequencies of the vibrations are. On the other hand, the intensity I of scattered light can be described in terms of the laser power l, the laser frequency ω_L and the polarizability α of the electrons in the molecule:

$$I = Kl\alpha^2\omega_L^4. \tag{3.5}$$

The polarizability α in turn can be described by the Kramer Heisenberg Dirac (KHD) expression

$$(\alpha_{\rho\sigma})_{GF} = k \sum_I \left(\frac{\langle F| r_\rho |I\rangle \langle I| r_\sigma |G\rangle}{\omega_{GI} - \omega_L - i\Gamma_I} + \frac{\langle I| r_\rho |G\rangle \langle F| r_\sigma |I\rangle}{\omega_{IF} + \omega_L - i\Gamma_I} \right), \tag{3.6}$$

with ρ and σ the incident and scattered polarization directions, k a constant, G the ground vibronic state, I a vibronic state of an excited electronic state and F the final vibronic state of the ground state. G and F are simply the initial and final states of the Raman scattering process. The operators r_σ and r_ρ are the dipole operators with the incident and scattered polarization directions σ and ρ, respectively. The denominator contains the transition frequencies, the laser frequency and Γ_I the intrinsic linewidth of the intermediate vibronic state I and relates to the lifetime of the excited state. The sum is taken over all the vibronic states of the molecule [194].

It can be proven that this equation can be divided in purely vibrational and electronic components using a Born-Oppenheimer approximation [195]. From that, it follows that the Raman scattering will only be non-zero when there is only one quantum energy difference between the initial state and the final state and that overtones are not present in Raman scattering, unless resonance conditions are fulfilled.

Resonance Raman scattering Under the resonance condition, *i.e.* the energy of the laser light equals the energy difference between the vibrational I and G states ($\omega_{GI} = \omega_L$), *resonance* Raman scattering occurs. Note that the transitions are not purely virtual anymore (see Fig. 3.4). Under these conditions, the first term in the KHD equation will dominate, increasing the polarizability:

$$(\alpha_{\rho\sigma})_{GF} = k \frac{\langle F| r_\rho |I\rangle \langle I| r_\sigma |G\rangle}{\omega_{GI} - \omega_L - i\Gamma_I}. \tag{3.7}$$

An immediate consequence is that vibrational states that are selected by the resonance condition will have enhanced Raman scattering than others. Whereas in normal Raman scattering, the intensity of the scattering is a fourth power of the frequency, in resonance scattering, the intensity can vary with respect to the electronic nature. In general, resonant processes are more complex than this, and result in very selective enhancements in the Raman spectrum.

Experimental setup Experimentally, laserlight is directed to the sample and focused onto the sample using a lens. The backscattered light will be directed via the lens towards a filter that blocks the incident laser frequency and allows the scattered, wavelength-shifted light to pass through. After that, the light is passed through a grating, splitting the different wavelengths which are detected using a CCD device.

The rRaman spectroscopy in this work was carried out at room temperature using a ChiralRaman-2X spectrometer (BioTools, Inc., Jupiter, Florida, USA). Unpolarised rRaman spectra were recorded in backscattering geometry, using a green laser beam from a frequency-doubled Nd:YVO_4 laser (532 nm). The instrument was running at a spectral resolution of 7 cm^{-1}. The Raman experiments shown in this thesis were recorded and interpreted by dr. Roberta Sgammato (TSM^2, Dept. of Chemistry).

3.3.2 Resonance Raman of heme proteins

In general, Raman spectroscopy can be used to detect the stretching and bending modes of most common groups that make part of a molecule. The nitro –NOO stretching mode for example, has specific bands in the 1800–200 cm^{-1} region which is commonly referred to as the fingerprint region.

The heme gives rise to a specific absorption spectrum and is therefore a suited chromophore to study with resonance Raman spectroscopy [196, 197, 198]. Typically, heme containing systems are excited at Soret intensity or at Q-band. When in resonance, large selective enhancement of the vibrational modes of the chromophore are observed. We can obtain information in form of "marker bands" defined by previous research on heme proteins [196, 199]. Besides vibrational stretching and breathing modes of the heme group itself, we obtain the oxidation state, spin state and oxygenation/ligation state of the heme iron. Structural changes as a consequence of a reaction mechanism at the heme can be picked up via the Raman shifts, making it a versatile, complementary tool to UV-vis, ECD and EPR spectroscopy.

3.4 Electron paramagnetic resonance

3.4.1 Introduction to EPR

EPR spectroscopy belongs to the field of magnetic resonance which includes also the better known NMR and magnetic resonance imaging (MRI). The EPR counterpart of MRI is EPR imaging (EPRI), which is able to determine tissue microenvironment parameters non-invasively *via* paramagnetic probes, but its biomedical application is still limited to small animals. In 1944, EPR was discovered and later on developed by the Russian physicist Zavoisky [200] and is used to study the electronic structure of organic and inorganic paramagnetic molecules and more generally paramagnetic spin systems. The technique makes use of strong magnetic fields and microwave EM radiation in order to perturb the magnetic moment of a paramagnetic center.

The underlying fundamental principle of EPR is the electron-Zeeman effect, which states that the degeneracy of the m_S eigenstates is lifted in a magnetic field. When the energy difference between the states is exactly equal to the energy of the incident microwave radiation, a transition between states is possible. The exact energy at which these transitions occur, contains a lot of information about the system as it depends on the local field described by the spin Hamiltonian.

3.4.2 EPR in one equation: the spin Hamiltonian

For a system with electron spin S surrounded by n nuclei placed in an external magnetic field $\mathbf{B_0}$, the spin Hamiltonian is expressed as the sum of the contribution from the electron Zeeman effect (EZE) (always), the hyperfine interaction (HI) and nuclear Zeeman effect (NZE) if there is a nucleus, the zero-field interaction (ZFI) if $S > \frac{1}{2}$ and the nuclear quadrupole interaction (NQI) if $I > \frac{1}{2}$:

$$H = +\underbrace{\mu_B \mathbf{B_0^T g \hat{S}}}_{\text{EZE}} + \underbrace{\mathbf{\hat{S}^T D \hat{S}}}_{\text{ZFI}} - \underbrace{\sum_i \mu_n g_{n,i} \mathbf{B_0^T \hat{I}_i}}_{\text{NZE}} + \underbrace{\sum_i \mathbf{\hat{S}^T A_i \hat{I}_i}}_{\text{HFI}} + \underbrace{\sum_i \mathbf{\hat{I}_i^T Q_i \hat{I}_i}}_{\text{NQI}}, \tag{3.8}$$

with μ_B the Bohr magneton ($9.271 \times 10^{-24}\,\mathrm{J\,T^{-1}}$), $\mathbf{g}$ the $\mathbf{g}$-tensor, $\mathbf{\hat{S}}$ the electron spin operator, $\mathbf{\hat{I}_i}$ the nuclear spin operators, $\mathbf{A_i}$ the hyperfine tensors, $\mathbf{Q_i}$ the quadrupole tensors, μ_n and g_n, the nuclear magneton and nuclear g-value, respectively (i indicates the nucleus).

The free electron - understanding the Zeeman effect A free electron is the most simple paramagnetic system with spin $S = \frac{1}{2}$. The magnetic moment $\boldsymbol{\mu}$ is defined as

$$\boldsymbol{\mu} = \gamma_e \hbar \mathbf{S} = -g_e \mu_B \mathbf{S} \tag{3.9}$$

with γ_e, the gyromagnetic ratio and g_e the g-value of the free electron and $hbar = \frac{h}{2/pi}$ the reduced Planck's constant. Two $m_S = \pm\frac{1}{2}$ states exist with the plus sign referred to as *spin up* and the minus sign as *spin down*. The degeneracy between the energy of two states in a magnetic field (along the z-axis) is lifted by the Zeeman effect and is expressed as:

$$E =< \psi|H_{EZE}|\psi >= g_e \mu_B B_0 < \psi|\hat{S}_z|\psi >= g_e \mu_B B_0 m_S, \tag{3.10}$$

showing that the energy depends on B_0 and m_S. This principle is demonstrated in Fig. 3.5 and can be easily extended for an electron confined in a molecule. The g-value will not be a scalar but a tensorial quantity. More generally we write in matrix notation:

$$H_{EZE} = \mu_B \mathbf{B_0^T g \hat{S}}. \tag{3.11}$$

The $\mathbf{g}$-tensor is fully defined by its 3 principal g-values and corresponding principal axes.

The zero-field interaction For systems with an electron spin larger than $\frac{1}{2}$ (e.g. the high-spin, $S = \frac{5}{2}$ heme state), the ground state is $2S + 1$ times degenerate, a degeneracy that is lifted already in absence of a magnetic field by the zero-field interaction originating from dipole-dipole coupling between the individual electrons and spin-orbit coupling.

The zero-field interaction is described by the traceless $\mathbf{D}$-tensor. In its diagonalized form, two parameters E and D describe $\mathbf{D}$:

$$(D_x, D_y, D_z) = (-\frac{1}{3}D + E, -\frac{1}{3}D - E, \frac{2}{3}D), \tag{3.12}$$

such that $|D_x| > |D_y| > |D_z|$.

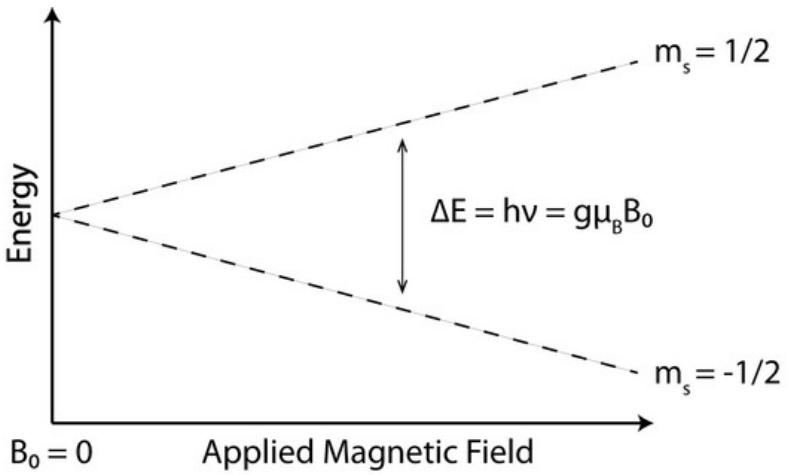

FIGURE 3.5: Electron Zeeman effect for a free electron ($S = 1/2$) in an external magnetic field B_0. In the presence of a magnetic field ($B_0 \neq 0$), the degeneracy is lifted corresponding to the two spin states $m_S = 1/2$ and $m_S = -1/2$. The energy split is proportional to the applied magnetic field intensity B_0 with the g-value.

Coupling with neighbouring nuclei - the hyperfine interaction The magnetic moment $\boldsymbol{\mu}$ of the electron spin ($S > 0$) interacts with the local magnetic field originating from neighbouring magnetic nuclei ($I > 0$). This contribution is expressed in the hyperfine interaction term:

$$H_{HFI} = \hat{\mathbf{S}}^{\mathbf{T}}\mathbf{A}\hat{\mathbf{I}}, \tag{3.13}$$

in which $\mathbf{A}$ consists of an isotropic part (Fermi-contact) and an anisotropic part from the dipolar interaction between the spin magnetic moment and the nuclear magnetic moment.

The hyperfine interaction causes a further splitting of each state in $2I+1$ levels, agreeing with $m_I = -I, -I+1, ..., +I$. For a simple $S = \frac{1}{2}$, $I = 1$ system, this means that instead of one EPR transition, three EPR transitions are allowed ($|\Delta m_S| = 1, \Delta m_I = 0$) between the (m_S, m_I) states:

$$\begin{aligned} (-\tfrac{1}{2}, -1) &\leftrightarrow (\tfrac{1}{2}, -1) \\ (-\tfrac{1}{2}, 0) &\leftrightarrow (\tfrac{1}{2}, 0) \\ (-\tfrac{1}{2}, 1) &\leftrightarrow (\tfrac{1}{2}, 1) \end{aligned} \tag{3.14}$$

Nuclear Zeeman effects and nuclear quadrupole interaction The presence of nuclei in the spin system has another consequence expressed as the nuclear Zeeman interaction (see eq. 3.8), which is of the same type as the electron Zeeman interaction.

When $I \geq 1$, the nuclear quadrupole interaction needs to be taken into account

$$H_{NQI} = \widehat{\mathbf{I}}^{\mathbf{T}}\mathbf{Q}\widehat{\mathbf{I}}. \tag{3.15}$$

The principal values of this traceless **Q**-tensor, are described by the asymmetry parameter

$$\eta = \frac{Q_1 - Q_2}{Q_3}, \tag{3.16}$$

with $|Q_1| \leq |Q_2| < |Q_3|$ and $Q_3 = e^2qQ/[2I(2I-1)h]$ with Q the quadrupole moment and q is the electrostatic field gradient.

3.4.3 Continuous wave EPR

The basics The energy difference between the spin states in an external magnetic field is measured by continuously sending in microwave radiation to a sample contained in a resonator. In a continuous-wave (CW) experiment, the microwave frequency is kept constant and the magnetic field is varied. Microwave frequencies used in EPR vary from 9.5 GHz (X-band), 35 GHz (Q-band), 95 GHz (W-band), 360 GHz and nowadays, specialized broadband THz spectrometers are under development [201, 202].

When the *resonance condition* (see eq. 3.10) is met for an $S = \frac{1}{2}$ system

$$\Delta E = h\nu = g\beta B_0, \tag{3.17}$$

with ΔE the energy difference between two m_S spin states at a magnetic field B_0, a microwave quantum will be absorbed and a transition is induced. The selection rule is $|\Delta m_S| = 1$, $|\Delta m_I| = 0$ in CW EPR. The CW-EPR spectrum shows the absorbed microwave as a function of the magnetic field intensity B_0. The main physical quantity extracted from a CW-EPR experiment is the **g** tensor which is characteristic for the molecule. In case of a molecule in a non-viscous solution, only the average of the principal g-values, the so-called isotropic g-value, can be determined.

In a single crystal, all molecules are organized in a lattice and the sample needs to be rotated in the magnetic field to obtain the principal components of the **g**-tensor. For powders and frozen solutions, the molecules take on all orientations versus the magnetic field and the CW-EPR spectrum reflects the sum of all corresponding g-values. Powder CW-EPR spectra, depending on the symmetry of the **g**-tensor are illustrated in Fig. 3.6. If the hyperfine coupling is strong, the hyperfine interaction with different nuclei can be seen as a $\prod_i(2I+1)$ splitting of the EPR lines. For some high-spin ($S > 1/2$) electron systems, the zero-field interaction can be significantly stronger than the electron Zeeman effect, leading to so-called Kramers' doublets for half integer spins and non-Kramers' doublets (for integer spins). In the 'weak-field' case ($D \gg h\nu$), which is usually valid for the high-spin Fe(III) heme state ($S = \frac{5}{2}$) at X-band frequency, a two-fold degeneracy between the Kramers' doublets remains. When the external magnetic field is turned on, the degeneracy between the doublets is lifted and EPR transitions can occur. However, the X-band microwave quantum is too small to induce EPR transitions ($|\Delta m_S| = 1$) other than the ones in the $\frac{1}{2} \leftrightarrow -\frac{1}{2}$ transitions. The effective $\mathbf{g_{eff}}$-tensor contains both information on the actual g-value of the system and on the zero-field interaction. For a high-spin $S = 5/2$ system with a g-value close to the free electron, the $g_{\text{eff},||} = 2$ and $g_{\text{eff},\perp} = 6$. Depending on the rhombicity of the **D**-tensor, the effective g-values vary and can be determined by matching the experimental spectrum with simulations.

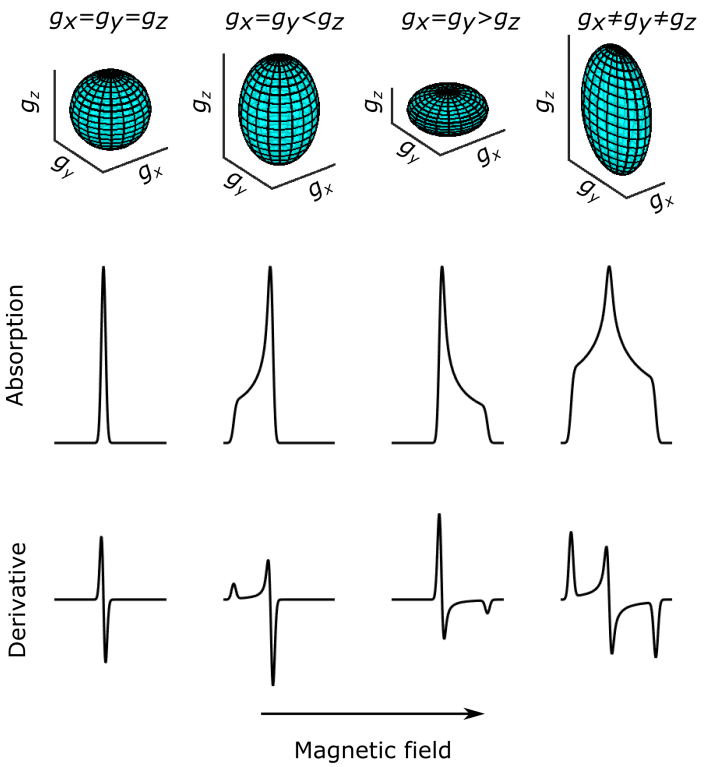

FIGURE 3.6: Powder CW-EPR spectra of an $S = 1/2$ system with no resolved hyperfine coupling depending on the **g**-tensor symmetry. From left to right: isotropic, axial, axial, rhombic. Top row shows the **g**-tensor in an ellipsoid representation. Second and third row show the corresponding EPR spectra in absorption or first derivative mode, respectively. The latter is the common form of a CW EPR spectrum due to the use of a modulation of the magnetic field.

Experimental setup A conventional CW-EPR spectrometer consists of a cavity resonator placed in an electromagnet. The sample is placed in the resonator, with a size such that the microwaves generated by a klystron source or Gunn diode result in standing waves. The reflection of mw can be minimised via a coupling antenna (iris). The efficiency of a resonator is given by the Q-factor:

$$Q = \frac{\nu}{\Delta\nu}, \tag{3.18}$$

with $\Delta\nu$ the FWHM of the reflection resonance 'dip'. An EPR signal arises when a microwave quantum is absorbed which alters the coupling profile of the cavity, resulting in a reflection of microwaves, that reach the detector via waveguides and a circulator. Under non-saturating conditions, the microwave power P is related to the signal-to-noise ratio

$$(S/N) \propto \sqrt{P}. \tag{3.19}$$

For a phase-sensitive detection and noise reduction, the magnetic field is modulated defined by a modulation amplitude and frequency, which is adjusted to the linewidth of the EPR signal to increase the signal-to-noise ratio, without distorting the lineshape. This results in a derivative of the absorption signal, explaining the somewhat unusual form of the CW-EPR signal (see Fig. 3.6, bottom curves).

In this thesis, the X-band CW-EPR measurements were performed on an ESP300E (Bruker) spectrometer with a microwave frequency of 9.45 GHz equipped with a gas-flow cryogenic system (Oxford Instr. Inc.), allowing for operation from room temperature down to 2.5 K. The magnetic field was measured with a Bruker ER035M NMR Gauss meter.

3.4.4 Pulsed EPR

A more informative, yet more complicated method than the CW-EPR experiment is a pulsed EPR experiment. Pulsed EPR makes use of short microwave pulses instead of continuous microwave irradiation, and sometimes in combination with radio-frequency pulses. Such a detection method has a lot of advantages compared to the conventional CW experiment. Pulsed EPR is capable of detecting hyperfine and quadrupole effects that are often not resolved in a CW experiment. It also allows detection of the NZ interaction and thus identifying the type of magnetic nuclei surrounding the electron spin. To understand how 'on resonance' microwave pulses affect the spins in an EPR sample, we need to consider *polarization*, *coherence* and *relaxation*. Next to a classical picture, a quantum-mechanical description making use of the *density operator formalism* is briefly introduced to describe the spin dynamics during, and after an array of microwave pulses. Finally, commonly used pulsed EPR experiments executed in this work are discussed.

Powder patterns: orientation selectivity The g-anisotropy as illustrated in Fig. 3.6 is a result of the fact that for each orientation, the resonance condition will be fulfilled at a different B_0-value, due to the tensory characteristics of $\mathbf{g}$. In pulse EPR, the excitation bandwidth of the microwave pulse is often smaller than the width of the spectra, which

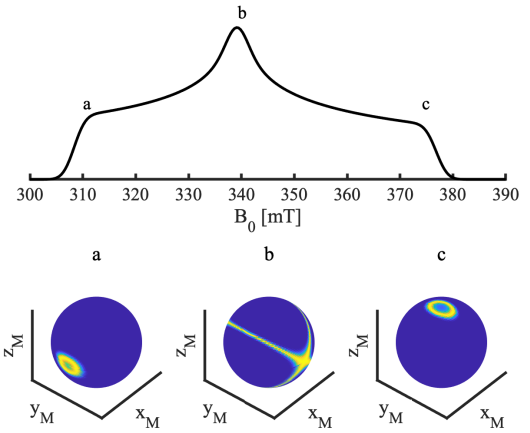

FIGURE 3.7: Orientation selectivity: simulated absorption X-band (9.5 GHz) CW-EPR powder spectrum of a rhombic $S = \frac{1}{2}$ system with $\mathbf{g} = [2.2, 2.0, 1.8]$. The selected spins excited by a mw-pulse with an excitation width of 100 MHz at field positions indicated by a-c, is mapped and shown on the unit sphere in yellow.

means that we only excite spins with a specific orientation and cannot excite all spin packets with a single mw-pulse at a fixed B_0-field. For rhombic systems with non equal principal g-values, $g_z \neq g_y \neq g_x$, pulse EPR experiments performed at the outer positions corresponding with g_x and g_z only select a small amount of orientations. At g_y or other field positions, more spins are excited, since multiple orientations have their resonance condition fulfilled (Fig. 3.7). By collecting spectra at different magnetic field positions, we can obtain the hyperfine tensor and quadrupole tensor of coupled nuclei, which is often the aim of pulsed EPR experiments.

Population, coherence and relaxation In a classical picture, each spin can be described as a magnetic moment $\boldsymbol{\mu}$ that 'precesses' with the larmor frequency $\omega_s = \frac{g\beta_e B_0}{\hbar}$ about the $\mathbf{B_0}$ axis (gyromagnetic effect) and results in a time-averaged $< \boldsymbol{\mu} >$ along the magnetic field axis. Taking into account all the spins in the magnetic field $\mathbf{B_0}$, we define a netto magnetization vector $\boldsymbol{M_z} = \frac{1}{V}\sum_i < \boldsymbol{\mu_i} >$ along the z-axis as a consequence of the Boltzmann distribution between the energy eigenstates.

$$P = \frac{N_\beta}{N_\alpha} = e^{-\frac{\Delta E}{k_B T}}. \tag{3.20}$$

For a simple $S = \frac{1}{2}$ system, more spins are in the $m_S = -\frac{1}{2}$ state than in the $m_S = \frac{1}{2}$ state. Application of an 'on resonance' microwave pulse $\boldsymbol{B_1}(t)$ along the x-axis, 'rotates' the total magnetization $\boldsymbol{M_z}$ out of equilibrium ($\theta \sim t_p \times B_1$) and creates *phase coherence* between the different spin packets in the (x, y)-plane. At the end of the mw pulse, this magnetization will start to precess around $\boldsymbol{B_0}$.

Different *relaxation processes* will cause a return to equilibrium. The spin-lattice or longitudinal relaxation (T_1) describes the return of M_z magnetization and the spin-spin relaxation (T_2) describes the loss of transverse magnetization $\mathbf{M_{xy}}$ (dephasing). It is the latter that happens usually much faster and is the limiting factor to obtain pulsed EPR signals, because only transverse magnetization is detected in an EPR experiment. The dephasing after a $\frac{\pi}{2}$ pulse ($\theta = 90°$) is given by

$$\mathbf{M_{xy}} = \mathbf{M_{xy,0}} e^{-\frac{t}{T_2}} \quad (3.21) \qquad \mathbf{M_z} = \mathbf{M_0}(1 - e^{-\frac{t}{T_1}}) \quad (3.22)$$

The density operator formalism The density operator formalism is introduced to describe pulsed EPR in a quantum-statistical framework, because the classical picture is not sufficient to correctly describe all the aspects of spin dynamics. Using this principle, it is easier to understand how the microwave pulses affect the spin packets and what information can be extracted from such an experiment in terms of coherences and transition frequencies. Only some basic aspects of this formalism will be discussed, for a detailed description, see [203, 204].

Large spin systems can be described statistically as an 'ensemble'. Within the ensemble, we have sub-ensembles that have an arbitrary wave function Ψ, which can be written in its eigenbasis as:

$$|\Psi\rangle = \sum_{n=1}^{N} c_n |n\rangle . \quad (3.23)$$

A measurement is the expectation value of a *mixed state* A. This means that, next to the quantum-mechanical uncertainty, a statistical uncertainty is present. Therefore, a second averaging using a general probability function $P(\Psi)$ is needed as follows:

$$\overline{\langle A \rangle} = \int P(\Psi) \langle \Psi | A | \Psi \rangle \, d\tau = \mathrm{tr}\,(\hat{\sigma}\hat{A}), \quad (3.24)$$

in which the matrix elements of density matrix $\hat{\sigma} = \int P(\Psi) |\Psi\rangle \langle \Psi| \, d\tau$ are[5]

$$\overline{c_n c_m^*} = \sigma_{nm} = \langle n | \hat{\sigma} | n \rangle . \quad (3.25)$$

The time evolution of the density operator is given by the Liouville and von Neumann equation:

$$\frac{d\hat{\sigma}(t)}{dt} = i\left[\hat{\sigma}(t), \hat{H}\right] \quad (3.26)$$

Solving this equation for a time-independent Hamiltonian $\hat{H}_e$, results in an expression for the time evolution of the density operator in the rotating frame (see further).

$$\hat{\sigma}^r(t) = e^{-i\hat{H}_e t} \hat{\sigma}(0) e^{i\hat{H}_e t} \quad (3.27)$$

[5] note that $c_n c_n^* = \langle n|\Psi\rangle \langle \Psi|m\rangle$ with $|\Psi\rangle \langle \Psi|$ the projection operator.

Quantum picture of an $S = \frac{1}{2}$ and $I = \frac{1}{2}$ system (Paragraph based on [205].) Since pulsed EPR experiments are described by a time-dependent Hamiltonian, a unitary transfer to a frame in which this Hamiltonian becomes time-independent is necessary. In EPR experiments, this is a frame that rotates about the **z**-axis with the microwave frequency (so-called rotating frame).

Let us consider the Hamiltonian of a $S = \frac{1}{2}$ and $I = \frac{1}{2}$ system in frequency units:

$$\hat{H}_0 = \omega_S \hat{S}_z + \omega_I \hat{I}_z + A\hat{S}_z\hat{I}_z + B\hat{S}_z\hat{I}_x \tag{3.28}$$

with ω_S the resonance offset and ω_I the nuclear Zeeman frequency in a frame with the electron spin at the origin and the nucleus in the (x, z) plane with $A = A_{zz}$ and $B = \sqrt{A_{zx}^2 + A_{zy}^2}$ the secular and pseudo-secular hyperfine coupling constants. The diagonalized form of the Hamiltonian is obtained after a unitary transformation to its eigenbasis using the unitary transformation operator

$$\hat{U} = \exp\big(-i(\zeta\hat{I}_y + \eta 2\hat{S}_z\hat{I}_y)\big) \tag{3.29}$$

with

$$\eta = \frac{1}{2}\left[\underbrace{\tan^{-1}\left(\frac{-B}{A+2\omega_I}\right)}_{\eta_\alpha} - \underbrace{\tan^{-1}\left(\frac{-B}{A-2\omega_I}\right)}_{\eta_\beta}\right] \tag{3.30}$$

and

$$\zeta = \frac{\eta_\alpha + \eta_\beta}{2}, \tag{3.31}$$

and results in

$$\hat{H}_0^d = \omega_S\hat{S}_z + \omega_{12}\hat{S}^\alpha\hat{I}_z + \omega_{34}\hat{S}^\beta\hat{I}_z. \tag{3.32}$$

This diagonalized Hamiltonian contains operators in z with the polarization operator matrices defined as:

$$\hat{S}^\alpha = \begin{pmatrix} 1 & 0 \\ 0 & 0 \end{pmatrix}, \hat{S}^\beta = \begin{pmatrix} 0 & 0 \\ 0 & 1 \end{pmatrix} \tag{3.33}$$

and nuclear frequencies

$$\omega_{12} = (\omega_I + \frac{A}{2})\cos\eta_\alpha - \frac{B}{2}\sin\eta_\beta \tag{3.34}$$

$$\omega_{34} = (\omega_I - \frac{A}{2})\cos\eta_\alpha + \frac{B}{2}\sin\eta_\beta \tag{3.35}$$

The energy level diagram corresponding to this Hamiltonian is that of a four-level system with energies in frequency units[6]:

$$
\begin{aligned}
|\alpha\alpha\rangle = |1\rangle &= \frac{\omega_S}{2} - \frac{\omega_{12}}{2} \\
|\alpha\beta\rangle = |2\rangle &= \frac{\omega_S}{2} + \frac{\omega_{12}}{2} \\
|\beta\alpha\rangle = |3\rangle &= -\frac{\omega_S}{2} - \frac{\omega_{34}}{2} \\
|\beta\beta\rangle = |4\rangle &= -\frac{\omega_S}{2} + \frac{\omega_{34}}{2}
\end{aligned}
\tag{3.36}
$$

A visual representation of these energy levels can be found in Fig. 3.8.

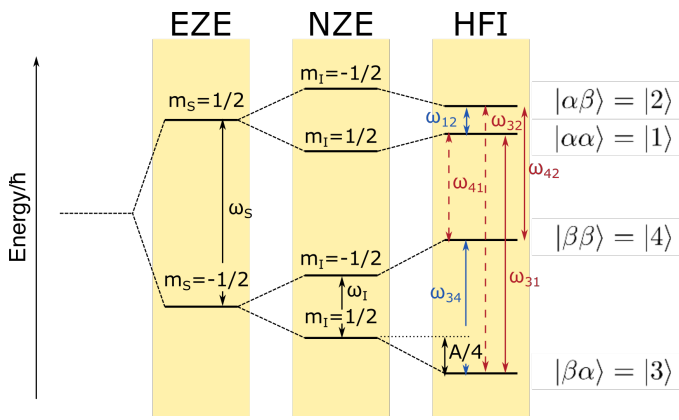

FIGURE 3.8: Illustration of the Energy level diagram of an $S = \frac{1}{2}$, $I = \frac{1}{2}$ system for positive A and g_n in the case of weak-coupling. From left to right, the EZE, NZE and HFI. The EPR allowed transitions ($|\Delta m_S| = 1$, $|\Delta m_I| = 0$) are indicated with a solid line, the EPR forbidden transitions ($|\Delta m_S| = 1$, $|\Delta m_I| = 1$) with a dashed line, and the nuclear transitions ($|\Delta m_S| = 0$, $|\Delta m_I| = 1$) are indicated with blue arrows.

Electron Spin Echo Envelope Modulation Electron spin echo envelope modulation (ESEEM) [206] refers to a group of pulsed hyperfine EPR experiments that are – next to electron nuclear double resonance (ENDOR) experiments (see further on) – very well suited to detect nuclear couplings in the spin system. The ESEEM experiments consist of a combination of microwave pulses that generate a spin echo and whereby the time between those pulses is varied (see Fig. 3.9). The echo intensity will decay exponentially with the inter-pulse time and is modulated in function of the evolution time when nuclei are coupled to the electron spin. A Fourier transformation of the time-domain ESEEM signal will lead to a frequency domain spectrum from which the nuclear Zeeman and hyperfine and quadrupole tensors can be (partially) reconstructed.

[6]Note that this is referred to the energy of the $S = 1/2$ system prior to the application of the magnetic field and introduction of the nuclear spin.

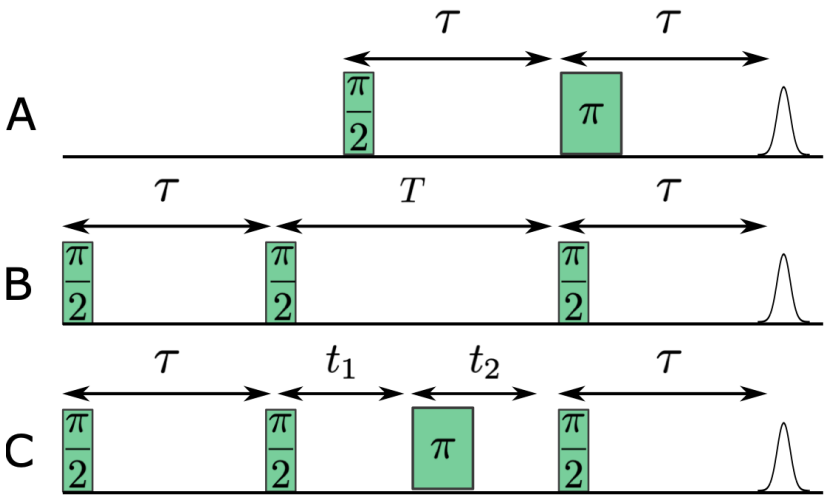

FIGURE 3.9: ESEEM pulse schemes of (A) a two-pulse, (B) a three-pulse and (C) a four-pulse or HYSCORE [207] experiment. The detected signal is the echo intensity $I(\tau)$ (A), $I(T)$ (B) and $I(t_1, t_2)$ (C).

The detailed physics on the origin of the modulation can be found elsewhere [204]. Here we briefly touch some important concepts to gain more insight in ESEEM experiments based on [205]. From the pulse schemes in Fig. 3.9 we can understand that the density operator will evolve differently depending on which pulse is on or off. When a pulse is off, the time evolution of the density operator will be subjected to the spin Hamiltonian, and when a pulse is on, the evolution occurs under influence of the pulse Hamiltonian and spin Hamiltonian. For sufficiently short pulses, the effect of the latter can be neglected.

In the rotating frame, the Hamiltonian during the pulse is given by

$$\hat{H}_e = \omega_1 \hat{I}_x. \tag{3.37}$$

The density operator during that pulse will evolve according to Eq. (3.27), on the condition that we will make the Hamiltonian time independent by moving to a new frame: the rotating frame. In that case, the density operator has the form of a rotation operation, with θ the flip angle of the pulse

$$\hat{R}_x(\theta)\hat{\sigma}(0)\hat{R}_x^{-1}(\theta). \tag{3.38}$$

Choosing $\theta = \frac{\pi}{2}$, we turn the electron magnetization away from equilibrium from the z-axis to the y-axis in the classical picture. This results in

$$\underbrace{\hat{\sigma} \propto -\hat{S}_z}_{\text{Equilibrium}} \xrightarrow{(\pi/2)\hat{S}_x} \hat{S}_y. \tag{3.39}$$

Transforming $\hat{S}_y$ by using Eq. 3.29 to the eigenbasis results in

$$\hat{S}_y \xrightarrow{\hat{U}} \cos(\eta)\hat{S}_y - \sin(\eta)2\hat{S}_x\hat{I}_y. \tag{3.40}$$

with η related to the secular and pseudo-secular hyperfine coupling constants as defined above. The matrix representation for $S = \frac{1}{2}, I = \frac{1}{2}$, shows that a $\pi/2$-pulse converts a diagonal density matrix to a density matrix with off-diagonal elements, creating electron coherence (EC).

After the first $\frac{\pi}{2}$-pulse, the density matrix evolves under the spin Hamiltonian. The evolution of the density matrix elements for which $\sigma_{ij} \neq 0$ can be interpreted as a precession of a corresponding vector in the (x, y) plane gaining a phase $\Omega_S^{(i,j)}\tau = \omega_{ij} - \omega_{mw}$.

Two-pulse ESEEM The second pulse in a 2-pulse ESEEM scheme (Fig. 3.9 A) is a π-pulse. This pulse rotates the magnetization vectors 180° around the x axis but also redistributes the EC among all the electron spin transitions (so-called branching). During the second evolution time τ, these redistributed components k, l will gain a non-equal phase $(\Omega_S^{(k,l)})\tau = (\omega_{kl} - \omega_{mw})\tau$ such that after a time τ, the refocusing echo is not completely restored. The echo intensity is dependent on the difference between the phase gain after and before the π-pulse: $(\omega_{kl} - \omega_{ij})\tau$. This agrees with nuclear frequencies (*i.e.* $(\omega_{31} - \omega_{41}) = \omega_{34}$) that can be determined by detecting the echo as a function of the time τ.

Two-pulse ESEEM is a simple and fast technique, but is generally limited by its dependence on the short T_2 values.

Three-pulse ESEEM In a three-pulse ESEEM sequence (Fig. 3.9B), nuclear coherence (NC) is generate by the $\frac{\pi}{2} - \tau - \frac{\pi}{2}$ sequence. This NC evolves during time T and is transferred back to EC by the last $\frac{\pi}{2}$ pulse. Time T is varied in the experiment. The overall line width of the peaks is narrower, since the experiment is limited by the phase memory time of the nuclei which is approximately equal to the electron spin-lattice relaxation ($T_{m,n} \approx T_{1,e}$). However, three-pulse ESEEM needs to be collected at different τ values, in order to remove τ-dependent blind spots.

Four-pulse ESEEM The last and most informative way to collect an ESEEM spectrum is the four-pulse ESEEM or HYSCORE experiment (Fig. 3.9 C) [207, 208]. In this experiment interpulse times t_1 and t_2 are varied creating a two-dimensional dataset.The HYSCORE spectrum after Fourier transformation will contain four quadrants which are symmetrical deducting it to two informative quadrants $(+, +)$ and $(-, +)$. Cross-peaks in the HYSCORE spectrum relate the nuclear frequencies of 2 m_S manifolds. An advantage in HYSCORE is that we can separate weak couplings $|\frac{A}{2}| \ll |\omega_I|$ in the $(+, +)$ quadrant from the strong couplings $|\frac{A}{2}| \gg |\omega_I|$ in the $(-, +)$ quadrant. Overall, the main advantage of this technique is obtaining 2D-information and correlations that were previously unresolved.

Electron Nuclear Double Resonance Another hyperfine method to detect nuclear frequencies is the so-called ENDOR experiment which can be obtained in a CW- or pulsed mode. I will only focus on the pulsed ENDOR experiments here and refer the

reader to references on the technique [209, 204, 210, 203]. The two most popular pulsed detection schemes are Davies ENDOR [211] and Mims ENDOR [206] (see Fig. 3.10 A and B, respectively). Essential to Davies ENDOR is the selective[7] microwave pulse and a radio frequency (RF) π-pulse. The first mw π-pulse inverts the electron spin polarization ("hole burning"). The effect of the rf-pulse is shown in Fig. 3.11: When the rf-pulse is on resonance with an NMR transition, that is connected with an inverted EPR transition, then a change in polarization will occur that is detected *via* the detection scheme in Fig. 3.10, being a Hahn echo, but also an FID detection can be used. By changing the rf-frequency, we will observe an effect in the echo intensity when a nuclear transition occurs. ENDOR can therefore be considered to be an NMR experiment, using the electron spin as an observer. The length of the RF π-pulse is optimized in order to obtain a perfect π-pulse.

The Mims ENDOR is less straight-forward to comprehend. It relies on the three-pulse ESEEM scheme, with an RF pulse during the mixing period T. When this RF-pulse hits nuclear frequencies, the effect will be detected in the stimulated echo. Mims ENDOR experiments are collected at multiple τ-values as well to overcome blind spots (see also 3-pulse ESEEM). Whereas Davies ENDOR is better suited to detect large (> 3 MHz) hyperfine couplings, Mims ENDOR is sensitive to small couplings.

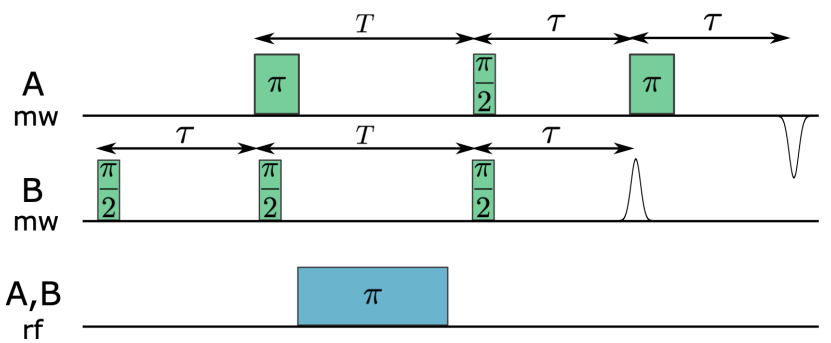

FIGURE 3.10: ENDOR pulse schemes of (A) Davies ENDOR [211] (B) Mims ENDOR [206] experiment. The detected signal is the echo intensity $I(\tau)$

[7] length depends on nuclear spin you want to excite

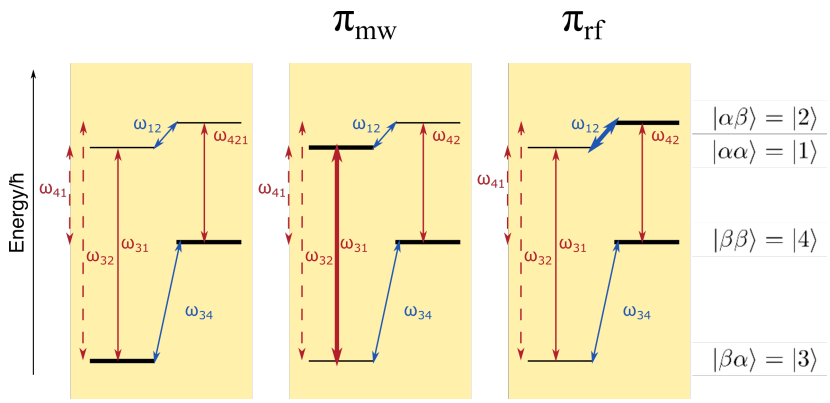

FIGURE 3.11: Population changes in Davies ENDOR: the effect of the different state in an $S = \frac{1}{2}$, $I = \frac{1}{2}$ spin system. Magnitude of the populations is indicated by the thickness of the level line. π_{mw} is the microwave pulse inverting the 1-3 population and π_{rf} the RF pulse. If π_{rf} hits the NMR transition 1-2 it will result in a change in the polarization compared to the case where no transition is hit and this difference is detected.

Experimental setup *X-band pulsed EPR* experiments were performed on a Bruker E580 or W/X E680 ELEXSYS spectrometer with a microwave frequency of ∼9.74 GHz, equipped with a gas-flow cryogenic system (Oxford Instr Inc.), allowing for operation from room temperature to 4 K. Experiments were performed at 6.5 K unless stated otherwise. A shot repetition time of 1 ms was taken, unless stated otherwise. The detailed pulse lengths and inter-pulse times are explicitly reported in the result chapters of this thesis. The three-pulse ESEEM and HYSCORE spectra were baseline-corrected using a third-order polynomial, apodized with a Hamming window and zero-filled. After Fourier transformation, the absolute-value spectra were calculated. *W-band ESE-detected EPR* experiments were performed on a Bruker E680 ELEXSYS spectrometer with a microwave frequency of ∼94.0 GHz. All EPR spectra were computer simulated using EasySpin [212], a toolbox for MATLAB (MathWorks, USA).

3.4.5 EPR of heme proteins

Spin states of systems with *d*-electrons Heme proteins are frequently studied with EPR and hyperfine spectroscopy because of the paramagnetic nature of many heme states [96]. The electronic configuration of the Fe(III) heme iron cation is

$$1s^2 2s^2 2p^6 3s^2 3p^6 3d^5 = [Ar]3d^5, \tag{3.41}$$

or $[Ar]3d^6$ when Fe(II). The heme iron is commonly hexa-coordinated (6c) or penta-coordinated (5c) and is arranged in an octahedral (6c) or square pyramidal (5c) conformation (see Fig. 3.12 (A,B)). The geometry of the first coordination sphere affects the energy and lifts the five-fold degeneracy of the $3d$-orbitals, which can be easily understood via a simplified crystal-field theory. An octahedral geometry leads to a splitting of the three-fold degenerate t_{2g}-orbitals (d_{xy}, d_{yz} and d_{xz}), on the one hand, and the two-fold

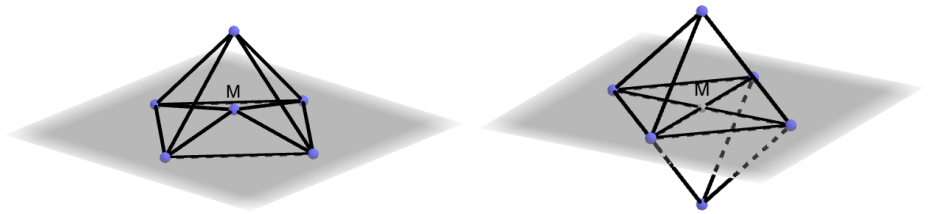

(A) (B)

FIGURE 3.12: Low- and high-spin heme Fe(III): (A) Square pyramidal coordination as found in 'pentacoordinated gbs' leaving a vacant position for ligands to bind and octahedral coordination (B) as found in 'hexacoordinated gbs'.

degenerate e_g orbitals (d_{z^2} and $d_{x^2-y^2}$) on the other hand. Depending on the energy gap Δ_O between those sets, which is affected by the distal heme ligand, the electrons pair up in the t_{2g} to form a low-spin (S=1/2) configuration, or spread out over the t_{2g} and e_g orbitals resulting in a high-spin ($S = 5/2$) configuration. Intermediate spin ($S = 3/2$) and admixed states are also possible (see later, chapter 6 on *Ma*Pgb). Lowering the symmetry of the system leads to another lift in degeneracy in the t_{2g} orbitals, as illustrated in Fig. 3.13.

For low-spin Fe(III) complexes, the ligand-field parameters V and Δ are closely related to the principal g-values we obtain by an EPR experiment *via*

$$\frac{V}{\lambda} = \frac{g_x}{g_z + g_y} + \frac{g_y}{g_z - g_x} \tag{3.42}$$

and

$$\frac{\Delta}{\lambda} = \frac{g_x}{g_z + g_y} + \frac{g_z}{g_y - g_x} - \frac{V}{2\lambda}, \tag{3.43}$$

with $g_z > g_y > g_x$, the tetragonal splitting parameter Δ, the rhombic splitting parameter V (Fig. 3.13) and with λ, the spin-orbit coupling [213]. Using these in the combination with the so-called 'truth tables' of Peisach and Blumberg [214] gives us an indication of the type of ligand that is coordinated with the heme Fe(III) ion. However, these tables are only of a qualitative use and more advanced EPR methods and DFT calculations are recommended to gain more insight on the metal complex.

In the $S = 5/2$ high-spin state (left panel, Fig. 3.13 A), a common configuration in heme proteins, the zero-field interaction in the spin Hamiltonian becomes of importance resulting in a lift in degeneracy between the m_S manifolds (see also §3.4.2). In that case, the system can also be described as an 'effective' $S = \frac{1}{2}$ system.

CW EPR The difference between high- and low-spin heme centers is strongly reflected in the CW-EPR spectrum. As an example, the X-band CW spectrum of ferric Mb at pH 7.5 is given in Fig. 3.13 (B), as it shows high-and low-spin spectral features simultaneously, and matches well the theory (see also Fig. 3.6). The (CW)-EPR spectrum of ferric Mb was already known in the mid-fifties and many other heme proteins coordinated

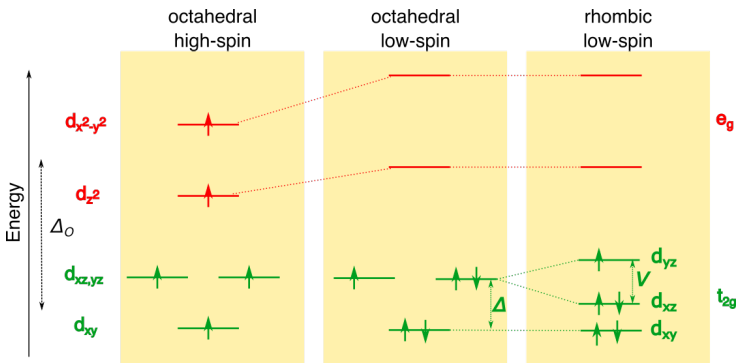

(A)

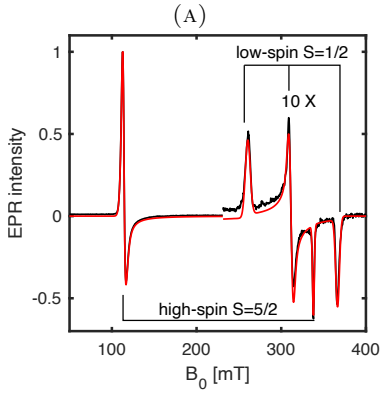

(B)

FIGURE 3.13: The diagram in (A) shows how the energy level scheme is influenced by Δ_O and the ligand-field parameters V and Δ for a rhombic distortion of an octahedral configuration are indicated. (B) Illustration of a typical high- and low-spin signal as commonly observed in heme proteins. A frozen solution of Mb (black) and simulation (red) in a Tris pH 7.5 buffer collected at T=12 K, P=1 mW and a modulation amplitude of 0.5 mT. The low-spin region is shown 10 × amplified. At pH 7.5, both signals due to a high-spin ($S = 5/2$) and low-spin ($S = \frac{1}{2}$) system are observed. The former arises from a water-coordinated Fe(III)metMb, whereas the low-spin form is due to a OH^--ligated Fe(III)Mb state (alkaline transition).

to various ligand resulting in different spin states were analysed using EPR spectroscopy thereafter [215, 216, 217].

Pulsed EPR Next to CW EPR, the previously introduced pulsed hyperfine methods have a lot of potential to gain more structural and electronic properties of heme-containing proteins [96, 218] and reveal the many nuclei surrounding the heme iron environment, especially on the hyperfine interaction with the ($I = 1$) pyrrole N's and proximal/distal histidine N's and protons ($I = \frac{1}{2}$).

The 4-level energy diagram of an $S = \frac{1}{2}$, $I = \frac{1}{2}$ system was already introduced in Fig. 3.8, revealing the two EPR-allowed and forbidden transition frequencies. In case of an $S = \frac{1}{2}$ and $I = 1$ system, we can describe the energy-splitting diagram in the presence of an external magnetic field as shown in Fig. 3.14, which shows the energy levels under the strong-coupling regime ($|a|/2 \gg \omega_I$). Six nuclear transitions are indicated in which one distinguishes between single quantum (sq) $|\Delta m_I| = 1$ and double quantum (dq) $|\Delta m_I| = 2$ transitions. When the hyperfine interaction is dominating, the dq-peaks positions can be found in ESEEM spectra at

$$\nu_{DQ\pm} = 2\sqrt{(\nu_I \pm \frac{A}{2})^2 + \kappa^2(3+\eta^2)}, \tag{3.44}$$

with $\kappa = \frac{e^2qQ}{4h}$. The single-quantum transitions are typically more broadened than cross peaks linking dq frequencies, because of their first-order dependence of the nuclear quadrupole coupling. The ^{14}N HYSCORE experiment is very useful for the analysis of heme proteins. For example, an important study by García-Rubio *et al.* [219] disentangled the ^{14}N hyperfine crosspeaks in the ESEEM spectra of a cytochrome b559 distinguishing the contributions from the pyrrole nitrogens and the ligated His N, and led to more insight in many heme proteins [220, 221].

3.5 Native mass spectrometry

Native mass spectrometry has become a reliable technique in structural biology allowing the characterization of the proteins' oligomerization, architecture, and/or ligand binding [222, 223, 224]. Unlike in conventional proteomics approaches [225], where the protein is denatured and/or digested in solution, native MS enables the protein to be still in its native, folded state before entering the gas phase [226] upon the application of soft ionization techniques such as nano-electrospray ionization. Thus, the technique provides information on the quaternary biomolecular structure and ligand association [227]. In this work, native MS is the only analytical technique that does not make use of EM radiation. Instead, the protein sample solubilized in a volatile solution experiences a high voltage capable of generating gas-phase ions which, based on the charge-state distribution, provide information on the mass as well as the folded character of the protein complex. The average charge state directly correlates with the proteins' solvent accessible surface area allowing to discriminate (un)folded protein structures [228]. Here, we apply

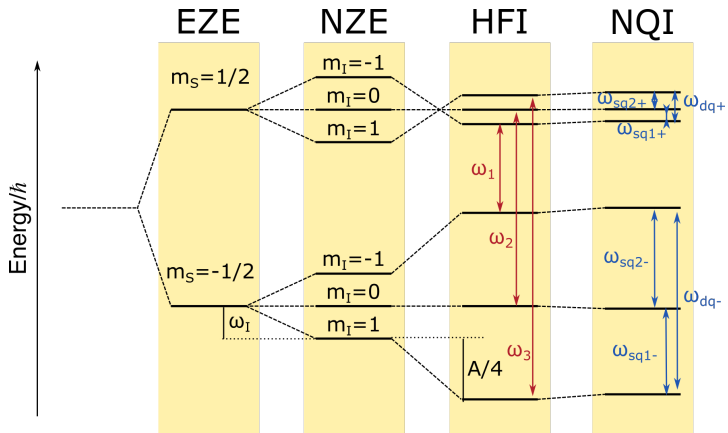

FIGURE 3.14: Energy level diagram of an $S = \frac{1}{2}$, $I = 1$ systems: in the "strong coupling regime" ($\nu_I \ll |A|/2$). From left to right, the effect of the EZE, NZE, HFI and NQI. The sq or 2 dq nuclear transitions ($|\Delta m_S| = 0$, $|\Delta m_I| = 1$) are indicated.

native MS on heme proteins [229, 230] in combination with collision-induced dissociation (CID). CID is a gas-phase fragmentation technique that exploits collisions between the analyte ions and an inert gas, e.g. Ar or N_2, to build up internal energy which consequently leads to covalent bond breakage. Native MS along with CID is therefore a useful application to enforce protein unfolding, subunit dissociation, and most importantly in our case, the release of the heme group [231, 232]. The oxidation and/or coordination state of the heme iron affects the stabilization of the protein-heme complex and thus has a direct impact on the required collision energy [233].

Experimental setup Protein samples (10 µM) were buffer exchanged into a volatile ammonium acetate (100 mM NH_4OAc, pH 6.8) solution using P-6 micro Bio-Spin columns (Bio-Rad). A few microliters of the buffer-exchanged sample were loaded into in-house produced gold-coated borosilicate glass capillaries for infusion into a Synapt G2 HDMS (Waters, Wilmslow, UK) mass spectrometer. Native MS experiments were conducted by using nano-electrospray ionization (nanoESI) to generate ions of the protein complex which were drawn into the vacuum of the mass spectrometer. Crucial instrument settings to retain the native, quaternary structure were as follows: 1.2 kV capillary voltage, 60 V sampling cone, 3 V extractor cone, 10 V and 2 V collision energy in the trap and transfer collision cell, respectively. Pressures throughout the instrument were adjusted to 3.8 mbar for backing, 4.8×10^{-3} mbar source, and 2.7×10^{-2} mbar in the trap and transfer collision cell. Spectra were also acquired under elevated trap collision energies (50 V) which led to protein unfolding and the release of the heme group. The MS experiments shown in this thesis were recorded and interpreted by dr. Dietmar Hammerschmid (PPES/BAMS, Dept. of Biomedical Sciences/Chemistry).

Part II

Results

Chapter 4

The effect of pH and nitrite on the heme pocket of GLB-33, a globin-coupled neuronal transmembrane receptor of *Caenorhabditis elegans*

Redrafted after [234]
N. Van Brempt, R. Sgammato, Q. Beirinckx, D. Hammerschmid, S. Dewilde, L. Moens, W. Herrebout, C. Johannessen, and S. Van Doorslaer, "The effect of pH and nitrite on the heme pocket of GLB-33, a globin-coupled neuronal transmembrane receptor of *Caenorhabditis elegans*".
Own contribution
Over-expression and purification of GLB-33GDΔCys, UV-vis absorption, CW-EPR and pulsed EPR experiments on the ferric form, corresponding simulations, overall interpretation and discussion and writing of original draft.

4.1 Abstract

Out of the 34 globins in *Caenorhabditis elegans*, GLB-33 is a putative globin-coupled transmembrane receptor with a yet unknown function. The GD contains a particularly hydrophobic heme pocket, that rapidly oxidizes to a low-spin hydroxide ligated heme state at physiological pH. Moreover, the GD has one of the fastest NiR activity ever reported for globins. Here, a combination of ECD, rRaman and EPR spectroscopy with MS was used to study the pH dependence of the as-purified ferric form of the recombinantly over-expressed GD domain in the presence and absence of nitrite. The competitive binding of nitrite and hydroxide is examined as well as nitrite-induced heme-modifications at acidic pH. From comparison of the spectroscopic results with data from other heme proteins, the important effect of Arg at position E10 in the ligand stabilization is deduced. Furthermore, CW and pulsed EPR indicate that ligation of nitrite occurs in a nitrito mode at pH 5 and above. At pH 4, an additional formation of a nitro-bound heme form is observed along with fast formation of a nitri-globin.

4.2 Introduction

Gbs are small heme-containing α-helical globular proteins widespread throughout the kingdoms of life [1, 42]. Besides the well-known role of gbs in the O_2 transport and storage in vertebrates, gbs are shown or hypothesized to be involved in a large variety of biochemical processes, including scavenging of ROS and RNS, redox reactions and ligand (e.g. O_2) sensing [42]. Based on their lineage, gbs are classified into three families: myoglobin-like (M), sensor (S) and truncated globin (T) family [1, 42, 235, 19, 236]. Next to SD proteins, consisting of a globin protein only, chimeric proteins consisting of a GD coupled to other domains, such as a transmitter domain, have been identified [1, 42]. The classical globin fold, with Mb as archetypical example, consists of eight α-helices, labeled A to H from N- to C-terminus, that are organized in a 3-over-3 (3/3) sandwich, with the heme group situated in the hydrophobic center and the heme iron coordinated at the proximal side to the conserved His at position 8 of the F helix (F8His). This fold is found in the M and S families, with variation in this structure mainly occurring by N- and C-terminal extension and variation in length of the inter-helical segments [235]. Furthermore, gbs from the T family are shorter, exhibiting the 2-over-2 globin fold (2/2), i.e. an α-helical sandwich of the B-E and G-H helices. They are normally shorter than the 3/3 gbs and therefore indicated as truncated Hbs [7].

Ce is found to be exceptionally rich in gbs and thus offers an ideal system to unravel the diversity of globin functions and globin structures. In distinct cell types of this species, 34 globin-like proteins are transcribed and expressed [110, 111]. Some of these gbs have been partially characterized and putative functions have been ascribed to them [114, 115, 74, 119, 117, 149, 237, 118]. GLB-33 is the largest of the *Ce* gbs and consists of a GD and a 7 α-helical 7 TM domain, typical for GPCRs. Homology modelling predicts that the GD has the classical globin fold with eight α-helices in a canonical 3/3 sandwich [118]. Similar to Mb, the heme iron of GLB-33GD has no distal ligand in its reduced ferrous form (so-called pentacoordination of the heme iron). However, this form oxidizes

fast, resulting in a ferric heme iron that is ligated to hydroxide in a broad range of slightly acidic to basic conditions [118]. This is in contrast with the majority of other gbs in which distal OH^- ligation only sets in at alkaline pH. To our knowledge, only the *Thermobifida fusca* (*Tf*)-TrHbs show a similar pH-dependent behaviour [238]. Hydrogen bonding networks with distal heme-pocket amino-acid residues are thought to stabilize the ligation of hydroxide at physiological pH [238, 239]. Whereas the in vivo function of GLB-33 is unclear, in vitro experiments show that the GD reduces nitrite to NO 10× faster than Mb [118]. NO_2^- is a precursor of RNS and has been linked to cellular signalling, intestinal relaxation, vasodilation, neurotransmission, and neuromodulation in a broad range of species [240, 50]. Many gbs have been indicated to play a role as NO scavengers or NiRs [240, 241, 242, 243, 244, 245]. Moreover, many other heme proteins are involved in nitric-oxide pathways in different organisms and function as NO generators or deliverers, or convert nitrite to other reactive nitrogen species [241, 246], suggesting the involvement of the full-length GLB-33 protein in the NO metabolism of *Ce*.

The globin-nitrite interaction is complex with many intermediates identified in vitro depending on the initial heme iron state (Fe(III), Fe(II), Fe(II)-O_2, ...). Under specific conditions, heme modifications and partial heme loss have been observed [82, 100, 99, 247]. After entering the heme pocket, NO_2^- can coordinate the iron ion in either the favoured N-linked nitro (−NOO) and the less favoured O-linked nitrito (−ONO) ligation mode (see Figs. A.1 (A, B)) for representation), which has implications for the subsequent NiR mechanism [247, 91, 248, 86, 249]. In the nitro mode, a formal double protonation of one of the nitrite O-atoms precedes the release of a water molecule and generation of an Fe(III)-NO species, which then dissociates. In the O-linked nitrito mode, NO is released through an ON-O bond homolysis after protonation of the iron-bonded nitrite oxygen atom, resulting in NO and an Fe(III)-hydroxo complex [91].

Optical and magnetic-resonance methods are here combined with native MS to study the pH-dependent distal heme ligation, heme modifications and overall stability of the ferric form of the GLB-33GDΔCys variant in the absence and presence of nitrite. More specifically, CW and pulsed EPR techniques, rRaman, UV/Vis absorbance (Abs) and ECD spectroscopy are used, since they are excellent complementary tools to probe the interaction of heme proteins with various ligands [96, 250, 189]. EPR is also used to study the nitrosylated ferrous form of the protein that appears during NiR activity in the presence of a reducing agent. The GLB-33GDΔCys variant was taken such as to prevent unspecific in vitro multimerization of the protein at the higher protein concentrations needed for EPR.

4.3 Materials and methods

4.3.1 Expression and purification

The cDNA coding for GLB-33GD and double mutant C40S/C55S (GLB-33GD ΔCys) (glb-33 gd, bp 1120 to 1629) was cloned into a pET23a vector with a C-terminal His-tag (Novagen) using NdeI and XhoI restriction enzymes (Biolabs) as described elsewhere

[118]. After growing BL21(DE3)PlysS with coding cDNA, cells were resuspended (50 mM Tris at pH 7.5, 300 mM NaCl) followed by repeated freeze-thaw cycles and sonication to lyse the cells. After centrifugation (10 min, 10000 g, 4 °C), the supernatant was loaded onto a Ni Sepharose High Performance column (GE Healthcare), pre-equilibrated with equilibration buffer (50 mM Tris-HCl at pH 7.5, 300 mM NaCl, 20 mM imidazole) and eluted (50 mM Tris at pH 7.5, 250 mM imidazole). The eluate was dialyzed with a solution of 50 mM Tris at pH 7.5, 0.5 mM EDTA, 150 mM NaCl, and then concentrated and loaded onto a G75 gelfiltration self-packed column as a final purification step. The validity of using the variant was tested by comparing the UV-Vis and some EPR spectra of GLB-33GD and GLB-33GDΔCys at neutral pH. Horse skeletal muscle (hs)Mb was purchased from Merck KGaA (Darmstadt, Germany) and dissolved in the same buffers as GLB-33GDΔCys unless stated otherwise.

4.3.2 UV-Vis absorption and electronic circular dichroism spectroscopy

UV-visible Abs/ECD spectra of GLB-33GDΔCys were recorded on a Chirascan®-Plus spectrophotometer (Applied Photophysics, Leatherhead, Surrey, UK). The instrument was continuously flushed with nitrogen gas (4 L/ min flow rate), and the measurements were carried out at 20 °C. For all the recorded spectra, 0.2 cm path length SUPRASIL quartz sample cells (Hellma BeNeLux, Kruibeke, BE) were used. The final spectra were subtracted by the corresponding spectrum of the solvent used for the respective measurement (Tris-HCl for pH 7.5 and 6, or sodium acetate buffer for pH 5 and 4, in presence of 100 mM NaCl). The globin concentration was calculated using the absorption at the Soret peak (412 nm), and the extinction coefficient value of human neuroglobin $\varepsilon_{412\ \mathrm{nm}} = 130\,000\ \mathrm{M}^{-1}\ \mathrm{cm}^{-1}$ [251]. 2.5 µM GLB-33GDΔCys was measured in the spectral range between 260 nm and 800 nm and between 195 nm and 260 nm (3 s nm^{-1}, 1 nm bandwidth). All buffer exchanges were obtained via Micro Bio-Spin chromatography columns (BioRad, Hercules, California USA). Nitrite solutions were freshly prepared prior to each measurement.

4.3.3 Resonance Raman spectroscopy

rRaman spectroscopy was carried out at room temperature using a ChiralRaman-2X spectrometer (BioTools, Inc., Jupiter, Florida, USA). Unpolarised rRaman spectra were recorded in backscattering geometry, using a green laser beam from a frequency-doubled Nd:YVO4 laser (532 nm). The instrument was running at a spectral resolution of 7 cm^{-1}. 60 µL sample was centrifuged at 14000 rpm for 5 min, at 4 °C prior to each measurement, and then loaded into 3×4×10 mm quartz cuvette (Starna Scientific Ltd, Ilford, London, UK). The laser power was set at 0.3 W at the source, and the samples were illuminated in stretches of 2 s to prevent them from heating up. The total acquisition time varied depending on the sample stability. The protein sample, prepared in sodium acetate or Trizma® hydrochloride buffer in presence of 100 mM NaCl and having final molar concentration of 25 µM, was measured in the as-purified form and upon incubation with nitrite in one to fifty molar ratio, at pH 5 or 7.5, respectively. rRaman spectra of the

samples were subtracted by the corresponding spectrum of the solvent and subsequently baseline corrected according to the Eilers-Boelens procedure [252]. For experiments with the isotopically labelled ligand, $Na^{15}NO_2$ (95 atom %) as well as $Na^{14}NO_2$ were purchased from Merck KGaA (Darmstadt, Germany).

4.3.4 Electron paramagnetic resonance

Globin solutions were diluted in glycerol until a final concentration of 10-25 % (v/v) glycerol. The X-band CW acEPR measurements were performed on an ESP300E (Bruker) spectrometer with a microwave frequency of 9.45 GHz equipped with a gas-flow cryogenic system (Oxford Instr. Inc.), allowing for operation from room temperature down to 2.5 K. The magnetic field was measured with a Bruker ER035M NMR Gauss meter. Paramagnetic O_2 was removed from the sample via several freeze-pump-thaw cycles. The spectra were measured with a modulation frequency of 100 kHz and a modulation amplitude of 0.5 mT unless stated otherwise. The microwave power is mentioned in the corresponding figure captions. X-band pulsed EPR measurements were conducted on a Bruker E580 Elexsys spectrometer (microwave frequency $\approx$ 9.74 GHz) equipped with an Oxford Instr. Inc. gas-flow cryogenic system to obtain an operating temperature of 6.5 K. A shot repetition time of 1 ms was used in all experiments. X-band electron-spin-echo (ESE)-detected EPR experiments [204] were recorded using the 2-pulse sequence $\frac{\pi}{2} - \tau - \pi - \tau - echo$, with pulse lengths $t_{\pi/2} = 16$ ns and $t_\pi = 32$ ns and the inter-pulse distance τ varied from 96 ns to 4184 ns in steps of 8 ns. The X-band three-pulse ESEEM experiments [204] were done using a $\frac{\pi}{2} - \tau - \frac{\pi}{2} - T - \frac{\pi}{2} - \tau - echo$ microwave pulse sequence with pulse lengths of $t_{\pi/2} = 16$ ns and are the sum of spectra recorded at 10 τ-values in the range of [96-240] ns in steps of 16 ns with T varied from 96 ns to 4880 ns in steps of 16 ns. HYSCORE spectra [207] were recorded using the microwave pulse sequence $\frac{\pi}{2} - \tau - \frac{\pi}{2} - t_1 - \pi - t_2 - \frac{\pi}{2} - \tau - echo$ with $t_{\pi/2} = 16$ ns and $t_\pi = 32$ ns and t_1 and t_2 were varied from 96 ns to 4480 ns in steps of 16 ns. HYSCORE measurements were recorded with different τ-values and added together as indicated in the figure captions. All spectral treatment and analysis were done using MATLAB (R2020a, MathWorks, USA). The three-pulse ESEEM and HYSCORE spectra were baseline-corrected using a third-order polynomial, apodized with a Hamming window and zero-filled. After Fourier transformation, the absolute-value spectra were calculated. All EPR spectra were computer simulated using EasySpin package (v.5.2.28) [212], a toolbox for MATLAB.

4.3.5 Mass spectrometry

GLB-33GDΔCys (20 µMM) was incubated with 50-fold molar excess of $NaNO_2$ (1 mM) at pH 4.0 (50 mM sodium acetate) and pH 7.5 (50 mM Tris-HCl) for 24 hours at room temperature. After $NaNO_2$ treatment, the samples were buffer exchanged to a volatile ammonium acetate solution (100 mM, pH 6.8) using P-6 Micro Bio-Spin columns (Bio-Rad). Each sample was loaded into homemade gold-coated borosilicate glass capillaries and mounted onto a Synapt G2 HDMS mass spectrometer (Waters, Wilmslow, UK), where native nano-electrospray ionisation (ESI) mass spectrometry experiments were performed. The following instrument parameters were carefully optimized to avoid ion

activation and protein unfolding (Ion mobility mode): capillary voltage: 1.2 kV, sampling cone: 25 V, extractor cone: 3 V, trap collision energy: 10 V, trap DC bias: 45 V, and transfer collision energy: 2 V. Pressures were set to 3.8 mbar in the source region (backing), 2.7×10^{-2} mbar in both trap and transfer collision cells (collision gas: Ar), and 3.0 mbar in the IMS cell. Spectra were also acquired under elevated trap collision energies (50V) to cause protein unfolding and the release of the prosthetic heme group.

4.4 Results

Some of the key AA residues in the heme pocket of gbs are, besides the conserved His at position 8 of the F-helix, the residues at positions B10, E7, and E11 (Fig. A.1). In a large amount of the gbs, a His residue is found at position E7 (Fig. A.1), but this is an Ile residue in GLB-33GD [118]. Moreover, homology modelling of GLB-33GD places two Ile residues (E7, E11), Leu (CD3) and Ala(B10) near the heme on the distal side, leading to an unusually hydrophobic distal heme pocket [118]. Furthermore, on position E10 an Arg residue is found, while this is Val in horse heart (hh)Mb. Research on the double mutant H64V/V67R hhMb (mutating the residues at positions E7 and E10) has shown that Arg plays an important role in directing the ligation of nitrite in the heme pocket [253]. In view of the high NiR activity of GLB-33GD and the alkaline transition at unusual low pH, we here investigate spectroscopically the pH dependence of ferric GLB-33GD and its nitrite ligation in relation to its heme-pocket structure. Also the EPR spectrum of the NO-ligated Fe(II) form (the final product from the NiR reaction) is considered. In the discussion section, all data will be compared to that of other heme proteins in order to understand the important role of Arg(E10).

4.4.1 pH dependence of ferric GLB33-GD

Fig. 4.1 (A, top) depicts the UV/Vis Abs spectra of ferric GLB-33GDΔCys at pH values 4, 5, 6 and 7.5. These spectra show that ferric GLB-33GDΔCys changes from a high-spin ($S = \frac{5}{2}$) ferric heme form (potentially with distal water ligation to the heme iron) at low pH to a hydroxo-ligated ferric heme form at neutral pH, in agreement with earlier findings on GLB-33GD as reported by my promotor and others [118]. This transition can be deduced from the red shift of the Soret band from 406 nm to 413 nm upon pH increase and the concomitant drastic change of the spectrum in the green-to-red range (Q bands). At low pH, a Q band appears at 502 nm with a charge-transfer band at 636 nm, which is characteristic of a 6-coordinated high-spin (HS) heme iron (6c/HS), while at neutral pH, the Q_β and Q_α bands are situated at 544 nm and 577 nm, respectively, with a small shoulder at 595 nm. The latter spectrum agrees with a hexacoordination of heme iron in a low-spin (LS) state (6c/LS), such as found for the distal hydroxo-ligation of the ferric heme.

The simultaneously collected ECD spectra (Fig. 4.1 (A, bottom)) exhibit positive and negative Soret ellipticity with the maxima corresponding to the respective Soret absorption bands and with minima at 362 nm and 439 nm. Under the acidic buffer conditions, the ECD spectra are reduced in Soret ellipticity, with only positive features

remaining in the 300-700 nm range. The two broad CD bands, observed at 584 nm and 611 nm in the spectrum of ferric GLB-33GDΔCys at pH 7.5, are absent at low pH in agreement with the changes observed in the Q-bands of the UV-vis Abs spectra. The heme optical activity has been ascribed to the interaction of the heme with aromatic amino-acid residues of the globin [254]. However, the sign of the Soret ECD band of heme proteins has also been shown to be influenced by the heme insertion [254, 255, 192], and the interaction of the heme side chains, particularly the propionate side chains, with the protein matrix [254] and by the in-plane and out-of-plane deformations of the heme group [256]. ^{1}H NMR studies have revealed heme rotational disorder in both reconstituted gbs and gbs produced in *E. coli* [257] with a related strong change of the Soret ECD band [192]. The positive sign of the Soret ECD peak of ferric GLB33-GD at low pH agrees with what has been reported for aquomet Mb with a correctly inserted heme [254]. The appearance of the minima at 362 nm and 439 nm in the ECD spectra at higher pH are therefore not linked to a reversed heme insertion since only a buffer exchange was done, but can be related to the change in the spin state (HS$\rightarrow$LS) and/or small conformational changes in the heme pocket and/or heme ruffling and saddling [256]. Finally, the ECD spectra in the far UV (Fig. A.2) show that the appearance of the aquomet form at the lowest pH is not accompanied with drastic changes in the secondary structure of the protein. In agreement with the UV/Vis Abs data, the spin-state rRaman marker bands indicate the presence of a 6c/LS Fe(III) species at pH 7.5 (ν_3 = 1506 cm^{-1}), while a significant contribution of a 6c/HS state appears at pH 5 (ν_3 = 1470 cm^{-1}) with only a small residual contribution of a 6c/LS state (Fig. 4.1 (B)) [118, 95]. The oxidation marker (ν_4 = 1376 cm^{-1}) does not change and is in agreement with the ferric state.

In the absence of any hydrogen bond, the ν(Fe-OH) stretching mode is typically found around 550 cm^{-1} for 6c/LS hydroxo-heme species, while the wavenumber of this mode decreases with increasing H-bond strength [238, 258, 259, 260]. This is illustrated by a combined rRaman and molecular dynamics study on *Tf*-TrHb, which revealed that the unusually low ν(Fe-OH) value found in this protein (489 cm^{-1}) is due to presence of strong hydrogen-bonding Trp and Tyr residues in the heme pocket [238, 260]. No clear signal is observed around 550 cm^{-1}in the low-wavenumber region of the rRaman spectrum of ferric GLB-33GDΔCys at pH 7.5 (Fig. 4.1 (C)). Instead, a dominant composite signal is found around 487 cm^{-1}, indicating a ν(Fe-OH) mode $<<$ 550 cm^{-1} and hence significant hydrogen bonding of the hydroxide ligand. The exact value of ν(Fe-OH) can, however, not be determined without isotope labelling experiments due to the expected overlap with other modes in this region [238].

At pH 5, the rRaman spectral signature changes completely in this wavenumber region with two signals now observed around 485 cm^{-1} and 520 cm^{-1} (Fig. 4.1, C). While ν(Fe-OH) $\approx$ 490 cm^{-1} is typically reported for 6c/HS species in an aquomet form [259], the observation of a peak at 520 cm^{-1} may point to the presence of residual 6c/LS form with weaker hydrogen-bonding stabilization [258]. This interpretation should, however, be considered with caution, because no isotope labelling was performed.

CW-EPR spectra of ferric hydroxo-ligated gbs are known to be strongly influenced by the degree of hydrogen bonding to the hydroxide ligand. Fig. 4.2 (A) shows the experimental and simulated X-band CW-EPR spectra of GLB-33GDΔCys at different

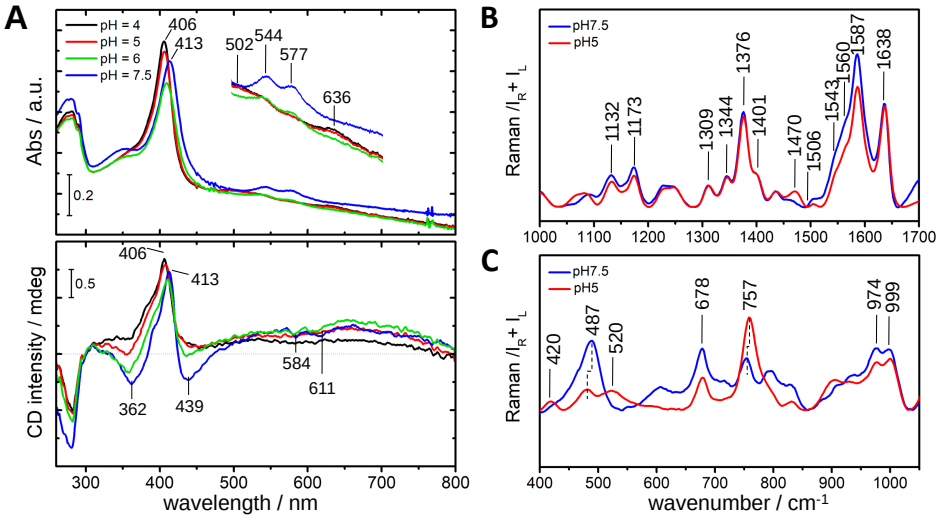

FIGURE 4.1: (A) UV/Vis Abs (top) and ECD (bottom) spectra of 25 µM ferric GLB-33GDΔCys in sodium acetate (pH 4, 5) or Tris-HCl buffer (pH 6.2, 7.5). Inset: The Q-band area of the spectrum is shown magnified for facile comparison. B and C: high and mid frequency rRaman spectral regions, respectively, of 25 µM ferric GLB-33GDΔCys at pH 5 and 7.5.

pH. At neutral pH, the spectrum is dominated by the contribution of two 6c/LS forms, with a negligible fraction of a HS heme (Table 4.1). The two 6c/LS forms, indicated by LS1 and LS2, agree with what was observed earlier at pH 8.5 for GLB-33GD [118]. The assignment of the different spectral components to LS1 and LS2 is confirmed by temperature-dependent EPR (Fig. A.3).

LS2 has principal g values that agree with what has been reported before for the hydroxo-form of Mb and related gbs and are indicative of minor to no hydrogen bonding of the hydroxide [262]. In contrast, the dominant LS1 species is more similar to the hydroxo-ligated species found in the TrHbs and their variants in which strong hydrogen bonding networks keep the hydroxide in place (Table 4.1, [238, 264]). This corroborates the above tentative conclusions drawn on the basis of the rRaman spectra (Fig. 4.1 (C)). The CW-EPR spectrum of GLB-33GDΔCys at pH 5 shows a minor LS fraction next to a large signal due to HS heme species, whereas at pH 4, only the contribution of the HS centres remains. The E/D values of the HS forms (Table 4.1) are characteristic for 6c/HS [261] and thus confirm the room-temperature rRaman and UV/Vis Abs data. The slight variations in the EPR data of the HS forms may result from pH-dependent small changes in the dielectric constant and/or small variations in the orientation of the axial water ligand in the heme pocket. The relatively small E/D-values of some of the HS/6c forms are in line with what has been observed for aquomet gbs.

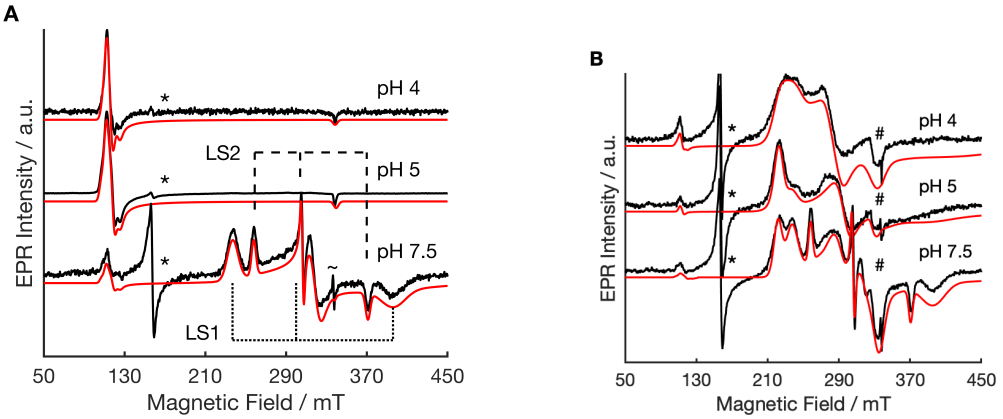

FIGURE 4.2: A. Experimental (black) and simulated (red) X-band CW-EPR spectra of frozen solutions of $\approx$ 1 mM ferric GLB-33GDΔCys in the absence (A) or presence (B) of 50$\times$ molar excess nitrite at pH 4, 5 and 7.5. Nitrite-treated samples (B) were immediately frozen after mixing to minimize the formation of green pigment (nitri-globin formation). The spectra were recorded at 10 K with a microwave power of 100 mW. Organic radical ($\sim$), background signal due to Cu(II) traces in the sample (#) and non-heme iron ($*$).

4.4.2 Effect of addition of nitrite to ferric GLB-33GDΔCys at different pH values

In a second step, the effect of addition of a 50-fold excess of sodium nitrite to ferric GLB-33GDΔCys is studied at different pH values. Only a small reduction in the high wavelength flank of the Q_α band of the UV/Vis Abs spectrum of ferric GLB-33GDΔCys is observed with increasing nitrite concentration at pH 7.5 (Appendix, Fig. A.5). The respective ECD spectrum shows no significant changes compared to the untreated sample at pH 7.5 (Fig. 4.3 (C)). In contrast, the nitrite treatment at pH 4 and 5 leads to

System	Label	g_x	g_y	g_z	E/D	%	coordination	Ref
GLB-33GDΔCys pH 7.5	LS1	1.70	2.20	2.84	n.a.	75	His/OH-	This work, [234]
	LS2	1.82	2.22	2.61	n.a.	23	His/OH-	
	HS1	1.957	1.957	1.984	0.0069	1	His/H2O	
	HS2	1.958	1.958	1.999	0.0180	1	His/H2O?	
GLB-33GDΔCys pH 5	LS1	1.70	2.20	2.84	n.a.	9	His/OH-	This work, [234]
	LS2	1.82	2.22	2.61	n.a.	2	His/OH-	
	HS1	1.957	1.957	1.984	0.0069	67	His/H2O	
	HS2	1.958	1.958	1.999	0.0180	33	His/H2O?	
GLB-33GDΔCys pH 4	HS1	1.968	1.968	1.991	0.0045	65	His/H2O?	This work, [234]
	HS2	1.950	1.950	1.999	0.0159	35	His/H2O	
Mb pH = 7.5	n.a.	1.98	1.98	2.00	0.0025	n.d.	His/H2O	[261]
Mb alkaline	n.a.	1.85	2.17	2.55	n.a.	n.d.	His/OH-	[262]
*Al*Mb pH 10.0	n.a.	1.75	2.10	2.72	n.a.	n.d.	His/OH-	[263]
LpHbII alkaline	n.a.	1.82	2.20	2.61	n.a.	n.d.	His/OH-	[262]
Tf-TrHb pH 6	n.a.	1.60	2.32	2.82	n.a.	n.d.	His/OH-	[238]
	n.a.	1.76	2.19	2.73	n.a.	n.d.	His/OH-	
	n.a.	1.81	2.19	2.66	n.a.	n.d.	His/OH-	
Cr-TrHb1 K53R	n.a.	1.66	2.21	2.78	n.a.	n.d.	His/OH-	[264]

TABLE 4.1: Principal g values and zero-field parameters (E/D) of the low-spin ($S = 1/2$) and high-spin ($S = 5/2$) species of ferric GLB-33GDΔCys obtained through simulation of the spectra in Fig. 4.2 (A) in comparison with literature data. Simulations of the individual components contributing to the spectra in Fig. 4.2 (A) are shown in Fig. A.4. n.a. = not applicable; n.d. = not determined; Mb = myoglobin; LpHb II = Hb II from Lucina pectinata; *Tf*-TrHb = truncated Hb 1 from *Thermobifida fusca*; *Cr*TrHb1 = truncated Hb 1 from *Chlamydomonas reinhardtii*. Experimental errors are in brackets for principal g-values of LS species (±0.01), HS species (±0.003), E/D (±0.005) and % (2).

substantial changes in the UV-Vis Abs/ECD spectra of GLB-33GDΔCys (Figs. 4.3 (A) and 4.3 (B)). An initial redshift of the Soret band from 406 nm to 416 nm and $Q_{\beta,\alpha}$ bands at 564 nm and 544 nm was observed in agreement with the reported spectra of nitrite-ligated cytochrome c' [265]. They indicate a shift from a 6c/HS to a 6c/LS state. These Abs spectra are considerably different from those observed for ferric Mb after addition of NO_2^- near neutral pH [266]. The ECD spectra of GLB-33GDΔCys with nitrite at acidic pH exhibit reduced, red-shifted Soret ellipticity, with a sharp, negative dichroic band and a broader, negative, and less pronounced ECD band appearing at 426 nm and 570 nm, respectively (Figs. 4.3 (A), 4.3 (B)).

Fig. 4.3 also shows the effect of incubation time with nitrite on the UV/Vis Abs and ECD spectra of ferric GLB-33GDΔCys at pH 7.5, 5 and 4. At pH 4 and 5 the formation of a green pigment could be observed visually, in line with the strong spectral modifications in the Abs/ECD spectra (Figs. 4.3 (A), 4.3 (B)). Long (24h) incubation times at pH 4 and 5 with nitrite lead to a reduction in the Soret Abs band, a broadening of the B band, and the appearance of a maximum at 356 nm. Green pigment formation with these associated Abs spectra point to the formation of a vinyl-nitrated globin derivative (nitri-globin) [101]. In the corresponding ECD spectra of nitrite-incubated GLB-33GDΔCys , the Soret ellipticity broadens over time with a concomitant broadening of the band at 426 nm, which shifts up to 448 nm. Finally, the negative ellipticity centred around 351- 356 nm becomes dominant, with a corresponding disappearance of the negative ellipticity at 570 nm. ECD spectroscopy in the far UV-region demonstrates that the secondary structure composition is largely retained at the experimental conditions used for our purpose (Fig. A.2).

The rRaman spectra of the nitrite-treated ferric GLB-33GDΔCys at various pH-values follow the observations with Abs spectroscopy (Fig. 4.4, Fig. A.6). At pH 7.5, the spectrum did not reveal changes in the spin and/or ligation state of the heme iron with respect to ferric GLB-33GDΔCys (Fig. A.5). At pH 4 and 5 in contrast, a strong reduction in the ν_{10} Raman intensity and changes in the relative ratio between the Raman bands ν_{37} and ν_{10}, and between ν_5 and ν_{30} are observed (Figs. 4.4 and A.6).

In the presence of nitrite, the vinyl stretching mode ν_{21} is found to be pH dependent (Fig. A.6). Fig. 4.4 highlights the nitrite-concentration dependence and isotopic dependence of this mode at pH 5.0. This dependence agrees with nitrovinyl formation in line with the visually observed formation of a green pigment (nitri-globin formation, see Fig. A.1 (C, F) for schematic representation and example of nitrivinyl formation).

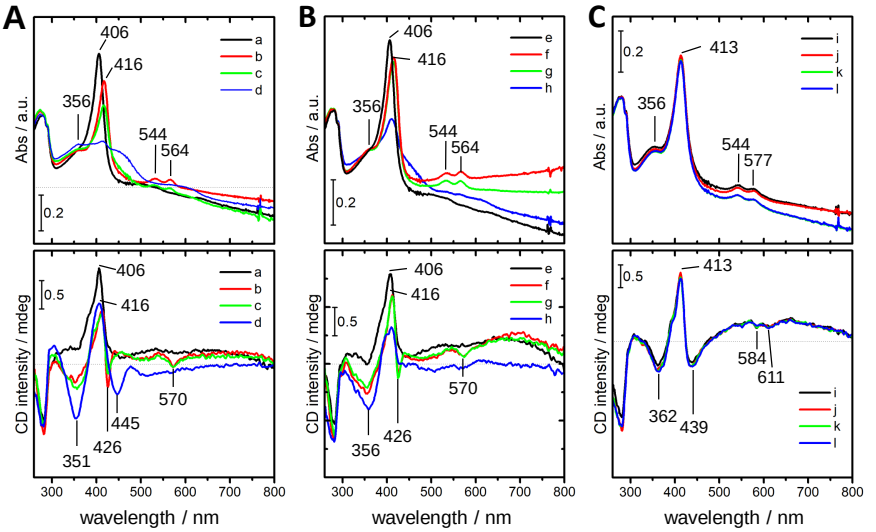

FIGURE 4.3: UV/Vis Abs (top) and ECD (bottom) spectra of 0.025 mM GLB-33GDΔCys before (a, e, i) and after addition of 1.2 mM $NaNO_2$ at $t = 0$ min (b, f, j), at $t = 240$ min (c, g, k), and at $t = 24$ hrs. (d, h, l). The spectra were collected at pH 4, 5 and 7.5 (Panel A, B and C, resp.).

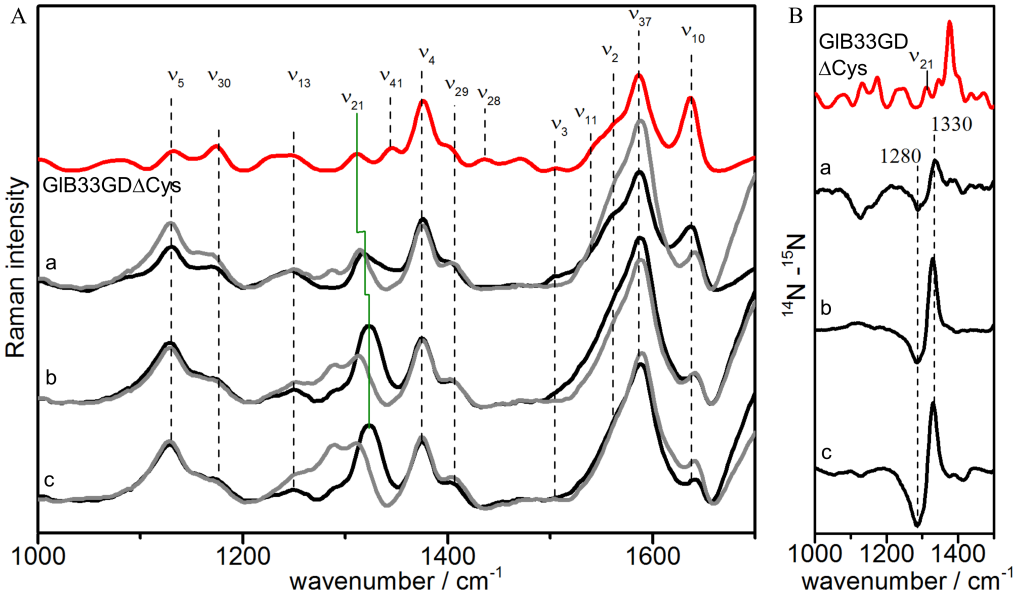

FIGURE 4.4: Panel A: rRaman spectrum of GLB-33GDΔCys (red) treated with (a) 50, (b) 280 and (c) 500 molar excess of $^{14}NO_2^-$ (black) and $^{15}NO_2^-$ (grey) in acetate buffer at pH 5. In green the rRaman shift of the mode ν_{21} is marked. Panel B: high frequency difference rRaman spectra of GLB33GDΔCys-$^{14}NO_2^-$ minus GLB33GDΔCys-$^{15}NO_2^-$.

While the optical methods used above (Figs. 4.3 and 4.4) clearly indicate nitration of the heme vinyl groups, they are less informative on the heme-iron ligation. At pH 7.5, little to no changes are observed in the UV/Vis Abs, ECD and rRaman spectra of ferric GLB-33GDΔCys upon addition of nitrite. Nevertheless, an additional component due to a 6c/LS species is observed in the corresponding EPR spectrum (Figs. 4.2 (B), Fig. A.7 for assignment of peaks). This component (LS3) has EPR parameters that are similar to the ones observed for nitrite-ligated Mb (Table 4.2). The lower g_x value is hard to determine, but it can be estimated using ESE-detected EPR at X-band (Fig. A.8). Note that at pH 7.5, only partial replacement of the hydroxide ligand by nitrite is observed for ferric GLB-33GDΔCys. A previous study of nitrite binding to human Hb revealed a replacement of the nitrite ligand by hydroxide at high pH [89], indicative of a stronger affinity of the heme center to hydroxide than to nitrite. The contribution of a HS ferric heme form remains negligible (<1%). As evidenced by the rRaman spectra, nitrite-binding at this pH does not trigger a further nitration of the heme vinyl groups.

System	Label	g_x	g_y	g_z	%	Coordination	Ref.
GLB-33GDΔCys pH 7.5	LS1	1.70	2.12	2.84	41	His/OH-	This work
	LS2	1.82	2.20	2.61	8	His/OH-	
	LS3	∼1.53	2.29	3.03	51	His/NO_2^-	
GLB-33GDΔCys pH 5	LS3*	∼1.53	2.26	3.00	93	His/NO_2^-	This work
	LS1*	1.70	2.07	2.84	7	His/NO_2^-	
GLB-33GDΔCys pH 4	LS3	∼1.53	2.13	3.01	46	His/NO_2^-	This work
	LS4	∼1.38	2.35	2.84	54	His/NO_2^-	
(sw)Mb pH 7	n.a.	1.57	2.20	2.95	100	His/NO_2^-	[248]
H64V (sw)Mb pH 7	n.a.	n.d	∼2.1-2.3	3.16	89	His/NO_2^-	[267]
	n.a.	n.d.	∼2.1-2.3	2.93	10	His/NO_2^-	
Hb pH 5-10	LS (A)	1.45	2.30	2.87	(a)	His/NO_2^-	[89]
	LS (B)	1.45	2.12	3.02	(a)	His/NO_2^-	
NP7 pH 7.2	n.a.	1.46	2.34	2.86	n.d.	His/NO_2^-	[107]
	n.a.	1.46	2.40	2.78	n.d.	His/NO_2^-	
NP4 pH 7.2	n.a.	1.51	2.42	2.74	n.d.	His/NO_2^-	[107]
	n.a.	n.d.	n.d.	3.38	n.d.	His/NO_2^-	
Cyt c' pH 7	n.a.	1.56	2.36	2.84	n.d.	His/NO_2^-	[265]
	n.a.	n.d	2.2	3.25	n.d.	His/NO_2^-	
Cld pH 7	n.a.	1.55	2.18	2.93	n.d.	His/NO_2^-	[268]

TABLE 4.2: Principal g values of the 6c/LS species observed in the EPR spectra of ferric GLB-33GDΔCys after addition of sodium nitrite at different pH values. Small contributions (∼1%) of residual 6c/HS species were observed. Numbers as obtained through simulation of the spectra in Fig. 4.2 (B). The parameters are shown in comparison with literature data for other NO_2^--bound gbs. n.a.= not applicable; n.d. = not determined; (sw)Mb = (sperm whale) myoglobin; Hb = vertebrate hemoglobin; NP = nitrophorin; Cyt c'= cytochrome c', *Cld* = chlorite dismutase.

At pH 4.0 and 5.0, a strong change in the EPR spectra of nitrite-ligated GLB-33GDΔCys is observed. The HS contributions almost completely disappear (<1%) and new signals due to two 6c/LS species appear (LS3 and LS4, Table 4.2, Figs. 4.2 (B), Fig. A.7 for assignment of peaks). The shift in the spin state indicates that next to nitration of the vinyl, also nitrite-ligation to the ferric heme iron occurs. Again, the g_x value for the low-pH 6c/LS species of GLB-33GDΔCys is not detectable in the CW-EPR spectra due to the large g-strain, but from ESE-detected EPR experiments an upper limit for the g_x value can be estimated (Fig. A.9). At pH 5, LS3 is dominating the spectrum, while at pH 4, the dominant contribution shifts to LS4. Small pH dependent shifts of the g_z value are observed for the EPR parameters of LS3. Similar small shifts have been observed for the EPR parameters of LS (B) in nitrite-ligated human Hb (Table 4.2) [89].

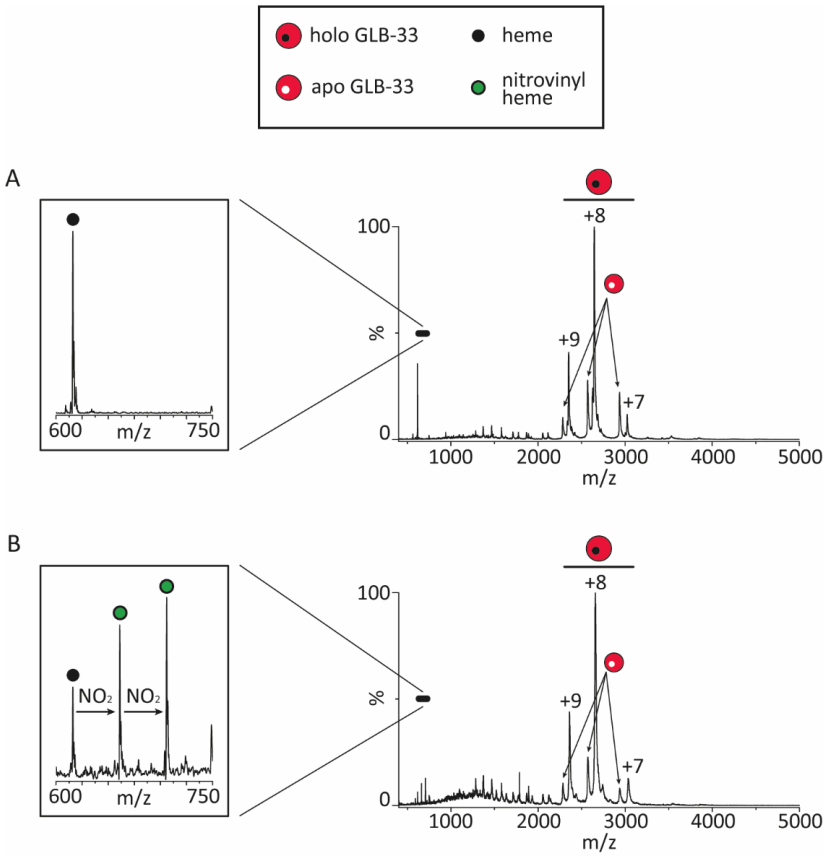

FIGURE 4.5: Native MS spectra of GLB-33GDΔCys after incubation with 50-fold excess of sodium nitrite at pH 7.5 (A) and 4.0 (B). The narrow charge state distribution (+7 to +9) corresponds to monomeric holo GLB-33GDΔCys. Satellite peaks indicate a minor fraction of the apo-form. The inset shows the m/z area between 600 and 750, which highlights that nitrite binding only occurs at pH 4.0.

To corroborate the spectroscopic findings on the pH-dependent effect of nitrite addition to ferric GLB-33GDΔCys, we performed native MS measurements after incubation with 50-fold molar excess of sodium nitrite at pH 4.0 and 7.5 for 24 hours. Native MS describes a method in which analytes are transferred from solution to the gas phase while aiming to maintain the solution-phase structure through careful control of crucial parameters [226, 269, 270, 271, 227, 272, 273]. Hence, in case of GLB-33GDΔCys, we can retrieve information of whether the treatment with sodium nitrite leads to covalent nitrite-ligation of the heme group.

The spectra show for both samples, i.e. sodium nitrite treatment at pH 4.0 and 7.5, a narrow charge state distribution of monomeric GLB-33GDΔCys, indicating the native, folded character of the holo protein (Fig. 4.5). Only a minor population of the protein is unfolded – evidenced by the presence of higher charged complexes at around 1000-2000

m/z - and/or lacks the heme group (apo form). Such minimal protein unfolding was also observed in the negative control (no nitrite addition) of GLB-33GDΔCys (Fig. A.10), indicating that unfolding occurred due to non-optimal solution conditions, or the protein being kept at room temperature for 24 hours rather than by the sodium nitrite treatment. The inset highlights the range between 600 and 750 m/z, the area where (nitrovinyl) heme would be expected. Nitrovinyl heme – covalent modification of the vinyl groups with one and even two nitrite molecules (Fig. A.1 (C, F)) – is only present after sodium nitrite treatment at pH 4.0, confirming previous spectroscopic findings that the pH is crucial for the binding of nitrite. The formation of nitrovinyl heme is indicated by an increase of 44.98 m/z (heme: 616.13 m/z; nitrovinyl heme: 661.11 m/z; charge state: +1), implying the replacement of an H-atom for each nitrite molecule bound heme.

Nitro or nitrito binding to the heme iron?

Both species LS3 and LS4 seem to be due to a nitrite-ligated heme species, albeit with a different pH dependence (Table 4.2). The observation of multiple LS species in the EPR spectra of ferric heme proteins after addition of nitrite is not uncommon [248, 265, 267, 89, 107]. The variation in the EPR spectra has been ascribed to multiple effects, such as hydrogen-bonding effects, heme ruffling or nitro- versus nitrito-ligation [248, 274]. The principal g values can be linked to crystal-field parameters by a simple calculation [213]. In the supplementary material (Table A.1, Fig. A.11), the crystal-field parameters of LS3 and LS4 and other nitrite complexes of heme proteins are calculated and plotted in a "Blumberg-Peisach" diagram. LS3 and LS4 fall in different regions of the diagram. In a recent work on the nitrite complexes of chlorite dismutases by one of my supervisors and others [248], a link was made between the area in which the crystal-field parameters fall and the nitrite binding mode (N-nitro versus O-nitrito), corroborated by X-ray diffraction (XRD) and molecular modelling. Following this reasoning, the nitrite complex observed at pH 7.5 (LS3) is tentatively ascribed to the nitrito-complex, while lowering the pH induces the nitro binding mode (LS4).

In order to substantiate this assumption, pulsed EPR experiments were performed. At pH 7.5, the presence of the EPR contribution of the hydroxide complexes of GLB-33GDΔCys (LS1 and LS2) complicate the analysis of the nitrite-ligated species. Only the magnetic field position agreeing with $g = g_z$ of species LS3 can be attributed solely to the nitrite-ligated GLB-33GDΔCys. Fig. 4.6 (A) shows the two-pulse ESEEM time trace taken at this position for a frozen solution of GLB33DΔCys in the presence of $Na^{14}NO_2$ (red) and $Na^{15}NO_2$ (blue). Small changes due to the isotope change are observed in the modulation pattern. By dividing the two traces (Fig. 4.6 (A), inset) and subsequent Fourier transformation (4.6 (B)), a clear peak at 7.4 MHz is observed, with smaller signals at lower frequency. The three-pulse ESEEM experiment performed at the same observer position also showed small changes in the low frequency range (Fig. A.12). In the corresponding HYSCORE spectra, the differences were less clear (Fig. A.13). However, for this experiment, the observer position had to be set slightly more up field in order to still have a significant echo signal. At this observer position, contributions of LS1 will start to contribute, potentially masking the small isotope-labelling-induced differences in the LS3 contribution. The clearest isotope-induced changes are seen in the two-pulse

ESEEM experiment. The assignment of the peaks remain unclear, but indicate ^{14}N hyperfine couplings < 7 MHz (in absolute value).

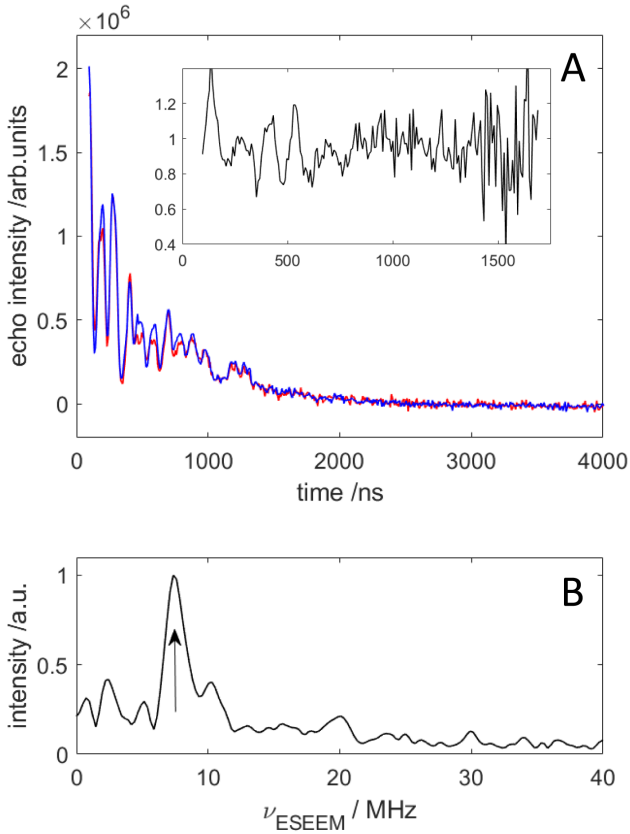

FIGURE 4.6: (A) Comparison between the two-pulse ESEEM time traces of frozen solutions of ≈ 1 mM ferric GLB-33GDΔCys at pH 7.5 after addition of a 50-fold excess of Na^{14}NO$_2$ (red) and Na^{15}NO$_2$ (blue). 25 % (v/v) glycerol was added to the solution as a cryoprotectant. The spectra were recorded at 235 mT, an observer position agreeing with $g = g_z$ of LS3. The inset shows the division of the two time traces. Only the first half of the trace is shown, since for signals near zero intensity, the noise increasingly contributes. (B) Fourier transform of the time-domain signal in the inset.

4.4.3 Nitrosylated GLB-33GD

Ferrous GLB-33GD can act as a nitrite reductase, leading to an NO-bound GLB-33GD (Fe^{2+}–NO) form with Q-band absorption bands at 545 and 570 nm [118]. This ligation state is here confirmed by low-temperature X-band EPR spectrum of ferric GLB-33GD reduced using dithionite and subsequently treated with nitrite (Fig. 4.7), revealing the typical EPR characteristics of a His–Fe^{2+}–NO coordination also found in other gbs [275, 276, 277, 278]. The EPR spectrum consists of two components, characterized by an axial and a rhombic **g** tensor, respectively (Fig. 4.7), in line with the presence of at least two conformational states of the distal NO ligand in line with findings for other nitrosylated gbs [275, 276, 277, 278]. The rhombic form also shows additional splitting due to the hyperfine interactions with the ^{14}N nucleus of the distal NO ligand and of the Fe-bound nitrogen of the proximal His, with the hyperfine values being $[A_1\ A_2\ A_3] = [32\ 62\ 39] \pm 3$ MHz for ^{14}N(NO) and $[A_1\ A_2\ A_3] = [25\ 20\ 30] \pm 2$ MHz for ^{14}N(His).

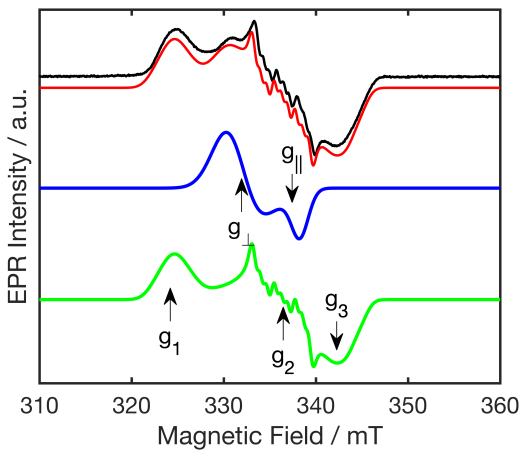

FIGURE 4.7: The experimental (black) and simulated (red) EPR spectrum of a frozen nitrosylated GLB-33GD solution recorded at $T = 6$ K. The simulated spectrum is build up by a component with an axial **g** tensor (blue, $g_\perp = 2.0361$ and $g_\parallel = 1.9946$) and one with a rhombic **g** tensor (green, $g_1 = 2.0776$, $g_2 = 2.0047$ and $g_3 = 1.9682$). Magnetic field positions corresponding to the g values are indicated by the arrows. The ^{14}N hyperfine couplings are mentioned in the text §4.4.3.

4.5 Discussion

Caenhorhabditis elegans is a promising model for globin studies as it encodes 34 gbs out of which only a handful have been characterized biochemically in vitro. GLB-33 is the largest of its kind, chimeric, consisting of an FMRF-amide binding and membrane binding domain, and a globin domain. An initial biochemical characterization by my supervisor and others [118] revealed both an unusual hydroxo ligation of the ferric state at slight acidic pH and a fast NiR activity. Here we show that the NiR reaction leads to

formation of a nitrosylated ferrous form in which the heme is still bound to the proximal histidine. NO ligation is known to weaken the Fe−N(His) bond and leads in some gbs and other heme proteins to the breaking of this bond [94, 279]. Earlier work using combined high-field EPR and quantum-chemical computations, ascribed the observation of the two forms in the EPR spectrum of nitrosylated Mb to changes in the stabilization of the NO ligand via H-bonding with the E7His residue, with strong H-bonding inducing the species with rhombic **g** tensor, and a weaker interaction leading to the species with axial **g** tensor [280]. GLB-33GD has, however, no His on the E7 position and has a highly hydrophobic heme pocket [118]. Furthermore, earlier work on a variant of neuroglobin in which the E7 residue was mutated to Leu also showed the presence of the two nitrosylated ferrous forms [277], indicating that the formation of the two forms is governed by more than the capacity of the E7 ligand to form H-bonds.

The EPR spectrum of ferric GLB-33GDΔCys at pH 4-5 is typical for a HS ferric form with a weak distal ligand in line with the presence of an aquomet form. However, at pH 7.5 an alkaline transition to two hydroxo-ligated forms has happened, of which one form (LS1) has EPR parameters similar to those observed in gbs [238] in which the hydroxide is stabilized in a strong hydrogen bonding network. In heme proteins, the pK_a of the alkaline transition (distal water to hydroxo ligand) is known to be determined by many factors, including the presence of distal hydrogen-bonding networks [238], distal salt bridges [281] and the proximal ligand [267]. In contrast to ferric sperm whale Mb (swMb) that exhibits an alkaline transition at pK_a 8.9 [267], the pK_a of the alkaline transition in Mb from *Aplysia limacina* (*Al*) (*Al*Mb) is found to occur at lower pH (pK_a 7.5) [282]. The latter Mb resembles GLB-33GD(ΔCys) with hydrophobic residues on postions E7 (Val) and E11 (Ile). Both *Al*Mb and GLB-33GD(ΔCys) have an Arg on position E10. In *Al*Mb, the Arg at position E10 is found to be able to swing into the distal heme region and stabilize anionic ligands bound to the heme iron (Fig. A.15), an effect that can be also induced in sperm whale (sw)Mb variants carrying the His(E7) to Val mutation [283, 284]. A similar process seems to occur here, where LS1 then points to a form in which the hydroxo ligand is stabilized by Arg(E11) and LS2 is a less stabilized form, potentially related to a movement of the Arg residue. Interestingly, the heme iron in ferric *Al*Mb is five-coordinated below the alkaline transition (Fig. A.15 (A), [285]). This seems to be in contrast with GLB-33GD(ΔCys), for which the EPR spectrum at low pH is typical for axial ligation of a weak ligand, most likely water.

A comparable pH effect has also been observed for chlorite dismutase from *Cyanothece sp.* PCC7425 (*CCld*) [281]. In this heme-*b* containing peroxidase that can decompose chlorite, a distal arginine (Arg127) is known to play a crucial role in enzyme activity. Arg127 can switch between two conformations in and out of the distal region, whereby the outward conformation is hydrogen-bonded to Gln74. The alkaline transition occurs in wild-type ferric *CCld* at pK_a 8.11 and EPR reveals the presence of 3 LS forms at high pH, with the principal g values agreeing with varying degrees of H-bonding, comparable to what is observed for GLB-33GDΔCys. When Arg127 is halted in the outward position through a salt bridge to glutamic acid in the Q74E *CCld* variant, the pK_a shifts upwards (9.33), while a mutation of Gln74 to Val, thus allowing more flexibility of Arg127, leads to a considerable down-shift of the pK_a (7.41). This also has a large impact on the

relative ratio of the three LS forms in the EPR spectra with the form that points to the strongest H-bonding with Arg127 becoming more prevalent in the Q74V variant and almost disappearing in the Q74E variant, where the Arg127 is locked in the outward position.

The pH-dependent ECD spectra of GLB-33GDΔCys in the near UV to visible range differ from those of hhMb (Fig. A.14). The ECD spectra of hhMb are showing a much higher magnitude of the Soret ellipticity and less negative contribution in the N region (300-350 nm) compared to GLB-33GD at neutral to alkaline pH. This shows that the substitution of hydroxide ligand is not a major contributor to the observed negative ellipticity for GLB-33GD, but rather the differences in heme pocket structure are determining the spectral fingerprint. This is corroborated by the comparison with the pH-dependent ECD spectra of *CCld* and its Q74 variants [281], where the alkaline transition reduces the negative ellipticity in contrast to what is observed here. Although the ECD spectra are highly dependent on amino acids surrounding the heme, the planarity of the heme itself, and the heme insertion [254, 255, 192, 256], there is still a lack of theoretical understanding that hampers a facile linking of these data to specific features of the heme pocket. This can potentially be circumvented by using MCD in future studies [286], as demonstrated for nitrite ligation to Mb [267].

Addition of nitrite to ferric GLB-33GDΔCys leads at neutral pH to a competition of nitrite with the hydroxo ligands, with a co-existence of both hydroxo (LS1, 2) and nitrite-ligated (LS3) species observed with EPR (Table 4.2). Comparison of Table 4.1 and Table 4.2 reveals that the hydroxo ligand of LS2 gets more easily replaced by nitrite than is the case for LS1. This is in line with the stronger hydrogen bonding to the Arg ligand in the latter complex. The principal g values of LS3 are typical for nitrite-ligated heme proteins exhibiting a nitrito bonding mode (Fe−O bond) (Table 4.2, Fig. A.11) and this assignment is corroborated by the ESEEM analysis showing signals that agree with ^{14}N hyperfine values (in absolute value) well below 7 MHz. A DFT study on the linkage isomers of nitrite-ligated Mb predicts small ^{14}N hyperfine coupling parameters for the nitrito form, while a nitro form would lead to hyperfine values around 20 MHz (in absolute value) [287]. At pH 5, LS3 has become the dominant species, while at pH 4, the EPR spectrum broadens and a second LS complex is found (LS4) to co-exist with an LS3-like species. Moreover, the UV/Vis Abs and ECD spectra show that acidic pH leads to formation of a vinyl-nitrated heme (nitri-globin), an effect that is more pronounced at the lowest pH and is also observed for other heme proteins [99]. The principal g-values of LS4 seem to be more consistent with a nitro-form (Fe−N bond) (Table 4.2, Fig. A.11).

X-ray crystallography of nitrite complexes of ferric hhMb and variants revealed an interesting interplay between the E7 and E10 ligand in directing the nitrite binding mode [287]. While ferric nitrite-ligated hhMb shows a nitrito form with the nitrite ligand H-bonded to E7His (Fig. A.1 (E)), mutation of the E7His to Val (H64V) in Mb leads to a weakly bound nitro form (Fig. A.1 (D)). Interestingly, the nitrito form is recovered in the double mutant carrying also the E10Val-to-Arg mutation (H64V/V67R) in which Arg now acts as the H-bonding residue (Fig. 4.8 (B)). This is accompanied by a swinging of the Arg into the heme pocket (Fig. 4.8, [109]). A similar effect is proposed to happen in GLB-33GD(ΔCys). Also in nitrite-ligated ferric *CCld* the distal Arg residue stabilizes

the nitrito form [248]. ArgE10 is therefore crucial in stabizing the LS3 nitrito form of ferric GLB-33GDΔCys. Formation of the nitro form (LS4) at pH 4 may potentially be due to the nitriglobin formation and, potentially even some onset of protein denaturation upon freezing of the solution. Although the latter can never be excluded at any pH, it is more likely to occur at pH 4.0, because freezing can lower the pH even further [288]. This will alter the heme pocket and can influence the conformation and orientation of the E11Arg residue. If no H-bonding residue is nearby, the nitro form will be formed, in line with the observation for H64V hhMb (Fig. A.1 (D) [253]).

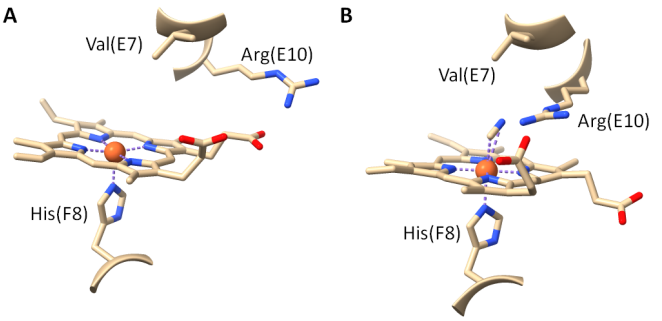

FIGURE 4.8: Structural change observed in the heme pocket of H64V/V67R variant of hhMb upon binding of nitrite. Val64 is at position E7, Arg67 is at position E10. (A) Structure with no distal ligand present (PDB ID: 3HEN). (B) Structure with nitrite in nitrito form (PDB ID: 3HEO). The figure illustrates the swinging of the Arg residue in (B) and out (A) of the heme pocket. A similar effect is proposed here for GLB-33GD(ΔCys).

The ECD spectra of ferric GLB-33GDΔCys with nitrite at pH 4 and 5 (Figs. 4.3 A, B) showed a considerable evolution over time in at least three of the four main regions where the plane polarized transitions were detected (Q: 470 - 600 nm; B: 380 - 450 nm ; N: 300-350 nm; L: 250-320 nm). While absorption and ECD spectra in the aromatic region remained unchanged upon the treatment of the globin with NO_2^-, a gradual increment of the overall ellipticity with a minimum at 351 and 356 nm for pH 4 and 5, respectively, was observed. A large enhancement of the N dichroic band (300-400 nm) has been described in literature for the model system of *Lucina pectinata* (*Lp*) Hb (*Lp*Hb) as the result of a resonant interaction between the electronic transition of the aromatic residues and those of the N and L bands, because of their simultaneous excitation [193]. However, this effect is less likely to happen in GLB-33GDΔCys, since the amount of aromatic residues near the heme is much lower than in *Lp*Hb. Noteworthy, at pH 4 and 5, the B dichroic band at 416 nm is in first instance slightly reduced in magnitude (during the first 8 hours), and at the same time the two negative dichroic bands appear. In particular, the sharp negative ECD band at 426 nm and the broader negative ellipticity at 570 nm are prominent after addition of nitrite. Potentially, these signals are markers for the nitrite ligation. Finally, acidified solutions of NO_2^- contain NO (disproportionation reaction). Therefore, besides an Fe(III)$^-$ NO_2- complex, a fraction of Fe(III)$-$NO could in principle be formed [289]. EPR spectroscopy is not suited to detect such species as it is EPR silent ($S = 0$), and

UV-vis Abs spectroscopy is not showing any evidence either. Therefore, the formation of a nitrosylated ferric form is excluded.

The NiR activity of GLB-33GD is modelled with a fast second order rate constant k_{NIR} of $36.3\,\mathrm{M^{-1}\,s^{-1}}$ [118]. This is high in comparison with other gbs (e.g. for hhMb k_{NIR} values of $5.5\,\mathrm{M^{-1}\,s^{-1}}$ [253] to $6.1\,\mathrm{M^{-1}\,s^{-1}}$ [290] are reported). Interestingly, the H64V hhMb mutant has a strongly reduced NiR activity ($k_{NIR} = 0.35\,\mathrm{M^{-1}\,s^{-1}}$), while this is partially restored in the H64V/V67R double mutant ($k_{NIR} = 1.8\,\mathrm{M^{-1}\,s^{-1}}$) [253]. This illustrates again the important effect of E10Arg when no H-donating residue is present on position E7, in line with our findings for binding of hydroxide or nitrite. However, the presence of the E10Arg is clearly not enough to explain the enhanced NiR activity of GLB-33GD. While the H64A hhMb variant shows a strong reduction of the NiR activity ($k_{NIR} = 0.1\,\mathrm{M^{-1}\,s^{-1}}$), a remarkable increase of this activity is reported for the F43H/H64A variant ($k_{NIR} = 49.8\,\mathrm{M^{-1}\,s^{-1}}$); Phe43 is located at the CD1 position [290]. The F43H mutant in contrast has much lower activity ($k_{NIR} = 1.4\,\mathrm{M^{-1}\,s^{-1}}$) [290].

This shows that the NiR results from an intricate interplay of different effects, of which the stabilization of the nitrite ligand by ArgE10 in the absence of an H-bonding residue on position E7 is an important factor, but not the only factor. The EPR spectrum of NO-bound ferrous GLB-33GD shows similar conformational states as found for other nitrosylated gbs (Fig. 4.7).

Based on its localization and its sequence, GLB33 has been suggested to be a putative neuropeptide receptor in *Ce* [118]. Since binding of nitrite requires a movement of the Arg residue into the distal heme pocket, the concomitant change of the globin structure may act as sensor, but future work on the full-length globin is needed to support this.

Chapter 5

A closer look into the heme pocket from the globin domain of GLB-33 in *Caenorhabditis elegans*

Manuscript in preparation (crystallization and mutagenesis trials excluded)
N. Van Brempt*, Q. Beirinckx*, V. Van Nieuwenhove, S. Dewilde and S. Van Doorslaer, "The hydroxide bound and nitrosyl complex of globin-33, a heme based sensor in *Caenorhabditis elegans*: an EPR study".

*Both authors contributed equally.

Own contribution
Over-expression and purification of GLB-33GD(ΔCys) and heme-pocket mutants, UV-vis absorption, CW-EPR and ESEEM EPR experiments on the ferric form, corresponding simulations and interpretation of the spectra, original draft writing.

5.1 Abstract

GLB-33 is a (recently) discovered and partially characterized putative globin-coupled neuropeptide receptor in the nematode *Caenorhabditis elegans* predicted by homology modelling and AlphaFold to consist of a 7α-helical TM domain and a GD with an unusually hydrophobic heme pocket. The latter possesses an extraordinary fast NiR activity when ferrous *in vitro*. In the previous chapter, the ferric form of the GD was characterized by two overlapping LS complexes in the CW-EPR spectrum, associated with two hydroxo-conformers at the distal side of the heme pocket that persist at slightly acidic buffer conditions at which many gbs favour a water molecule, exhibiting an axial EPR spectrum. The nitrosylated form was characterized by an axial and a rhombic $\boldsymbol{g}$ tensor, as commonly observed for His$-$Fe$^{2+}-$NO coordinated hemes. Here, I extend our previous work on the hydroxo complexes of the GD with additional experiments such as crystallization trials, site-directed mutagensis, and more advanced EPR spectroscopy such as ESEEM- and in particular HYSCORE spectroscopy and Davies ENDOR in comparison with studies on MbOH and other hydroxo-gbs as a reference. The nitrosyl complex of the GLB-33GD is investigated with a variety of EPR techniques, revealing clear differences with hhMb, and the crucial role of ArgE10 is again monitored.

5.2 Introduction

Globins are small α-helical heme-containing proteins widespread throughout the kingdoms of life, see the introduction in Chapter 1. Triggered by the in silico discovery of up to 34 different *Ce* gbs [112], different studies subsequently revealed novel globin functionality and structural diversity within this set of proteins [113, 114, 148, 118, 117, 74, 119, 149, 115, 237, 234]. GLB-33 is an exceptional member within this set of *Ce* gbs due to its chimeric nature, see also state-of-the-art on GLB-33 in Chapter 2, and the introduction in Chapter 4. In summary, the main characteristics of the GD are its very hydrophobic heme pocket with Ile instead of the conserved His/Gln on helix position E7, its capacity to bind CO and O_2 and $NO_2{}^-$. Furthermore, it has a fast auto-oxidation rate and a 10-fold faster NiR activity *in vitro* than Mb, making it one of the most efficient nitrite reductases within the globin family [118, 234].

The globin domain of GLB-33GD consists of 166 AAs and has a theoretical molecular weight of 19.54 kDa (20.36 kDa with His_6-tag) + 0.62 kDa (heme). A comparison between the protein sequence of GLB-33GD and the globin domains of *Ce* gbs GLB-1, 6, and 12, together with well-known human gbs Ngb, Cgb, and hhMb is shown as a sequence alignment in Fig. 5.1. Additionally, GLB-3a (see Chapter 7) is aligned with these proteins. From this, we observe the typical conservation of amino acid residues in globins, such as F8His, but also deviations from the highly conserved CD1Phe [291], in this case Val, as well as deviations from the conserved E7His (E7Ile) and an Arg at position E10.

```
4BJA_GLB-12/1-266    1 -----------MGATLSAPKKKKTQVGAS-WVGNESEN--PFDLALNKKDRTLLRETWQRL  47
4MPM_hNGB/1-151      1 ----------------------------------------------MERPEPELIRQSWRAV  16
1WLA_hhMb/1-153      1 ---------------------------------------------GLSDGEWQQVLNVWGKV  17
2WTG_GLB-1/1-159     1 ------------------------------------MSMN----RQEISDLCVKSLEGRMVGT  23
3MVC_GLB-6/1-160     1 ---------------------------------------------LHLTQPQILFVRKTWNHA  18
glb-33GD/1-171       1 ---------------------------------------------GQLLGDRLSILKSSWEKA  18
1V5H_hCGB/1-193      1 -------------------------GSHMEKVPGEMEIERRERSEELSEAERKAVQAMWARL  37
GLB-3a/1-210         1 -----------MGNNVPSRRMSRATVHLENSNGADNMS-FVDAIHLSPHQVQLLTSTWPRI  49

4BJA_GLB-12/1-266   48 DDPKD-IVGLIFLDIVNDIEPDL--------KKVFGVD---RAPRAAMLKMPKFGGHILRF  96
4MPM_hNGB/1-151     17 SRSPL-EHGTVLFARLFALEPDL--------LPLFQYNCRQFSSPEDCLSSPEFLDHIRKV  68
1WLA_hhMb/1-153     18 EADIA-GHGQEVLIRLFTGHPET--------LEKFDK-FKHLKTEAEMKASEDLKKHGTVV  68
2WTG_GLB-1/1-159    24 EAQNI-ENGNAFYRYFFTNFPDL--------RVYFKGAE--KYTADDVKKSERFDKQGQRI  73
3MVC_GLB-6/1-160    19 RNQGALEPAISIFRNSFFKNPEI--------RQMIMFG-------TKNEGHERLKKHAQLF  64
glb-33GD/1-171      19 NEMTNGEIGVRVAWNMVRKHPNLCKNDEPEKVSLLNGSCKR------SIDHAKFQEIGGRI  73
1V5H_hCGB/1-193     38 YANCE-DVGVAILVRFFVNFPSA--------KQYFSQ-FKHMEDPLEMERSPQLRKHACRV  88
GLB-3a/1-210        50 KTQSS-LF-TQVFKVLMQRSPVC--------REMFQKM-S-IVGGFSSNSVCDLNSHTKLL  98

4BJA_GLB-12/1-266   97 YEFMEQLTSMLGTSENLTGAWQ-LVRKTGRSHVRQ--GFLEQNQNQMEKNYFEIVINVFIE 154
4MPM_hNGB/1-151     69 MLV---IDAAVTNVEDLSSLEE-YLASLGRKHRAV--GV-----K---LSSFSTVGESLLY 115
1WLA_hhMb/1-153     69 LTA---LGGILKKKG---HHEA-ELKPLAQSHATK-HKI-----P---IKYLEFISDAIIH 113
2WTG_GLB-1/1-159    74 LLACHLLANVYTNEE----VFKGYVRETINRHRIY--KM-----D---PALWMAFFTVFTG 120
3MVC_GLB-6/1-160    65 TVL---MDDLIANLDSPSATVA-GLREAGEKHVWPTRNQYG---CPFHAHLLDQFATAMIE 118
glb-33GD/1-171      74 TSFISELLELMQNNQPESYIVM-RIRRVGAVHYDK--GI------VFTSSVWKEFKHTIQT 125
1V5H_hCGB/1-193     89 MGA---LNTVVENLHDPDKVSS-VLALVGKAHALK-HKV-----E---PVYFKILSGVILE 136
GLB-3a/1-210        99 CEL---LDSLMTDLHQPAKIVLAKCQDVGAAHVNMNEKC-----C---GVVFDQLGEAFTE 148

4BJA_GLB-12/1-266  155 RLIPFLTGEQELPSSEGKENKKVRFAQNYTTSQITDVWKKFLNTVISQMTDSFELERAKQK 215
4MPM_hNGB/1-151    116 -MLEKCL-------------------GPAFTPATRAAWSQLYGAVVQAMS-----RGWDGE 151
1WLA_hhMb/1-153    114 -VLHSKH-------------------PGDFGADAQGAMTKALELFRNDIAAKYKELGFQG- 153
2WTG_GLB-1/1-159   121 -YLES---------------------VGSLNDQQKAAWMALGKEFNAESQTHLK------- 152
3MVC_GLB-6/1-160   119 RTLEWGE-------------------KKDRTETTQRGWTKIVLFVTEQLKEGFQDEQKRAR 160
glb-33GD/1-171     126 -IISEVQ-----------------FSSPQEREAALDAWNIFISFIIREMKMGIWAIGDT-- 166
1V5H_hCGB/1-193    137 -VVAEEF-------------------ASDFPPETQRAWAKLRGLIYSHVTAAYKEVGWVQQ 177
GLB-3a/1-210       149 -LITKVE-------------------CVRSKREAVKSWMCVISYMADSIKSGYMEEWAKKR 189
```

FIGURE 5.1: Sequence alignment of the partially characterized gbs from *C. elegans*; GLB-1, -3a, -6, and -12, together with hhMb, hNGB, hCGB. Cys residues of GLB-33GD are highlighted together with the E7 residues in red.

The E7 residue is strongly conserved in mammalian gbs (E7His) whereas in nematodes and other non-vertebrate, plant and bacterial globins, other amino-acid residues are more frequently found at this position, which is translated in a wide functional diversity of the related gbs [114, 292, 134]. The E7 residue usually functions as a distal ligand stabilizer via hydrogen-bond formation or, in the case of E7His, the residue can coordinate directly to the heme and thus compete with the binding of an exogenous ligand, such as O_2.

Since the E7 AA residue in GLB-33GD cannot form hydrogen bonds, ligand stabilization is either not present or taken over by other residues. In the previous chapter, it was shown that ferric GLB-33GD exhibits an alkaline transition at unusually low pH, and the crucial involvement of E10Arg was hypothesized. Two low-spin (LS) ferric heme forms were detected with EPR (Fig. 4.2 (A), Table 4.1). The current hypothesis is that the two distinct LS forms are associated with two geometric conformations of the distal side of the heme pocket. The Arg at position E10 is hypothesized to swing in and out of the heme pocket and stabilize the anionic ligand, likely stabilizing the hydroxo ligand resulting in LS1 and a less stabilized 'out' form LS2 ([234], Chapter 4).

In an attempt to further understand and substantiate the role of E10Arg in the alkaline transition, different experiments were set up, as discussed in this chapter. First, attempts were made to grow crystals of both GLB-33GD and GLB-33GDΔCys for protein

crystallography, but unfortunately, these failed as described in §5.4.1. In the next set of experiments, attempts were made to construct and purify different mutants, namely I69H GLB-33GD (replacing E7Ile with His), R72V GLB-33GD (replacing E10Arg with Val), and the double mutant I69H/R72V GLB-33GD, as described in section §5.4.2. The choice of the point mutations was made to mimic the residues at these positions in horse heart Mb (Fig. 5.2). Unfortunately, it was discovered that an unintended extra point mutation had occurred in the glycerol stocks of the bacteria used. This point mutation was at F111S. Since F111 is predicted by modelling to be in the heme pocket, it was decided to study these mutants as well, since Mb does not have a bulky Phe at this position.

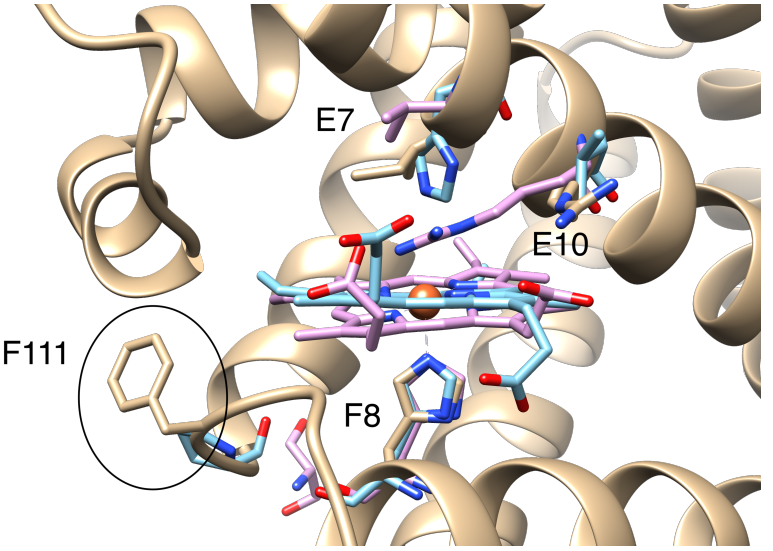

FIGURE 5.2: Swiss Model of GLB-33GD (beige) in overlay with hhMb (PDB:1WLA, color blue) and *Al*Mb (PDB:3MBA, color purple). The amino-acid residues of interest are shown in a stick representation for GLB-33GD, hhMb and *Al*Mb, respectively: at position E7 (Ile, His and Val), E10 (Arg, Val, Arg) and F8 (His, His, His), and finally F111, Pro100 and 102Ser.

In §5.4.3, I discuss the analysis of the ferric form of GLB-33GD(Δ)Cys with different pulsed EPR techniques. The obtained ^{1}H and ^{14}N hyperfine and nuclear quadrupole data are compared to the findings for the alkaline form of mammalian Mb. Finally, the interplay between the AA residue at position E7 and other AA residues in the heme pocket is also found to be essential for the enzymatic activity of globins, such as NiR activity.

This activity is indeed strongly influenced by the amino-acid residue at position E7, as shown by site-directed mutagenesis studies of the distal E7His in mammalian neuroglobin and Mb, revealing increased nitrite reduction rates by several orders of magnitude compared to the wild-type forms [293, 266]. During the NiR cycle of globins, nitrite gets reduced to NO, which can bind both the ferric and ferrous form of the globin. NO complexes of ferrous heme proteins have been extensively studied by many spectroscopic

techniques, including EPR as it provides immediate information on the heme pocket, which led to renewed insights on the electronic structure of NO-ligated complexes in gbs [294] [92]. In Chapter 4 (Fig. 4.7), I showed that a nitrosylated ferrous heme form is indeed the result of the NiR activity of GLB-33GD, but did not analyse this form further at that stage. In §5.4.4, detailed temperature dependent CW-EPR experiments and HYSCORE experiments are presented, revealing clear differences with how Mb of Aplysia stabilizes NO.

5.3 Materials and methods

5.3.1 Protein expression, purification and mutagenesis

Recombinant GLB-33GD, ΔCys and heme-pocket mutants Recombinant GLB-33GD and a double Cys→Ser mutant (GLB-33GDΔCys) were expressed and purified as described earlier [118]. Concentrated eluate after NiAC was loaded on a HiLoad 16/600 superdex 200 pg (GE Healthcare Life sciences) or a self-packed superdex 200 and pure fractions were collected and concentrated to a final sample. The proteins were concentrated until a final concentration of roughly 1 mM in 50 mM Tris pH 7.5, 150 mM NaCl. The globin concentration was calculated using the extinction coefficient of neuroglobin ϵ_{412nm}= 130 000 M^{-1} cm^{-1} [251]. The ferrous nitrosyl-form (20 µM) was obtained by adding a freshly prepared nitrite solution to a dithionite-reduced GD until a 100-fold molar excess nitrite/globin ratio was reached. HsMb and hhMb was purchased from Merck KGaA (Darmstadt, Germany). The gbs were dissolved in the 50 mM tris, 150 mM NaCl, pH 7.5. For the EPR experiments, glycerol was added to all samples (25% v/v) prior to flash-freezing in liquid nitrogen.

Mutations were introduced by using the Quick-change^{TM} site-directed mutagenesis kit (Stratagene). To construct GLB-33GD from the ΔCys construct for the GD, two serines were mutated to cysteines on position 41 and 56. The mutation primers used to create these mutations, together with specific heme pocket mutations are listed in Table B.1. The cDNAs were subsequently cloned, expressed and purified as described above and below.

Small-scale overexpression of heme-pocket mutants The three mutants of GLB-33GD (I69H, R72V and double mutnat I69H/R72V) were overexpressed and purified as follows. For the *E. coli* overexpression: 4 × 3 LB cultures were innoculated with glycerol stocks of the 3 different mutants and the GLB-33GDΔCys as a reference in a pET23a vector. The cultures were grown with antibiotics chloramphenicol and ampicilin overnight. When an optical density OD_{600} of 0.8 was reached, inoculated TB cultures were induced with Isopropyl β-d-1-thiogalactopyranoside (IPTG). Growth medium was centrifuged (4000 RPM, 20 min, 4 °C). Supernatant was discarded and pellets were resuspended (50 mM Tris pH 7.5, 300 mM NaCl). After repeated freeze-thaw cycles and sonication, lysed cells were centrifuged (10 min at 10 000 RPM at 4 °C). After a second centrifugation step, the supernatant was loaded onto a self-packed Ni-NTA resin (Qiagen). Subsequently, to remove non-specific binding, the bound protein-Nickel matrix

was washed with 10 ml (50 mM Tris pH =7.5, 300 mM NaCl and 20 mM imidazole). The protein was eluated (10 ml of 50 mMTris pH 7.5, 300 mM NaCl, 300 mM imidazole) and 1 ml fractions were collected. Absorption spectra were collected on a Thermo Scientifc GENESYS 6 UV-Vis Spectrophotometer, 10 mm pathlength in quartz cuvettes, 1 ml sample volume. After obtaining unexpectd results (see §5.4.2), a sequencing test revealed that an unexpected additional point mutation had occurred (Phe111 → Ser).

5.3.2 Crystallization experiments

Protein crystallization experiments were kindly set up by Prof. Alessandra Pesce from the Università di Genova. GLB-33GD(ΔCys) crystals were grown in a vapour diffusion hanging drop setup. The drops contain 1 µL protein ($\sim 20\,\mathrm{mg\,ml^{-1}}$) and 1 µL of precipitant solution that was screened in order to optimize precipitation and crystal growth. The protein containing solutions were incubated at 4 °C.

5.3.3 Electron paramagnetic resonance

X-band pulsed EPR experiments were performed on a Bruker E580 ELEXSYS spectrometer with a microwave frequency of 9.74 GHz, equipped with a gas-flow cryogenic system (Oxford Instr.) allowing for operation from room temperature to $T = 4$ K. For all experiments a shot repetition time of 1 ms was taken, unless stated otherwise. The three-pulse ESEEM [295] experiments were done using a $\pi/2 - \tau - \pi/2 - T - \pi/2 - \tau - echo$ microwave pulse sequence with pulse lengths of $t_{\pi/2}$= 16 ns and are the sum of 10 τ-values in the range 96-240 ns in steps of 16 ns with T varied from 96 ns to 4880 ns in steps of 16 ns. HYSCORE spectra were recorded using the microwave pulse sequence $\pi/2 - \tau - \pi/2 - t_1 - \pi - t_2 - \pi/2 - \tau - echo$ with $t_{\pi/2} = 16$ ns and $t_\pi = 32$ ns and t_1 and t_2 were varied from 96 ns to 4480 ns in steps of 16 ns. HYSCORE measurements were recorded with different τ-values and added together as indicated in the figure captions. The three-pulse ESEEM and HYSCORE spectra were baseline-corrected using a third-order polynomial, apodized with a Hamming window and zero-filled. After Fourier transformation, the absolute-value spectra were calculated. The Davies ENDOR [211] were carried out with the pulse sequence $\pi - T - \pi/2 - \tau - \pi - \tau - echo$ with pulse lengths $t_{mw,\pi} = 100$ ns and $t_{mw,\pi/2} = 50$ ns and an inter-pulse time $\tau = 260$ ns and T= 14.5 µs. A radiofrequency π-pulse of 12 µs was applied during T and a shot repetition time of 4 ms was used. W-band ESE-detected EPR experiments were performed on a Bruker E680 ELEXSYS spectrometer with a microwave frequency of 94.0 GHz. The spectra were recorded using the pulse sequence $\pi/2 - \tau - \pi - \tau - echo$, with pulse lengths $t_{\pi/2} = 120$ ns and $t_\pi = 240$ ns and an inter-pulse distance $\tau = 300$ ns. EPR spectra were computer simulated using EasySpin [212] package (v.5.2.28), a toolbox for MATLAB (R2020a, MathWorks, USA).

The CW-EPR spectra were measured on a Bruker ESP300E spectrometer (microwave frequency 9.43 GHz) equipped with a liquid helium cryostat (Oxford Instr. Inc.) that allows operation from room temperature to 2.5 K. The spectra were measured with a microwave power of 0.1 mW (1 mW for $T \leq 115$ K), a modulation frequency of 100 kHz, and a modulation amplitude of 0.5 mT. The magnetic field was measured with a Bruker

ER035M NMR Gaussmeter. The EPR sample was first cooled to 2.5 K, and then the temperature was gradually increased. Sufficient time was allowed at each temperature change for the temperature to stabilize before proceeding with the measurement. Measurements were performed over a temperature range of 2.6-190.0 K.

5.4 Results and discussion

5.4.1 Protein crystallization trials

High-purity protein samples were prepared for crystallization trials. Both GLB-33GD and GLB-33GDΔCys were purified and the purity was assessed with high-performance liquid chromatography (HPLC) (16/600 Superdex 200 preperative grade) and sodium dodecyl sulfate–polyacrylamide gel electrophoresis (SDS-PAGE) (Figs. 5.3 and 5.4). The preparative chromatograms in both samples show a main elution peak at 88 min, corresponding to monomeric globin. Interestingly, the deletion of the Cys residues in GLB-33GDΔCys results in the disappearance of a shoulder peak observed at 75 min that was observed for the GLB-33GD. This indicates that GLB-33GD tends to form dimers/multimers since the 370 nm absorption (heme) peak nicely follows the 280 nm (protein) peak at 78 min. Note that the main peak at 88 min (Fig. 5.3 (A)) looks distorted because we reached the maximum sensitivity of the UV-vis detector. Therefore, it is not possible to estimate the ratio between the multimeric fraction and the monomeric fraction from this experiment. 5 µL extracts from the collections at the indicated elution times were loaded on polyacrylamide gels (Fig. 5.4). A contaminant between 31 and 45 kD was observed. To exclude this contaminant as much as possible, without compromising too much the protein yield, the fractions in the tail of the main chromatogram peak were pooled and concentrated (see coloured fraction numbers in red in Fig. 5.3) to result in the final batches. Overall, the ΔCys mutant has a higher purification yield than the wild-type GD and both proteins samples remained stable in solution.

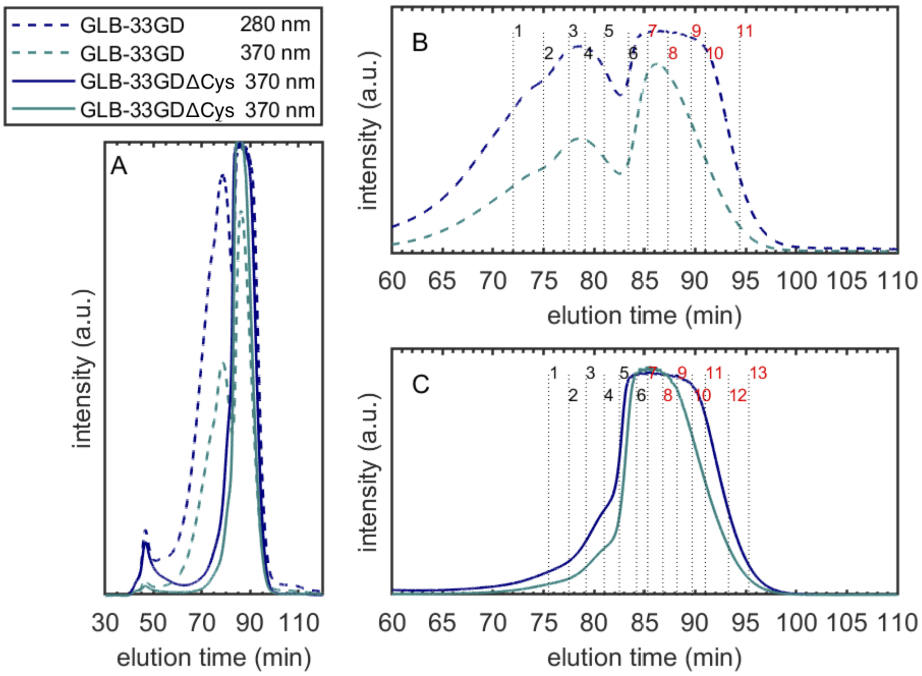

FIGURE 5.3: (A): Chromatograms of GLB-33GD (dashed) and GLB-33GDΔCys (full). (B): Zoom of the chromatogram of GLB-33GD. (C): Zoom of the chromatogram of GLB-33GD ΔCys. The collected elution fractions are indicated with an integer. In red: the fractions that were concentrated to become the final batch, based on the SDS-page results (Fig. 5.4).

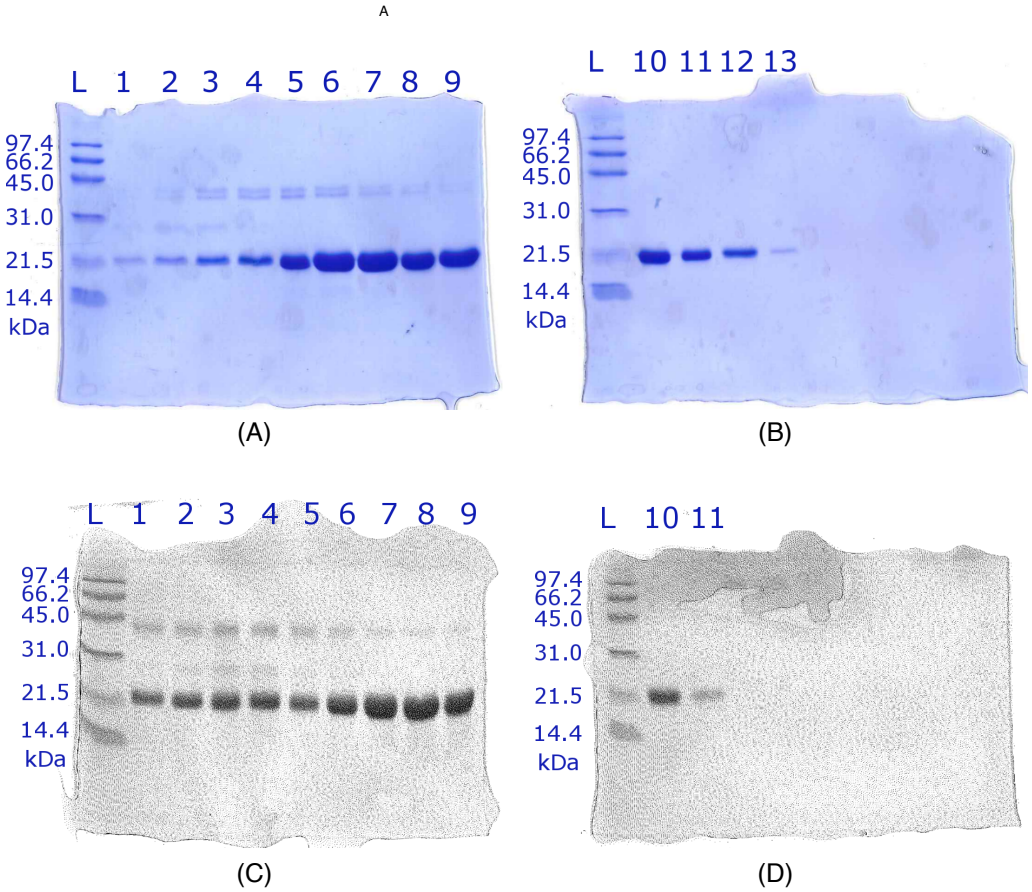

FIGURE 5.4: SDS-pages of different collected fractions after chromatography, numbered as indicated on the chromatograms in Fig. 5.3. The respective molecular weights of the protein standard ("L", Biorad) are indicated. (A): GLB-33GD gel 1, (B): GLB-33GD gel 2, (C): GLB-33GDΔCys gel 1 and (D): GLB-33GDΔCys gel 2

SDS-pages.png

For control purposes, the UV-vis spectra of purified GLB-33GD were compared with GLB-33GDΔCys, and surprisingly, some differences were observed in the Soret absorption band and Q-bands. GLB-33GD exhibited additional small peaks at 504 nm and 625 nm, and the Soret band was blue-shifted compared to GLB-33GDΔCys. This observation was unexpected, as it was not reported in [118], nor observed in previous smaller scale expression batches. This potentially suggests the co-existence of an OH^--ligated LS- and HS-form in GLB-33GD. However, caution should be exercised, as the spectrum also contains a broad peak around $\sim$ 660 nm, which may indicate the presence of biliverdin (see also §5.4.2), and hence the onset of protein degradation. Nevertheless, due to the high yield and purity of the sample, and the planned buffer exchanges during

crystallization experiments, it was decided to proceed with crystallization trials using this batch.

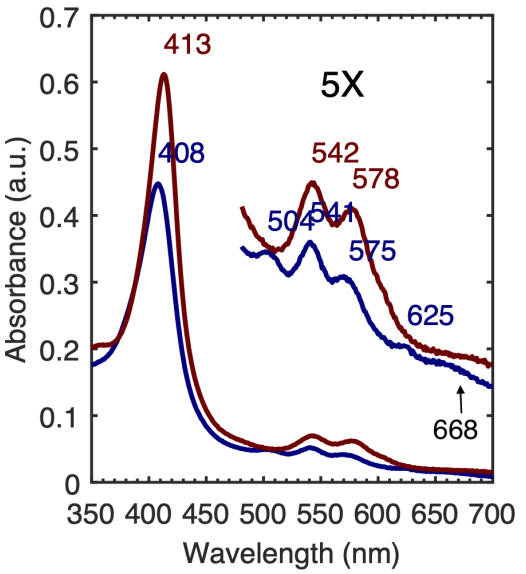

FIGURE 5.5: UV-vis absorption spectra of GLB-33GD (blue) and GLB-33GDΔcys (brown) at pH 8.5, 100 × diluted.

Crystal growth Numerous optimization trials resulted in an improvement in the quality of the protein precipitate. Initially, a promising stick-like precipitate was observed, but it was later identified as glassy aggregates. The best results were obtained for GLB-33GDΔCys using a precipitant solution containing 1.0 M sodium acetate trihydrate and 0.1 M imidazole at pH 6.5, resulting in small red aggregates (Fig. 5.6). However, the quality of the precipitate remains insufficient for X-ray diffraction experiments, and the optimization trials are ongoing. Due to the limited time frame of the PhD, no further structural results could be obtained. This highlights that X-ray crystallization is often a bottleneck in structural studies, and therefore, we have continued the investigation using advanced EPR as a complementary alternative to gain structural insights (§5.4.3).

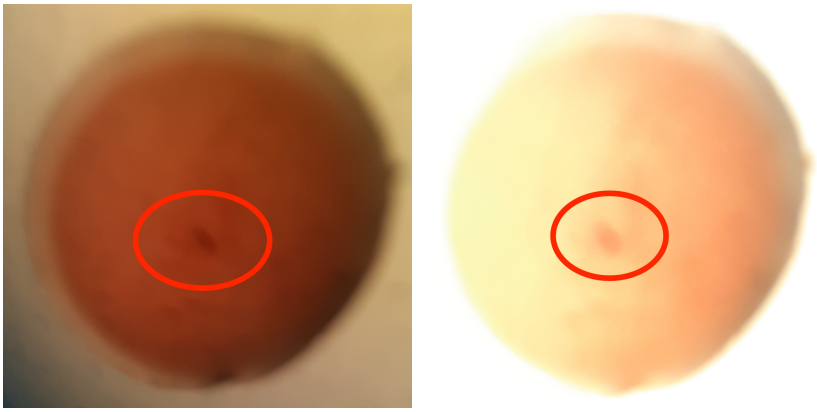

(A) (B)

FIGURE 5.6: Slightly out-of-focus images for illustrative purpose of the red crytals (circle) in the vapour diffusion drops.

5.4.2 Engineering the heme-pocket region of GLB-33GD

As outlined in the introduction, the following GLB-33GD mutants were constructed and purified: I69H/F111S, R72V/F111S, and I69H/R72V/F111S. While the point mutations of the E7 and E10 amino acid residues were intended, the point mutation of Phe111 → Ser was not. However, since Phe111 is modelled to be near the heme, and the additional point mutation was discovered only later in the subsequent trials to purify the mutants, I will discuss the results here. Furthermore, Phe111 is 7 amino acid residues away from F8His. In hhMb and swMb, a Pro is located at this position, but in *Al*Mb, there is a Ser residue (Fig. 5.2). Similar as GLB-33GD, *Al*Mb has an Arg residue at position E10. Different LB cultures were inoculated with glycerol stocks of the 3 above mutants and of GLB-33GD (see §5.3.1).

FIGURE 5.7: Photograph of the samples collected after NiAC. From left to right: GLB-33GDI69H/F111S, R72V/F111S, I69H/R72V/F111S and GLB-33GD.

The cell pellets from the harvested TB cultures showed equally large size and color. After lysis, GLB-33GD supernatant looked slightly more pink than the others, which becomes better pronounced after NiAC (Fig. 5.7).

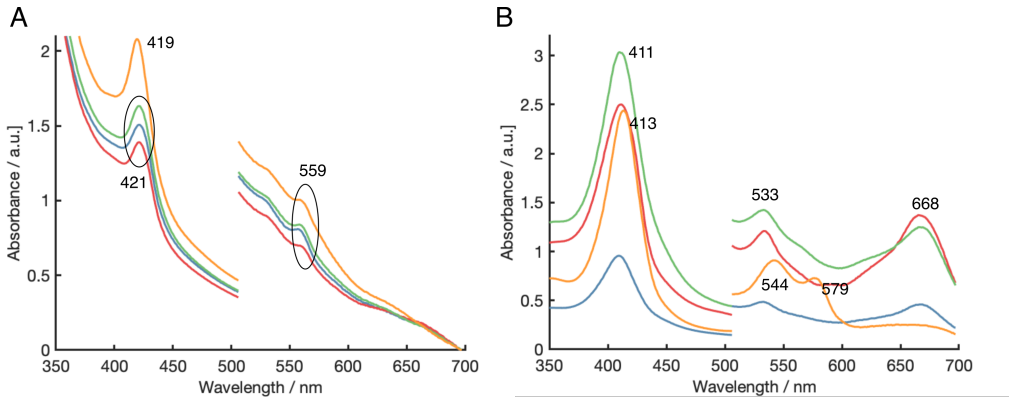

FIGURE 5.8: UV-vis Abs spectra of the GLB-33GD (orange) in comparison with the GLB-33GD mutants I69H/F111S (blue), R72V/F111S (red) and I69H/R72V/F111S (green). Panel A shows the UV-vis spectra of the crude eluate after cell lysis, panel B shows the spectra of the fractions obtained after NiAC.

In order to understand the more yellow/greenish colour of the mutants observed by the naked eye, UV-vis Abs spectra were collected of the crude eluate after cell lysis and of the fractions after NiAC (Fig. 5.8).

For the crude soluble fraction after cell lysis, the Soret peak appears around 419 nm for GLB-33GD and 421 nm for the mutants (Fig. 5.8 (A)). Because of the relatively low concentration and large fraction of contaminants, the Q-bands are less distinguishable. However, a notable shoulder is present around 559 nm in all samples. This may point to the presence of a LS deoxy Fe(II) heme form potentially in equilibrium with a HS Fe(II) [296]. The reduced form occurs because of the presence of reductants in the cell lysis. After NiAC, all the mutants show a large peak around 668 nm and a Q-band at 533 nm. This is clearly different from the GLB-33GD, which shows similar spectra as observed earlier. Next to this, the width of the Soret-peak of the mutants is larger than the Soret-peak of GlB-33GD. Samples varied in concentration because the amount of Ni beads for each column was not standardized.

The peak at 668 nm may indicate the presence of biliverdin (BV), a degradation product of heme. BV has been reported to absorb light at 380 nm and 670 nm [297]. Attempts were made to remove BV from the sample, but failed, indicating that in some of the proteins BV is nested in the cavity normally taken by heme. It is unclear how and whether the presence of BV is linked to the point mutations.

Although the AA residue 7 positions further from F8His is Pro in Mb, a structural overlay of the homology model with Mb shows that F111 is located at the FG loop, at a similar location as I99 (FG5) found in Mb, which is known to strongly influence heme affinity. A study by Hargrove et al. [298] showed that an apolar side chain at position 99 is important for keeping the heme pocket anhydrous and observed that the I99S mutation, which is exactly the AA mutant in our case, results in a 90-fold increase in hemin loss at pH 5. Therefore, it is likely that this unforeseen mutation is related to the observation of BV in the protein.

Fig. 5.9 (red) shows the UV-Vis Abs spectrum of GLB-33GD I69H/F111S after the NiAC in detail. Besides the broad peak at 668 nm, a Soret peak at 408 nm, a Q_β-band at 532 nm, with a small Q_α shoulder at 565 nm, is observed. This is substantially different from the absorption bands of GLB-33GD, which is in a Fe(III)−OH^- state as outlined in Chapter 4 and shown in figure 5.8 B. Instead, the Q-bands are more in line with a LS/6-coordinate Fe(III) heme form, such as found for bis-histidine coordinated gbs [299]. The Soret seems somewhat blue-shifted compared to other bis-His globins, but this may be an effect of the underlying contribution of BV or a sign of an equilibrium with a ferric high-spin form. When dithionite is added, the spectral features of a bis-His ferrous state are formed (Soret at 421 nm and Q-bands at 523 nm, 556 nm, with the Q_α band of larger intensity than the Q_β band) (Fig. 5.9 (blue)). To substantiate the assignment to a bis-histidine coordination of the heme iron, CW-EPR experiments were performed on the ferric form.

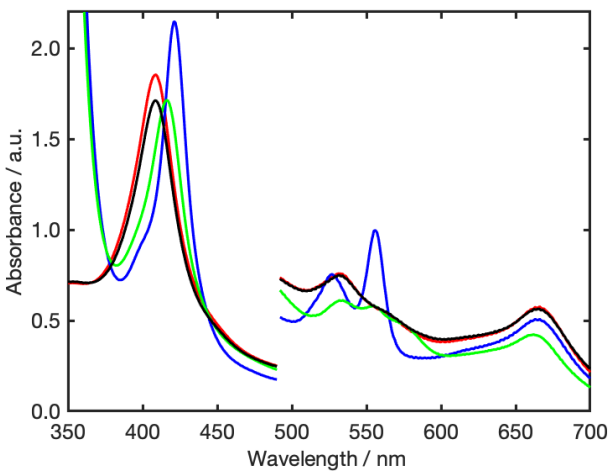

FIGURE 5.9: UV-vis spectra of GLB-33GD mutant I69H/F111S as purfied after NiAC (red), reduced with dithionite (Fe(II)-deoxy) (blue), reduced with dithionite in presence of 100 × excess of $NaNO_2$ (green) and as purfied form with 100 × excess of $NaNO_2$ (black).

The baseline corrected CW-EPR spectrum as well as the corresponding simulation of the individual components are shown in Fig. 5.10. Different components can be identified. Several are not related to the heme center of the globin: a contribution at $\sim$ 160 mT ($g_y = 4.28$), originating from non-heme-bound iron ($g_z = g_y = 4.28$, $g_x = 4.1$), and an unknown radical, likely a background signal from the cavity at 337 mT ($g \sim 2.0015$).

Relevant to the heme system is the signal due to a ferric HS form with effective g-values $[g_z, g_y, g_x] \sim [6, 5.8, 2] \pm 0.01$, and at least one signal due to a LS ferric form. Of this LS heme form, the signals at principal g-values $g_z = 2.99$, $g_y = 2.24$ and $g_x = 1.42$ $\pm$ 0.02 are visible. These values are in line with what has been observed before for other ferric gbs with bis-His coordination [93, 300] (see also Chapter 7 for examples). This confirms that in I69H/F111S GLB-33GD the distal E7 His coordinates to the heme

iron, with a tiny fraction being in the HS form. This differs from hhMb that is in an aquomet form (HS) at neutral pH. Potentially, the presence of E10Arg forces the E7 ligand to coordinate with the heme iron. In hhMb, a smaller Val residue is at position E10. Furthermore, the spectrum shows a Cu(II) cavity background signal ($g_z = 2.27$, $g_y = g_x = 2.042 \pm 0.02$; $|A_x| = |A_y| = 40 \pm 5$ MHz, $|A_z| = 492 \pm 5$ MHz).

Important to notice is that also the R72V/F111S mutant no longer gives the absorption bands of the hydroxo-ligated ferric heme (Fig. 5.8 (B)), corroborating our findings in Chapter 4 that the E10Arg is crucial to stabilize this ligation. In Chapter 4, we showed that nitrite can bind to the ferric form of GLB-33GD(ΔCys). Addition of a 100 × excess of $NaNO_2$ to the ferric form of I69H/F111S GLB-33GD does not lead to nitrite ligation at the heme, as the optical spectrum remains identical to the ferric as-purified form (Fig. 5.9, black). The E7His ligand is protecting the heme iron from nitrite binding in this mutant.

In line with this, addition of dithionite, followed by addition of $NaNO_2$, does not lead to a full conversion to the nitrosylated ferrous heme form. The resulting UV-Vis spectrum is a sum of two components (Fig. 5.9, green). This is clearly seen in the Q-band region, where three signals appear at 532 nm, 579 nm, and a broad peak from 545-560 nm. NO-ligated ferrous gbs have the Q_β-band at 542-546 nm and the Q_α band at 570-571 nm [301], and the Soret around 413 nm. Here, the Soret band is found at 417 nm. The optical spectrum of I69H/F111S GLB-33GD after addition of dithionite and $NaNO_2$ in air is a mixture of the contribution of a nitrosylated ferrous form and the ferric form, indicating that the NiR activity is significantly reduced in comparison to GLB-33GD.

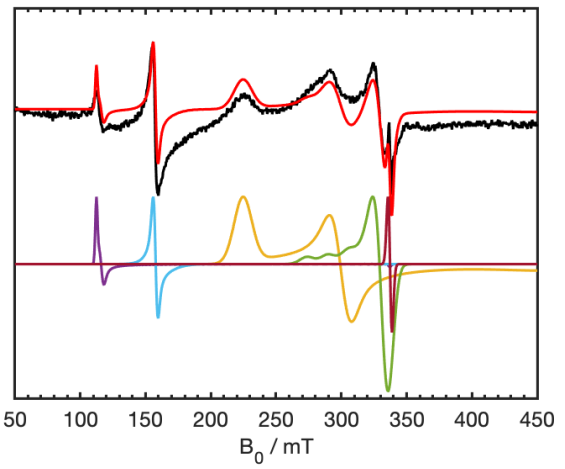

FIGURE 5.10: Experimental X-band CW-EPR spectrum (black) and corresponding simulation (red) of the concentrated batch of GLB-33GD I69H/F111S in Tris buffer pH 7.5, with 25% glycerol, collected at $T = 10$ K with a modulation amplitude of 0.5 mT. The individual components making up the simulation are shown below: HS (purple), LS (yellow), non-heme iron (blue), Cu(II) (green), and radical (dark red).

5.4.3 The hydroxy-ligated GLB-33GD(ΔCys)

Proton hyperfine spectroscopy

As shown in Chapter 4 and [290, 234, 118], the ferric form of GLB-33GD(ΔCys) is hydroxo-ligated at neutral pH, with two forms LS1 and LS2 being observed (Table 4.1). The presence of these two forms is confirmed by high-field EPR (W-band, Fig. 5.11). While LS2 has principal g values very similar to what was reported for the alkaline forms of Mb and other gbs with minor hydrogen-bonding to the hydroxide ligand [234], the EPR data of LS2 suggest a stronger hydrogen bonding [238, 262], hypothesized to be linked to the movement of the Arg residue into the heme pocket.

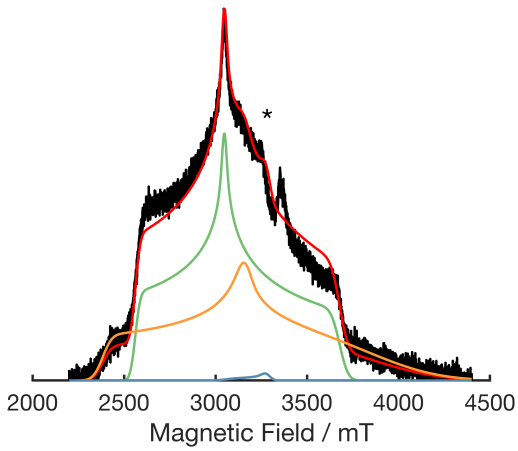

FIGURE 5.11: W-band EPR spectrum of GLB-33GD (black) and simulation (red). A two spin-system was used (LS1, gold) and (LS2, green), corresponding to the g-values reported in Table 4.1. A Cu background signal (blue) is indicated by (*).

Proton hyperfine interactions

The previous assignments of the two LS forms in ferric GLB-33GD to hydroxo-ligated heme forms was purely based on the comparison with principal g values of other alkaline forms of heme proteins. Here, I used Davies ENDOR, a technique suited to detect large nuclear frequencies [302], to detect the ^{1}H coupling of the OH^--ligand. An earlier ENDOR study on MbOH [303] revealed that A = [-11.3 -11.3 7.1] MHz, with the hyperfine principal axis frame being 35° tilted away from the g-tensor frame ($\beta = 35°$). The Davies-ENDOR spectra of ferric GLB-33GD at pH 7.5 are shown in Fig. 5.12 (A). They are taken at different magnetic-field values. At observed positions corresponding to the g_y-values of LS1 and LS2, a line splitting of $\sim$ 10 MHz is observed. The spectrum matches a simulation with A= [-10.3 -10.3 7.1] $\pm$ 0.4 MHz, with β = 35° $\pm$ 10°, confirming the presence of hydroxide ligands.

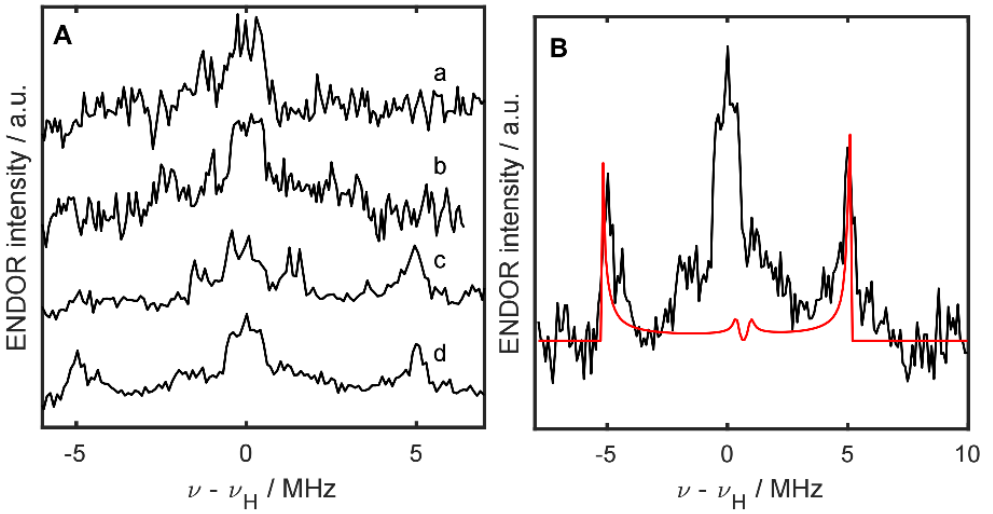

FIGURE 5.12: Panel A: Davies ENDOR spectra collected of a frozen solution of GLB-33GDΔCys at pH 7.5 at various magnetic fields corresponding to the principal g-values of LS1 and LS2. The spectra (a-d) are collected at g_z(LS1), g_z(LS2), g_y(LS2) and g_y(LS1), respectively. Panel B: The background-corrected Davies ENDOR spectrum of GLB-33GD (black) collected at observer position g_y(LS1) (B_0 = 327.2 mT) and Easyspin simulation (red) using a $\boldsymbol{A}$-tensor = [-10.3 -10.3 7.1] MHz

Nitrogen hyperfine spectroscopy

To study the effects of the hydroxide ligand on the hyperfine couplings of the ^{14}N nuclei surrounding the unpaired electron (*i.e.* heme and F8His nitrogens), ESEEM spectroscopy including 3- pulse ESEEM and 4- pulse ESEEM (HYSCORE) was employed. These techniques have shown to be very useful to study heme systems [217]. Overall, HYSCORE spectroscopy is advantageous compared to 3-pulse ESEEM spectra, as it provides a secondary frequency axis which disentangles the 3-pulse ESEEM spectra. Hence, I focus here on the HYSCORE spectra, the 3-pulse ESEEM can be found in the appendix of this chapter for comparison (Fig. B.2). The Fourier transformed time-domain signal results in a frequency spectrum containing either sq- or dq frequencies from ^{14}N nuclei (I = 1) surrounding the heme Fe. The dq frequencies correspond to the nuclear transitions $|\Delta m_I| = 2$ and the sq from $|\Delta m_I| = 1$ (see also Fig. 3.14). These transitions allow us to obtain information about the above-mentioned hyperfine and quadrupole couplings associated with these nuclei, which characterizes the heme system.

All GLB-33GDΔCys ESEEM spectra were collected at field positions corresponding to the principal g-values of both LS1 and LS2 species. The presence of two low-spin species, and the many N nuclei surrounding the heme, complicate the analyses and peak assignment tremendously. Therefore, we interpret these spectra first by looking at the canonical observer positions g_z (LS1) and g_x (LS1). These outer-field positions can be considered as pure LS1-state spectra, as LS2 lies completely within the outer fields of

LS1. At these positions, the resonance condition with the limited excitation bandwidth of the microwave pulses, is not fulfilled for the LS2 form. All other positions contain mixed information of the LS1 and LS2 states.

The experimental HYSCORE spectra collected at six different observer positions corresponding to the canonical positions of LS1 and LS2 together with the corresponding simulations using the parameters of Table 5.1 are given in Figs. 5.13 till 5.18.

	$[A_x\ A_y\ A_z]\pm0.2$	$[\alpha\ \beta\ \gamma]\ \pm30$	$[Q_1\ Q_2\ Q_3\ ]\ \pm0.2$	$[\alpha\ \beta\ \gamma]\ \pm30$
		LS1		
N_{His}	-[5.7 5.6 6.1]	[0 10 0]	[0.12 0.63 -0.75]	[0 10 0]
N_{pyr1}	-[4.6 4.7 5.7]	[0 0 0]	[0.9 -0.75 -0.15]	[0 10 0]
N_{pyr2}	-[4.6 4.0 5.5]	[0 0 90]	[0.9 -0.75 -0.15]	[0 10 90]
		LS2		
N_{His}	-[5.4 5.7 6.3]	[0 10 0]	[0.4 0.5 -0.9]	[0 10 0]
N_{pyr1}	-[4.8 5.2 5.3]	[0 0 0]	[0.9 -0.85 -0.05]	[0 10 0]
N_{pyr2}	-[4.9 5.2 5.5]	[0 0 90]	[0.9 -0.85 -0.05]	[0 10 90]

TABLE 5.1: Preliminary hyperfine values and nuclear-quadrupole parameters (MHz) used for the simulation of the HYSCORE contributions of the F8His and heme pyrrole nitrogens of ferric GLB-33GD at pH 7.5. The relative signs are determined using earlier considerations [220]. Hyperfine and quadrupole values are given in MHz and Euler angles α, β and γ in degree units (°).

We first focus on the HYSCORE spectra taken at magnetic field positions corresponding to g_z(LS1) (Fig. 5.13) and g_x(LS1) (Fig. 5.18). As indicated in Fig. 5.13 (top), crosspeaks linking dq frequencies and sq frequencies are recognized. Here, one broad crosspeak is observed, with a prominent maximum at (-7.23, 4.27) MHz and a more subtle extension at (-7.59, 4.58) MHz. The first crosspeak can be ascribed to the dq-transition frequencies of the four pyrrole Ns, and the second one potentially to the coupling with the HisF8 N [183]. The dq frequencies of these crosspeaks can be linked to the hyperfine coupling A at this observer position using.

$$\nu^{dq}_{\alpha,\beta} = 2\sqrt{\left(\frac{A}{2} \pm \nu_I\right)^2 + \kappa^2\,(3+\eta^2)}, \tag{5.1}$$

which leads to

$$|A| = \frac{\left(\nu^{dq_i}_{\alpha}\right)^2 - \left(\nu^{dq_i}_{\beta}\right)^2}{8\nu^i_I}. \tag{5.2}$$

Using the value of A, $\kappa^2(3+\eta^2)$ can be derived with $\kappa = \frac{e^2qQ}{4h}$. Since $0 \leq \eta \leq 1$, the possible values of κ can be deduced. This procedure can be iterated at the different observer positions and limits the degrees of freedom for the simulation. At observer positions where both LS1 and LS2 contribute to the EPR spectrum, the HYSCORE spectra will contain contributions from both forms, complicating the analysis. Using the EasySpin [212] simulation software package with a set of two equivalent heme nitrogens,

for which one axis is rotated by 90 degrees, and a third His F8 nitrogen, we can obtain a "fair" match between the experimental observations and the simulations (see Figs. 5.13-5.18, and the simulation parameters in Table 5.1). The simulation (red) corresponds to the spin system of LS1 and is shown for all field positions, whereas the system for LS2 (magenta) is only useful for the range that falls within the outer positions g_x and g_z of LS2.

The hyperfine and nuclear quadrupole values are similar to those observed for other LS heme forms [220] in which the F8His is not in an imidazolate, but in a neutral imidazole form. In Appendix, Fig. B.3, the HYSCORE spectra of MbOH at very high pH are shown. The CW-EPR spectrum resembles this of LS2 in GLB-33GD (Fig. B.1). When considering the HYSCORE spectrum corresponding to $g = g_z$ (MbOH), two clear dq crosspeaks are seen, while these were less differentiated at position g_z(LS1) in ferric GLB-33GD, indicating that there are substantial differences between the ^{14}N hyperfine data of both species. However, at present, insufficient data is available to translate this into structural information. A follow-up study should involve DFT computations to link EPR data to the heme-pocket geometry.

magnetic field (mT)	*dq peak positions (MHz)*	*dq calculated A (MHz)*	*sq peak positions (MHz)*
254.4 (g_z LS1)	(-7.59, 4.58) (-7.23, 4.27)	5.85 5.43	(-3.52, 1.78) (-3.24, 2.83)
270.0 (g_z LS2)	(-7.59, 4.44) (-7.18, 4.06)	5.7 5.28	(-3.52, 1.98) (-3.56, 2.83)
316.0 (g_y LS2)	(-7.93, 4.27) (-7.34, 2.90)	5.74 4.99	(-4.31, 1.05 (-3.32, 2.24 (-2.74, 2.34
327.5 (g_y LS1)	(-7.87, 4.01) (-7.23, 3.54) (-6.33, 2.67)	5.69 4.92 4.09	(-3.83, 0.59) (-3.04, 2.24) (-2.52, 2.02)
379.3 (g_x LS2)	(-7.86, 3.40) (-7.86, 3.43)	5.39 4.87	(-4.35, 1.56) (-2.96, 0.81)
402.4 (g_x LS1)	(-8.24, 3.58) (-7.32, 2.65)	5.56 4.69	

TABLE 5.2: Double- and single quantum peak positions as observed in the HYSCORE spectra of GLB-33GDΔCys. The calculated hyperfine values can be used as starting values to optimize the HYSCORE simulations.

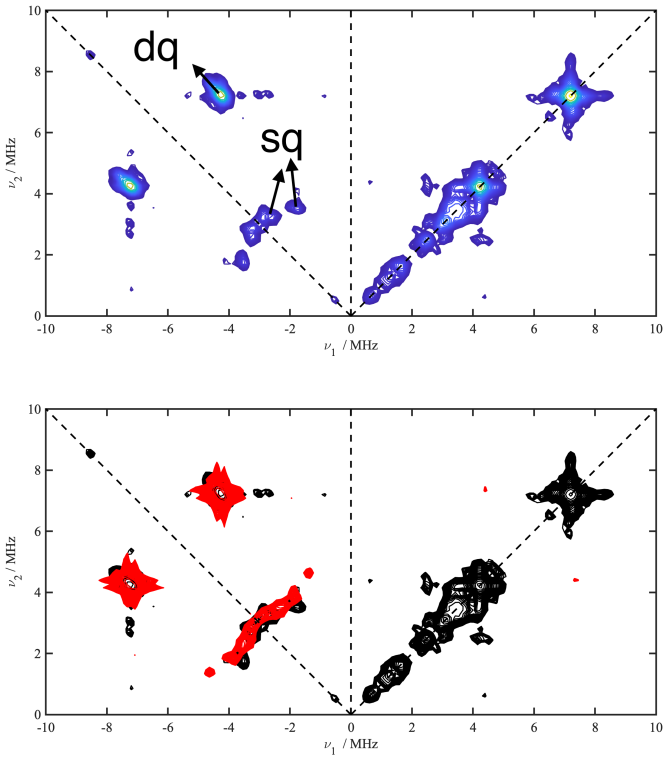

FIGURE 5.13: Panel top: experimental HYSCORE spectra of a frozen solution of GLB-33GDΔCys collected at the canonical positions g_z of LS1 (254.4 mT). The spectrum was collected at a temperature $T = 6$ K and is the sum of two τ-values (104 ns and 176 ns). Panel bottom: shows the simulated (red) and experimental (black) spectrum using the three-N simulation system for LS1, as reported in Table 5.1.

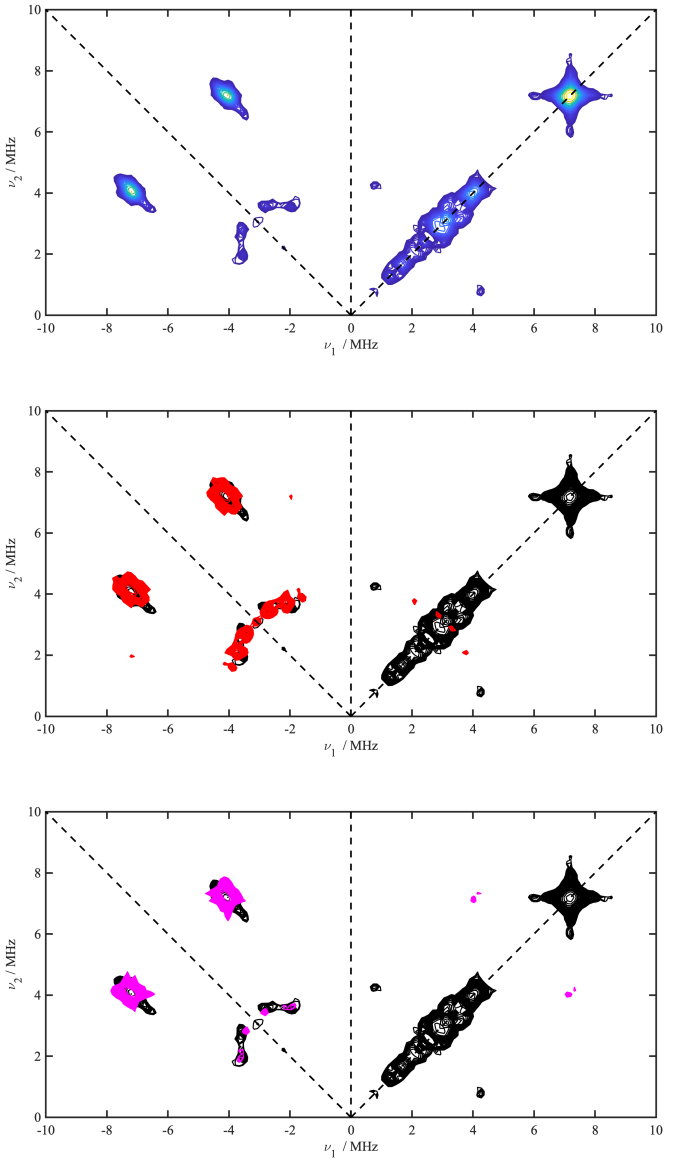

FIGURE 5.14: Panel top: experimental HYSCORE spectra of a frozen solution of GLB-33GDΔCys collected at the canonical positions g_z of LS2 (270.0 mT). The spectrum was collected at a temperature $T = 6$ K and is the sum of two τ-values (104 ns and 176 ns). Panel mid: the simulated (red) and experimental (black) spectrum using the three-N simulation system for LS1. Panel bottom: the simulated (magenta) and experimental (black) spectrum using the three-N simulation system for LS2. Details of the simulation systems are reported in Table 5.1.

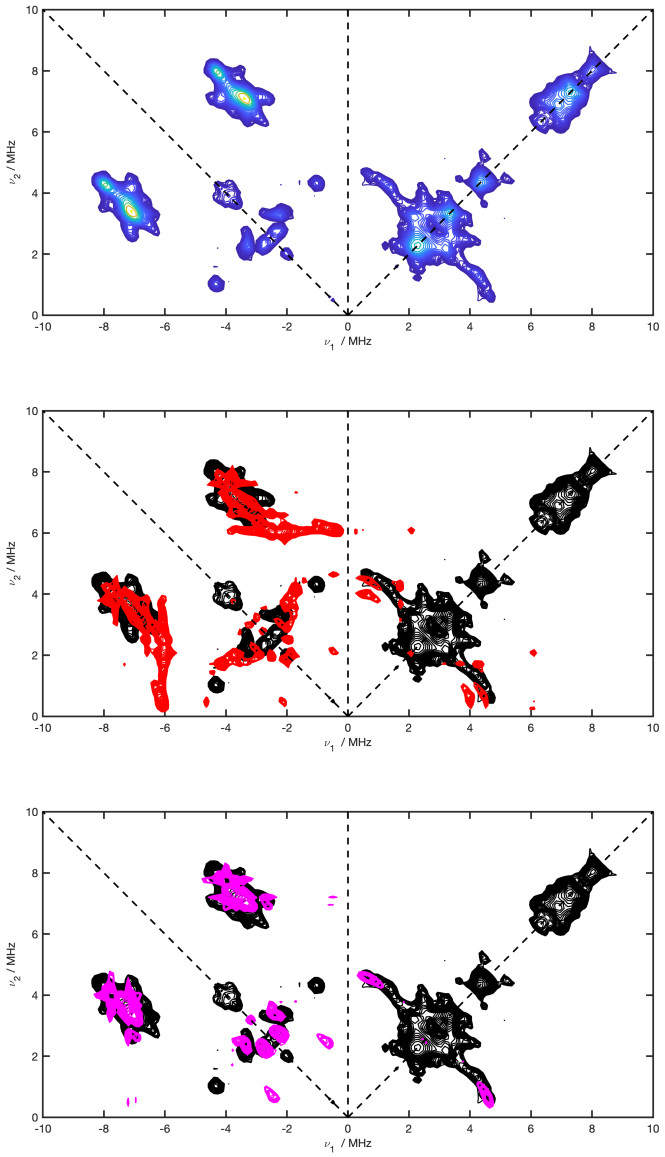

FIGURE 5.15: Panel top: experimental HYSCORE spectra of a frozen solution of GLB-33GDΔCys collected at the canonical positions g_y of LS2 (315.8 mT). The spectrum was collected at a temperature $T = 6$ K and is the sum of two τ-values (104 ns and 176 ns). Panel mid: the simulated (red) and experimental (black) spectrum using the three-N simulation system for LS1. Panel bottom: the simulated (magenta) and experimental (black) spectrum using the three-N simulation system for LS2. Details of the simulation systems are reported in Table 5.1.

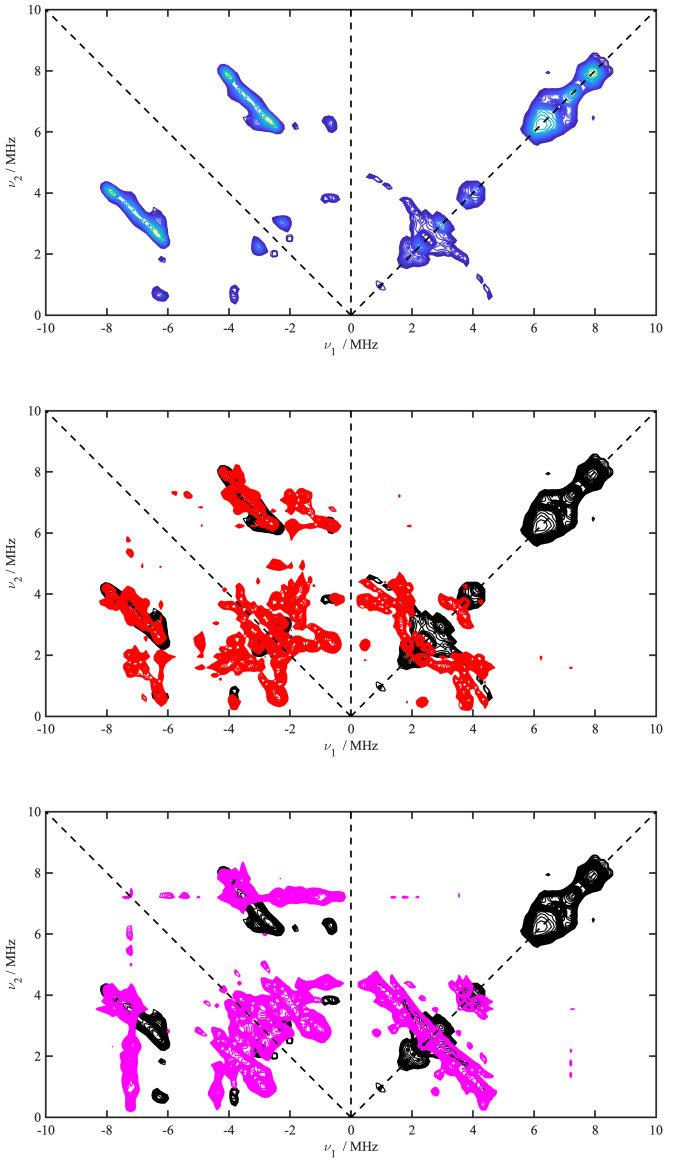

FIGURE 5.16: Panel top: experimental HYSCORE spectra of a frozen solution of GLB-33GDΔCys collected at the canonical positions g_y of LS1 (327.5 mT). The spectrum was collected at a temperature $T = 6$ K and is the sum of two τ-values (104 ns and 176 ns). Panel mid: the simulated (red) and experimental (black) spectrum using the three-N simulation system for LS1. Panel bottom: the simulated (magenta) and experimental (black) spectrum using the three-N simulation system for LS2. Details of the simulation systems are reported in Table 5.1.

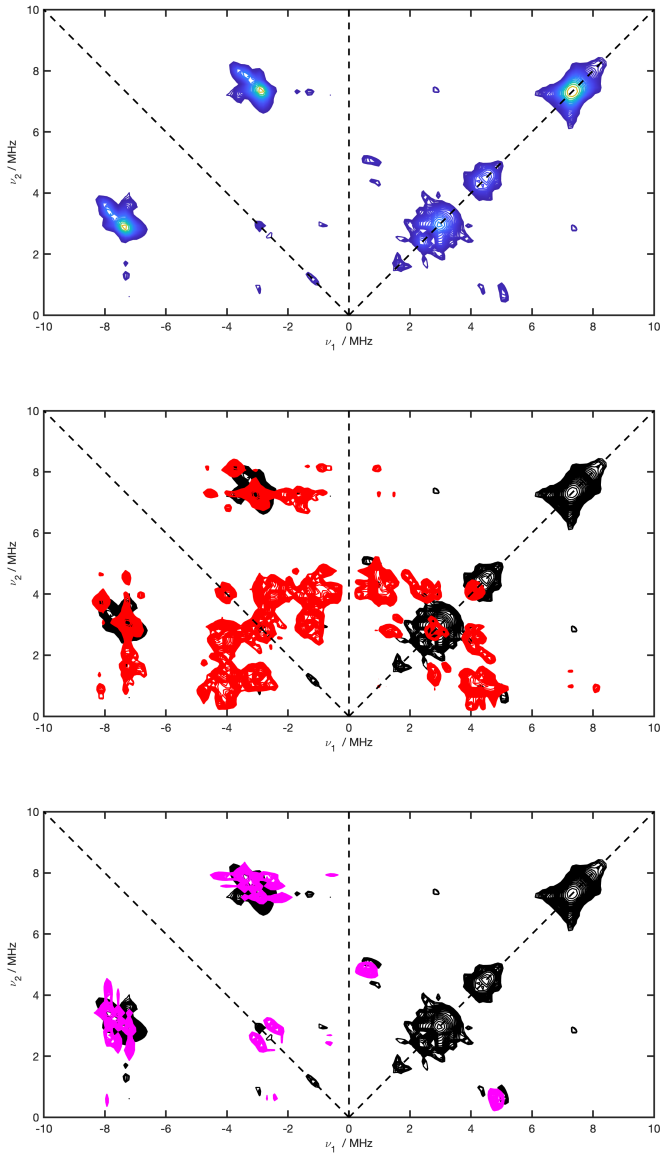

FIGURE 5.17: Panel top: experimental HYSCORE spectra of a frozen solution of GLB-33GDΔCys collected at the canonical positions g_x of LS2 (379.3 mT). The spectrum was collected at a temperature $T = 6$ K and is the sum of two τ-values (104 ns and 176 ns). Panel mid: the simulated (red) and experimental (black) spectrum using the three-N simulation system for LS1. Panel bottom: the simulated (magenta) and experimental (black) spectrum using the three-N simulation system for LS2. Details of the simulation systems are reported in Table 5.1.

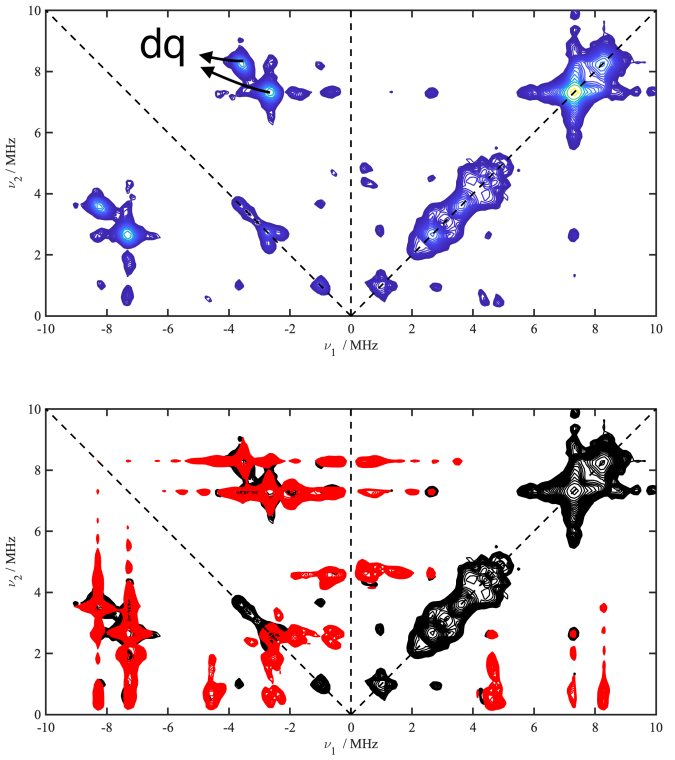

FIGURE 5.18: Panel top: experimental HYSCORE spectra of a frozen solution of GLB-33GDΔCys collected at the canonical positions g_x of LS1 (402.4 mT). The spectrum was collected at a temperature $T = 6$ K and is the sum of two τ-values (104 ns and 176 ns). Panel bottom: shows the simulated (red) and experimental (black) spectrum using the three-N simulation system for LS1, as reported in Table 5.1.

5.4.4 Nitrosylated ferrous GLB-33GD(ΔCys)

Temperature dependence of the CW-EPR spectra

The ferrous GLB-33GD reduces nitrite to NO at a fast rate and therefore we examined the reaction product of NO rebinding to the ferrous heme (GLB-33GD-NO) as a function of temperature. In Chapter 4 (Fig. 4.7), we already showed the CW-EPR spectrum of this form taken at 6 K. Here, different CW-EPR spectra were collected with a microwave power of 0.1 mW to overcome distortions due to power saturation. EasySpin simultations show that the temperature-dependent EPR spectra of GLB-33GD contain at least two forms being an axial (A) and a rhombic (R) one (Figs. 4.7, 5.19). The large hyperfine splitting due to the strong coupling with the ^{14}N nucleus of the NO molecule is visible in the rhombic component of the EPR spectrum, especially below T= 60 K. Fig. 5.20 (B) shows the % of the R component as a function of temperature, showing that with increasing temperature, component A is enhanced but the 50 percent turning point between R and A form is not even reached at 190 K for GLB-33GD.

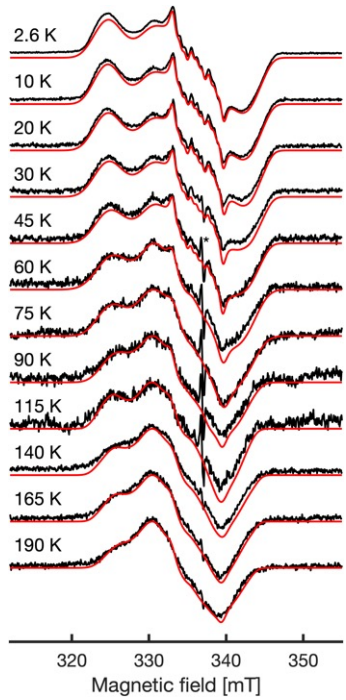

FIGURE 5.19: X-band CW-EPR spectra (black) and simulation (red) of GLB-33GD-NO in function of temperature with P = 0.1 mW. The presence of a radical is indicated (*).

The principal g-values shift as a function of temperature (Fig. 5.20 (A, C)), with the shift in g_x being the most pronounced. The variation in $(g_z - g_x)/g_y$ between 10 and 19 K equals 0.0117, which is smaller than the reported difference for the E7-Gln and E7-Leu mutants of Ngb [277]. The curve of $(g_z - g_x)/g_y$ in function of T has a plateau between 75 and 160 K, suggesting the presence of an intermediate state as observed for Mb-NO [275, 276, 304]. Furthermore, the non-linear behavior of $\ln \frac{A}{R}$ in function of T (Fig. 5.20 (D)), corroborates that for GLB-33GD, a simple two state model is invalid.

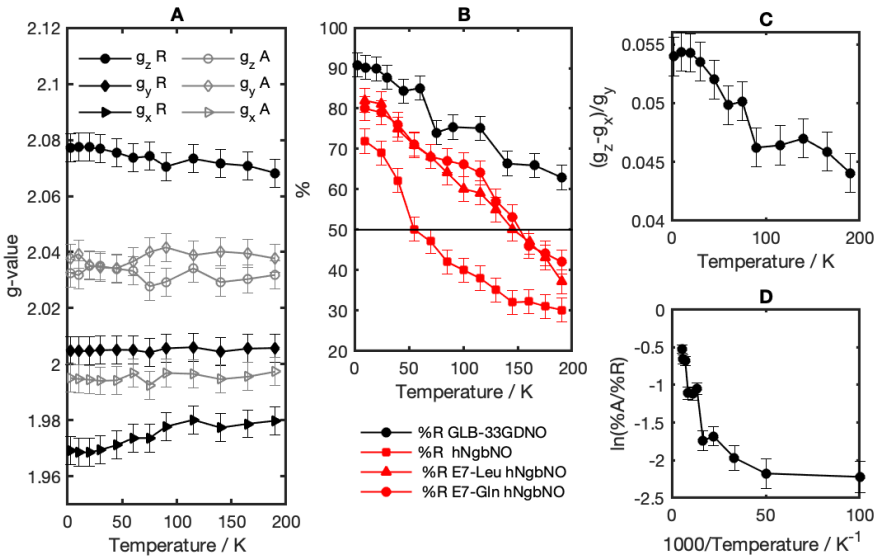

FIGURE 5.20: (A) the temperature dependence of the principal g-values of the A- and R-form of GLB-33GDNO. (B) % of contribution of the R form to the EPR spectrum of GLB-33GDNO as a function of temperature in comparison to the percentages reported for the NO-ligated form of human neuroglobin (hNgb), and the E7-Leu and E7-Gln muttant as reported in [277]. (C) Values of $(g_z - g_x)/g_y$ as a function of temperature for GLB-33GDNO. (D) values of $\ln\left(\frac{\%A}{\%R}\right)$ as function of $\frac{1}{T}$.

Indeed, in a thermodynamic two-state model (A $\leftrightarrow$ R), the ratio $\frac{\%A}{\%R}$ should follow the following Boltzman distribution

$$\frac{\%A}{\%R} \propto \frac{\exp\left(\frac{-\Delta G_A}{RT}\right)}{\exp\left(\frac{-\Delta G_R}{RT}\right)} = \exp\left(\frac{-\Delta G}{RT}\right), \tag{5.3}$$

with ΔG_A and ΔG_R the Gibbs free energy of A and R and $\Delta G = \Delta G_A - \Delta G_R$.

Although the appearance of the signatures of A and R forms in the EPR spectra of nitrosylated GLB-33GD is in agreement with what has been reported before for other gbs [276, 304, 277, 275], some clear differences can be found. For GLB-33GDNO, the contribution of component R to the EPR spectrum remains dominant up to at least 190 K (highest measuring point). In contrast, $\frac{\%A}{\%R} = 1$ is reached at $\sim$ 50 K, while it appears $\sim$ 150 K for its E7-Gln and E7-Leu mutants (Fig. 5.20 (B) [277]). This crossing point is reached at $T = 117$ K and 123 K for human Hb and hhMb, respectively [277]. More strikingly, the CW-EPR spectrum of *Al*MbNO has only a contribution of an R form [305] even at T up to 265 K. This clearly shows that the transition between the two forms is strongly influenced by the nature of the distal AA residues. Human neuroglobin has a His residue on position E7 that is bound to the heme iron in both the ferrous and ferric forms of the protein, unlike the situation in mammalian Mb and Hb, where the

E7His is ideally positioned to stabilize a distal O_2 or NO ligand. The R-form has been associated with a conformation in which the NO ligand is stabilized by H-bonding to the E7 His (in general a distal AA residue) [306]. In hNgb, the E7 His stabilization is less favored at higher temperatures.

Surprisingly, when E7His in hNgb is replaced by a non-coordinating AA (E7-Leu), the R-form dominates up till 160 K. In that respect, it is interesting to note that hNgb has a Lys at position E10 (Fig. 5.1), which may play an important role in stabilizing the ligand. Indeed, it has been previously shown that the E7Gln and E7Val mutants of neuroglobin show ligation of E10 Lys to the heme iron at high pH [307, 308]. This indicates that the E10 AA residue in hNgb can swing into the heme pocket. Similarly, the E7Val of *Al*Mb cannot stabilize the NO ligand, yet the R-form is found to be the only component present in the EPR spectra of *Al*MbNO. The distal ligand is then stabilized by E10Arg (See also Chapter 4). The fact that the point at which $\frac{\%A}{\%R} = 1$ has not been reached at T = 190 K for GLB-33GDNO is in light of the findings for *Al*MbNO further supporting the conclusions from Chapter 4 that E10Arg is playing a crucial role in distal-ligand stabilization. The interaction is, however, different than in *Al*Mb, since in GLB-33GDNO the A-form is also detected. The origin of this form remains elusive, but has been suggested to be linked to a conformation in which the NO is more freely rotating around the Fe-N axis and thus less stabilized by the distal AA residues. Similarly, only one hydroxo-ligated ferric LS form has been observed at alkaline pH for *Al*Mb [263], while two were observed for GLB-33GD.

X-ray diffraction of the nitrosylated forms of different ferrous swMb mutants has revealed that both the N and O atoms of the NO ligand can be involved in hydrogen bonding [266]. In wild-type swMbNO, the N(NO) is hydrogen-bonded to N_ϵ(His). In the related E7Gln mutant, O(NO) is stabilized by a hydrogen bond to N(Gln). Furthermore, in the E7Ala mutant, the absence of an amino acid residue capable of hydrogen bonding, and the distal void created by the small Ala, lead to a water-rich distal side with H_2O hydrogen bonding to the O(NO).

Nitrogen hyperfine spectroscopy

Three-pulse and HYSCORE spectra were collected on a frozen solution of GLB-33GD-NO to gain more insight in the hyperfine and nuclear quadrupole couplings with the surrounding ^{14}N nuclei not resolved in CW EPR. Three clearly distinguishable crosspeaks of ν_0, ν_- and $\nu_+ \approx \nu_0 + \nu_-$ in the low-frequency region < 3 MHz, and a double quantum peak ν^{dq}, are detected (Figs. 5.21, 5.22). This, together with the high intensity and narrow linewidth of the peaks at low frequency points out that the cancellation regime $\nu_I \approx |A|/2$ is valid, for which the nuclear frequencies in one of the M_S manifolds can be described as $\nu_0 = 2\kappa\eta$, $\nu_- = \kappa(3-\eta)$ and $\nu_+ = \kappa(3+\eta)$, with the quadrupole coupling constant κ and the asymmetry parameter η. The collected HYSCORE spectra , shown as the sum of two τ-values, indeed clearly show the three correlation peaks in both (+, +) and (+, -) quadrants. The hyperfine and quadrupole parameters (Table 5.3) were obtained by simulations using the EasySpin package [212] assuming an S= 1/2 system with two nitrogen atoms N_1 and N_2.

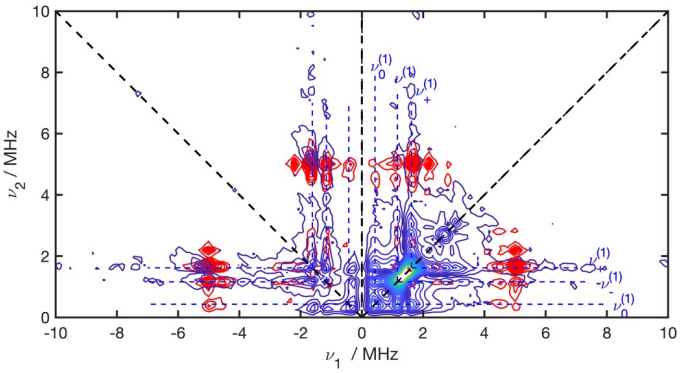

FIGURE 5.21: Experimental (color) and simulated (red) HYSCORE spectrum of a frozen solution of GLB-33GD-NO collected at field position $B_0 = 345.8\,\mathrm{mT}$ at a temperature $T = 20\,\mathrm{K}$. The experimental and simulated spectra are the sum of two τ values (96 ns and 120 ns).

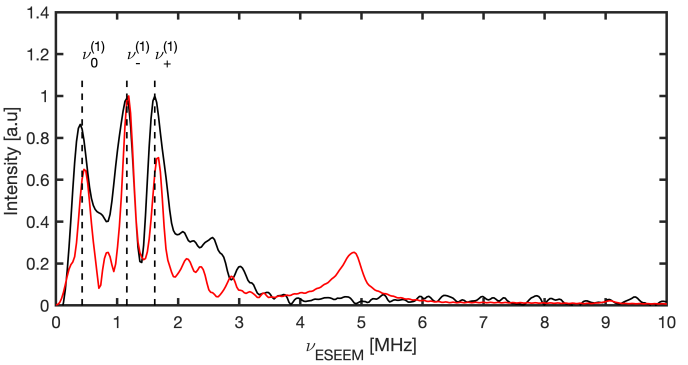

FIGURE 5.22: Experimental (black) and simulated (red) three-pulse ESEEM spectra of GLB-33GD-NO at a magnetic field B_0= 345.1 mT and a temperature T =18 K. The spectrum is the sum of 20 τ-values (96 ns to 400 ns).

	Hyperfine values			Quadrupole parameters		
	A_1 (± 0.2)	A_2 (± 0.2)	A_3 (± 0.05)	Q_1 (± 0.1)	Q_2 (±0.1)	Q_3 (±0.1)
$^{14}N_1$	2.95	1.80	1.90	-0.25	0.90	-0.65
$^{14}N_2$	1.64	2.85	1.90	0.85	-0.20	-0.65

TABLE 5.3: Hyperfine and quadrupole parameters in MHz of the pyrrole nitrogens obtained by the simulation of the HYSCORE spectra of GLB-33GD-NO.

The ^{14}N ESEEM data on nitrosylated heme proteins are scarce. Tyryshkin *et al.* investigated the NO-ligated forms of the α- and β-chains of Hb and NO-ligated Mb with 3-pulse ESEEM and HYSCORE [294]. ^{14}N hyperfine values in the range of 1.57 - 2.92 MHz, with quadrupole couplings similar to the ones observed here, were assigned in this work

to the interaction of the unpaired electron with the pyrrole nitrogens of the heme. The authors also found extra signals in the ESEEM of βHbNO that they tentatively assigned to the N_ε of E7His stabilizing NO. Here, no comparable interaction with the Arg N-nuclei was detected, but the strong modulations of the interactions with the pyrrole nitrogens induced by the cancellation condition may hamper the detection of nuclei with hyperfine values that do not fulfill this condition.

5.5 Conclusion

GLB-33GD, the globin domain of GLB-33 in *Caenorhabditis elegans* has extraordinary features such as its hydrophobic heme pocket with key AAs E7Ile and E10Arg, and a high NiR activity. The role of these residues were investigated in the light of their potential role in ligand stabilization and NiR. First, high-purity protein samples of GLB-33GD(ΔCys) were prepared for crystallization trials. The purity was assessed and UV-vis spectra showed some differences between GLB-33GD and the ΔCys variant, indicating potential co-existence of different forms.

Next, GLB-33GD mutants were constructed and purified, including I69H/F111S, R72V/F111S, and I69H/R72V/F111S. The point mutations of E7 and E10 amino acid residues were made intentionally, but the unintended additional point mutation F111S was discovered later on. The UV-vis Abs spectra of the mutants may indicate the presence of biliverdin (BV) and also suggested that they may have a LS/6c ferric heme. In particular, the R72V/F111S mutant lacks absorption bands indicative of hydroxo-ligated ferric heme, confirming the importance of E10Arg in stabilizing this ligation. The I69H/F111S mutant was further investigated with CW-EPR suggesting that the distal E7 His coordinates to the heme iron, with a small fraction being in the HS form. Addition of nitrite or dithionite to the ferric form of I69H/F111S GLB-33GD does not lead to full conversion to nitrosylated ferrous heme, indicating reduced NiR activity compared to GLB-33GD. Overall, the mutagenesis studies reveal the crucial role of the key amino acids IleE7 and ArgE10, but further research is needed in which the unintended F111S mutation is deleted and studied separately.

In a second part of this chapter, high-field EPR spectroscopy confirmed the existence of the earlier observed LS1 and LS2 form in ferric GLB-33GD(ΔCys). Proton hyperfine spectroscopy was used to study the ferric form of GLB-33GD(ΔCys) at neutral pH. Davies ENDOR was used to detect the ^{1}H coupling of the hydroxide ligand, revealing a line splitting of approximately 10 MHz and confirms the presence of a hydroxide ligand with the hyperfine principal axis frame being tilted away from the g-tensor frame. Nitrogen hyperfine spectroscopy, specifically HYSCORE, was then employed to study the effects of hydroxide ligand on the hyperfine couplings of the ^{14}N nuclei in the heme pocket. Experimental HYSCORE spectra were collected at different observer positions corresponding to the canonical positions of LS1 and LS2, and simulations were performed using preliminary hyperfine values and nuclear-quadrupole parameters. The analysis of the spectra revealed crosspeaks linking dq and sq frequencies, which were attributed to the couplings of pyrrole Ns and HisF8 N. However, the presence of two overlapping LS

forms complicated the analysis significantly. Therefore, our data should be complemented with further DFT calculations on the heme pocket, which requires high-resolution structural information. First trials in to acquire that via X-ray crystallography were unsuccessful within the timeframe of my research.

At last, the temperature dependency on the CW-EPR spectra of nitrosylyted GLB-33GD earlier shown in Chapter 4 was investigated. With the aid of simulations, it was shown that the percentage of the R component in the spectrum decreased with increasing temperature, but even at the highest measured temperature of 190 K, remained dominant. The principal g-values of the A and R forms shifted as a function of temperature, with the most pronounced shift observed in g_x. The behaviour of the EPR spectra was found to deviate from a simple two-state model. We compared our findings and highlighted the differences with studies on other nitrosylated globins, especially hNgbNO mutants and AlMbNO. The origin of the A-form in GLB-33GDNO remains elusive, but is possibly linked to a more freely rotating NO ligand.

Chapter 6

Interaction of Nitrite with Ferric Protoglobin from *Methanosarcina acetivorans*

Part of this chapter was published in [309]:
R. Sgammato*, **N. Van Brempt***, Roy Aerts, S. Van Doorslaer, S. Dewilde, W. Herrebout, C. Johannessen, "Interaction of Nitrite with Ferric Protoglobin from Methanosarcina acetivorans – An Interesting Model for Spectroscopic Studies of the heme-Ligand Interaction."
*are joint first authors.

Own contribution:
UV-vis absorption and CW-EPR of *Ma*Pgb-ligand complexes and spin-trapping experiments. Data visualization and writing original draft.

6.1 Abstract

Pgb from *Ma* is a dimeric globin belonging to the same lineage of the globin superfamily as globin-coupled sensors. A putative role in the scavenging of reactive nitrogen and oxygen species has been suggested as a possible adaptation mechanism of the host organism to different gaseous environments in the course of evolution. A combination of optical absorption, ECD, rRaman, and EPR reveal the unusual in vitro reaction of ferric *Ma*Pgb with nitrite. In contrast to other globins, a large excess of nitrite did not induce the formation of a nitriglobin form in *Ma*Pgb. Surprisingly, the addition of nitrite in mildly acidic pH led to the formation of a stable nitric-oxide ligated ferric form of the protein (*Ma*Pgb-NO). Furthermore, the 300-700 nm ECD spectrum of ferric *Ma*Pgb is reported and discussed for the first time, showing strong differences in the Soret and Q ellipticity compared to ferric Mb, in line with the unusually strongly ruffled heme group of *Ma*Pgb and the related quantum-mechanical admixture of the $S = 5/2$ and $S = 3/2$ state of its ferric form. The Soret and Q ellipticity change strongly upon formation of *Ma*Pgb-NO, revealing a significant effect of the nitric-oxide ligation on the heme group and pocket. The related changes in the asymmetric pyrrole half-ring stretching vibration modes observed in the rRaman spectra give experimental support to earlier theoretical models, in which an important role of the in-plane breathing modes of the heme was predicted for the stabilization of the binding of diatomic gases to *Ma*Pgb.

6.2 Introduction

Pgbs, reviewed in Chapter 2, belong to the same lineage of the globin superfamily as GCSs and chimeric gene regulators comprising an N-terminal globin domain [310, 168, 169, 163]. The key-characteristics of *Ma*Pgb are the following: it has an expanded version of the 3/3 α-helical fold, consisting of nine α-helices Z, A, B, C, E, F, G, H, and a 20 AA long N-terminal extension almost completely burying the heme cofactor within the protein matrix (see Fig. 6.1). A system of two orthogonal apolar tunnels leads the exogenous ligands to the heme cavity. The heme of *Ma*Pgb is highly distorted, with the main out- and in-plane contributions to the heme distortion being the ruffling and breathing mode, respectively [172, 169]. It has been hypothesized that the combination of the above-mentioned modes has a sizable effect on the ligand binding [169, 170]. B9Trp and B10Tyr are H-bond donors in ligand stabilization and *Ma*Pgb has a distal E7Val, which is an unusual amino acid at that position compared to many other known globins that have a histidine on the 7th position of helix E (E7His). This residue is important during the ligand sensing, as it may trigger conformational changes at the heme pocket upon ligand binding. *Ma*Pgb therefore may exhibit a mechanism of ligand sensing based on the distal site adaptability [163, 176, 311, 174]. *Ma*Pgb is known to exist in a dimeric form in solution and in crystal form with the two subunits interacting mainly through the G- and H-helices [169, 176].

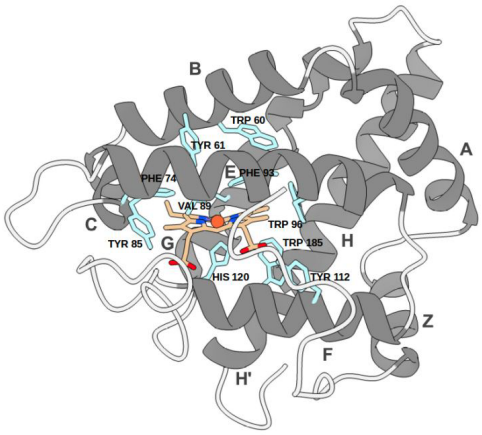

FIGURE 6.1: The figure shows one of the monomeric units of the dimer. The heme group has been shown in colour. The side chains constituting the heme pocket have been drawn in light blue. The corresponding letter labels have been added to the helices. The figures were created with the UCSF Chimera X program. For detailed visualization of the heme region, see Figure C.15 (ESI).

To date, the physiological role of *Ma*Pgb remains still unrevealed, with involvements in O_2 detoxification or CO sensor/supplier in methanogenesis being the most likely. Potentially, *Ma*Pgb can take up multiple functional roles: research carried out by Ascenzi *et al.* have underlined the possible involvement of *Ma*Pgb into the putative detoxification of RNS [164, 178].

Among the exogenous ligands of the heme moiety of human globins, nitrite has been attracting the attention of the pharmaceutical field in view of its ubiquitous involvement in many cellular, physiological and pathological processes [50]. Moreover, the nitrite anion is considered a viable source of NO and a precursor of RNS (see Chapter 1). During physiological and pathological hypoxia nitrite can be rapidly transformed into nitroso, nitrosyl heme species and NO, and it is therefore referred to as "hypoxic buffer", as it has the ability to generate RNS in an O_2-independent manner [240]. The transformation of nitrite into NO and other RNS, is widely known to involve either non-enzymatic pathways such as acidic reduction, but also xanthine oxidoreductase, Hb, Mb, Cgb and cytochrome *c* [312, 313]. The pH-dependent nitrite reductase activity of these proteins has important implications in the cellular homeostasis and nitrogen metabolism, since RNS are involved in, amongst others, the vasodilatation in vertebrates, cellular signalling and neurotransmission. Nitrite, nitrate, NO and NO_2 have also been shown to have an inhibitory effect on the methanogenesis of methanogenic bacteria [314]. Bacterial nitrite reductases, such as heme-containing enzymes, are known to play a role in the adaptation of bacteria to O_2 [241].

In line with the growing scientific interest in the nitrite metabolism of globins in general and with the recently hypothesized role of *Ma*Pgb as an RNS scavenger, this chapter focuses on the interaction of nitrite with ferric *Ma*Pgb in an acidic environment.

ECD and rRaman spectroscopies were used for the conformational analysis of *Ma*Pgb in aqueous solution in the absence and presence of nitrite. The data were complemented with an electron paramagnetic resonance (EPR) study. As shown in chapter 4, the combined use of ECD and rRaman spectroscopies represents a powerful tool for the investigation of heme-containing proteins, as these techniques display a selective sensitivity towards the heme moiety in its native protein environment (rRaman), and towards the optical activity of the heme chromophore (Visible ECD). The 532 nm laser excitation wavelength is in resonance with the Q electronic transitions of the heme group, enabling the selective targeting of the chromophore, as the protein backbone contributions are excluded from the rRaman spectrum. In the 260-700 nm spectral region of the visible Abs/ECD spectra the $\pi - \pi^*$ transitions of Fe(III) protoporphyrin IX (heme group) can be observed together with the charge transfer bands from the porphyrin to the iron. As a result, the combined ECD/rRaman approach provides an insight in the conformational change occurring upon binding of exogenous ligands to the heme protein in solution phase. To my knowledge, the visible ECD was used for the first time for the investigation of the ligand binding of ferric *Ma*Pgb. In turn, EPR has been shown to be an important analytical tool in globin research [96]. EPR allows monitoring the binding of nitrite to ferric *Ma*Pgb as well as monitoring the formation of NO from nitrite via spin trapping. Altogether, this combined spectroscopic approach provides insights in the interaction of nitrite with ferric *Ma*Pgb at both neutral and acidic pH, revealing large differences compared to other globins.

6.3 Material and methods

6.3.1 Over-expression and purification

The cDNA of full-length wild type (WT) *Ma*Pgb was cloned in a pET23a vector. The protein was then expressed in *E. coli* cells Bl21(DE3) pLysS and collected, as described previously in Chapter 2. For the first time the C-terminal His_6-tagged *Ma*Pgb (see appendix for sequence) was purified via affinity chromatography using 350 mM imidazole followed by dialysis to eliminate remaining imidazole from *Ma*Pgb against Trizma® hydrochloride buffer at pH 8.5 with 100 mM NaCl, at 4 °C. Without His-tag cleavage, *Ma*Pgb was further purified via size exclusion chromatography, using a Superdex^{200} ($10/300^{GL}$) column. The sample was finally checked for correct folding and purity via absorbance and ECD spectroscopy. *Ma*Pgb was stored at 4 °C in Trizma® hydrochloride buffer at pH 7.5 with 100 mM NaCl. When needed, the buffer was exchanged towards one at desired pH via Micro Bio-Spin® Chromatography columns P-6 (BioRad, Hercules, California, USA). The molecular weight of monomeric *Ma*Pgb (without His-tag) is 23.12 kDa. The corresponding calculated isoelectric point is low (pI = 5.07) [315]. Equine skeletal muscles Mb was purchased from Merck KGaA (Darmstadt, Germany).

6.3.2 Absorption and Electronic Circular Dichroism

The ECD setup, as described in Chapter 3, is used. The final spectra were subtracted by the spectra of the buffer used for the respective measurement for solvent correction (Trizma®) hydrochloride buffer for pH 7.5, or sodium acetate buffer for pH 5, in presence of 100 mM NaCl). The heme concentration of ferric *Ma*Pgb was estimated using the absorption at the Soret peak, and the extinction coefficient value of ferric *Ma*Pgb at pH 7 ($\epsilon(399\,\mathrm{nm}) = 138\,000\,\mathrm{M}^{-1}\,\mathrm{cm}^{-1}$) [164]. Measurements were performed in the spectral ranges 260-800 nm or 195-260 nm, respectively (3 sec / nm, 1 nm bandwidth). The kinetics data and NONOate-trapping data were recorded on a Varian Cary 5E UV-Vis-NIR spectrometer combined with 10 mm quartz cells (Hellma Analytics).

6.3.3 Resonance Raman spectroscopy

The rRaman setup, as described in Chapter 3, is used. 60 µL sample was centrifuged at 14 000 rpm for 5 min, at 4 °C prior each measurement, and then loaded into 3×4×10 mm quartz cuvette (Starna Scientific Ltd, Ilford, London, UK). The laser power was set to 0.3 W at the source, and the samples were illuminated in stretches of 2 seconds in order to prevent them from heating up. The total acquisition time varied depending on the sample stability. Raman spectra of the sample were subtracted by the respective solvent and subsequently baseline corrected according to the Eilers-Boelens procedure [316]. Matlab and Origin software were used for data processing and analysis. 0.057 mM Fe(III) *Ma*Pgb ($1.4\,\mathrm{mg\,ml}^{-1}$) was measured in free form at different pH values and in the presence of $NaNO_2$. For experiments with the isotopically labelled ligand $Na^{15}NO_2$ was purchased from Merck KGaA (Darmstadt, Germany), as was $NaNO_2$.

6.3.4 Electron Paramagnetic Resonance

All EPR simulations were done with the Easyspin Matlab toolbox [212].

Low temperature CW EPR

The EPR setup, as described in Chapter 3, is used. The X-band continuous-wave (CW) Electron Paramagnetic Resonance (EPR) experiments were recorded on a Bruker ESP300E spectrometer at T = 10 K with a microwave power of P_{mw}= 1.59 mW, a modulation amplitude of 0.5 mT and a modulation frequency of 100 kHz unless explicitly stated otherwise. 20-25 % (v/v) glycerol was added to all EPR samples recorded at low temperature to assure a homogeneous glass formation during flash freezing with liquid N_2. 100 µL was transferred to an EPR tube which was then repeatedly freeze-pump-thaw cycled to remove O_2 prior to the measurement. Over-expressed *Ma*Pgb was thawed and spun down to remove the denatured fraction and the brilliant red supernatant was diluted or concentrated using Millipore Microcon centrifugal filter units. The buffer was exchanged towards the one at desired pH via Micro Bio-Spin® Chromatography columns P-6 (BioRad, Hercules, California, USA). A protein concentration of 0.5 to 1 mM was used. $NaNO_2$ was added with molar ratios described in the figure captions or legend. Other protein-ligand complexes were prepared in the protein buffer at pH 7.5 using the

following molar ratios: a 400x molar excess [*Ma*Pgb]:[NO_2^-] complex, a 5x molar excess [*Ma*Pgb]:[imidazole] complex, a 100x molar excess [*Ma*Pgb]:[nicotineamide] complex and a 100x molar excess [*Ma*Pgb]:[azide] complex.

Spin-trap experiments

The X-band CW EPR experiments with 2-(4-trimethylammonio)phenyl-4,4,5,5-tetramethylimidazoline-1-oxyl 3-oxide (TMA-PTIO) were recorded on a Bruker Elexsys E580 EPR spectrometer (using a cylindrical cavity) at room temperature with a microwave power of 1.5 mW, a modulation amplitude of 0.1 mT and a modulation frequency of 100 kHz. Samples consisting of [NO_2^-]:[*Ma*Pgb]:[TMA-PTIO] with a 400:1:25 and a 100:1:25 molar ratio were prepared with 10 µM *Ma*Pgb in 0.1 N sodium acetate buffer pH 5. Negative controls were prepared without *Ma*Pgb and TMA-PTIO. Immediately after preparation, the time was recorded. The EPR samples were made by transferring the solutions to glass capillaries using a Hamilton syringe. The capillaries were quickly spun down, sealed with a gas burner and transferred to an EPR tube prior the measurement.

6.4 Results

6.4.1 Spectroscopic characterization of ferric *Ma*Pgb

Optical and vibrational spectroscopy

The UV-vis spectra of as purified Fe(III) *Ma*Pgb show the characteristic Soret band at 399 nm, and a Q-band at 506 nm with a small shoulder at 547 nm, and a charge transfer (CT) band at 640 nm associated with a CT transition from the porphyrin to iron [317, 161], which is in good agreement with the ferric Met*Ma*Pgb observed earlier [161] (Fig. 6.2 (A) and Tab. 6.1). Although these features were previously assigned to a high-spin (HS, $S = \frac{5}{2}$) ferric heme state [160, 161], this assignment is not fully correct. The Soret peak is considerably broader and blue-shifted and the CT band is red-shifted compared to what is normally associated with these HS ferric heme proteins, as can be seen from the comparison with the absorption spectrum of aquomet Mb (Fig. C.1). The bands are indicative of a quantum-mechanically mixed-spin heme species with pentacoordination of the heme iron (5c/QS) [318, 199, 319]. This state is an admixture of an intermediate ($S = \frac{3}{2}$) and high ($S = \frac{5}{2}$) spin state [199].

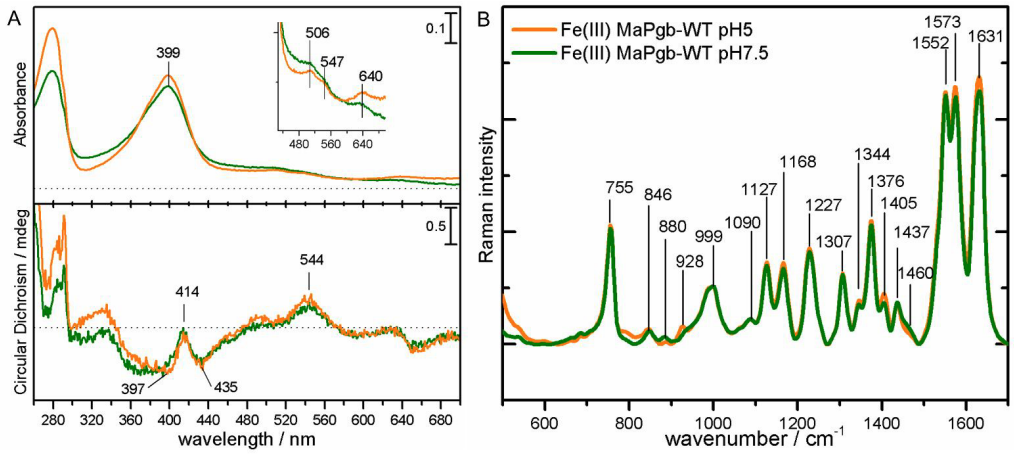

FIGURE 6.2: Ferric *Ma*Pgb (0.057 mM heme concentration) in Trizma® hydrochloride buffer (pH 7.5) or in sodium acetate buffer (pH 5). In Panel A: absorption (top) and ECD (bottom) spectra are presented. In Panel B the rRaman spectra of the corresponding samples are shown. rRaman spectra were normalized by the oxidation marker band ν_4 (1376 cm^{-1}).

	Absorbance [nm]				
	Soret	Q_β	Q_α	CT	Assignment
*Ma*Pgb(III)	399	506	547	638	5c/QS
*Ma*Pgb(III)-NO	425	538	570	none	6c/LS
	wavenumber [cm^{-1}]				
	ν_4	ν_3	ν_2	ν_{10}	Assignment
*Ma*Pgb(III)	1376	1460	1573	1631	5c/HS-QS
*Ma*Pgb(III)-NO	1376	1460/1506	1580	1631	6c/LS

TABLE 6.1: Main Abs and rRaman bands of various *Ma*Pgb complexes.

The rRaman marker bands ν_{10} at 1631 cm^{-1}, ν_2 at 1573 cm^{-1} and ν_4 at 1376 cm^{-1} (oxidation state marker) are in line with a 5c/QS heme state, although the shifts are also in the range of what is known for HS heme states (Fig. 6.2 (B), Tables 6.1 and C.1) [320, 321, 318]. Neither absorption/ECD nor rRaman spectroscopy highlighted major differences between the spectra of ferric *Ma*Pgb at the investigated pH values (Fig. 6.2), suggesting that the overall secondary structure of the protein was retained and that no heme loss occurred (Fig. C.2). Ferric *Ma*Pgb exhibited a very unusual ECD with respect to other globins, with a small Soret ellipticity close to zero at 414 nm, much less pronounced in comparison to the one of ferric Mb (Fig. C.1). The Soret ECD was characterized by a slightly asymmetric, negatively biased ellipticity having a minimum at 397 nm and a maximum at 414 nm, and also showed an additional minimum at 435 nm (Fig. 6.2 (A)).

The absorbance spectral region 250-350 nm is governed by overlapping bands arising from porphyrin ring $\pi - \pi^*$ and aromatic side chain excitations. The porphyrin $\pi - \pi^*$ bands are referred to as the L (250-300 nm) and N (300-350 nm) transitions [322]. Ferric *Ma*Pgb exhibits one prominent absorbance band centred at 280 nm, with a small shoulder at 291 nm, which is much larger than the corresponding signal for ferric Mb (Fig. C.1). This large difference can partially be explained considering the different aromatic composition of the globins. *Ma*Pgb comprises a number of aromatic amino-acid residues (17 Tyr, 5 Trp, 9 Phe) that is three times higher than the one of ferric equine skeletal muscle Mb (2 Tyr, 2 Trp, 7 Phe), resulting in higher absorption of the protein in the near-UV range. However, based on the amount of aromatic amino-acid residues the ratio of the absorbance at 399 nm versus 280 nm is expected to be higher than observed here for *Ma*Pgb. While a high absorbance at 280 nm may point to the presence of a significant amount of other proteins, this is excluded by SDS page and gel chromatography (not shown). More likely, a mixture of the apo and holoform of *Ma*Pgb is present. Upon lowering of the pH a small increase in the absorbance at 280 nm relative to the Soret peak is observed (Fig. 6.2 (A)), indicating that some further heme loss is induced by the pH change.

The ECD spectrum of ferric *Ma*Pgb substantially differs from that of ferric Mb in the region 260-350 nm. Instead of the ECD band having maxima at 274 nm and 290 nm, two minima were observed at the same wavelength in the spectrum of ferric *Ma*Pgb.

6.4.2 Reaction of nitrite with ferric *Ma*Pgb

Optical and vibrational spectroscopy

Different studies have shown that for many ferric globins, among which aquomet Mb, addition of excess nitrite at (mildly) acidic pH results in the greening of the protein, because of the formation of a nitrovinyl group on the heme pigment [323, 98, 99]. Here, ferric *Ma*Pgb was treated with a molar excess of nitrite at pH 5 (Fig. 6.3, Supplementary Table C.2). Upon addition of nitrite, a clear change in the absorption spectrum is observed at acidic pH (Fig. 6.3 (A)). During sample preparation, the samples incubated with the highest concentration of nitrite showed an immediate change in colour from red-brownish towards brilliant red, in line with a red shift of the Soret band of 26 nm. No visual greening of the heme pigment was observed. Upon addition of an increasing concentration of nitrite the Soret maximum shifts from 399 nm to 425 nm (Fig. 6.3, Panel A), with an isosbestic point at 405 nm. Furthermore, a clear splitting of the Q-bands was observed, with Q_β and Q_α bands detected at 538 nm and 570 nm, respectively, indicative of a full transition to a hexacoordinate low-spin (6c/LS) complex (see Fig. 6.3). Moreover, the decrease in the CT band of the QS form of *Ma*Pgb corroborates the transition to the LS form [317]. All the samples incubated with nitrite exhibited an additional broad absorption signal with maximum absorption at 366 nm, arising from free NO_2^- [324, 265]. None of the complexes exhibited the CT band, indicating that the LS form must be predominant in the sample mixture [317].

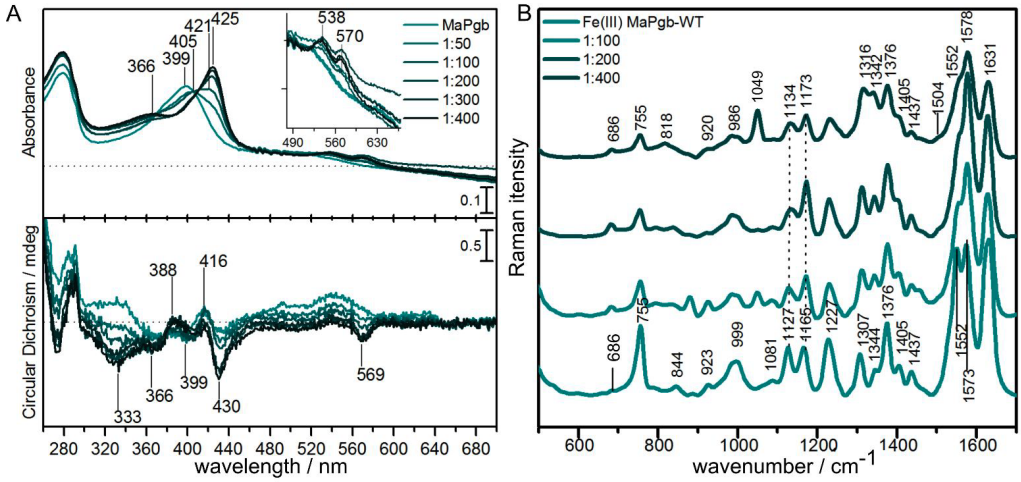

FIGURE 6.3: In Panel A: Abs (top) and ECD (bottom) spectra of ferric *Ma*Pgb (0.057 mM heme content) and its complexes with nitrite in sodium acetate buffer at pH 5. Ferric *Ma*Pgb (0.056 mM) was incubated with 50, 100, 200, 300 and 400 molar ratio excess nitrite, respectively. (For the far-UV spectra see Fig. C.5). In Panel B: the respective rRaman spectra are reported. The raw rRaman data showed a fluctuation of the baseline when comparing spectra of ferric *Ma*Pgb incubated with different amount of NO_2^-, probably due to difference in the fluorescence background (not shown). Hence, they were normalized by the oxidation-state marker band ν_4.

The conversion from a quantum-mechanically mixed state (QS) to LS ferric form of *Ma*Pgb at pH 5 was confirmed by the appearance of the rRaman marker band ν_3 at 1504 cm^{-1} and the oxidation state marker band ν_4 at 1376 cm^{-1}, typical for Fe(III)-6C/LS heme [325, 265](Fig. 6.3 (B))). The rRaman spectral pattern in the high-frequency region of ferric *Ma*Pgb treated with nitrite at acidic pH highly resembled the one of NO-NP1 [326, 327]. This strongly suggested the presence of nitric oxide as the sixth axial coordination ligand of the heme iron. The vibrational modes located in the low-wavenumber range (700-200 cm^{-1}) are characterised by lower Raman intensities than in the higher wavenumber range (Supplementary Fig. C.3) [328, 329, 330]. The rRaman bands located at 1168 cm^{-1} and 1127 cm^{-1} referred to as ν_{30} and ν_{14}, respectively, were assigned to asymmetric pyrrole half-ring stretching vibration, and their relative ratio seems to change in a ligand dependent manner. A change in the relative ratio between the rRaman intensities of ν_{30} and ν_{14} in favour of ν_{30} (Fig. 6.3 (B)) was observed after treatment of the globin with the nitrite [331]. A similar behaviour was also exhibited by the marker bands ν_2 and ν_{11} (1573 and 1552 cm^{-1}, respectively) in the high frequency spectral region, in favour of ν_{11} (Table C.1). The band at 1049 cm^{-1} might be due to NO_3^- present in solution [332], although this assignment needs to be taken with caution, since the laser excitation frequency is not in resonance with nitrite.

The absorption spectrum of ferric *Ma*Pgb treated with the highest concentration of nitrite, resembles the one of ferric *Ma*Pgb treated with spermine NONOate (diethylammonium (Z)-1-(N,N-diethylamino) diazen-1-ium-1,2–40 diolate) (Soret band at 425 nm

and Q bands at 570 and 538 nm), as can be seen in Fig. C.4. This supports that the spectral changes observed upon addition of nitrite to ferric *Ma*Pgb at acidic pH can be ascribed to formation of an Fe(III)-NO ligated state, instead of the nitrite-ligated ferric form.

This is further supported by low-temperature EPR spectroscopy (Fig. C.4): the addition of sodium nitrite to ferric *Ma*Pgb leads to a disappearance of the ECD signal of the ferric form, in line with the formation of the diamagnetic Fe(III)-NO species. Moreover, ECD does not show the presence of a ferrous nitrosylated species, indicating that no reductive nitrosylation takes place.

In the ECD spectra, the most notable changes upon addition of nitrite were observed in the 350-700 nm spectral region, where the sample exhibited almost exclusively negative ellipticity (Fig. 6.3). The Soret ECD band underwent a clear NO_2^--dependent modification with reduction in the negativity of the band at 399 nm together with its red shift; at the same time, the negative ECD band at 430 nm became dominant when the concentration of $NaNO_2$ was increased. In addition, a second negative ECD band at 569 nm became more pronounced having a minimum at 569 nm in correspondence of the Q_α absorption band (Fig. 6.3, Panel A). In the near-UV region, the absorption bands between 260-300 nm remained quite unperturbed, but the ECD band at 273 nm exhibited increased ellipticity. A major difference between the treated and untreated sample was observed in the range 300-375 nm, where a sign flip of the broad positive so-called "N" dichroic band (centred at 330 nm) occurred upon incubation with $NaNO_2$ [333]. For the protein incubated with the highest concentration of ligand, two distinct minima can be identified at 333 and 366 nm, together with a positive signal at 388 nm. Finally, the ECD spectra in the far UV (190-250 nm) prove that the addition of nitrite did not impact the overall folding of the protein (Appendix, Fig. C.5). Interestingly, nitrite addition to ferric Mb led to different absorption and ECD spectra than in the case of *Ma*Pgb (Fig. 6.4) [323]. A strong decrease and minor red shift of the Soret band to 411 nm was observed when the highest concentration of $NaNO_2$ was added to ferric Mb. Similarly, a strong decrease of the positive ellipticity is observed at 407 nm in the ECD spectra. Additionally, the Q_α and CT absorption bands were shifted to 566 nm and 615 nm, respectively [323].

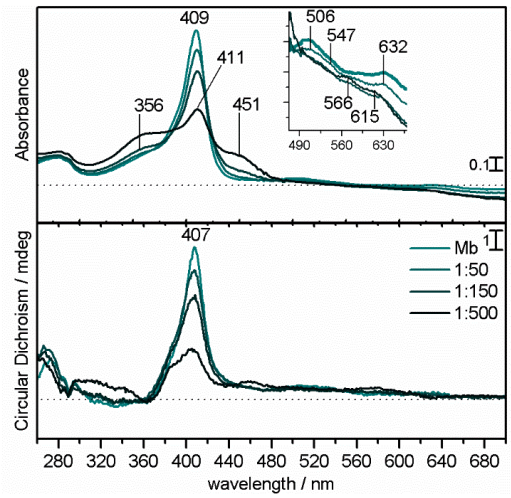

FIGURE 6.4: Abs (top) and ECD (bottom) spectra of 0.057 mM Mb and its complexes with nitrite in sodium acetate buffer at pH 5 were recorded in the range 260–700 nm. 0.057 mM Mb was incubated with 50, 150, and 500 molar ratio excess nitrite, respectively.

EPR spectroscopy

LS nitrite-bound heme proteins usually exhibit a large g-anisotropy with g_z-values around 3.0, but no such a contribution is detected in our case, neither at pH 5 nor pH 7.5 showing that nitrite does not coordinate the heme iron (Fig. C.4). Instead, an unknown g_z contribution with $g = 2.70$ is seen at pH 5 but due to low signal-to-noise ratio, a valuable simulation to extract the complete g-tensor is not possible. No signal of ferrous nitrosylated *Ma*Pgb is observed, confirming that NO binding to the ferric form is not succeeded by a further reductive nitrosylation step as is observed at pH 7 and higher [178].

6.4.3 NO binding to *Ma*Pgb

Since the formation of an Fe(III)-NO species upon addition of nitrite to a ferric heme protein may point to nitrite dismutase activity of the protein [327], additional experiments were performed. As pH increased, a lower amount of Fe(III)-NO species was observed, indicating the crucial role of the acidic condition (Fig. C.6). Furthermore, the conversion occurred both in aerobic and in anaerobic conditions (Fig. C.6). When a 400-fold excess of sodium nitrite was added to ferric *Ma*Pgb, an almost full conversion to the ferric *Ma*Pgb-NO form is observed as evidenced by a gradual Soret shift to 425 nm, together with the appearance of Q-bands at 538 and 572 nm (Fig. 6.5 (A)).

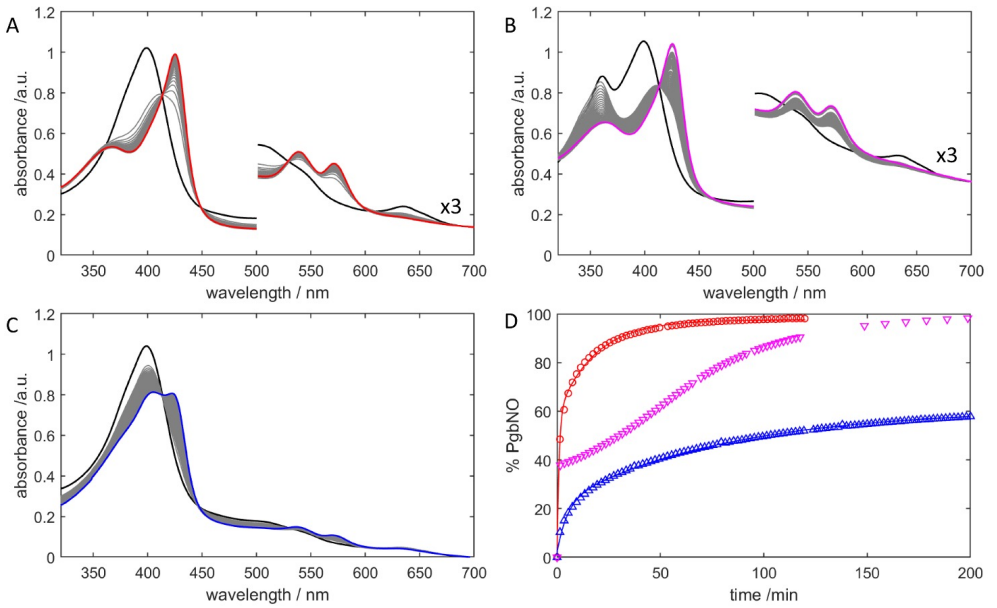

FIGURE 6.5: (A, B) Optical absorption spectra collected over time of *Ma*Pgb (10 µM heme concentration) reacted with 4 mM sodium nitrite in a sodium acetate buffer at pH 5 in absence (A) or presence (B) of 25 µM TMA-PTIO at 20 °C. The black trace shows the absorption spectrum before addition of nitrite, the red and magenta trace show the absorption spectra at the end of the time trace. (C) Optical absorption spectra collected over time of *Ma*Pgb (10 µM heme concentration) reacted with 1 mM sodium nitrite in a sodium acetate buffer at pH 5. (D) Time traces showing the percentage of the *Ma*PgbFe(III)-NO complex in time, derived from the absorbance at 425 nm (Soret maximum of the Fe(III)-NO complex). The traces correspond to the 3 cases shown in (A-C): (A) = red curve; (B) = magenta curve and (C) = blue curve. Solid lines show the simulation assuming a bi-exponential time dependence.

The time-dependent formation (%) of ferric *Ma*Pgb-NO can be derived from tracing the absorbance at 425 nm over time (Fig. 6.5 (D), red curve). The curve can be satisfactorily fitted by a bi-exponential time dependence with apparent fast and slow first-order rate constants k_f and k_s (Fig. 6.5 (D)).

$$\%PgbNO = C(1) - C(2)e^{-k_f t} - C(3)e^{-k_s t}. \tag{6.1}$$

The importance of the nitrite excess on the Fe(III)-NO formation was already highlighted in Fig. 6.3 (A). When only a 100-fold excess of sodium nitrite is added, only partial formation of the Fe(III)−NO complex is observed (Fig. 6.5 (C), Fig. 6.5 (D) blue curve), of which the apparent first-order rate constants are a factor 4-5 smaller than those observed for the 400-fold excess (Appendix, C.4). It is known that in acidic environment spontaneous formation of NO from nitrite can occur via a nitrite disproportionation reaction. In order to confirm this disproportionation reaction under the current experimental conditions, the NO scavenger TMA-PTIO was used. TMA-PTIO reacts with NO to form TMA-PTI and NO_2, whereby both TMA-PTIO and TMA-PTI can be detected by EPR

spectroscopy [334] (see Appendix, Figs. C.7-C.13). When sodium nitrite is added to a solution of 25 µM TMA-PTIO at pH 5, a complete conversion to TMA-PTI is observed, confirming that nitric oxide is spontaneously formed under these acidic circumstances (Fig. C.10).

Optical absorption spectra of the *Ma*Pgb-nitrite (1:400 molar ratio) mixture were then recorded as a function of time in the presence of 25 µM TMA-PTIO (Fig. 6.5 (B)). TMA-PTIO exhibits an absorption band at ∼350 nm. While there is a rapid initial formation of *Ma*Pgb-NO, similar to the fast phase observed without the presence of TMA-PTIO, the slow binding phase is hampered by the presence of TMA-PTIO and full conversion to the ferric *Ma*Pgb-NO form occurs only around 200 minutes after addition of nitrite (Fig. 6.5 (D), magenta curve). The corresponding time-dependent EPR analysis shows a trapping of NO by TMA-PTIO in the first ∼160 min (Fig. 6.6) and the corresponding second order reaction constant is similar to the one found when no protein is present (Fig. C.10 for model analysis). This indicates that TMA-PTIO competes with *Ma*Pgb in the trapping of NO and/or is capable of capturing *Ma*Pgb bound NO. Comparison of Fig. C.10 with Fig. 6.6 (B), shows that the stability of TMA-PTI is reduced in the presence of ferric *Ma*Pgb, but this seems to be an unspecific response, since this is also observed for similar experiments with ferric Mb (Fig. C.11). When 25 µM TMA-PTIO was added to a 1:100 mixture *Ma*Pgb:nitrite that was left to incubate overnight, a disappearance of the *Ma*Pgb-NO form with corresponding formation of ferric *Ma*Pgb was observed, revealing that TMA-PTIO can capture the *Ma*Pgb-bound NO (Fig. C.12). Moreover, when 1 mM sodium nitrite was added to 10 µM *Ma*Pgb in the presence of 25 µM TMA-PTIO, no ferric *Ma*Pgb-NO form could be determined with optical absorption spectroscopy, not even after longer times (Fig. C.13).

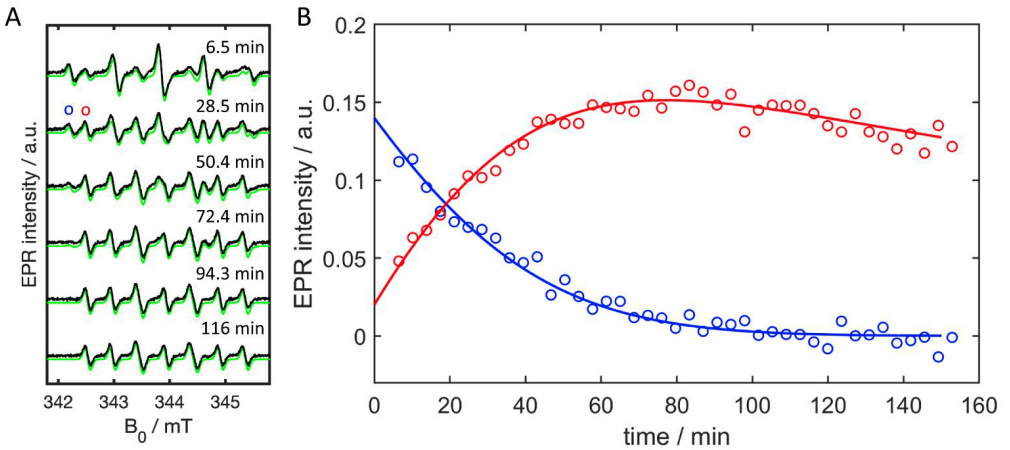

FIGURE 6.6: A: the room temperature X-band CW EPR spectra (black) and corresponding simulations (green) of 25 µM TMA-PTIO in the presence of 10 µM *Ma*Pgb collected over time after addition of 4 mM nitrite. Experiments were performed in sodium acetate buffer at pH 5. All spectra were collected with a microwave power $P = 1.5$ mW and a modulation amplitude of 0.1 mT. Each simulation consists of a linear combination of the spectra of pure TMA-PTIO and TMA-PTI, respectively (see Figs. C.7-C.9). B: time dependence of the experimental signal intensity of TMA-PTIO (represented by the peak maximum indicated by 'o' (blue circle) in the right spectrum) and TMA-PTI (represented by the peak maximum 'o' (red circle) in the right spectrum). The solid lines are simulations considering the model described in the Appendix C.

6.5 Discussion and conclusion

Ferric *Ma*Pgb has an unusual, strongly ruffled heme group [169]. Absorption spectroscopy (Fig. 6.2) strongly suggests that ferric *Ma*Pgb is in a quantum-mechanically mixed state (QS) with a pentacoordination (5c) of the heme iron. rRaman (Fig. 6.2) and EPR spectroscopy (Fig. C.4) corroborate this finding. While this state is found in peroxidases, it has, to my knowledge, not been reported in wild-type globins [199, 335]. Although it is yet unclear what causes the occurrence of this type of QS ferric states, two possible origins have been suggested, *i.e.* a weak ligand field [336] and saddle-shaped heme deformations [337]. The heme of *Ma*Pgb is much more ruffled and saddled than that of other globins [170]. As previously reported by some of my supervisors and others, these heme deformations have a marked influence on the electronic structure of ferric cyanide-ligated variants of ferric *Ma*Pgb [170]. Furthermore, the presence of a Val instead of a His on position E7 will strongly influence the ligand field. Interestingly, point mutation of the E7His in *Arabidopsis thaliana* Hb to a Leu induced a QS state in this non-symbiotic plant Hb. This suggests that besides the heme distortion, the presence of the E7Val may play a role in inducing the QS state in protoglobin [318]. As demonstrated in previous studies on *Ma*Pgb, the high ruffling and breathing distortions of the heme group have a biological relevance for the globin, linked to a very unusual modulation of the ligand binding mechanism [169, 177, 163, 171]. ECD is particularly suited to

study the heme group in an asymmetric environment. Although free heme in solution is not per se optically active (Appendix, Fig. C.14), when incorporated into the protein matrix, the heme electronic transitions in the range 260-700 nm become optically active [193, 190, 255, 192]. As illustrated in Figs. 6.2 and C.1, the ECD spectrum of ferric *Ma*Pgb yielded a quite unique pattern in that particular region, consisting of a negatively biased ellipticity having a minimum at 397 nm and a maximum at 414 nm and exhibiting an additional minimum at 435 nm. Furthermore, a positive ECD band was observed at 544 nm (Fig. 6.2). Moreover, the ECD spectrum of ferric *Ma*Pgb was very different from the one of ferric Mb (Fig. C.2). These spectral features indicate that there is a high non-planarity of the chromophore of ferric *Ma*Pgb in a unique way (Fig. C.15).

For a long time it has been thought that the Soret peak in the ECD spectrum would only arise from the coupling between the $\pi - \pi^*$ electronic dipole transitions of the porphyrin with those of the aromatic side chains surrounding the heme moiety [255, 338]. The number of aromatic side chains in the heme pocket of *Ma*Pgb is noticeably different from Mb (Fig. C.15), which also contributes to the deviation in ECD pattern between the two heme proteins. In addition, the interactions of the heme side chains (vinyl and propionic groups) with the distal amino acids also contributes to the heme optical activity, and as such yield a different magnitude and/or sign of the Soret ECD band [255, 192]. In the present case the magnitude of the Soret ellipticity of ferric *Ma*Pgb (Fig. 6.2) may indeed be influenced by the torsion of the heme side chains with respect to the heme plane (Fig. C.15), because of its high distortion from planarity [255, 192]. Furthermore, the mainly negative sign of the Soret ellipticity of *Ma*Pgb can reflect the low conjugation of the vinyl groups with the heme plane and/or the steric interaction of the propionate groups with the distal amino acids in the binding pocket. This can be observed in the visualizations in Fig. C.15: in the case of Mb the propionate side chains have the freedom to move around and can interact with three residue side chains, whereas the propionates of *Ma*Pgb are completely surrounded by five residue side chains, preventing conformational flexibility of the heme side chains.

After incubation with increasing concentrations of nitrite at pH 5 the absorption spectrum of ferric *Ma*Pgb showed marked spectral changes with isosbestic behaviour around 405 nm, until full conversion of the spectrum into a 6c/LS ferric form. The absorbance spectrum is identical to the one obtained after treatment of ferric *Ma*Pgb with NONOate (Fig. 6.7), indicating that an exclusive NO-Fe(III) heme complex is formed, instead of distal nitrite ligation of the heme iron. This is confirmed by the disappearance of the EPR signal upon treatment of ferric *Ma*Pgb with nitrite (Fig. C.4). This is further corroborated by the similarities with the UV-Vis absorption spectra of NPs exhibiting the same ligation mode [327, 107, 339]. Ferric *Ma*Pgb was earlier shown to easily bind NO at neutral to alkaline pH with a subsequent reduction of the heme iron and formation of ferrous *Ma*Pgb-NO [178]. This reductive nitrosylation requires the presence of OH-, explaining why this follow-up step is not observed in the present study (too low pH). Although the observation of *Ma*Pgb-NO formation after addition of nitrite to ferric *Ma*Pgb may point to nitrite dismutase activity of the protein as observed for NP [327, 107, 339, 340], some observations indicate that this may not be biologically relevant and even argue against such dismutase activity for *Ma*Pgb. First of all, the formation

of the *Ma*Pgb-NO form upon addition of nitrite is only observed in acidic conditions, contrasting the observations for NPs where the effect was already clear at pH 7.5 [327]. Nitric oxide is formed in a spontaneous disproportionation reaction of nitrite at acidic pH [341], as is confirmed under the current experimental conditions by spin-trapping EPR (Fig. C.10). At least part of the observed *Ma*Pgb-NO formation at low pH will thus be due to simple trapping of NO by ferric *Ma*Pgb, as has been described before at higher pH [178]. Contrary to the observations for NPs [339, 340], addition of nitrite to *Ma*Pgb does not lead to the observation of a nitrite-ligated *Ma*Pgb form in EPR at low temperature (Fig. C.4). Instead, the disappearance of the EPR signal supports the sole formation of the EPR-silent ferric *Ma*Pgb-NO complex. Moreover, the apparent fast and slow first-order rate constants k_f and k_s, describing the time-dependent build-up of the ferric nitrosylated heme form, seem to depend more or less linearly on the nitrite concentration (Table C.4). The nitrite dismutase reaction by NPs involves a general disproportionation reaction [327] $3\,NO_2^- + 2\,H^+ \longrightarrow 2\,NO + NO_3^- + H_2O$, proceeding via two sequential steps, whereby the first step is rate limiting and involves the binding of two nitrite ions, which would lead to a second-order dependence on $[NO_2^-]$ [339]. Although our current data are limited, this is not confirmed for *Ma*Pgb. Furthermore, the experimental dependence of the relative ratio [*Ma*PgbNO]/[*Ma*Pgb] on the nitrite concentration (Fig. 6.3(A)) indicates the binding of only one ligand and seems to be more in line with a simple NO-trapping reaction (Fig. C.16). The formation of *Ma*Pgb-NO can be described by a biexponential behavior (Fig. 6.5 (A); Fig. 6.5 (D), red curve). Different explanations can be given for such a bi-exponential time dependence. It may result from a step-wise NO-trapping mechanism with a fast trapping step to form *Ma*PgbNO and a slower rearrangement step to a second form, *Ma*PgbNO*, in which NO is stabilized differently in the heme pocket, as has been described for NO trapping in NPs [342]. On the other hand, two orthogonal apolar tunnels that guide diatomic ligands to the heme cavity, have been identified in *Ma*Pgb [169]. Potentially these two entrance routes may explain a biexponential binding behavior for ligands, although additional experiments using variants of *Ma*Pgb are needed to substantiate this assumption and to understand any relevant interplay between the two pathways. Alternatively, the observation of a bi-exponential behavior may result from the mixture of a direct NO-trapping reaction (fast phase) and a nitrite dismutase effect (slow phase). The assignment of the fast kinetics to the direct NO-trapping mechanism is based on the very fast NO-binding kinetics observed for ferric *Ma*Pgb at neutral and alkaline pH 14, while the nitrite dismutase in NPs is reported to be markedly slower [327], more in line with the slow phase kinetics observed here. However, the dependence on the nitrite concentration does not support a similar dismutase mechanism (if any) as in NPs (see above). Finally, the presence of mixed holo/apo dimers may also influence the results.

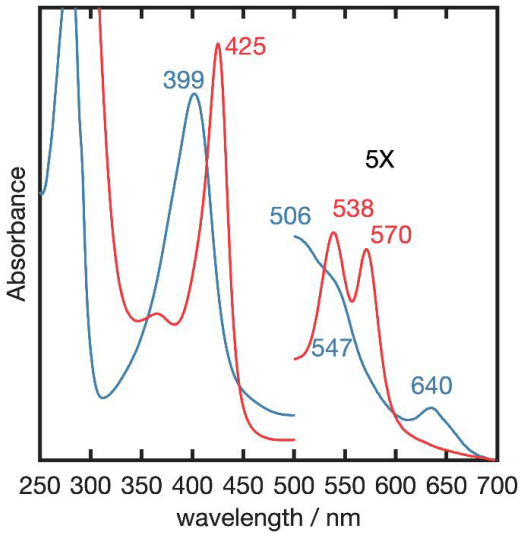

FIGURE 6.7: Absorption spectrum of ferric *Ma*Pgb (10 µM heme concentration) in unbound form (blue) and after incubation with 4 mM spermine NONOate in a Trizma® hydrochloride buffer at pH 7.5 (red).

The presence of TMA-PTIO in the *Ma*Pgb:NO_2^-(1:400) mixture seems to effect mostly the kinetics of the slow phase (Fig. 6.5 (D), magenta curve), but this is merely due to the fact that TMA-PTIO traps NO at a slower rate than the fast NO-trapping phase of *Ma*Pgb (compare k_s and k_f (Table C.4) with the apparent first-order NO-trapping constant of TMA-PTIO ($\sim$2.4 $10^{-4}s^{-1}$)). While NO-binding to the heme protein is reversible, the reaction of TMA-PTIO with NO is not, so its effect will be felt until all TMA-PTIO has been converted to TMA-PTI (after $\sim$160 minutes under the given conditions), both by direct trapping of NO from the solution or by depleting *Ma*PgbNO. The likelihood of the latter reaction has been confirmed here (Fig. C.12). When the concentration of nitrite (and hence NO) is lower, TMA-PTIO is effectively depleting all NO from *Ma*Pgb and no evidence of *Ma*PgbNO formation is observed, not even after long reaction time (Fig. C.13). This is in line with the lower values of k_s and k_f at lower nitrite concentration (Table C.3) and the lower amount of NO. The reaction of TMA-PTIO with NO remains the same in the presence of *Ma*Pgb (Fig. 6.6) or Mb (Fig. C.11) as in the absence of a heme protein (Fig. C.10) and giving no indication of dismutase activity. Interestingly, ferric Mb is not trapping NO under similar nitrite treatment (Fig. 6.4). Instead, the changes in the absorption spectra of ferric Mb in the presence of a large excess of nitrite agree with the formation of nitriMb. This effect has been reported for Mb and other globins and results from the reaction of an NO_2 radical with the heme vinyl groups and corresponding formation of a nitrovinyl group [99]. The fact that ferric *Ma*Pgb resists nitration of the heme and that it selectively binds NO molecules in the presence of a large excess of nitrite anions is remarkable, more so, because the acidic disproportionation reaction of nitrite also generates NO_2 next to NO, in the following way [343]:

$$
\begin{aligned}
NO_2^- + H^+ &\longrightarrow HNO_2 \\
2\,HNO_2 &\longrightarrow N_2O_3 + H_2O \\
N_2O_3 &\longrightarrow NO + NO_2
\end{aligned}
$$

As there is no spectroscopic evidence for NO_2 binding by ferric *Ma*Pgb, it appears that NO_2 is not entering the heme cavity. The resilience of the protoglobin against nitriglobin formation supports earlier suggestions that protoglobin is involved in RNS detoxification [178, 164]. It is surprising that ferric *Ma*Pgb, in contrast to other ferric globins [89], is not binding nitrite, while its ferrous form shows substantial nitrite reductase activity [178, 164].

Regarding the preferential binding of NO, the analysis of the rRaman spectra is interesting (Fig. 6.3). These spectra also reflected the change in the ligation state of ferric *Ma*Pgb after incubation with nitrite at acidic pH: (i) the appearance of the band ν_3 at $1504\,cm^{-1}$ in combination with the retention of ν_4 at $1376\,cm^{-1}$ (indicative of 6c/LS ferric state) and (ii) the variation in the relative ratio of the bands ν_2 and ν_{11}, as well as ν_{30} and ν_{14}, in a ligand concentration dependent manner. These findings confirmed the presence of an exogenous ligand coordinating the iron at the distal site of the heme pocket in line with the NO ligation. The variation in ratio between the rRaman bands ν_{30} and ν_{14}, assigned to the asymmetric pyrrole half-ring stretching vibration [331] (Fig. 6.3) reflects the compression of the heme moiety due to the breathing mode of the chromophore. Interestingly, quantum-chemical calculations already predicted a crucial effect of the in-plane breathing mode on the ligand binding affinity for the case of dioxygen coordinating to ferrous *Ma*Pgb [172]. The heme compression was predicted to be key in the stabilisation of ligand binding, overcoming the destabilization due to ruffling. The variation in the pyrrole stretching vibration as a consequence of ligation of NO thus reflects the mechanism in which *Ma*Pgb stabilises the exogenous ligand at the sixth axial position of the heme iron and underlines the importance of the in-plane breathing mode of the heme in this process. It may be key in the unique behaviour of ferric *Ma*Pgb in the presence of nitrite and NO.

Upon incubation of *Ma*Pgb with nitrite at pH 5, the ECD spectra indicated a gradual evolution of the Soret ellipticity, in concert with the changes in the iron-ligand interaction. In particular, the negative ECD band at 430 nm became dominant and the second negative ECD band at 569 nm became more pronounced when the globin was incubated with higher concentrations of $NaNO_2$ (Fig. 6.3). Unfortunately, the specific structural changes in the heme pocket and the exact origin of the observed ellipticities cannot be directly extracted from empirical data, nor are there standard ECD calculation procedures available that can. However, the analysis of the crystal structures of ferric *Ma*Pgb ligated with cyanide, azide, imidazole, and nicotinamide can aid [177]. This variety of ligands can be bound due to the conformational adaptability of the distal amino-acid side chains and the size and hydrophobicity of the heme distal cavity. In fact, when binding cyanide, azide and imidazole, the side chain of B9Trp(60), B10Tyr(61), and E11Phe(93) (Fig. C.15) rearrange themselves, allowing the former two to form hydrogen bonds with the ligand. We expect a similar conformational rearrangement and ligand stabilization

of the mentioned aromatic side chain residues to take place upon the coordination of NO. Therefore, by comparing the ligand-free and bound ECD spectra (Fig. 6.3), the relative contribution of the change in orientation of these three distal aromatic side chains and the effects of the heme compression upon NO binding to the ECD spectral region 260-700 nm can be observed. The three aromatic side chains of B9Trp(60), B10Tyr(61), and E11Phe(93) reorient themselves with respect to the heme plane, inducing a more negative Soret band at 430 nm – here together with the heme compression upon NO binding – and a sign flip of the N dichroic band at ∼330 nm.

6.6 Conclusions

*Ma*Pgb, and its treatment with nitrite have been extensively studied using optical absorption, electronic circular dichroism (ECD), resonance Raman (rRaman), and electron paramagnetic resonance (EPR). Ferric *Ma*Pgb has been found to be in a quantum-mechanically mixed state (QS; S=3/2 and S=5/2) with a pentacoordination (5c) of the heme iron, something that has only been observed for peroxidases as of yet. In contrast with what is typically observed for globins, nitrite addition to ferric *Ma*Pgb at acidic pH does not lead to formation of nitriglobin. This resilience of the protein may be related to its suggested role in the RNS detoxification process. Moreover, unlike what is found for other globins, it is NO formed during the acidic disproportionation reaction of nitrite, and not nitrite itself, that is stably bound by ferric *Ma*Pgb.

Chapter 7

The enzymatic activity of GLB-3, a bis-histidyl cysteine-rich globin found in the nematode *Caenorhabditis elegans*

Redrafted after [237]:
Z. Hafideddine, T. Loier, **N. Van Brempt**, S. De Henau, H. Y. V. Ching, S. Neukermans, S. Defossé, H. Berghmans, R. Sgammato, R. Aerts, D. Hammerschmid, R. Moons, T. Breugelmans, F. Sobott, C. Johannessen, W. Herrebout, B.P. Braeckman, L. Moens, S. Dewilde and S. Van Doorslaer, "GLB-3: A resilient, cysteine-rich, membrane-tethered globin expressed in the reproductive and nervous system of *Caenorhabditis elegans*".

Own contribution

Design, cloning, over-expression and purification GLB-3 isoforms HisE7Ala (HE7A) mutants, over-expression and purification GLB-3 isoforms WT, UV-vis absorption experiments with different ligands, simulations on the CW-EPR (measured by dr. Z. Hafideddine) and both measurement and simulation on the mutant. Flash photolysis experiments on the HE7A mutants (mainly analysis) and finally, development of a potentiometric titration setup.

7.1 Abstract

The popular genetic model organism *Ce* encodes 34 gbs, whereby the few that are well-characterized show divergent properties besides the typical oxygen carrier function. GLB-3 is predicted to exist in two isoforms and is expressed in the reproductive and nervous system. Knockout of this globin causes a 99% reduction in fertility and reduced motility. Spectroscopic analysis reveals that GLB-3 exists as a bis-histidyl-ligated LS form in both the ferrous and ferric heme form. A function in binding of diatomic gases is excluded on the basis of the slow CO-binding kinetics. Unlike other gbs, GLB-3 is also not capable of reacting with H_2O_2, H_2S, and nitrite. Intriguingly, not only does GLB-3 contain a high number of cysteine residues, it is also highly stable under harsh conditions (pH = 2 and high concentrations of H_2O_2). The resilience diminishes when the N- and C-terminal extensions are removed. Redox potentiometric measurements reveal a slightly positive redox potential ($+8 \pm 19$ mV vs. SHE), suggesting that the heme iron may be able to oxidize cysteines. EPR shows that formation of an intramolecular disulphide bridge, involving Cys70, affects the heme-pocket region. The results suggest an involvement of the globin in (cysteine) redox chemistry.

7.2 Introduction

From the introductory Chapter 1 of this thesis we know that the central heme-b iron (Fe(III)/Fe(II)) in gbs is coordinated to an N atom from a His residue (helix F, position 8, HisF8) at the proximal side of the heme, four pyrrole Ns from the heme, and the sixth coordination site at the distal side is either occupied by a ligand or an endogenous amino acid (mostly helix E, position 7 or 11). For the well-known Mb and Hb, the sixth site remains open (pentacoordination) when ferrous, readily available for ligands such as O_2 to bind, but for other well-characterized gbs such as vertebrate Ngb, Cgb and many others such as the nonsymbiotic plant Hbs (nsHbs), insect Hbs, nematode gbs, and some bacterial truncated Hbs, a proximal E7His occupies this vacant site (so-called bis-histidine coordination or short, bis-His) [344, 299, 345, 94, 346, 347, 348, 115, 349]. This structural organization has raised many questions regarding the functional role of these gbs.

The reversible bis-histidyl coordination of the heme iron retains the ability to bind exogenous ligands such as O_2, CO, and NO [350]. More often, low effective binding affinities for exogenous ligands are reported, so other functions are proposed for bis-His coordinated heme proteins, such as involvement in redox transfer processes, such as NiR [351, 352, 353]. In some cases, the bis-His coordination is very strong, which suggests potential functions in electron transport, rather than O_2 transport/storage, NO scavenging, and substrate reduction or oxidation [354, 116]. Moreover, bis-His coordinated gbs show generally high reduction kinetics [351], *i.e.* they are more rapidly reduced by $SO_2{}^-$ than pentacoordinated globins, for example, which further suggests that this structural organization might facilitate electron transfer.

Out of the 34 distinct gbs in the nematode, only seven *Ce* gbs are characterized to some extent, out of which, GLB-6, GLB-12, GLB-26 are characterized *in vitro* as bis-histidyl gbs [148, 119, 114]. Based on sequence alignments, it is very likely that other, lesser-studied *Ce* gbs have the same coordination state, such as the Ngb ortholog GLB-13 [149]. Vertebrate Ngb is expressed in tissues such as the nervous system and neuronal cells, and is thought to play a neuroprotective role [355]. Given the predominant neuronal expression of the gbs in *Ce*, it is likely that they carry a signaling or redox function or similar role [117, 119].

A few *Ce* gbs are proposed to be membrane bound since they are myristoylated and/or palmitoylated. One such example, GLB-12, was shown to be anchored to the plasma membrane in the neurons and somatic gonad [119]. Also the full-length chimeric GLB-33, of which the GD was extensively studied in previous chapters, has a palmitoylation site, and is shown to be membrane anchored [118]. Although membrane association of globins has been reported in other species [356, 357, 358, 31], it is still a poorly defined attribute of globins.

In contrast to the other chapters, I will not present the full collaborative work on GLB-3, as it has already been presented elsewhere (see doctoral thesis of Zainab Hafideddine and [237]). Instead, in this chapter, I will mainly present my personal contributions that (partially) contributed to the published biophysical characterization and expression analysis of *Ce* globin-3 (GLB-3). Moreover, pitfalls encountered in the process, especially regarding flash-photolysis and redox titration experiments, are discussed. The biochemical and spectroscopic analyses were performed to explore the working mechanism of GLB-3 in *Ce*. Both GLB-3 isoforms showed similarities with other bis-His ligated gbs. The peroxidase activity, NiR activity, and hydrogen sulfide binding of both GLB-3 isoforms were tested. Furthermore, the redox properties of GLB-3 were explored. Finally, the effect of the distal E7His was examined by the HE7A point mutation, and the spectroscopic properties of this GLB-3 HE7A mutant were evaluated.

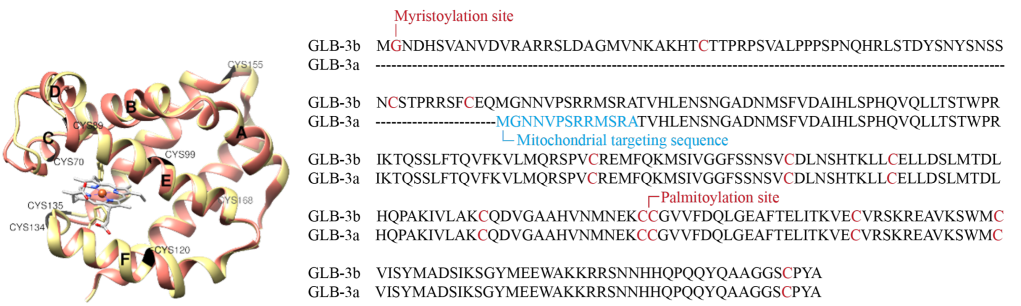

(A) (B)

FIGURE 7.1: (A): Superimposition of GLB-3a (yellow) and hNgb (PDB:1OJ6) (pink) with the heme cofactor. The cysteine residues of GLB-3a are highlighted in black and the helices are illustrated with the corresponding letter (from A to H). (B): Full protein sequence alignment of the isoforms GLB-3b and GLB-3a. The predicted myristoylation and palmitoylation sites are highlighted in red, and the putative MTS cleavage site in GLB-3a is marked in blue. The cysteine residues in both isoforms are highlighted in red.

7.3 Materials and methods

7.3.1 Cloning, expressing and purification

The pET23a expression vector harboring the glb-3a gene (analogue for glb-3b) was transformed into *Escherichia coli* (*E. coli*) strain BL21(DE3)pLysS (Invitrogen). The expression was done analogously as described elsewhere [237, 299]. Alternatively, 10 mM of Dithiothreitol (DTT) was added to the protein solution after nickel chromatography for protein stabilization (not for experiments requiring absence of DTT). GLB-3 was concentrated by means of a stirred 1 Cell (Millipore, 10 kDa cut-off) under air pressure and loaded onto a pre-equilibrated (50 mM Tris-HCl pH 7.5, 500 mM NaCl) PD-10 desalting column (GE Healthcare). The proteins were loaded on an equilibrated (50 mM Tris-HCl pH 7.5, 150 mM NaCl) HiTrap SP FF and eluted (50 mM Tris-HCl, 1 M NaCl). Purified protein fractions were collected and exchanged (50 mM Tris-HCl pH 7.5, 500 mM NaCl, ± 10 mM DTT). The purified protein sample was then concentrated and stored at −80 °C. The purity of the recombinantly expressed protein was analyzed by 12.5 % SDS-PAGE and to be >90 %. The HE7A mutants were obtained using the QuickChange^{TM} site-directed mutagenesis kit (Stratagene) with forward primer 5‘-GT GAT CTC AAT TCG GCT ACG AAA TTG CTC TGC -3’ and reverse complement primer 5‘-GCA GAG CAA TTT CGT AGC CGA ATT GAG ATC AC-3’. the cDNAs were subsequently cloned, expressed and purified as described above.

7.3.2 UV-Vis absorption spectroscopy

The UV-Vis absorption spectra of Fe(III), ferrous and CO-ligated ferrous GLB-3 isoforms were measured in the 250-700 nm range using a T85 double beam UV-Vis spectrophotometer or a Cary-5E UV/Vis/NIR spectrophotometer (Agilent). GLB-3a and GLB-3b were in the ferric form after protein purification. The reduced deoxy (Fe(II)) and CO-ligated ferrous form of both isoforms were prepared by flushing 1 ml of buffer solution (50 mM Tris-HCl pH 7.5, 500 NaCl with or without DTT) in a sealed quartz cuvette for 15 minutes with N_2 and CO gas, respectively. Subsequently, 10 µL of a saturated sodium dithionite solution and a highly concentrated purified protein solution were added using an airtight Hamilton syringe. The globin concentration was estimated using the absorption at the Soret peak, and the extinction coefficient value of human Ngb at 413 nm 122 000 $M^{-1}\,cm^{-1}$ [359]. The spectra were subtracted by the spectra of the buffer solutions. The oxy-form of the protein could neither be obtained by exposing the deoxygenated ferrous form of the globin to air nor by the method proposed by Hayashi *et al.* [360] due to the fast auto-oxidation. Various ligands that are known to interact with gbs including $NaNO_2$, Na_2S and H_2O_2, and stock solutions thereof were prepared and diluted in 50 mM Tris-HCl pH 7.5 + 500 mM NaCl and added to the protein solutions in the same buffer were added to the ferric form of the wild-type (WT) GLB-3ab isoforms and the HE7A mutants.

7.3.3 Flash photolysis

Different CO concentrations (200-800 µM) were obtained by equilibrating the buffer solution with a mixture of CO and N_2 in different ratios by means of a High-Tech gas mixer (Bronkhorst) (100 % CO equals 1000 µM CO). Next, 10 µL of a saturated sodium dithionite solution was added and a concentrated protein solution was injected to a final concentration of 5 µM. CO rebinding kinetics measurements were monitored at 414 nm and carried out on a laser flash photolysis spectrophotometer (Edinburg Instruments LP920) at 20 °C. This system is equipped with a Q-switched, frequency-doubled Nd:YAG laser (Spectra Physics Quanta-Ray) at 532 nm. CO photolysis was achieved by a short laser pulse (5-8 ns) and recombination reactions were monitored at 414 nm for different time scales (from 2000 ns till 100 ms). The obtained kinetics curve per CO concentration is averaged for 20 measurements. MATLAB R2019b (MathWorks) was used to link the exponential decays of the different time scales together to obtain the final kinetics curve. CO association was measured by photo-dissociating CO-ligated GLB-3 HE7A GD by a short laser pulse (5–8 ns) and then following the recombination of the photo-dissociated CO ligand at different time scales, ranging from 2000 ns for the geminate recombination of CO to 100 ms for the bimolecular rebinding of the ligand at 414 nm. Exponential decays from the consecutive time scales were joined together to give the complete ligand-rebinding curve. The rate of geminate rebinding (k_{gem}) was obtained by fitting a single exponential curve through the data points collected in the first 2000 ns after photodissociation according to

$$\Delta\mathrm{OD}_t = \Delta\mathrm{OD}_{\mathrm{gem}} \exp(-k_{\mathrm{gem}} t) + \Delta\mathrm{OD}_{\mathrm{obs}}. \tag{7.1}$$

After logarithmic re-sampling of the data points, pseudo first-order fast observed rebinding rate constants ($k_{\mathrm{obs},f}$) and slowly observed rebinding rate constants ($k_{\mathrm{obs},s}$) were determined by least square fitting of the decays with the following bi-exponential

$$\Delta\mathrm{OD}_{\mathrm{obs}} = \Delta\mathrm{OD}_f \exp\left(-k_{\mathrm{obs},f} t\right) + \Delta\mathrm{OD}_s \exp(-k_{\mathrm{obs},s} t). \tag{7.2}$$

Fast and slow CO-rebinding association rate constants ($k_{\mathrm{on},f}$ and $k_{\mathrm{on},s}$, respectively) were calculated from the dependence of $k_{\mathrm{obs},f}$ and $k_{\mathrm{obs},s}$ on the CO concentration according to Eq. 7.3 and Eq. 7.4 [361].

$$k_{obs,f} = k_{\mathrm{on},f}[CO] + k_{\mathrm{off},f} \tag{7.3}$$

$$k_{obs,s} = k_{\mathrm{on},s}[CO] + k_{\mathrm{off,s}} \tag{7.4}$$

7.3.4 Stopped flow experments

Stopped-flow or rapid mixing experiments were performed in 50 mM Tris-HCl pH 7.5 + 500 mM NaCl with or without the addition of DTT in the protein solution. The buffer solution is flushed with N_2 and 11.5 mM of sodium dithionite is added. One syringe was filled with this buffer solution and equilibrated with CO, while the second syringe contained a protein solution of 10 µM and 10 µl of a saturated sodium dithionite solution. Solutions were rapidly mixed obtaining final CO concentrations ranging between

100-1000 µM. All measurements were conducted at 20 °C and 1 atm using a thermostated stopped-flow apparatus (Applied Photophysics) at 418 nm. Origin (OriginLab Corporation) was used for further data analysis.

7.3.5 Electron paramagnetic Resonance

X-band CW EPR measurements were conducted on a Bruker ESP300E spectrometer with a microwave frequency of ∼9.44 GHz. The spectrometer is equipped with a liquid helium cryostat (Oxford Inc.), allowing operation from room temperature down to 2.5 K. All EPR spectra were recorded at 10 K with a modulation amplitude of 0.5 mT, modulation frequency of 100 kHz and microwave power of 3 mW. Furthermore, all samples were deoxygenated via a sequential freeze-pump-thaw cycle prior to the EPR measurements and were continuously pumped during the experiment to avoid a background signal from frozen dioxygen $^3O_2$. Both GLB-3 isoforms were measured in 50 mM Tris-HCl (pH 7.5), 500 mM NaCl with or without DTT. GLB-3a HE7A was measured in absence of DTT. All EPR spectra are simulated using Easyspin (version 5.2.28), a MATLAB® (r2020a) (MathWorks)-based simulation toolbox [212].

7.3.6 Potentiometric titrations

Potentiometric redox titrations were performed following the procedure in [299] and [293]. A schematic diagram of the experimental setup used for the determination of the redox potential is given in Fig. 7.2.

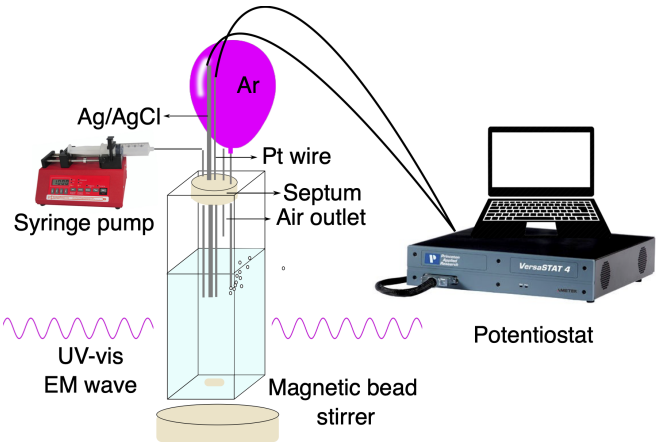

FIGURE 7.2: Schematic diagram of the experimental setup used for the determination of the redox potential measurements. A sealed cuvette is fitted with a Ag/AgCl and Pt reference electrode pair. The cuvette is kept under Ar atomsphere via a balloon filled with Ar using a needle. The sample is stirred after titration with a dithionite solution with a syringe pump prior to UV-vis measurements in order to obtain a homogeneous solution.

Diaminodurene (E_m =275 mV), trimethylhydroquinone (E_m =115 mV), phenazine methosulfate (E_m = 85 mV), phenazine ethosulfate (E_m = 65 mV), 2-methyl-1,4-naphthoquinone

($E_m = 10\,\text{mV}$), tetramethyl- p-benzoquinone (Duroquinone) ($E_m = 5\,\text{mV}$), indigo tetrasulfonate ($E_m = -46\,\text{mV}$) 2-hydroxy-1,4-naphthoquinone ($E_m = -137\,\text{mV}$), anthraquinone-2,6-sulfonate ($E_m = -184\,\text{mV}$) and riboflavin-5'-monophosphate ($E_m = -219\,\text{mV}$) were used as redox mediators at concentrations between 1 and 5 µM. Ferric GLB-3a or hNgb (with final concentration of $\sim 10\,\mu\text{M}$) were added to the Ar-purged mediator mixture in 100 mM sodium phosphate buffer (pH 7.0) inside disposable Polystyrene UV-Vis cuvettes (BRAND®). The mediators act as a redox buffer and equilibrate the potential between the protein and the electrodes. The cuvette was sealed by a septum and kept under Ar atmosphere using an Ar gas-filled balloon during the experiments. A Hamilton syringe attached to SyringeONE Programmable Syringe Pump (New Era Instruments) was used for microliter titrations of dithionite solutions. The potentiometric titration was executed in the UV-Vis cuvette serving as an undivided three-electrode electrochemical cell. A PFA insulated Pt wire of 200 µM diameter (Science Products) counter electrode and saturated Ag/AgCl reference electrode was used. The PFA coating was stripped at the edges to expose Pt to the solution and to allow connection to a VersaSTAT potentiostat (Ametek) running on VersaStudio 2.60.6. A leak-free reference electrode (W3 69-00) was used (Harvard Apparatus). The three electrodes were positioned at 1 mm of each other to avoid the contribution of solvent resistance to the cell potential. The open circuit potential of the cell was monitored during the titration.

After each titration, the sample was stirred using a magnetic bead which is placed inside the cuvette. Spectrophotometric measurements were taken after a stabilization of the potential (± 1 min afterwards) at 25 °C on a Cary-5E UV/Vis/NIR spectrophotometer (Agilent). For all the recorded spectra, 1 cm path length SUPRASIL® quartz sample cells (Hellma BeNeLux) were used (2 nm bandwidth, 3 seconds nm-1).The one-electron midpoint potentials were determined from the difference spectra. The oxidized fraction after each titration was calculated based on the Q-band absorption (559 nm) relative to the initial oxidized and final reduced spectrum. Oxidation experiments were done by leaving the sample unperturbed. Before and after each potentiometric titration set, the electrode was calibrated by measuring the potential of a saturated solution of quinhydrone in 50 mM potassium hydrogen phtalate at 25 °C (E_0= 463 mV).

7.4 Results

7.4.1 UV-vis spectroscopy

The Fe(III), ferrous and Fe(II)-CO states The UV-Vis absorption spectra of ferric and ferrous GLB-3a with DTT exhibit a Soret band at 413 nm and Q_α and Q_β bands at 567 and 533 nm for the ferric form, and 426 nm, 560 and 530 nm for the ferrous form, respectively (Fig. 7.3, GLB-3b similar, data not shown). The high absorbance ratio Q_α/Q_β of the ferrous form is typical of a hexacoordinated LS (6c/LS) heme iron. The most likely distal ligand is here E7His. Due to the cysteine-rich nature of GLB-3, DTT was added (to GLB-3a and GLB-3b), because DTT enhances the overall stability of the globin as it reduces potential inter- and intramolecular disulfide bridges that cause GLB-3 to aggregate and precipitate in solution [230]. This effect on the stability was confirmed by MS and ECD analysis [237]. DTT cannot reduce the heme iron to the ferrous state and overall, UV-vis absorption changes due to the addition of DTT remain absent.

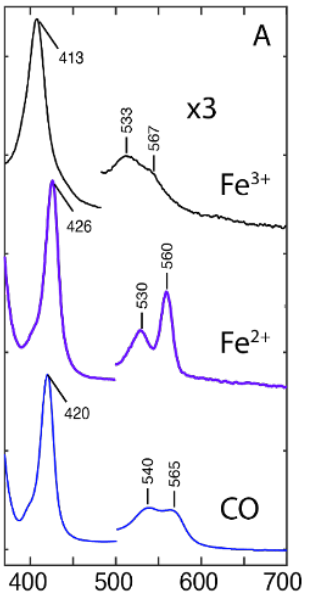

FIGURE 7.3: UV-Vis absorption spectra of GLB-3a in the purified ferric form, the ferrous deoxy form and the Fe(II)−CO ligated form at pH 7.5 with DTT (A) (similar spectra without DTT). The Q bands are magnified by a factor of 3.

The addition of CO to the ferrous form gives rise to a CO-ligated form, with the Soret band located at 420 nm and the $Q_{\alpha,\beta}$-bands at 540 nm and 565 nm, respectively. Upon exposure to air, no intermediate O_2-bound form of GLB-3 was observed and the protein spontaneously oxidized to the ferric state.

All spectroscopic evidence points to a distal endogenous E7His (His94) ligation to the heme iron in both the ferric and ferrous form (Fig. 7.1 (A), see [237] for full rRaman and EPR analysis). In order to further explore the effect of the distal ligation, the GLB-3 HE7A mutant was constructed. Since the Ala residue cannot ligate iron, this point mutation was expected to induce a high-spin (HS) pentacoordinated heme form (5c/HS). Surprisingly, the UV–Vis absorption spectra showed a slightly altered ferric and ferrous spectrum indicative for a 6c/LS form with the Soret band at 420 nm and the Q_α and Q_β bands at 571 and 539 nm (Fe(III) form), and a Soret band at 426 nm with the Q_α and Q_β bands appearing at 560 and 530 nm (Fe(II) deoxy form), respectively (Fig. 7.4). In all cases, a band is found around 660 nm, potentially being a charge-transfer (CT) band. The absorption spectrum resembles that of the cytochrome c mutant in which the axial

heme ligand Met80 is replaced by Cys giving rise to a CT band around 660 nm [362], potentially also a slight contribution of heme degradaton product biliverdin, as observed previously in Chapter 5. The ferrous CO-ligated form showed a Soret band at 421 nm and Q_α and Q_β at 569 and 537 nm, respectively.

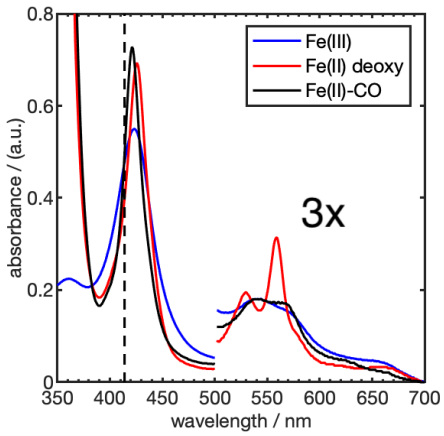

FIGURE 7.4: UV-Vis absorption spectra of GLB-3a HE7A in the purified ferric form (blue), the ferrous deoxy form (red) and the ferrous CO-ligated form at pH 7.5 without DTT (black). The Q bands are magnified by a factor of 3. The indicator (dashed line, 414 nm) represents the observer wavelength during the flash photolysis experiment.

Functional activity tests Next, the catalase activity, hydrogen sulfide binding and NiR activity of both GLB-3 isoforms have been tested as well as GLB-3a C70S mutants (Fig. 7.5). The addition of various excesses of H_2O_2, to ferric GLB-3a led to no change in the UV/Vis absorption spectra, even at 2000-fold excess of H_2O_2 (Fig. D.1). This indicates that no peroxidase or catalase activity is present and that ferric GLB-3a is also very stable under extreme high H_2O_2 stress. Ferric GLB-3b also resists reaction with H_2O_2, but is less stable under high concentrations of H_2O_2 as can be deduced from the decrease of the Soret and Q-bands. This is in line with the earlier observed lower stability of GLB-3b versus GLB-3a, as seen from ECD measurements [237]. Addition of H_2S to the ferric GLB-3 isoforms and GLB-3a C70S (not shown) induces no spectral change (Fig. D.2) in contrast to the observations for hNgb and hsMb for which reaction with H_2S is reported (see appendix Fig. D.3) [352, 363]. In a third set of experiments, the nitrite reductase activity of the ferrous deoxy GLB-3a and GLB-3b and GLB-3a C70S was tested (Fig. 7.5). Addition of high concentrations of nitrite to ferrous deoxy GLB-3a and GLB-3b and GLB-3a C70S led to no spectral changes indicating no nitrite reductase activity. Nitrite addition to the ferric form did not lead to spectral changes associated with nitrite ligation at the heme, neither to the wild-type, nor to the mutants. In contrast, addition of nitrite to ferrous HE7A GLB-3a induces spectral changes in line with the formation of an Fe(II)−NO state (Abs_{Soret}= 420 nm, Q_β and Q_α equal to 539

and 575 nm, respectively), revealing that HE7A GLB-3a can act as a nitrite reductase and that the E7His is key in hampering the NiR activity in the GLB-3 isoforms.

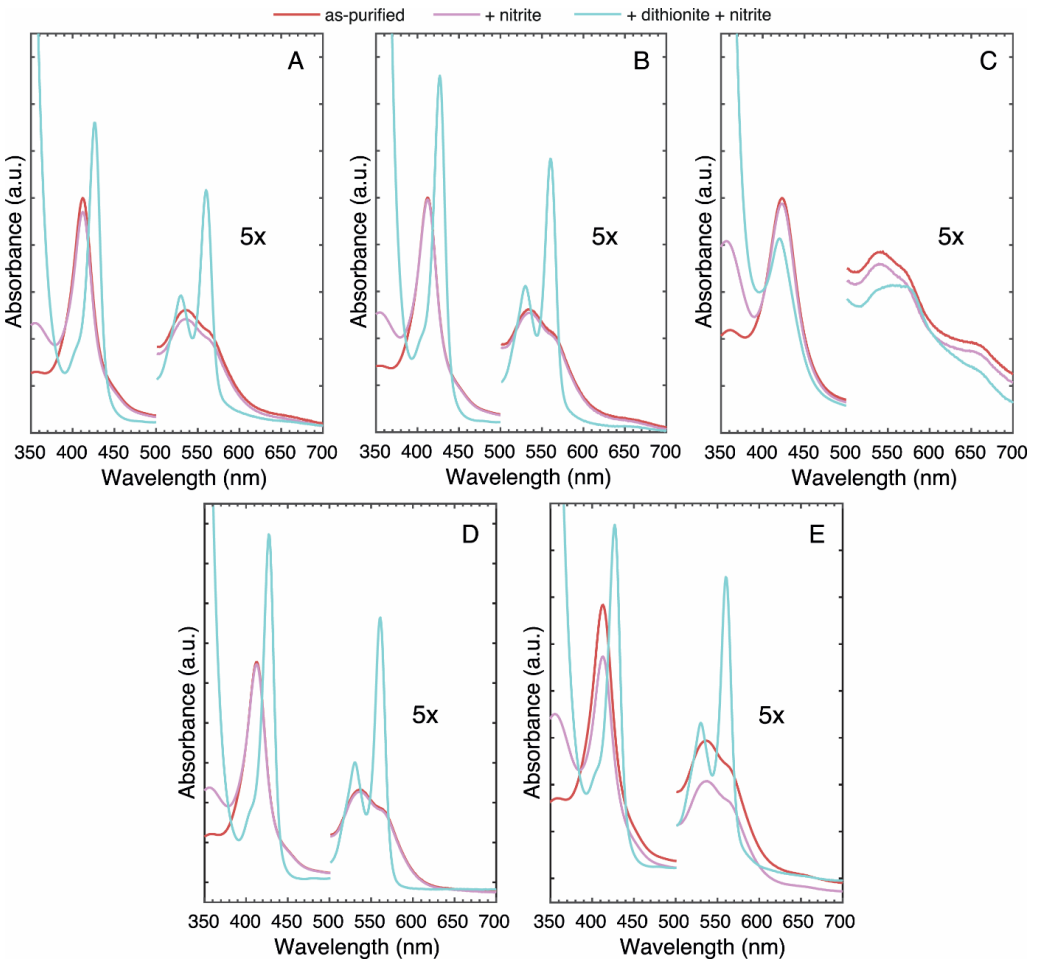

FIGURE 7.5: UV-Vis absorption spectra of A) GLB-3a, B) GLB-3b, C) GLB-3a HE7A, D) GLB-3a C70S and E) GLB-3 GD in the as-purified ferric form in presence and absence of a 1000-fold excess of sodium nitrite with and without dithionite. If the protein has nitrite reductase activity, a change to the UV-Vis absorption spectrum to the ferrous NO-ligated heme protein will occur. This is only observed for GLB-3a HE7A (C). For all other variants the protein remains in the deoxy ferrous form if sodium nitrite and dithionite is added to the ferric form.

7.4.2 CW-EPR spectroscopy

Both ferric GLB-3 isoforms and the HE7A mutant were studied using (CW) EPR (Fig. 7.6). GLB-3a was studied with and without DTT and GLB-3b with DTT. Due to protein instability, GLB-3b was not measured without DTT. The EPR spectra of ferric GLB-3a and GLB-3b with DTT show the expected feature of a 6c/LS ($S = 1/2$) ferric heme with the simulated g-values reported in Table D.1. The high-field feature g_x (g_{min}) is not observable because of large g-strain effects and therefore estimated using the approximation $g_z^2 + g_y^2 + g_x^2 \approx 16$ [364]. The difference between the EPR signals of both isoforms is negligible, highlighting that the N-terminal extension in GLB-3b does not alter the heme pocket conformation. Intriguingly, three 6c/LS forms are detected, denoted as LS1, LS2 and LS3, see table appendix Table D.1. These three forms can be ascribed to the F8His-Fe(III)-E7His with a different relative arrangement of the imidazole planes of the axial histidine ligands [165, 300, 93]. These spectra are in agreement with the LS forms observed for WT hNgb and mNgb (see Table D.1).

For ferric WT hNgb, it is thought that an intramolecular disulfide bridge formation causes a LS-form with very high $g_{max} = 3.26$, as a ΔCys hNgb mutant shows only one LS form with $g_{max} = 3.10$ [93]. To test whether a potential intramolecular disulfide bridge is formed, GLB-3a and GLB-3b were measured without addition of DTT (-DTT). As DTT is required for stability reasons, the spectra were measured of the supernatant, immediately after removing the precipitated aggregates by centrifugation. Due to stability issues, a meaningful spectrum of GLB-3b without DTT could not obtained[1]. Whereas the UV-vis absorption spectra were nearly identical, the EPR spectra show clear differences depending on the presence or absence of DTT. The spectrum of GLB-3a without DTT revealed a third LS-form with very high $g_{max} = 3.40$, suggesting that this novel LS form corresponds to a globin state with an altered conformation, potentially caused by intramolecular disulfide bridg(es). This evidence, together with a structural model of GLB-3, motivated us to create the C70S point mutation, as this Cys is the most likely candidate to participate in the formation of such disulfide bridge with AAs C89 or C135. Indeed, the EPR spectrum of the C70S mutant without addition of DTT reveals no sign of the LS-form that occurs at the WT GLB-3a without addition of DTT, hereby confirming that C70 is a crucial amino acid in maintaining a structurally different state by disulfide bridge formation.

The possible distal ligation of a Cys residue in ferric GLB-3a HE7A, as suggested by our UV-vis data earlier, is corroborated by the EPR data of ferric GLB-3a HE7A (Fig. 7.6 (f)). Site-directed mutagenesis of the distal E7His residue to Ala in GLB-3a leads to a complete change of the EPR spectrum of the ferric form. The earlier observed contributions of LS1–3 HALS is replaced by two overlapping, narrow LS species (LS4 and LS5) that contribute to the total spectrum by 63 % and 34 %, respectively. This finding is surprising as the mutation of a the E7His residue usually prevents hexacoordination, to a large HS-fraction [352, 365]. Only a minor rhombic feature points out the presence of a small amount 5c/6c HS form of the globin. The g-values (Table D.1) are in fair agreement with the sulfide-treated hNgb HE7A mutant and heme proteins with a cysteinate or

[1] Compared to optical measurements, EPR measurements require a higher protein concentration, which is not always achievable for proteins with low stability such as GLB-3b.

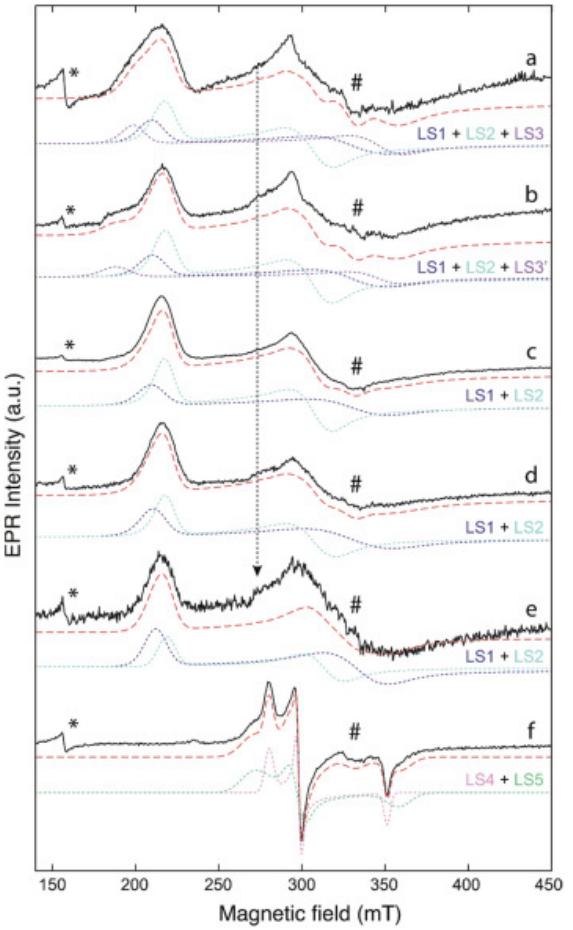

FIGURE 7.6: X-band EPR spectra of ferric GLB-3a and GLB-3b. Normalized X-band CW-EPR spectra of a frozen solution at pH 7.5 of a) ferric GLB-3a without DTT, b) ferric GLB-3a with DTT added ∼1 h prior to the EPR measurement, c) ferric GLB-3a with DTT added immediately after the purification process, d) ferric GLB-3b with DTT, e) ferric GLB-3a C70S without DTT and f) ferric GLB-3a HE7A without DTT measured at 10 K. The corresponding simulations are shown shifted down from the experimental spectra in red dashed lines with the individual LS components shown as dotted lines. An additional signal, indicated by the arrow, is observed at $g = 2.46$, most probably originating from an exogenous ligand from the buffer solution that has coordinated with the heme cofactor. *Indicates the contribution of a non-heme iron Fe^{3+} and # a Cu^{2+} background signal.

similar thiolate axial ligand ([352, 366], table D.1) suggesting that mutation of the distal His is accompanied by heme sliding or movement of the E-helix which contains the nearest Cys residues (Cys on E2 and E12). This confirms the flexibility of the heme pocket and reveals that E7His plays a key stabilizing role in the protein structure, besides its role in the protein's function. Alternatively, a buffer molecule may be ligated to the

heme iron.

7.4.3 CO ligand-binding kinetics

Flash photolysis measurements To investigate how fast CO-binding occurs in bis-His coordinated gbs, the CO rebinding kinetics were analyzed using laser flash photolysis and stopped-flow measurements on CO-ligated gbs. Immediately after a short laser pulse on the CO-ligated globin, dissociation of the CO ligand from the heme results in a ferrous pentacoordinated state. Rebinding of CO is monitored on various time scales by measuring the absorbance at 414 nm. A fraction of the CO ligands remains in the protein matrix. During this so-called geminate rebinding process (see Eq. 7.1), the CO ligand rebinds to the reduced heme iron independently of the CO concentration, in a geminate rebinding process of a few nanoseconds. Hence, a fraction of the geminate phase is a measure for the accessibility of the heme pocket. The rRaman data on CO-ligated GLB-31 indicate that locally, the CO is not so much stabilized [237]. They also show that after photolysis of the CO, E7His is immediately rebinding to the heme iron. In the non-geminate fraction, CO migrates to the solvent and rebinds in a CO concentration-dependent, bimolecular rebinding process (µs-ms range, see Eq. 7.2).The first phase in this process consists of the competition between the endogenous distal amino-acid residue and the CO ligands in binding the heme iron. This phase is then followed by the replacement of the distal amino-acid by CO. Assuming a steady-state equilibrium between penta- and hexacoordinated proteins, the observed $k_{\mathrm{obs,CO}}$ rate can be approximated by the equation [367]:

$$k_{\mathrm{obs,CO}} = \frac{k_{\mathrm{off,His}} k_{\mathrm{on,CO}} [\mathrm{CO}]}{k_{\mathrm{on,His}} + k_{\mathrm{off,His}} + k_{\mathrm{on,CO}} [\mathrm{CO}]}. \tag{7.5}$$

Stopped-flow measurements can thus be used to obtain $k_{\mathrm{on,His}}$ and $k_{\mathrm{off,His}}$.

In case of bis-His gbs, this process generally consists of a competition between the distal E7His and CO. This phase is then usually followed by the replacement of E7His by CO.

Stopped-flow measurements on GLB-3a and variants CO binding to the heme iron is observed by adding anaerobically an excess of CO to ferrous GLB-3. Flash photolysis and stopped-flow measurements were performed to study the binding kinetics of CO to the heme site of both GLB-3 isoforms. Stopped-flow rapid-mixing measurements in which deoxy ferrous GLB-3 was mixed with a solution equilibrated with CO allow to determine the binding of CO to the protein. In bis-histidine coordinated globins, the distal histidine must first dissociate from the heme iron in order to allow CO to bind. This is usually described by a biexponential process.

The stopped-flow measurements of the two GLB3 isoforms show that it takes around 300 seconds for the lowest CO concentration to replace the distal His (Fig. 7.7 (A) and (B)). This is extremely slow in comparison with other hexacoordinated globins, such as human neuroglobin [299], non-symbiotic hemoglobins from *Lotus japonicus* [368] and various insect hemoglobins [348], which require less $\leq$ 1 s under similar conditions. CO

binding to pentacoordinated ferrous gbs, like Mb, occur even within 0.25 s [369]. To probe further the role of the distal His, the stopped-flow CO binding of the HE7A GLB-3 mutants were also measured. In contrast to the GLB-3 proteins, only a few seconds are needed for the complete replacement of the distal ligand with CO (Fig. 7.7 (C) and (D)), but this is still slower than most other globins. The slow transition of the hexacoordinated deoxy form to the CO-ligated form is also obvious from the UV-Vis spectra taken at different times after mixing with CO (Fig. 7.8). Full conversion to a CO complex is only obtained after several minutes, which is in principle too long for flash photolysis measurements. This is evidenced by the fact that UV-Vis spectra taken after flash photolysis show again a mixture of deoxy ferrous and CO-ligated ferrous species. In accordance, the obtained kinetic curves after flash photolysis of GLB-3a and GLB-3b show that the rebinding phase is too slow since after 100 ms the difference in absorbance is still not zero (Fig. D.4 (A) and (B)). Around 20 % of the CO ligands did not rebind to the heme iron, due to the high histidine affinity and/or limited accessibility of the heme pocket (a similar effect is observed without DTT).

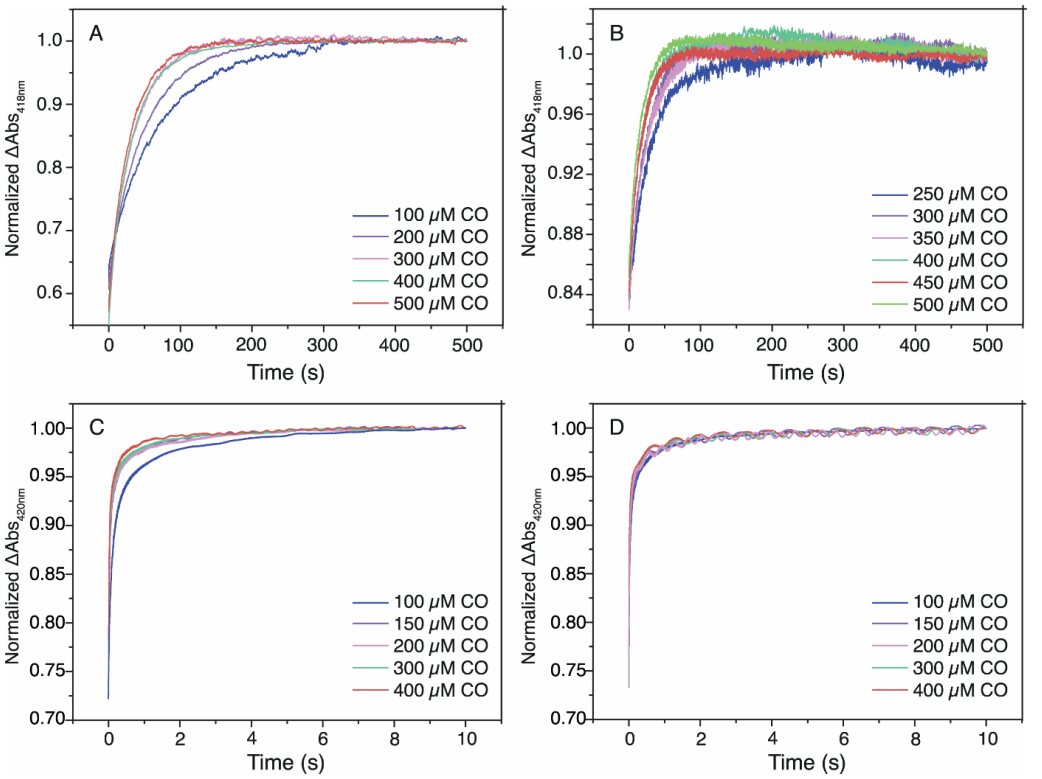

FIGURE 7.7: Stopped-flow measurements to determine CO-binding kinetics for 10µM A) GLB-3a and B) GLB-3b both with DTT at 418 nm (similar without DTT), and C) GLB-3a HE7A and D) GLB-3b HE7A without DTT at 420 nm. The conversion of the hexacoordinated deoxy form to the CO-ligated complex is observed as ΔAbs over time.

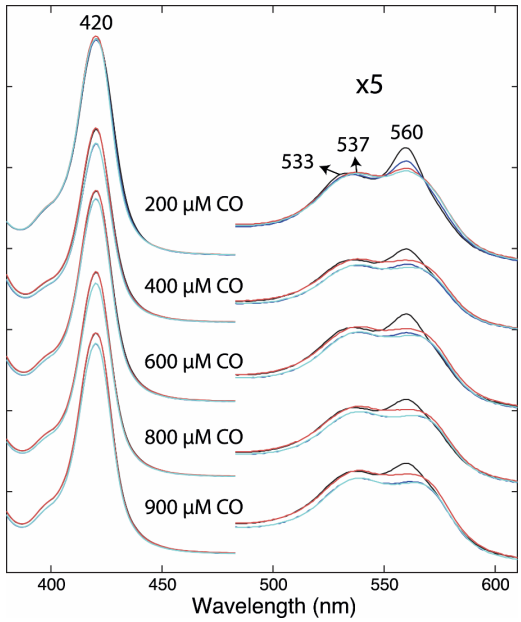

FIGURE 7.8: Non-normalized UV-Vis absorption spectra of ferrous GLB-3a incubated at different CO concentrations before (black - red) and after (blue - cyan) flash photolysis (analogous results are obtained with DTT). Before the flash photolysis, the protein is mixed with a CO flushed buffer solution with a specific CO concentration and sodium dithionite. After the mixing, the protein sample is measured (black) and a Soret band at 420 nm and an intense Q_α-band at 560 nm are observed, implying a mixture of a CO and deoxy form in the protein sample. After 2 minutes, the protein sample is measured again (red) and a decrease of the α-band is detected, indicating a clear conversion to a CO complex. After flash photolysis measurements (blue), the protein sample again shows a slightly higher α-band at 560 nm, which decreases after 2 minutes (cyan). Note that this effect is more apparent at lower CO concentrations. A similar but slower CO formation is observed in GLB-3b (with or without DTT), suggesting a more closed protein structure or a lower CO affinity than GLB-3a (not shown). The Q bands are magnified by a factor of 5.

Because of the above, the flash photolysis data of CO-ligated GLB-3a and GLB-3b cannot be fitted by the earlier introduced biomolecular scheme. This observation was the main driving force behind the design of a distal HE7A mutant. If E7His rebinding is indeed obstructing CO rebinding, removal would result in altered ligand-binding kinetics. The UV-vis spectra of GLB-3a HE7A already showed surprisingly a hexacoordinate character of the ferrous state (7.5 (C)). This is reflected in the flash photolysis experiments: Attempts were undertaken to measure the CO-binding kinetics of ferrous GLB-3 HE7A. Despite numerous repeats, the data were not optimal. Here we describe the experiments and experimental details, especially the ones done on the HE7A mutant.

Triplicate flash photolysis experiments were done on the CO-ligated heme pocket mutants HE7A GLB-3a and HE7A GLB-3b (Fig. D.5). The batch-to-batch variation in the data is large compared to other CO rebinding curves reported in literature [166, 92, 95, 368]. Nevertheless, the CO-rebinding kinetic traces of both GLB-3a/b HE7A are

clearly different from those of the WT GLB-3 (Fig. D.5), but are not monophasic, or alike typical E7H mutations in gbs. Instead, a geminate rebinding phase is followed by a bimolecular phase. Furthermore, a clear plateau between the geminate rebinding and bi-molecular rebinding process is absent, indicating more complex processes that result in slow absorption changes over time. These processes usually resolve different intermediate stabilizations of the CO-ligand by the distal AA residues.

The CO-dependency of the kinetics confirms that the slower fraction is not a geminate rebinding process. However, the ligand competing with CO is unknown. The competing ligand is probably a Cys residue (see EPR part).

7.4.4 Redox titrations

With an envisaged function in redox transfer for GLB-3, it is interesting to obtain the redox potential of GLB-3. The redox potential highly depends on the heme-pocket structure and is unique for each protein and gives more insight in which potential electrocatalytic reactions the protein might play a role.

A possible method to determine the redox potentials of heme proteins is a cyclic voltammetry (CV) setup in which the protein is immobilized at a modified gold electrode. This method was successfully applied by our collaborators from the A-sense led by Prof. De Wael for different *Ce* gbs [117, 119]. Therefore, they repeated a similar setup for GLB-3, using a slightly different setup that was validated using commercially bought cytochrome *c*. However, they were not able to determine the redox potential of GLB-3 via this method, for causes that remain until now unclear. Potentially, the many cysteines in GLB-3 interacted with or precipitated at the used gold electrode, preventing efficient electron transfer.

Alternatively, we recreated an optical potentiometric titration method after [370, 371] to determine the redox potential of GLB-3, as various redox potentials of bis-histidyl proteins have been determined using such approach [299, 148, 293, 372]. This method relies on the fact that both ferrous and ferric bis-histidyl heme proteins have a very distinct UV-vis absorption spectrum (see Fig. 7.3). The ferrous state can be obtained by adding a reducing agent such as dithionite ($Na_2S_2O_4$) to the ferric form of the protein. Vice versa, potassium ferricyanide ($K_3Fe(CN)_6$) is able to fully oxidize the heme protein to the ferric state. The electrochemical potential at which this conversion occurs, can be obtained by carefully titrating a reducing or oxidizing agent to the protein in the presence of various redox mediators. By measuring the potential of the solution after each titration, the midpoint electrochemical potential can be determined by fitting the UV-vis spectral changes (Δ Abs_{Q-band}) in function to the electrochemical potential to a Nernst equation.

As it was the first time such method was implemented in our lab, we carried out various optimization phases. In a first set of experiments, the redox mediator solution was investigated. While the initial method papers [371, 370, 299] do not highlight any remarkable phenomena, the observations revealed poor solubility and challenging UV-vis absorption behavior of the mediator mixture. A second part of the optimization involved the reduction of the globin using a reducing agent. This is needed to be able to carefully control the absorbance changes, and therefore, various titration experiments

Table 7.1: Table containing the physicochemical properties of the used redox mediators according to [299].

	Properties				
Red. mediator	E_0 (mV)	solubility (H_2O)	light sensitivity	MW (Da)	Conc. (mM)
diaminodurene	+275	poor	yes	164.25	0.4
trimethyl-hydroquinone	+115	poor	no	152.19	0.1
phenazine ethosulfate	+65	good	yes	334.39	0.1
phenazine methosulfate	+85	good	yes	306.34	0.1
2-methyl-1,4 napthoquinone	+10	poor	no	172.18	0.4
tetramethyl-p-benzoquinone	+5	very poor	no	164.20	1.2
2-hydroxy 1-4 naphtoquinone	-145	good	no	174.15	0.015
riboflavin-5'-monophosphate	-219	good	yes	478.33	0.015

were done in order to obtain a reproducible titration curve. The last part of the setup that needed optimization is the potentiometric detection. As both UV-vis and potential of the solution should be measured simultaneously, the optical cuvette needed to be optimized accordingly.

In an initial trial, we were not able to reproduce the redox potential of hNgb [60] nor obtain results for GLB-3 within a reasonable error margin using our home built setup. In a next phase, improvements were made based on the insight that a very well-controlled anaerobic environment was needed to succeed, which has eventually led to the redox determination as reported in [237]. Here, the consecutive steps and improvements are reported.

Redox mediator optimization Redox mediator stock solutions were made in 100 ml of 0.1 M potassium phosphate. The final concentration of each component in the mixture was chosen according to [299], and is listed in Table 7.1. The stock solution was sonicated and mixed, however, a small undissolved fraction remained. One percent of DMSO (1%) was added to the mixture to increase the overall solubility. The mediator mixture absorbs in the UV-visible range, especially in the range for which we wanted to detect the changes between the protein oxidation states (Q-bands, 559 nm) (Fig. D.6). In principle, this could be easily resolved by a baseline subtraction. However, the mediator mix changes color over time from yellow to a dark green (Fig. D.7), accompanied with

absorbance changes (spectra not shown). The UV-vis spectrum of each redox mediator was measured over time (Fig. D.6) revealing that phenazine ethosulfate and phenazine methosulfate absorb increasingly over time in the Q-band region 500-700 nm. Storing the mixtures in dark resulted in more stable absorption spectrum, and therefore, subsequent experiments were carried out in dark except for the UV-vis detection part[2]. Besides light exposure, addition of dithionite to the redox mixture resulted in UV-visible absorption changes. This was not easily circumvented, as dithionite or any other reducing agent causes this effect and is inherently needed for the reduction of the heme. Therefore, to overcome the solubility problem on one hand, and to overcome the UV-vis background effects on the other hand, the mediator concentration was lowered to a final concentration of every component to 5 µM, in accordance with [293], in which they performed a similar experiment with redox mediators at concentrations between 1 and 5 µM. After undesirable initial experiments, it was decided to reproduce the mediator conditions of [293], instead of [299]. In that work, phenazine methosulfate ($E_m = 80$ mV), 2-methyl-1,4-naphthoquinone ($E_m = 10$ mV), indigo tetrasulfonate ($E_m = -46$ mV), 2-hydroxy-1,4-naphthoquinone ($E_m = -137$ mV), and anthraquinone 2,6-sulfonate ($E_m = -184$ mV) were used at concentrations between 1 and 5 µM.

Spectroscopic detection Prior to perform experiments on GLB-3, hNgb was tested because of its known redox potential [293]. hNgb was added to the redox mediator mixtures that were pre-flushed with Ar gas and the UV-vis spectrum was collected which shows the expected Soret and Q-bands, with a redox mediator background superimposed. Careful titration of an Ar-flushed, 1/10th or 1/20th diluted saturated dithionite solution with an airtight Hamilton Syringe resulted in limited changes in the UV-vis spectrum. Lower dilutions resulted in immediate turn-over to the ferrous state. The best results were obtained by carrying out the titration with freshly prepared and immediately Ar-flushed 20 mM dithionite solutions, using an automated syringe pump. Small increments resulted in intermediate forms between the ferrous and the ferric state, but overall, the experiment was difficult to control. Fig. 7.9 (A) shows an example of a titration experiment of hNgb dissolved in the mediator mix solution. Dithionite was titrated as indicated in the figure legend. The addition of dithionite resulted initially in a decrease of diaminodurene absorption band at 387 nm, until at after 46 µL titration volume, a sudden conversion occurred to the ferrous form. Leaving the sample over time after addition of an excess of dithionite resulted in the auto oxidation to the ferric state, which can be seen from the overall decrease in Q-bands (Fig. 7.9 (B)). The ferrous state was not stable in solution for a long time without adding an excess of dithionite, showing that leaking of air in the sample may be a crucial hampering factor.

Electrochemical detection A final adjustment to the setup included the addition of a Ag/AgCl and Pt counter electrode to the solution in order to measure the potential of the solution after each dithionite titration. A schematic diagram of the final setup is shown in Fig. 7.2. After each titration, we monitored the open circuit potential until it stabilized before measuring the spectrum. It should be noted that the potential did not

[2]Despite being stored under N_2 atmosphere, the color changes persisted

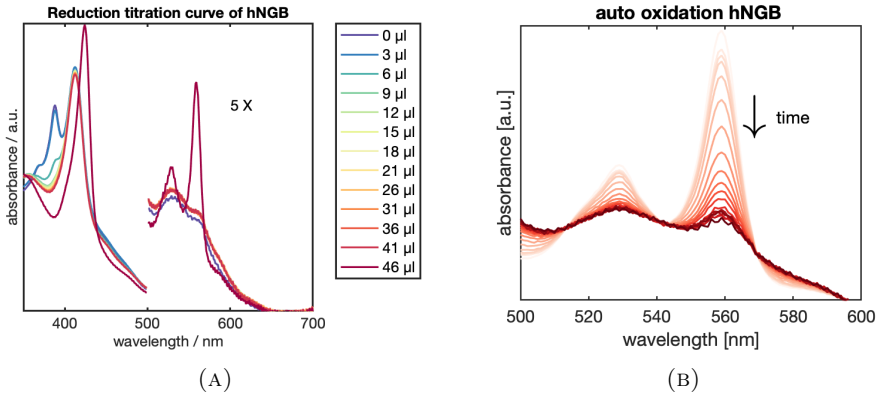

FIGURE 7.9: (A) UV-Vis absorption spectra of hNgb in the mediator mix (MM), after titration of various amount of a dithionite solution as indicated by the legend. The Q-band region is amplified by a factor of 5. (B) Collection of the same sample after addition of an excess (84 µL) of the same dithionite solution over time, indicating the auto oxidation to the ferric form.

always stabilize, likely due to O_2 leakage in the cuvette, which causes a degree of variation in our measurements. After we reached a fully ferrous state, we added a small excess of dithionite to the solution, and repeated the experiment by following the oxidation over time by leaving the sample unperturbed and collecting the potential and spectrum and various time points after a magnetic stir perturbation to assure a homegeneous solution.

Redox potential determination The redox potential of hNgb and GLB-3 was evaluated using the method described in [293]. Both proteins were stepwise reduced using a dithionite solution and the potential of the solution was measured after each titration. After the fully reduced state was reached, the auto-oxidation was monitored accordingly and the result of the triplicate experiment is plotted in Fig. 7.10. The potential was plotted versus the mean of the measured potential of a saturated solution of quinhydrone in 50 mM potassium hydrogen phtalate at 25 °C (E_0= 463 mV vs. SHE). The fraction of reduced proteins was calculated based on Q-band absorption at 559 nm, prior to dithionite addition (0) and after an excess of dithionite (1).

For both proteins we observe a strong hysteresis-like effect, depending on the direction (oxidation/reduction, empty 'o'/ filled 'o', respectively). Next to that, repeated measurements resulted in strongly deflected values. By comparing the results for GLB-3a and Ngb, we see that the data of Ngb is overall more dispersed compared to GLB-3a (which seems to have only one strong outlier) and that the mean midpoint potential is far more negative than for the GLB-3a experiments. Overall, it seems to be impossible to extract meaningful values out of these set of experiments for the redox potential of both proteins.

In a later stage of the project, an optimised experiment was executed inside a glovebox which was deoxygenated with N_2, which tremendously increased the reproducibility and

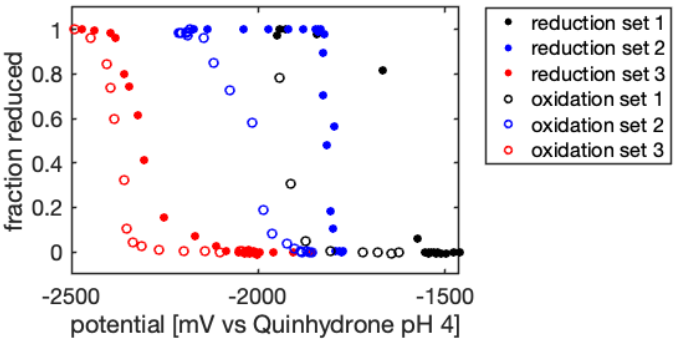

(A)

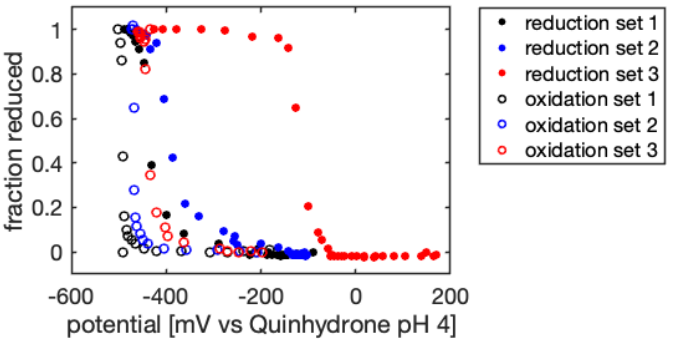

(B)

FIGURE 7.10: Potentials of hNgb (A) and GLB-3a (B) versus the fraction reduced. The plots show the fraction reduced (as determined from absorbance spectra) in function of the measured potential vs. the potential measured of a saturated quinhydrone solution at pH 4.

stabilization of the redox potential after each titration (see Appendix Fig. D.8 and D.9). For this set-up, a repeatable determination of the redox potential of hNgb could be done, in line with earlier results. The obtained redox potential E_m is +8 mV ± 19 mV vs. SHE, which falls within the wide range of E_m values reported for heme proteins (Table D.2). Note that, when discarding the outlier in the GLB-3a measurements in Fig. 7.10 (red) transitions in the reduction mode occurs in an area that matches the final results (i.e. -450mV versus quinhydrone). The strong deviations in the oxidation curve may be related to the different Cys that can get oxidized.

7.5 Discussion and conclusion

GLB-3a and GLB-3b are two isoforms of GLB-3 that contain a globin domain that is modelled to exhibit the classical 3/3 α-helical fold, and is a previously uncharacterised globin with a clear physiological function. Knock-out experiments performed by the group of

Prof. Bart Braeckman have shown that GLB-3 is responsible for a fecundity effect in the nematode [237]. The longest isoform, GLB-3b, is predicted to be palmitoylated and myristoylated, while the smaller isoform is predicted to have a palmitoylation site and an additional N-terminal mitochondrial targeting site (MTS) (Fig. 7.1). Moreover, the fact that two isoforms of GLB-3 exist indicates overlapping tissue-specific functions for GLB-3a and GLB-3b. Preliminary data motivated further biochemical characterization to shed light on this unknown, cysteine-rich member of the *Ce* gbs.

The UV-vis and EPR characterization reported in this chapter shows that both GLB-3 isoforms are strongly hexacoordinate bis-histidine-coordinated (6c/LS) in both the ferric and ferrous form. Addition of DTT was needed to enhance the stability, because precipitate would be formed otherwise over time, especially at high concentrations. It is highly expected that a disulfide bridge formation may modulate the heme pocket structure. Indeed, EPR reveals that three LS forms (LS1–3) are present in ferric WT GLB-3, whereby LS3 disappears upon addition of DTT and is thus linked to disulphide-bridge formation. LS3 is not present in ferric GLB-3a C70S (Fig. 7.6), indicating Cys70 as one of the partners in the disulphide bridge. Other partners could be AAs C89 or C135, as followed from modelling (Fig. 7.1 (A)).

The occurrence of different LS forms indicates a flexibility in the heme region. The EPR parameters of bis-histidine coordinated heme centres can be linked to the relative orientation of the two imidazole planes of the iron-ligating E7His and F8His [93, 373], with increasing g_z values indicating an increasing dihedral angle between the two imidazole planes and/or tilting of the imidazole plane away from the perpendicular position versus the heme plane. The g_z values found for LS1–3 (Table D.1) agree with dihedral angles between the imidazole planes larger than 40° [373]. LS3 has the largest g_z value revealing that formation of the disulphide bond exercises a strain on the heme pocket. This may point to control of the GLB-3 function through the redox state of the disulphide bridge, as suggested for human neuroglobin [374].

CO is known to tightly bind with gbs in general and, so far, it remains the only exogenous ligand for which a binding to the GLB-3 heme iron could be observed. In general, the CO-rebinding kinetics for bis-His gbs are slower than for pentacoordinate gbs but still relatively fast (on-rates in the order of $\sim 10^6$ vs. 10^7 M^{-1} s^{-1}, respectively). Here, we observed that the CO-rebinding rate is extraordinary slow. The relatively high geminate phase of the WT and mutant shows a hindered or limited escape of CO to the solvent. The CO-rebinding kinetics of the GLB-3a HE7A mutant still does not show very high CO-rebinding kinetics, which can be linked to a distal AA-residue rebinding. Although the strong changes in the UV–Vis and EPR features of the GLB-3a HE7A variant compared to the WT form (Fig. 7.5 (C)) confirm the distal ligation of E7His to the heme iron in the latter form, an unexpected binding of an S-containing ligand, most likely Cys, to the heme iron is observed, suggesting that mutation of the distal His is accompanied by heme sliding or movement of the E-helix (nearest Cys on E2 and E12). This confirms the flexibility of the heme pocket and reveals that E7His plays a key stabilizing role in the protein structure, besides its role in the protein's function.

Several in vitro observations, such as the slow binding of CO and the fast auto-oxidation, indicate that GLB-3 is not a transport/storage protein and is not involved in

binding of diatomic (signalling) gases. A fast auto-oxidation hampering in vitro study of the oxy form of the globin was also observed in the *Ce* proteins GLB-6 [148], GLB-12 [119], and GLB-26 [114, 117]. Even though the hydrophobic heme pocket of GLB-3 should prevent heme oxidation, polar amino-acid residues are observed at the entrance of the heme pocket. This is also the case for GLB-12, where the polar residues allow solvent access to the heme pocket and trigger heme iron oxidation [119].

A more likely function thus points towards a redox or electron-transfer function. In vitro, the GLB-3 forms showed no catalase activity nor nitrite reductase activity in contrast to many other globins. The lack of substantial changes in the absorption spectra in the presence of various concentrations of H_2O_2, NO_2, and H_2S confirms that an enzymatic or ligand scavenging function is not expected. The fact that a stable NO form can be produced with the HE7A GLB-3a mutant suggests that the strong affinity of the distal histidine residue in the WT form is preventing ligand binding at the heme and subsequent reactivity. Moreover, GLB-3 can withstand large amounts of H_2O_2, and remarkable stability is observed at very low pH as well. However, isoform b is clearly less stable than isoform a, and the N-terminal extension of GLB-3b, which contains three extra cysteine residues in addition to the already cysteine-rich globin domain, might be attributable for this effect [237]. However, the function, structural motif, and localization with respect to the heme of this N-terminal extension is unknown.

To get more insight in the redox behavior, we explored a potentiometric titration experiment after [370, 293, 299]. The determination of the redox potentials using our experimental setup was not achieved in the scope of the practical part of my PhD work, however, progress was made in the optimization of the redox titration experiments and later on, successful experiments were executed in strictly anaerobic environment (see Appendix Figs. D.8 and D.9). The setup [293], was used in a glovebox, therefore an anaerobic environment seemed to be a crucial determining factor for success. The high variation in measured potentials for both control experiment on hNGB as on GLB-3 (Fig. D.8 is most likely caused due to the leakage of O_2 inside the cuvettes, despite the attempts made by prior flushing with N_2 and working under a N_2 pressured atmosphere using a syringe and N_2-filled balloon attached to the cuvette (see setup in Fig. 7.2). Small traces of oxygen seem to be sufficient to disturb the experimental system, preventing us to determine the redox potential within an acceptable error margin. The poor stabilization of the potential measurement caused a large degree of variability in our data. The concentration of the mediators needed to be significantly reduced to overcome the unwanted absorbance effects in the Q-band region, the region we used to determine the ratio of reduced versus oxidised state of the protein. Therefore, their importance and mediated effect could be significantly reduced as well. The many cysteines in GLB-3, and potential effect of the mediator induced oxidation thereof, and thus effect on the protein structure, are all factors that should be taken into account.

The final experimentally determined redox potential for GLB-3a is slightly positive (vs. SHE). For bis-histidyl ligated globins, a wide range of redox potentials is found presumably determining their function (Table D.2). Such broad range is also observed for cytochromes; even though the oxidation and reduction involve a seemingly simple reaction of electron transfer from or to the heme iron, their redox potentials span a

range of several 100 s of mV (Table D.2). The redox potential is strongly influenced by the nature of the axial ligands to the heme iron, porphyrin peripheral substituents, solvent accessibility of the metal site, electrostatic interactions with protein side chains and other cofactors, and protonation state of neighboring amino-acid residues [375]. The E_m value of GLB-3a is higher than the reported redox potentials of the disulphide redox couples in human neuroglobin and human cytoglobin (Table D.2), suggesting that the ferric heme iron of GLB-3a can oxidize disulphide bonds better than neuroglobin and cytoglobin.

Finally, and on a broader scope, the open question remains: "Why do the GLB-3 isoforms possess so many Cys residues?". A high number of Cys residues in globins is found to be most common in nematode globins. Besides the well-known structural function of disulphide bonds and the earlier mentioned involvement in membrane linkage (palmitoylation sites), Cys residues are known to participate in different redox reactions. Redox-active Cys residues can play an important role in the regulation of the protein function as they may act as redox-sensing molecular switches which sense cellular oxidizing factors such as ROS and cellular reducing factors [376]. Additionally, like the redox-active Tyr and Trp residues, also Cys residues can act as intermediate charge carriers in electron transfer reactions as observed during the redox titration measurements [377]. A recent chemoproteomics study determined the reactivity of the *Ce* cysteine proteome under physiological conditions [378]. Unfortunately, this study only picked up GLB-1 (with a non-redox active Cys), and revealed no information on the other 33 globins. Nevertheless, this study revealed wide-ranging redox regulation via cysteine redox chemistry in *Ce*, and showed redox-sensitive events in translation, growth signalling and stress response pathways. The high resistance of the heme-pocket region of GLB-3 to H_2O_2 may indicate that the cysteine-rich GLB-3 protein is designed to function in the presence of ROS. As a protecting mechanism, the globin thiols in nematodes can have a key role in thiol-mediated redox signalling in response to oxidative stress.

Further systematic biochemical studies are needed to identify potential redox partners or even a possible involvement in electron-transport or sensory function.

Part III

Conclusion

Summary and outlook

Summary

Globins are an important protein family throughout the evolution of life. Each have a unique heme pocket structure that allows them to carry out highly specific functions, such as oxygen and nitrogen transport, as well as redox housekeeping within the cell. Driven by the *in-silico* discovery of 33 and recently 34 globin genes expressed in the small nematode *Caenorhabditis elegans*, this thesis contributes to the long-standing goal of characterizing its associated gbs structurally and functionally. In particular, we focussed our attention to the nitrite and NO specific binding properties and overall enzymatic activities of the gbs GLB-33 and GLB-3 in *Ce*, and the Pgb of the bacterium *Ma*. Each globin in this set possesses a very unique heme pocket structure, with GLB-3 having the more 'classical' His residue on helix E at position 7 (E7), whereas GLB-33 has E7Ile and Pgb, E7Val.

An overall introduction to gbs can be found in the first chapter of this thesis, with a special focus on their interaction with nitrite. The gbs from *Ce* and the Pgb from *Ma* are reviewed in Chapter 2. The former are very numerous, are structurally and functionally diverse, and have a cell-specific expression pattern. Protoglobin, on the other hand, is evolutionarily the oldest ancestral globin with unique structural and functional properties. Due to the iron-containing prosthetic heme group of (proto)gbs, spectroscopy has proven to be a very powerful tool to study them and elucidate their putative functions. In addition to conventional techniques (such as UV-vis and rRaman), in this thesis more advanced methodologies such as pulsed EPR and the underexploited ECD in the visible range were applied. The details and basic theory of these methods can be found in Chapter 3. The subsequent chapters contain the main results on the particular gbs: *Ce*GLB-33 (Chapter 4 and Chapter 5), *Ma*Pgb (Chapter 6), and *Ce*GLB-3 (Chapter 7).

In Chapter 4, the initial biochemical characterization of the GD of GLB-33, a chimeric globin-coupled putative neuropeptide receptor, as published in [118] was extended. Two key aspects of the GD were specifically studied : *(i)* the unusual hydroxide ligation at the heme, and *(ii)* its extremely fast nitrite reductase activity. The spectral features of the hydroxide ligation were characterized spectroscopically as two low-spin species associated with two hydroxide conformations. The pH-dependent nitrite ligation at the heme was also investigated in detail using rRaman, chiroptical methods, and native MS. Working at low pH has particular consequences on the nitrite-heme interaction, as shown by the covalent nitrovinyl modification of the heme group. In recent years, there has been ongoing debate between experimental and computational findings on the nitrite linkage isomer. Therefore, these binding modes were explored through a search for EPR signals of nitrite-ligated heme forms. The lack of these signals, in combination with all

complementary data, suggests an O-linked nitrito binding mode at slightly acidic pH. Finally, both hydroxide and nitrite binding modes were linked to a structural movement of the key amino acid residue, E10Arg, in and out of the heme pocket.

In the subsequent Chapter 5, a follow-up study was conducted in which we performed more advanced pulsed EPR on the hydroxide complex and temperature-dependent CW EPR and pulsed EPR on nitrosylated GLB-33GD, which provided us with EPR parameters of the heme pocket. Also, attempts to crystallize the protein were undertaken, and point mutations were introduced in the heme pocket of GLB-33GD to further study the effect of E10Arg. Although many problems were encountered, the study strengthened the identification of the hydroxo-ligation in ferric GLB-33GD and the role of E10Arg in ligand stabilization. The nitrosylated GD of GLB-33 showed a particularly persistent rhombic conformation at high temperatures compared to Ngb and mutants, in line with observations for *Aplysia* Mb that also has a Arg residue at position E10.

The study on *Ma*Pgb, done in Chapter 6, resulted from an internal collaboration within the TSM^2 research group. We related the outspoken ruffled heme group of Pgb to a quantum-mechanical admixture of the $S = 5/2$ and $S = 3/2$ states of its ferric form. Furthermore, stimulated by the previous study on GLB-33GD and nitrated gbs, we investigated the Pgb-nitrite interaction, which was hitherto unexplored. Interestingly, we observed strong spectral changes upon lowering the pH, and ascribed it to a ferric-NO state as a consequence of the acidic decomposition of nitrite. This provides more evidence for the envisaged NO-scavenging function of Pgb.

In the last chapter of this thesis, Chapter 7, we conducted the first characterization of GLB-3, a cysteine-rich globin that is expressed as two isoforms, a and b, with the latter containing a N-terminal extension. In close collaboration with Zainab Hafideddine, we found that the strong hexacoordination prevents exogenous ligand interactions, with CO being the only exception so far. Moreover, disulfide bridge formation is very likely to occur in the globin. Distal HE7A pocket mutants were created in order to confirm the E7His hexacoordination. This mutation caused unusual structural reorganizations, resulting in spectra similar to heme proteins with a cysteinate-like ligand character. In this case, E12Cys may take on the position of the distal ligand. The lack of ligand interactions, fast auto-oxidation rate, and cysteine-richness suggest a potential function in redox signalling. The chapter describes the optimization process preceding the determination of the slightly positive redox potential vs. SHE of the protein. An extensive comparison with other bis-His ligated gbs was made, and its peculiar properties are discussed in light of a potential redox signalling function. In the context of the previous chapters and the scope of this thesis, it was found that GLB-3 did not exhibit any NiR activity. This underlines the broad functional diversity observed not only in the gbs studied in this research but also across all gbs. Structural changes during the course of evolution have led to highly specialized gbs, and with continued research and exploration, the mysteries of these fascinating biomolecules can be unlocked, and their full range of roles and functions can be revealed.

Future outlook, what's next?

Globin research has evolved from the need to understand the molecular function of hemoglobin. Nowadays, numerous globin genes have been discovered in various organisms, and a key example is the nematode *Ce*, with its 34 gbs. This extraordinarily large number, compared to vertebrate gbs, has stimulated further investigation. Characterizing gbs, functionally and structurally, is a tedious task: after more than two decades since their discovery, we have only been able to characterize a handful of *Ce* gbs. Therefore, within the biology of *Ce*, we need to be selective and think about which globin-related questions we are trying to answer and which gbs deserve our attention. Researchers from the research group of Prof. Bart Braeckman (Ghent University), a leading *C. elegans* expert, have identified glb-4 as homozygously lethal or sterile and GLB-18 as very abundantly expressed over a wide variety of neurons. GLB-31 is considered as potentially interesting as well to investigate in more detail as it is a relatively small globin that is only expressed in three types of interneurons. The above-mentioned properties suggest a very specific function, which could reveal very interesting properties from a spectroscopic viewpoint as well.

GLB-33, the largest chimeric *Ce* globin, and GLB-3, with its cysteine-rich nature and clear phenotype upon knockout (sterility), were excellent subjects to study in depth. It is now clear that the unique heme pocket of each globin leads to specific ligand-binding properties and, therefore, carries out a highly specialized cell-specific function. Until now, spectroscopic studies on GLB-33, including the work in this thesis, have focused merely on the GD and not the full-length protein. In the next phase, it would be interesting to connect the globin and the membrane domain to unravel the protein's multimeric organization and biological function. Alternative higher eukaryotic expression systems should be explored to carry out a study on the full-length domain. Membrane proteins tend to be challenging to work with, and therefore, a buffer and detergent screen on a small scale would be a good starting point. Spectroscopically, on the other hand, it would be advantageous to set up a well thought-out mutagenesis experiment on the heme pocket. We initially identified interesting mutants, but the study was hampered, likely due to an unforeseen extra point mutation. Repeating this study and combining it with a structural study would give us a detailed insight into this hydrophobic heme pocket. Matching the spectroscopic data to the structure would stimulate computational DFT and MD simulations as well, which could further optimize our EPR data simulations.

Pgb from *Ma* is also fascinating due to its highly ruffled heme group and exceptional affinity for oxygen. As a result, Pgb remains an intriguing globin on which researchers continue to publish new insights to date. Pgbs can adopt different heme geometries depending on the buffer conditions and the presence of distal ligands. However, the dynamics of this interplay between the heme and the different ligands and conditions are not well known. In this thesis in particular we shed light on Pgb and its interaction with nitrite and consequently NO, which was present at acidic conditions. We linked the ruffled heme to its potential function in the NO metabolism. However, how Pgb modulates NO levels and biological responses in vivo or its potential role as a protector from oxidative stress, is not yet fully understood. Additionally, we used UV/Vis ECD on Pgb, and the other gbs investigated in this work, as it has the potential to gain complementary insights

relatively fast and easily. However, the interpretation of the spectra is far from clear. Using Pgb in combination with other well-characterized gbs and DFT computations to further interpret these spectra would be an interesting research direction.

The extensive, multi-disciplinary study characterized GLB-3 isoforms from scratch, which has led to many insights but created many open questions. The presence of the C- and N-terminal extensions has a clear influence on the GD. The large number of cysteine residues and overall instability of the GLB-3b isoform complicates its biophysical characterization. Therefore, the next stage would involve a focused pulsed EPR study on GLB-3a, which is the most stable at high concentrations, potentially aided by XRD studies. The strong bis-histidine character of the heme would be interesting to investigate with pulsed EPR and link the spectra with the dihedral angles between the proximal and distal histidine planes. The functional relevance of the extensions is still largely unclear, mostly because globin studies focus on the heme pocket. However, new insights show that these extensions might function as signal sequences for subcellular location, membrane anchoring, or even structural stability. More work on the interaction partners, as was done for GLB-12, which is known to interact with superoxide dismutase (SOD)-1, would aid in understanding the neuronal function of GLB-3. Currently, SOD-1 and 3 are most likely candidates, but further biochemical studies are needed to unravel the specific reaction mechanism.

Samenvatting

Globines (gbs) zijn een belangrijke eiwitfamilie sinds de evolutie van het leven. Elk globine heeft een unieke heemzakstructuur waardoor ze zeer specifieke functies kunnen uitvoeren, zoals zuurstof- en stikstoftransport, evenals redox-huishouding binnen de cel. Gedreven door de in-silico ontdekking van 33 en recentelijk 34 globine-genen geëxpresseerd in de kleine nematode *Caenorhabditis elegans* (*Ce*), draagt deze thesis bij aan het langdurige doel om de deze gbs zowel structureel als functioneel te karakteriseren. In het bijzonder richtten we onze aandacht op de nitriet- en NO-specifieke bindingseigenschappen en algemene enzymatische activiteiten van de gbs GLB-33 en GLB-3 in *Ce*, en de protoglobine (Pgb) van de bacterie *Methanosarcina acetivorans* (*Ma*). Elke globine in deze set heeft een zeer unieke heemzakstructuur, waarbij GLB-3 het meer "klassieke"His-residu heeft op helix E op positie 7 (E7), terwijl GLB-33 E7Ile heeft en Pgb E7Val heeft.

Een algemene introductie tot gbs is te vinden in het eerste hoofdstuk van deze thesis, met een speciale focus op hun interactie met nitriet. De gbs van Ce en de *Ma*Pgb worden besproken in Hoofdstuk 2. De eerste zijn zeer talrijk, hebben een structurele en functionele diversiteit en hebben een cel-specifiek expressiepatroon. Protoglobine is daarentegen evolutionair de oudste voorouderlijke globine met unieke structurele en functionele eigenschappen. Door de ijzerhoudende prosthetische heemgroep van (proto)gbs is spectroscopie een zeer krachtig hulpmiddel gebleken om ze te bestuderen en hun functies te achterhalen. Naast conventionele technieken (zoals UV-vis en resonante Raman (rRaman)) werden in deze thesis meer geavanceerde methoden toegepast, zoals gepulste elektronenparamagnetische resonantie (EPR) en het onderbenutte elektronische circulaire dichroïsme (ECD) in het zichtbare gebied. De details en de basis theorie van deze methoden zijn te vinden in Hoofdstuk 3. De daaropvolgende hoofdstukken bevatten de belangrijkste resultaten over de specifieke gbs: *Ce*GLB-33 (Hoofdstuk 4 en Hoofdstuk 5), *Ma*Pgb (Hoofdstuk 6) en *Ce*GLB-3 (Hoofdstuk 7).

In Hoofdstuk 4 werd de initiële biochemische karakterisering van het globinedomein (GD) van GLB-33, een chimerische globine-gekoppelde putatieve neuropeptide receptor, zoals gepubliceerd in [118], uitgebreid. Twee belangrijke aspecten van het GD werden specifiek bestudeerd: (*i*) de ongebruikelijke hydroxideligatie aan het heem en (*ii*) zijn extreem snelle nitrietreductase-activiteit. De spectroscopische kenmerken van de hydroxideligatie werden gekarakteriseerd als twee lage-spinsystemen geassocieerd met twee hydroxide-conformaties. De pH-afhankelijke nitrietligatie aan het heem werd ook in detail onderzocht met behulp van rRaman, chiroptische methoden en native massaspectrometrie (MS). Het werken bij lage pH heeft bijzondere gevolgen voor de nitriet-heeminteractie, zoals blijkt uit de covalente nitrovinyl-modificatie van de heemgroep. In de afgelopen

jaren is er aanhoudend debat geweest tussen experimentele en computationele bevindingen over de nitriet-bindingsisomeer. Daarom werden deze bindingsmodi verkend door te zoeken naar EPR-signalen van nitriet-gekoppelde heemvormen. Het ontbreken van deze signalen, in combinatie met alle aanvullende gegevens, suggereert een O-gekoppelde nitrito-bindingsmodus bij licht zure pH. Ten slotte werden zowel hydroxide- als nitriet-bindingsmodi gekoppeld aan een structurele beweging van het belangrijkste aminozuurresidu, E10Arg, in en uit de heemzak.

In het daaropvolgende Hoofdstuk 5 werd een vervolgstudie uitgevoerd waarbij we geavanceerd pulsed EPR onderzoek deden naar het hydroxidecomplex en temperatuurafhankelijke CW EPR en gepulste EPR op nitrosylerende GLB-33GD, wat ons EPR-parameters van de heemzak opleverde. Er werden ook pogingen ondernomen om het eiwit te kristalliseren en puntmutaties werden geïntroduceerd in de heemzak van GLB-33GD om het effect van E10Arg verder te bestuderen. Hoewel er veel problemen werden ondervonden, versterkte de studie de identificatie van de hydroxo-ligatie in ferrisch GLB-33GD en de rol van E10Arg in de stabilisatie van het ligand. Het genitreerde GD van GLB-33 vertoonde bijzonder aanhoudende rhombische conformatie bij hoge temperaturen in vergelijking met neuroglobine en mutanten, in lijn met observaties voor Aplysia myoglobine dat ook een Arg-residu heeft op positie E10.

Het onderzoek naar *Ma*Pgb, uitgevoerd in Hoofdstuk 6, is het resultaat van een interne samenwerking binnen de onderzoeksgroep TSM^2. We hebben de uitgesproken verfrommelde heemzak van Pgb gerelateerd aan een kwantummechanische menging van de $S = 5/2$ en $S = 3/2$ toestanden van zijn ferrische vorm. Verder hebben we, gestimuleerd door het vorige onderzoek naar GLB-33GD en genitreerde gbs, de Pgb-nitrietinteractie onderzocht, die tot nu toe onontgonnen was. Interessant genoeg hebben we sterke spectrale veranderingen waargenomen bij het verlagen van de pH, en hebben we dit toegeschreven aan een ferrisch-NO-toestand als gevolg van de zure ontleding van nitriet. Dit levert meer bewijs voor de beoogde NO-scavenger-functie van Pgb.

In het laatste hoofdstuk van deze thesis, Hoofdstuk 7, hebben we de eerste karakterisering uitgevoerd van GLB-3, een cysteïne-rijk globine dat tot expressie komt in twee isovormen, a en b, waarbij de laatste een N-terminale verlenging bevat. In nauwe samenwerking met Zainab Hafideddine hebben we ontdekt dat sterke hexacoördinatie exogene ligand-interacties voorkomt, met CO tot nu toe als enige uitzondering. Bovendien is de vorming van disulfidebruggen zeer waarschijnlijk in dit globine. Er werden distale HE7A-pocketmutanten gecreëerd om de E7His-hexacoördinatie te bevestigen. Deze mutatie veroorzaakte ongebruikelijke structurele reorganisaties, resulterend in spectra vergelijkbaar met heme-eiwitten met een cysteïnaat-achtige ligandkarakter. In dit geval kan E12Cys de positie van de distale ligand innemen. Het ontbreken van ligand-interacties, de snelle auto-oxidatiesnelheid en de cysteïne-rijkdom suggereren een mogelijke functie in redoxsignalering. Het hoofdstuk beschrijft het optimalisatieproces voorafgaand aan de bepaling van de licht positieve redoxpotentiaal versus de standaard-waterstofelektrodepotentiaal (SHE) van het eiwit. Er werd een uitgebreide vergelijking gemaakt met andere bis-His-gecoördineerde gbs, en de bijzondere eigenschappen ervan worden besproken in het licht van een mogelijke functie in redoxsignalering. In het kader van de vorige hoofdstukken

en de scope van deze thesis bleek dat GLB-3 geen NiR-activiteit vertoonde. Dit onderstreept de brede functionele diversiteit die niet alleen wordt waargenomen in de gbs die in dit onderzoek zijn bestudeerd, maar ook in alle gbs. Structurele veranderingen tijdens de evolutie hebben geleid tot zeer gespecialiseerde gbs, en met voortdurend onderzoek en verkenning kunnen de mysteries van deze fascinerende biomoleculen worden ontrafeld en kan hun volledige scala aan rollen en functies worden onthuld.

dutch

Appendix A

Supporting information Chapter 4

A.1 Nitrite-ligated heme forms and nitri-heme

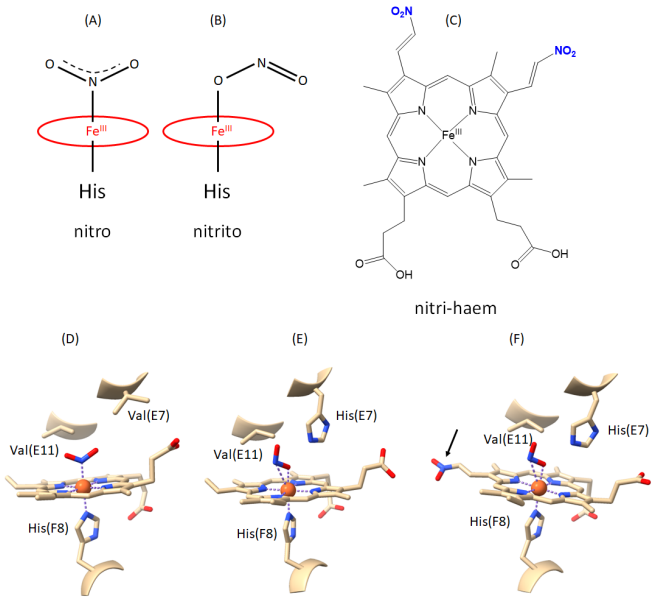

FIGURE A.1: Schematic representation of nitrite heme ligation forms, (A) nitro form and (B) nitrito form, as encountered in GLB-33GD and other heme proteins. The heme group is schematically indicated in red. (C) A nitri-heme with up to two nitrovinyl groups as observed in nitri-globins. (D) Example of nitro-ligation form in H64V variant of swMb (PDB ID 6CF0). (E) Example of nitrito-ligation form in wild-type hhMb (PDB ID 2FRF). (F) Example of nitri-heme formation in hhMb (with one nitrovinyl). The nitrovinyl is indicated with an arrow (PDB ID 3VAU). Note that in addition to the nitri-heme formation, also a nitrito ligation to the heme iron is observed.

A.2 pH-dependent stability of ferric GLB-33GDΔCys

The stability of Glb-33GD at different pH values in the presence and absence of a 50-fold molar excess nitrite was assessed via the analysis of the far UV region of the spectrum. The two negative ECD bands at 208 nm and 222 nm clearly indicated the α-helix secondary structure of GLB-33GD. Neither the buffer exchange towards sodium acetate buffer (pH 4 or 5) nor the presence of nitrite drastically affected the spectra, indicating that the secondary structure composition was retained at the conditions investigated.

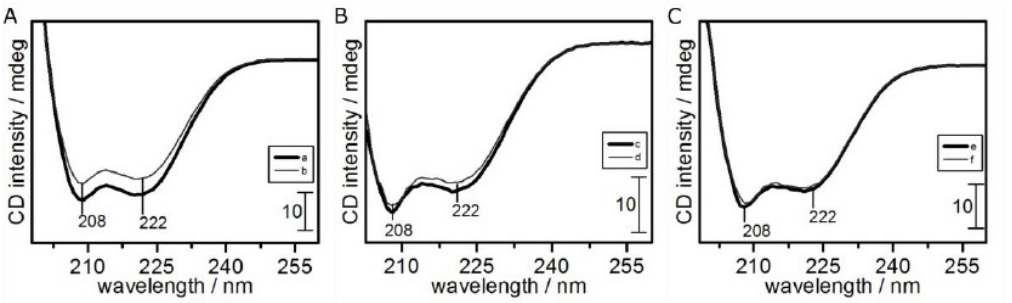

Figure A.2: The stability of GLB-33GDΔCys was assessed at pH 7.5 (A), 5 (B) and 4 (C), in the absence (a, c, e) and presence (f, d, f) of a 50-fold molar excess of sodium nitrite via the analysis of the far UV region of the ECD spectrum.

A.3 CW-EPR feature assignment – ferric GLB-33GD ΔCys at pH 7.5

To determine which signals are linked in the CW-EPR spectrum of a frozen solution of ferric GLB-33GD ΔCys at pH 7.5, the difference in the saturation behavior of the two LS species can be used. Fig. A.3 shows the spectra measured at different temperatures, normalized to the first low-field signal. It immediately identifies the signals that are linked to the same species.

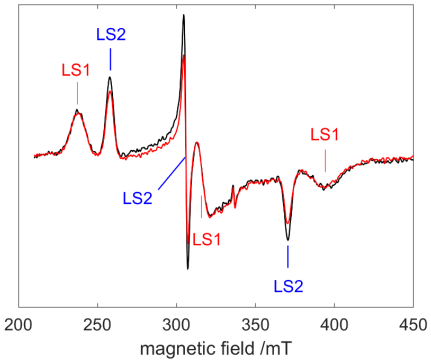

FIGURE A.3: Comparison of the X-band CW-EPR of ferric GLB-33GDΔCys at pH 7.5 recorded at 6 K (red) and 10 K (black) with a microwave power of 1 mW.

A.4 Simulations of CW-EPR spectra of ferric GLB-33GDΔCys at different pH

In this section, the different contributions to the simulations of the CW-EPR spectra of ferric GLB-33GD ΔCys at different pH are depicted. The corresponding EPR parameters are given in Table 4.1 of the main text.

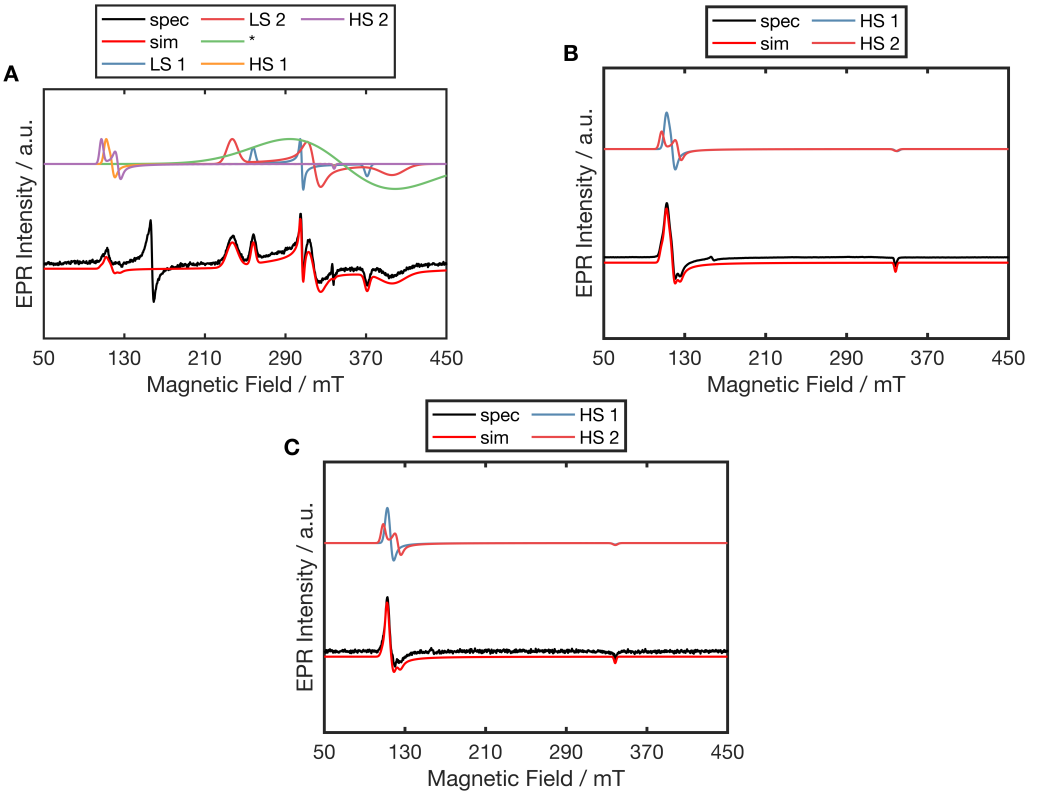

FIGURE A.4: Comparison of the X-band CW-EPR of ferric GLB-33GDΔCys at pH 7.5 (A), pH 5 (B) and pH 4 (C) recorded at 10 K with a microwave power of 1 mW. The spectral simulation is shown underneath, together with the individual components that make up the simulation. In panel A, a broad background signal is added for a better fit (*).

A.5 UV/Vis absorption spectrum of ferric GLB-33GD-ΔCys with increasing nitrite concentration

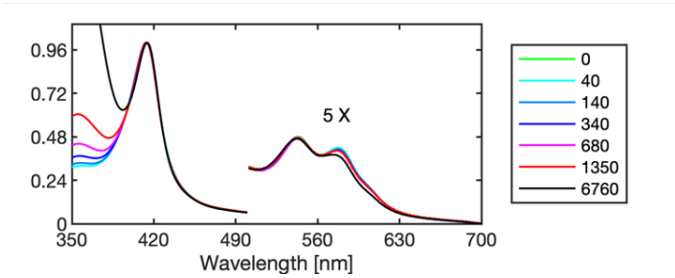

FIGURE A.5: Normalized UV-vis spectra of GLB-33GDΔCys in 50 mM Tris pH 7.5 in function of nitrite concentration. The legend indicates the molar ratio [nitrite]:[protein]. The large absorbance at 352 nm is due to the presence of nitrite in the sample.

A.6 rRaman spectra: Effect of incubation of ferric GLB-33GDΔCys with nitrite at different pH

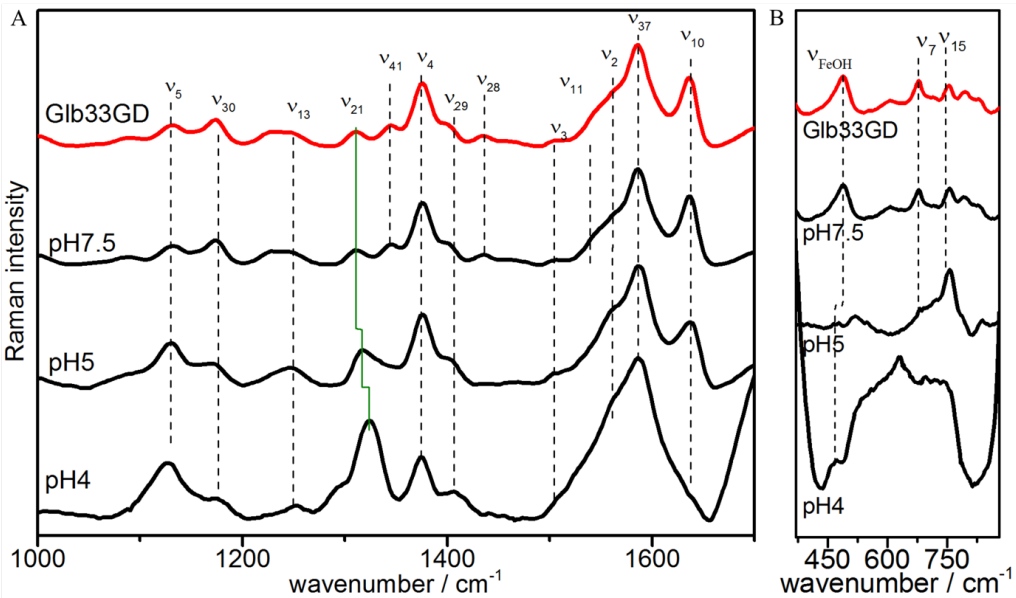

FIGURE A.6: High (Panel A) and low (Panel B) frequency rRaman spectrum of GLB-33GDΔCys (red) treated with 50 molar excess of nitrite at pH 7.5, 5 and 4 (black). In green the rRaman shift of the mode ν_{21} is marked.

A.7 Simulations of CW-EPR spectra of ferric GLB-33GDΔCys with sodium nitrite at different pH

In this section, the different contributions to the simulations of the CW-EPR spectra of ferric GLB-33GDΔCYS with sodium nitrite at different pH are depicted. The corresponding EPR parameters are given in Table 4.2 of the main text.

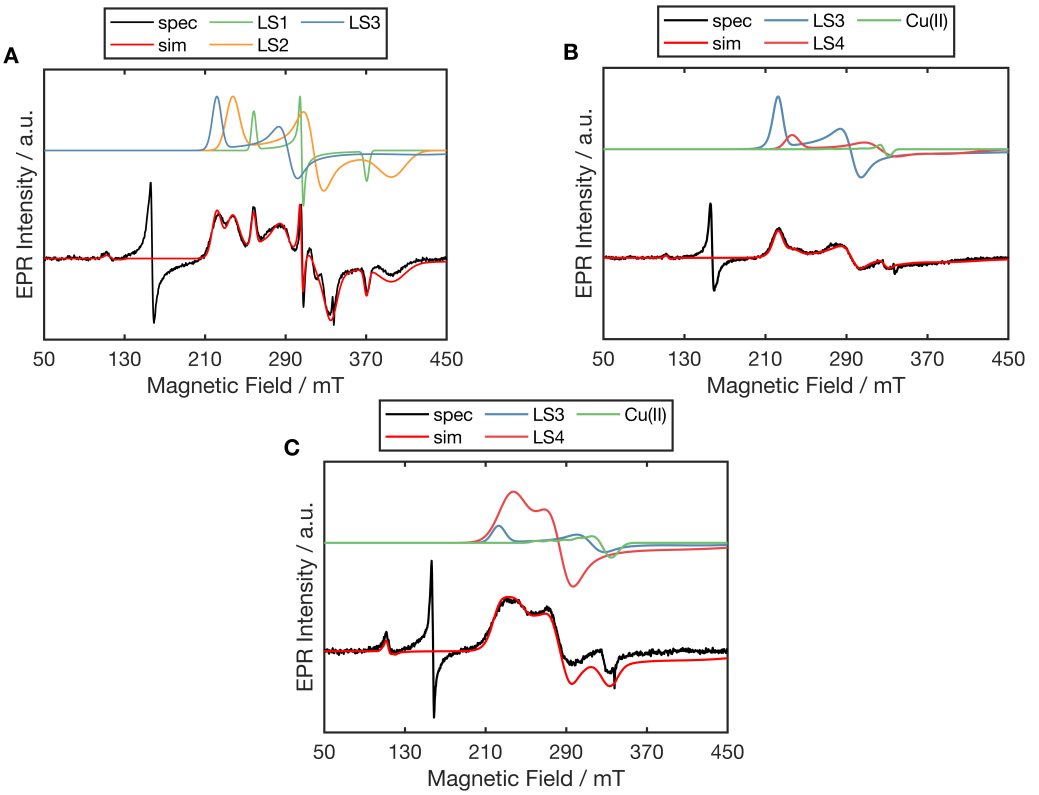

FIGURE A.7: Comparison of the X-band CW-EPR of ferric GLB-33GDΔCys with addition of a 50-times molar excess of $NaNO_2$ at pH 7.5 (A), pH 5 (B) and pH 4 (C) recorded at 10 K with a microwave power of 1 mW. The spectral simulation is shown underneath, together with the individual components that make up the simulation. Cu(II) represents a Cu(II) contaminant.

A.8 ESE-detected EPR

Fig. A.8 (A) shows the X-band ESE-detected EPR spectra of a frozen solution of ferric GLB-33GDΔCys with (black) and without (red) an excess of sodium nitrite at pH 7. The spectra are the sum of spectra recorded at 400 τ-values to circumvent as much as possible the effects of the deep nuclear modulations. Clear changes are observed upon addition of sodium nitrite in line with the observation in the CW-EPR spectra (Fig. 4.2,

main text). While the high-field feature of LS3 is hardly visible in CW-EPR, positive echo intensity is still found at high field in the ESE-detected EPR spectra allowing for a better estimation of the lower principal g value. Fig. A.8 (B) shows a comparison of the 2-pulse ESEEM spectra taken at 440 mT. While no modulation is seen for ferric GLB-33GD (magnetic field position falls outside of the spectral range of LS1 and LS2), a modulation is still visible when sodium nitrite is added. When comparing the ESE-detected EPR spectrum at the τ-value agreeing with the highest 2-pulse echo intensity (τ= 272 ns, dashed line in Fig. A.8 (B)), the high-field feature can be best seen (Fig. A.8 (D)). At an observer position of 480 mT, the 2-pulse ESEEM intensity has completely disappeared, indicating that this is the high-field limit of g_x feature of LS3 (Fig. A.8 (C)). The ESE-detected EPR at τ= 272 ns aids to determine the g_x value (simulation of LS3 in magenta in Fig. A.8 (D)). This assignment is further corroborated by the ESE-detected EPR spectra of a frozen solution of ferric GLB-33GD with an excess of sodium nitrite at pH 6 (Fig. A.9 (A)). While the 2-pulse ESEEM time trace at 480 mT is the same as the one taken at 200 mT (outside the EPR spectrum of LS3), there is still clear modulation at 440 mT in agreement with the observations at pH 7.5 (Fig. A.9 (B)). At pH4, the ESE-detected EPR still shows echo intensity at 480 mT (see arrow in Fig. A.9 (D)). Only at 550 mT, no echo modulation is observed (Fig. A.9 (C)). From this, the g_x value of LS4 is estimated to be $\approx$ 1.38 with an absolute lower limit of 1.26 (position where no signal is visible anymore).

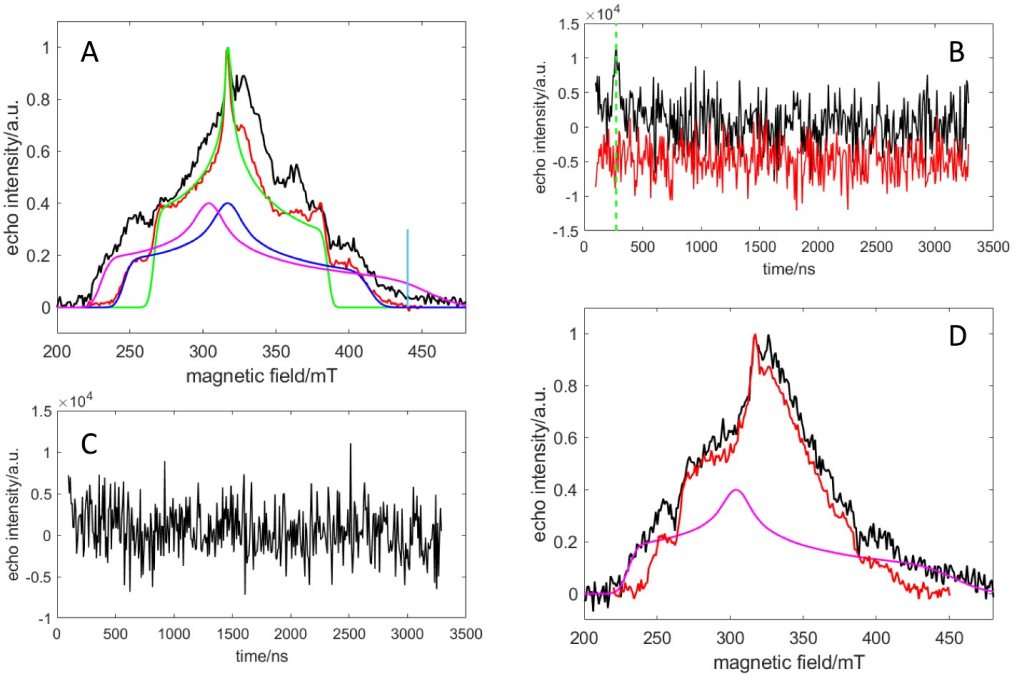

FIGURE A.8: (A) Experimental X-band ESE-detected EPR of a frozen solution of ferric GLB-33GDΔCys with (black) and without (red) an excess of sodium nitrite at pH 7. The spectra are the sum of spectra recorded at 400 τ-values from 96 ns to 3288 ns. The simulations of the different contribution of 6c/LS species are shown in blue (LS1), green (LS2) and magenta (LS3). The simulation parameters are given in Table 4.2, main text. The peak in the [327-340] mT area is due to a cavity background signal (Cu(II)) (B) Comparison of the 2-pulse ESEEM experiment at 440 mT for a frozen solution of ferric GLB-33GD with (black) and without (red) an excess of sodium nitrite at pH 7. The magnetic field setting is indicated in cyan in (A). The red curve is shown with an offset to facilitate comparison. (C) 2-pulse ESEEM experiment at 480 mT for a frozen solution of ferric GLB-33GD with an excess of sodium nitrite at pH 7. (D) Comparison of the experimental ESE-detected EPR spectrum for τ= 272 ns for a frozen solution of ferric GLB-33GD with (black) and without (red) an excess of sodium nitrite at pH 7. The τ-value was chosen at the maximum height of the 2p-ESEEM modulation at 440 mT (see dashed green line in (B)). The simulation of the contribution of LS3 is shown in magenta as a comparison.

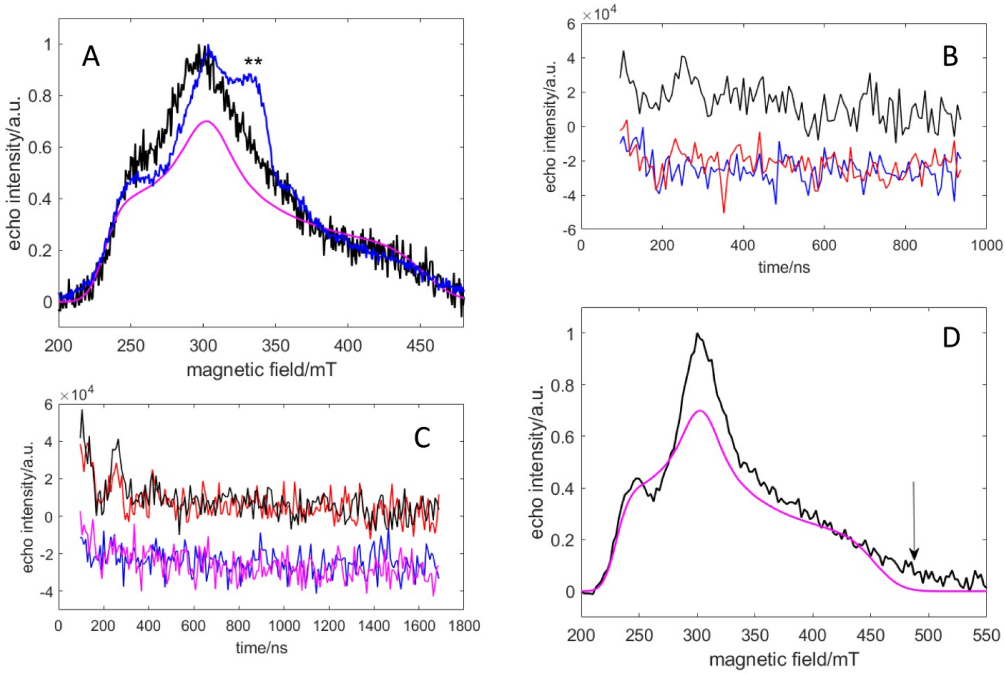

FIGURE A.9: (A) Experimental X-band ESE-detected EPR of a frozen solution of ferric GLB-33GD with an excess of sodium nitrite at pH 6 (blue). The spectrum is the sum of spectra recorded at 106 τ-values from 96 ns to 936 ns. The black spectrum is obtained by taking the Fourier-transform of the 2D ESE-detected EPR and summing the spectra in the [0-10] MHz range of the ESEEM dimension. This ESEEM area entails all the EPR contributions of species with 14 N hyperfine interactions (i.e. the heme centres). It allows to remove the cavity background signal (Cu(II) marked with **). The simulation of the contribution of LS3 is shown in magenta as a comparison; the corresponding EPR parameters are given in Table 4.2, main text. (B) Comparison of the 2-pulse ESEEM experiment at 200 mT (blue), 440 mT (black) and 480 mT (red) for a frozen solution of ferric GLB-33GD with an excess of sodium nitrite at pH 6. The red and blue curve are shown with an offset to facilitate comparison. (C) Comparison of the 2-pulse ESEEM experiment at 200 mT (blue), 440 mT (black), 480 mT (red) and 550 mT (magenta) for a frozen solution of ferric GLB-33GD with an excess of sodium nitrite at pH 4. The magenta and blue curve are shown with an offset to facilitate comparison. (D) Experimental X-band ESE-detected EPR of a frozen solution of ferric GLB-33GD with an excess of sodium nitrite at pH 4 (black). The ESE-detected EPR spectra were recorded for 200 τ-values from 96 ns to 1688 ns. The black spectrum is obtained by taking the Fourier-transform of the 2D ESE-detected EPR and summing the spectra in the [0-10] MHz range of the ESEEM dimension. The simulation of the contribution of LS3 is shown in magenta as a comparison; the corresponding EPR parameters are given in Table 4.2, main text. The arrow shows the high-field area where signal intensity is observed where this was not observed before.

A.9 Mass spectrometry

Fig. A.10 shows the control MS experiments on ferric GLB-33GDΔCys without the addition of sodium nitrite. The results should be compared with the ones reported in Fig. 4.5.

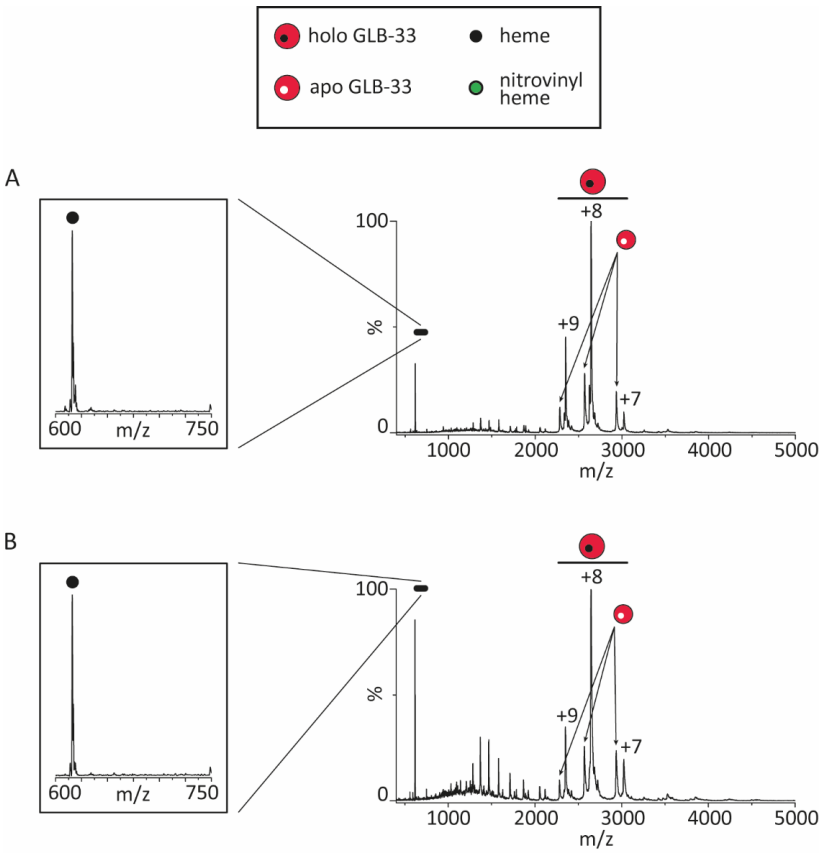

FIGURE A.10: MS measurements of ferric GLB-33GD|*delta*Cys (control, without addition of $NaNO_2$) at pH 7.5 (A) and pH 4.0 (B) at a collision energy of 50 V.

Protein	Species	nitrite binding	g-values			Crystal field parameters			Ref.
			g_x	g_y	g_z	V/λ	Δ/λ	V/Δ	
GLB-33GDΔCys pH 7.5	LS3	Nitrito	∼1.53	2.29	3.03	1.81	3.37	0.54	T.w. [234]
GLB-33GDΔCys pH 7.5	LS3	Nitrito	1.53	2.26	3.00	1.83	3.49	0.52	
GLB-33GDΔCys pH 4.0	LS3*	Nitrito	1.53	2.13	3.01	1.74	4.45	0.39	
	LS4	Nitro	∼1.38	2.35	2.84	1.88	2.26	0.83	
wild-type *C*Cld		Nitrito	1.64	2.24	2.87	2.14	4.03	0.53	[248]
		Nitro	1.62	2.40	2.73	2.48	2.58	0.96	
		Nitro	1.62	2.42	2.69	2.58	2.39	1.08	
wild-type *Nd*Cld		Nitrito	1.56	2.20	2.95	1.89	3.97	0.48	[248]
		Nitro	1.53	2.39	2.77	2.22	2.41	0.92	
HsMb		Nitrito	1.57	2.20	2.95	1.90	4.04	0.47	[248]
MetHb		Nitrito	1.47	2.16	2.90	1.80	3.59	0.50	[274]
		Nitrito	1.47	2.33	3.03	1.77	2.91	0.61	
NP4		Nitro	1.51	2.42	2.74	2.26	2.17	1.04	[107]

TABLE A.1: Principal g values and corresponding crystal field parameters for the low-spin NO_2^- complexes of GLB-33GDΔCys and related heme proteins as a reference. T. w. = this work..

A.10 Crystal-field analysis

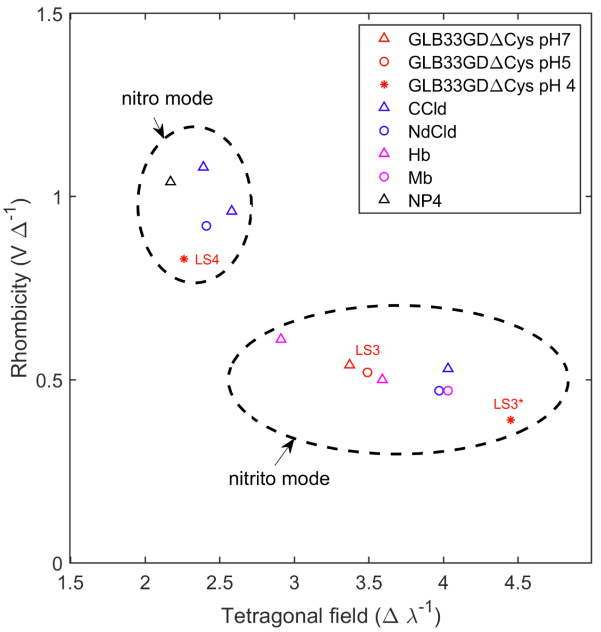

FIGURE A.11: "Blumberg-Peisach" diagram constructed with crystal-field parameters derived from the principal g values of nitrite-bound LS species together with reference nitrite-bound heme proteins as listed in Table A.1 and as indicated in the figure legend. The dashed circles highlight the apparent two different groups in which the LS-species can be divided and the assignment based on the literature [248] is given.

A.11 ESEEM and HYSCORE of GLB-33GDΔCys with excess of $Na^{14}NO_2$ and $Na^{15}NO_2$

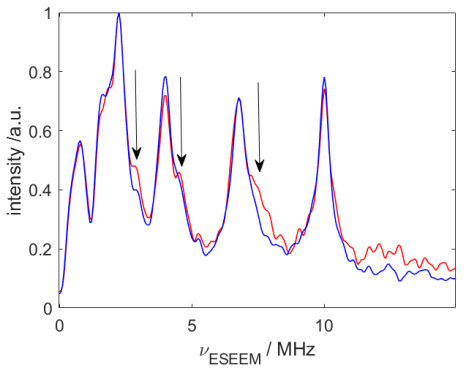

FIGURE A.12: Comparison between the three-pulse ESEEM spectra of frozen solutions of ≈ 1 mM ferric GLB-33GDΔCys at pH 7.5 after addition of a 50-fold excess of $Na^{14}NO_2$ (red) and $Na^{15}NO_2$ (blue). 25 % (v/v) glycerol was added to the solution as a cryoprotectant. The spectra were recorded at 235 mT, an observer position agreeing with $g = g_z$ of LS3. The arrows indicate small differences in the spectra.

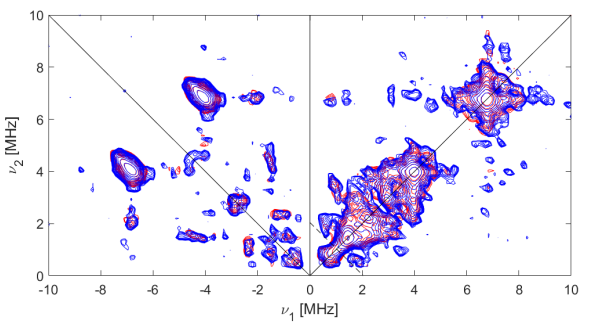

FIGURE A.13: Comparison between the HYSCORE spectra of frozen solutions of ∼ 1 mM ferric GLB-33GDΔCys at pH 7.5 after addition of a 50-fold excess of $Na^{14}NO_2$ (red) and $Na^{15}NO_2$ (blue). 25 % (v/v) glycerol was added to the solution as a cryoprotectant. The spectra were recorded at 237 mT, an observer position agreeing with $g = g_z$ of LS3.

A.12 Abs/ECD spectra of Myoglobin with nitrite at different pH

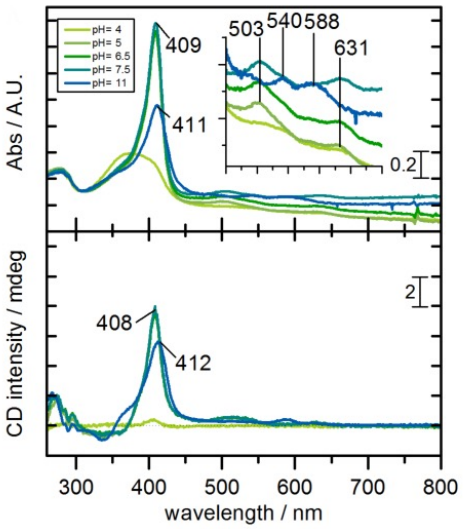

FIGURE A.14: Abs (top) and ECD (bottom) spectra of 57 µM Mb in sodium acetate (pH 4, 5) or Tris HCL buffer (pH 6.5, 7.5 and 11).

A.13 Movement of Arg in *Al*Mb heme pocket

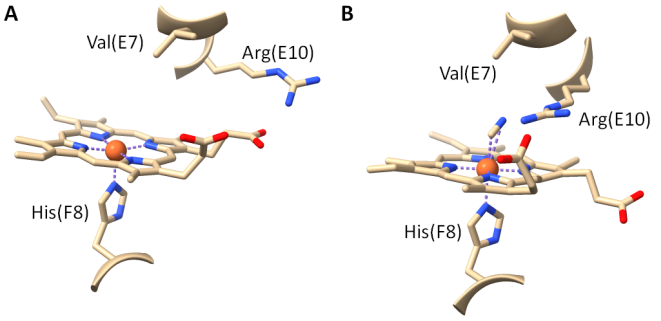

FIGURE A.15: Representation of the relative orientation of key residues in heme pocket of ferric *Al*Mb without a distal ligand (PDB ID: 1MBA) (A) and with a distal cyanide ligand (PDB ID: 2FAL) (B), highlighting the movement of the Arg residue in and out of the heme pocket.

Appendix B

Supporting information Chapter 5

B.1 Primers

Primer	SEQUENCE (5'–>3')
I69H f	CAT-GCC-AAG-TTT-CAA-GAG-CAC-GGA-GGT-CGA-ATC-ACC-TC
I69H r	GAG-GTG-ATT-CGA-CCT-CCG-TGC-TCT-TGA-AAC-TTG-GCA-TG
R72V f	AGT-TTC-AAG-AGA-TCG-GAG-GTG-TAA-TCA-CCT-CCT-TCA-TAT-CAG
R72V r	CTG-ATA-TGA-AGG-AGG-TGA-TTA-CAC-CTC-CGA-TCT-CTT-GAA-ACT
R72V I69H f	GAT-CAT-GCC-AAG-TTT-CAA-GAG-CAC-GGA-GGT-GTA-ATC-ACC-TCC-TTC-ATA-TCA-GA
R72V I69H r	TCT-GAT-ATG-AAG-GAG-GTG-ATT-ACA-CCT-CCG-TGC-TCT-TGA-AAC-TTG-GCA-TGA-TC
S41C f	CAT-CCG-AAT-TTG-TGT-AAA-AAC-GAT-GAA-CCC
S41C r	GGG-TTC-ATC-GTT-TTT-ACA-CAA-ATT-CGG-ATG
S56C f	CCC-TTC-TAA-ACG-GTT-CAT-GTA-AAC-GTA-GTA
S56C r	TAC-TAC-GTT-TAC-ATG-AAC-CGT-TTA-GAA-GGG

Table B.1: List of primers (forward (f) and reverse (r)) used for site-directed mutageneisis of the pET23a plasmids encoding GLB-33GD.

B.2 X-band CW EPR of GLB-33GD and Mb

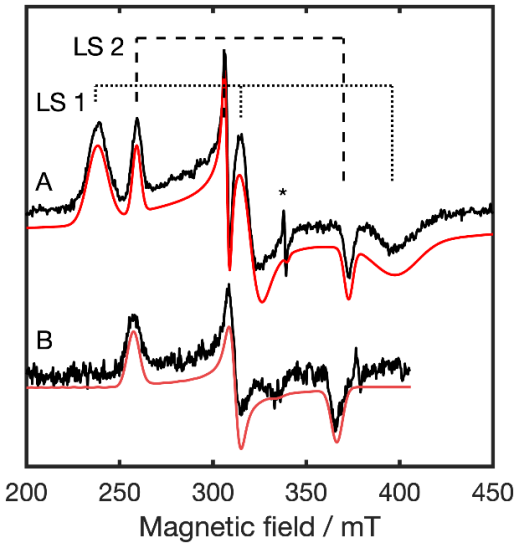

FIGURE B.1: X-band CW EPR spectra of GLB-33GD and Mb. The low-spin regions of the X-band CW-EPR spectra of frozen solutions of GLB-33GD at pH 7.5 (A) and Mb at pH 11.9 (B) at T = 10 K with corresponding Easyspin simulation (red). The two low-spin species LS1 and LS2 are indicated by a dotted line and a dashed line, respectively, and an unknown radical with (*). Based on the Easypin simulation shown in red, we can estimate the relative contribution of LS1 to LS2 as 60 to 40 %, respectively.

B.3 Three-pulse ESEEM spectra

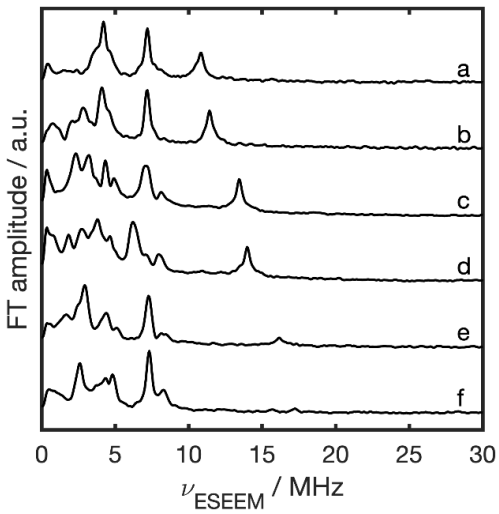

FIGURE B.2: Three pulse ESEEM spectra of a frozen solution of GLB-33GDΔCys at pH 7.5. Sample collected at canonical observer positions (g_z, g_y, g_x) of LS1 (a, d, f) and LS2 (b, c, e). The corresponding magnetic fields from (a-f) are 254.0 mT, 268.3 mT, 315.5 mT, 328.1 mT, 379.3 mT and 404.0 mT, respectively. The spectra were collected at $T = 6$ K and are the sum of 20 τ values ranging between [96:20:496] ns.

B.4 HYSCORE of Mb and simulations

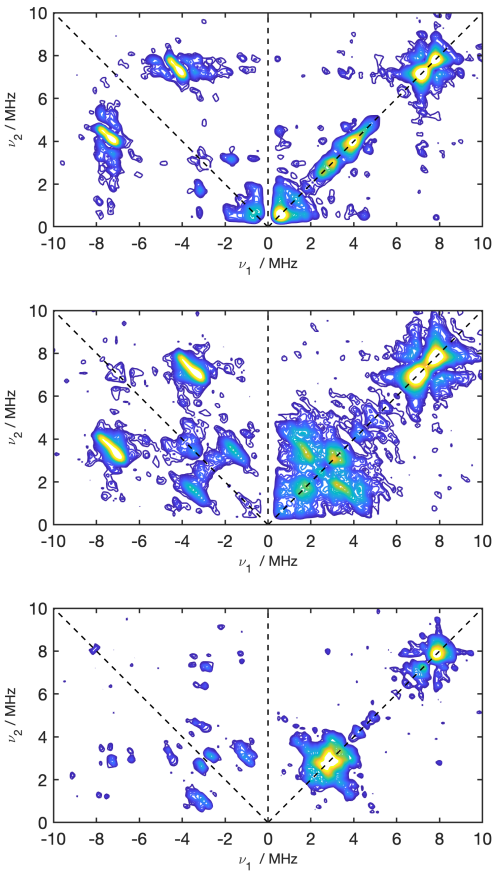

FIGURE B.3: The symmetrized HYSCORE spectra of a frozen Mb solution at pH 11.9 collected at 270 (top), 323.4 (mid) and 380.8 (bottom) mT corresponding g_z, g_y and g_x, respectively. The spectra are the sum of three τ-values: 88, 96 and 104 ns (top), 88, 104 and 148 ns (mid) and 88, 104 and 124 ns(bottom).

Appendix C

Supporting information Chapter 6

C.1 Sequence of C-terminal His$_6$-tagged *Ma*Pgb

MSVEKIPGYT YGETENRAPF NLEDLKLLKE AVMFTAEDEE YIQKAGEVLED QVEE-ILDTW YGFVGSHPHL LYYFTSPDGT PNEKYLAAVR KRFSRWILDT CNRSYDQAWL DYQYEIGLRH HRTKKNQTDN VESVPNIGYRY LVAFIYPIT ATMKPFLARK GHT-PEEVEKM YQAWFKATTL QVALWSYPYV YGDFLEHHH HHH

C.2 Absorbance and ECD spectra of ferric *Ma*Pgb and myoglobin at pH 7.5.

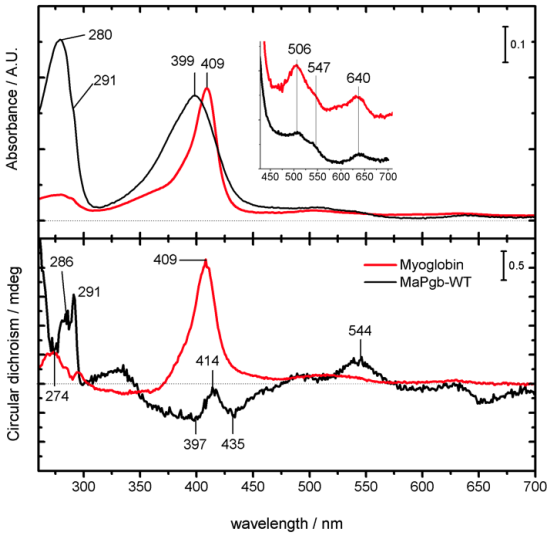

FIGURE C.1: As-purified ferric *Ma*Pgb (black) and ferric myoglobin (aquomet form) (red), both measured Trizma® hydrochloride buffer at pH 7.5. Absorption (top) and ECD (bottom) spectra were recorded in the spectral region 260-700 nm.

C.3 Secondary structure of ferric *Ma*Pgb

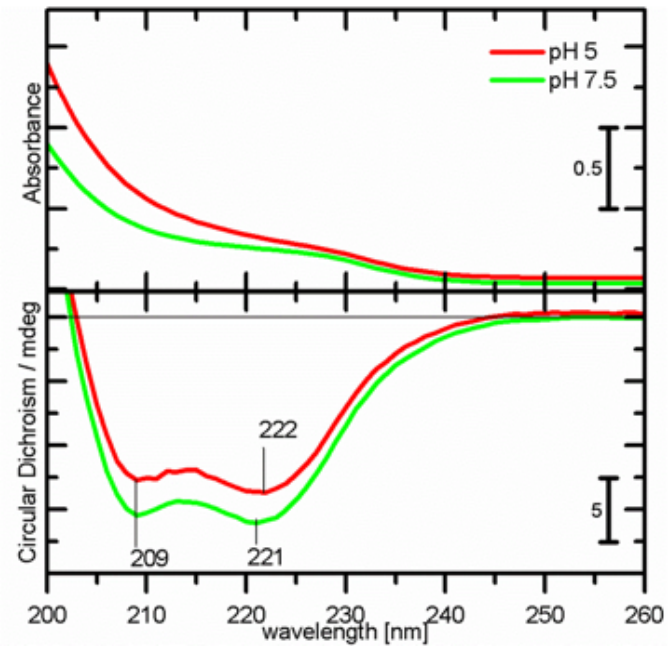

FIGURE C.2: Ferric *Ma*Pgb (0.056 mM of heme content) at pH 7.5 (green) in comparison with ferric *Ma*Pgb at pH 5 (red), measured in Trizma® hydrochloride buffer and acetate buffer, respectively. Absorption (top) and ECD (bottom) spectra were recorded in the spectral region 200-260 nm.

C.4 Low frequency rRaman spectrum of *Ma*Pgb upon nitrite treatment

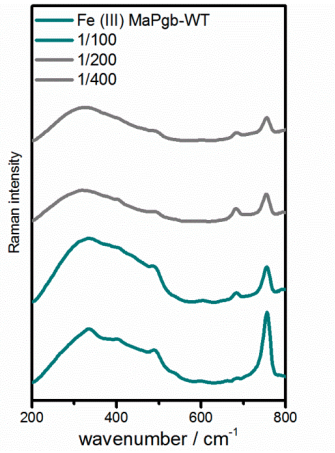

FIGURE C.3: rRaman spectra of 0.057 mM *Ma*Pgb and its complexes with nitrite in sodium acetate buffer at pH 5 in the spectral range 200-800 cm^{-1}. *Ma*Pgb (0.056 mM of heme content) was incubated with 50, 100, 200 and 400 molar ratio excess nitrite, respectively.

C.5 rRaman characterization of ferric *Ma*Pgb

This work			Reference	
Mode	**Wavenumber** [cm^{-1}]	**Assignment**	**Author**	**Wavenumber** [cm^{-1}]
ν_{10}	1631	5C/HS	[325]	
ν_2	1573	5c/HS	[325]	1573
ν_{11}/ν_2	1552	6C/HS	[325]	1556
ν_3	1460	5c/HS(FeII)	[325]	1470
	1437			
ν_{29}	1405		[197]	1403
ν_4	1376	5c/HS	[325]	1368-1374
ν_{41}	1344		[197]	1341
ν_{21}	1307	$\delta(C_aH{=})_{4or2}$	[197]	1301-1316
	1227			
ν_{30}	1165		[197]	1169
ν_{14}	1127		[197]	1121
	1081			
ν_{45}	999	C_β-vinyl stretch	[197]	989
	923	$\gamma(=C_bH_2)_s$	[197]	919
	844			
ν_{16}	755		[379]	751
	686			
ν_{48}	599		[379]	605
γ_{21}	540		[197]	547
	490			
	403	$\delta(C_\beta C_\alpha C_b)_4$	[197]	405
γ_6	335		[197]	337
	233			

Table C.1: Table of rRaman marker bands: position of main rRaman marker bands of ferric unligated *Ma*Pgb.

C.6 Low-temperature X-band CW experiments

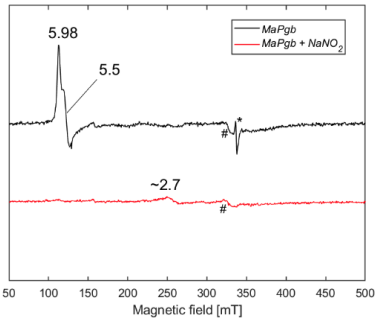

FIGURE C.4: X-band CW EPR spectra of frozen solutions of *Ma*Pgb at pH 5, with a 400 × molar excess of $NaNO_2$ in the presence of 25 % (v/v) glycerol used as cryoprotectant, collected at T=10 K. # is due to a background signal Cu(II). *shows the presence of radical contaminant.

The EPR spectrum of ferric *Ma*Pgb can be ascribed by a rhombic effective g tensor, indicative of an admixture of the $S = 5/2$ state with an $S = 3/2$ state (formation of a QS state) [319]. Since glycerol was added as a cryoprotectant to the sample, it is unclear whether the here observed signal is due to a 5c/QS or a 6c/QS species. In any case, the EPR confirms the occurrence of QS states in ferric *Ma*Pgb.

Addition of sodium nitrite to ferric *Ma*Pgb leads to a disappearance of the EPR signal of the ferric component in line with the formation of an EPR-silent NO-ligated ferric heme complex. No signal of ferrous nitrosylated *Ma*Pgb is observed, confirming that NO binding to the ferric form is not succeeded by a further reductive nitrosylation step as is observed at pH 7 and higher [176].

C.7 Protein stability in the presence of nitrite.

To rule out the possible denaturation of *Ma*Pgb in presence of high concentration of nitrite at pH5, far-UV ECD spectra were recorded (Fig. C.5). ECD spectra of *Ma*Pgb (0.0056 mM in heme concentration), incubated with 0.28, 0.56, 1.12, 1.68 and 2.24 mM $NaNO_2$ in sodium acetate buffer (pH 5), were measured in the range 260–195 nm. In the far-UV region of the ECD spectrum (Fig. C.5, Panel A) the presence of the two negative minima at 208 nm and 222 nm clearly indicated the alpha-helix secondary structure of *Ma*Pgb. Since the variation in the ratio between the ellipticity measured at 222 and 208 nm is indicative of the protein structural changes, it was plotted as function of the nitrite concentration incubated with *Ma*Pgb for the treatments at the pH 5. Minor variations were found in the 222/208 nm ratio when the concentration of the ligand was increased, as well as an overall decrease of the ECD intensity, indicating the unfolding of a minor fraction of the protein in presence of nitrite at mildly acidic pH values occurred.

Nevertheless, the treatment of the globin with increasing amount of nitrite in mildly acidic conditions did not affect the spectra drastically. Moreover, the ellipticity detected in the range 300-600 nm intrinsically proved that the heme chromophore was correctly located into the protein matrix. A total loss of the heme group as consequence of the protein degradation, would imply the disappearance of all optical activity of the protein in that specific spectral range (Fig. C.14). Therefore, we could conclude that the secondary structure composition was retained during the nitrite treatment.

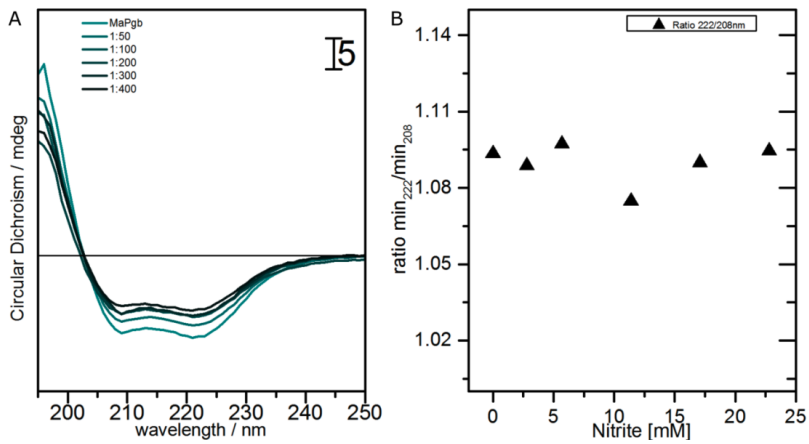

FIGURE C.5: Panel A: ECD spectra of *Ma*Pgb (0.056 mM in heme concentration) in complex with sodium nitrite in sodium acetate buffer at pH 5 in the spectral range 195-250 nm. Variations in the 222/208 nm ratio as function of the concentration of $NaNO_2$ used for the sample treatment at pH 5 (black triangle) are reported in Panel B.

C.8 pH variation

While the clear signature of a full conversion of ferric *Ma*Pgb to its Fe(III)−NO form is observed at pH 5 upon addition of a 400× excess of sodium nitrite, only the onset of the transformation can be seen at pH 6.2. At pH 7.5, no nitrosylated ferric *Ma*Pgb was observed under the same conditions (not shown). This indicates that pH plays a role in the formation of Fe(III)−NO form. The spontaneous decomposition of nitrite with formation of NO is known to increase significantly at lower pH (NO-formation rate in 22.8 mM $NaNO_2$ at pH 5 is 4.48 10^{-7} $M\,s^{-1}$ and at pH 6.2 is 2.88 10^{-8} $M\,s^{-1}$) [341].

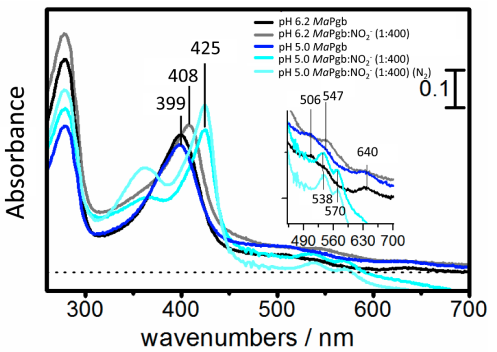

FIGURE C.6: Absorption spectra of ferric *Ma*Pgb (0.057 mM in heme content) at pH 5 (dark blue) and pH 6.2 (black). Effect of addition of a 400-fold excess of sodium nitrite to ferric *Ma*Pgb (0.057 mM in heme content) at pH 6.2 (grey) and pH 5 (cyan). The effect of the reaction in N_2 and with addition of air was also tested.

	Abs / nm					rRaman / cm^{-1}			
	Soret	Q_β	Q_α	CT	Assign	ν_4	ν_3	ν_2	ν_{10}
*Ma*Pgb Fe(III)	399	506	547	638	5c/HS	1376	1460	1573	1631
1:50	405								1631
1:100	421	538	570			1376	1460/1506	1578	1631
1:200	425	538	570		6c/LS	1376	1460/1506	1578	1631
1:300	425	538	570		6c/LS				
1:400	425	538	570		6c/LS	1376	1460/1506	1580	1631

TABLE C.2: Main Abs and rRaman bands of Fe(III) *Ma*Pgb and Fe(III) *Ma*Pgb in complex with nitrite.

this work (5c/QS)			Reference (Mb)	
Mode	Wavenumber cm^{-1}	Assignment	Reference	Wavenumber cm^{-1}
ν_{10}	1631	5c/HS, C=C vinyl stretch	[325]	
ν_2	1573	5c/HS	[325]	1573
ν_{11}, ν_2	1552	5c/HS	[325]	1556
ν_3	1460, 1437	5c/HS(FeII) (1460)	[325]	1470
ν_{29}	1405		[197]	1403
ν_4	1376	5c/HS	[325]	1368-1374
ν_{41}	1344		[197]	1301-1316
ν_{21}	1307	$\delta(C_a\mathrm{H}{=})_{4or2}$	[197]	1301-1316
	1227			
ν_{30}	1165		[197]	1169
ν_{14}	1127, 1081		[197]	1121
ν_{45}	999	C_β-vinyl stretch	[197]	989
	923	$\gamma(=C_bH_2)_s$		919
	844			
ν_{16}	755, 686		[379]	751
ν_{48}	599		[379]	605
γ_{21}	540, 490, 403	$\delta(C_\beta\ C_a\ C_b)_4$ (403)	[197]	547, 405
γ_6	335, 233		[197]	337

Table C.3: Position of main rRaman marker bands of ferric *Ma*Pgb and their assignments.

C.9 Bi-exponential fit to the time traces in Fig. 6.5 (D)

	k_f / s^{-1}	k_s / s^{-1}	C(1)	C(2)	C(3)
1:400 *Ma*Pgb:NO_2^-	17.35 $\times 10^{-3}$	0.92 $\times 10^{-3}$	97.6	58.4	39.1
	($\pm 1.5 \times 10^{-3}$)	($\pm 0.04 \times 10^{-3}$)	(± 0.5)	(± 1.9)	(± 1.4)
1:100 *Ma*Pgb:NO_2^-	3.39 $\times 10^{-3}$	0.21 $\times 10^{-3}$	61.2	20.0	38.8
	($\pm 0.4 \times 10^{-3}$)	$\pm 0.01 \times 10^{-3}$)	(± 0.5)	(± 0.9)	(± 0.5)

Table C.4: Bi-exponential fit to the time traces in Figure 6D.

C.10 TMA-PTIO spin-trapping experiments

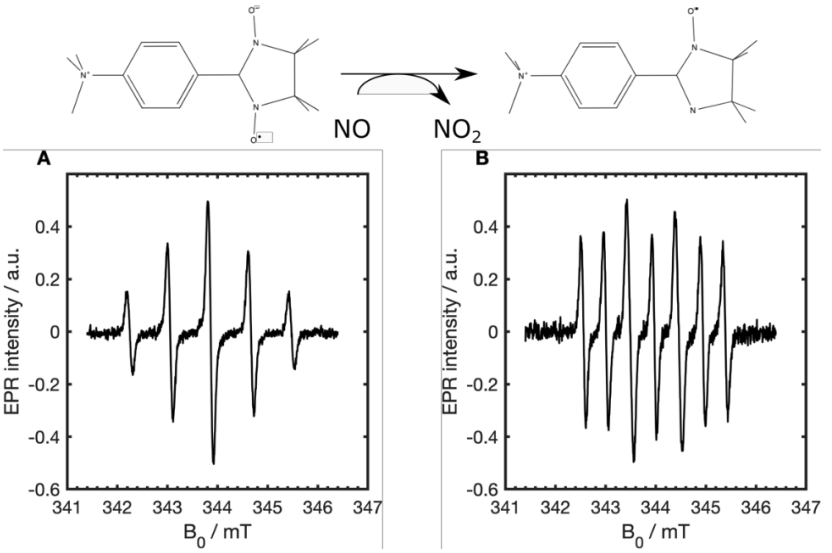

FIGURE C.7: Reaction mechanism of TMA-PTIO (A) to TMA-PTI (B) conversion in the presence of NO. The corresponding room temperature X-band CW-EPR spectra are given underneath the chemical structures of the radicals.

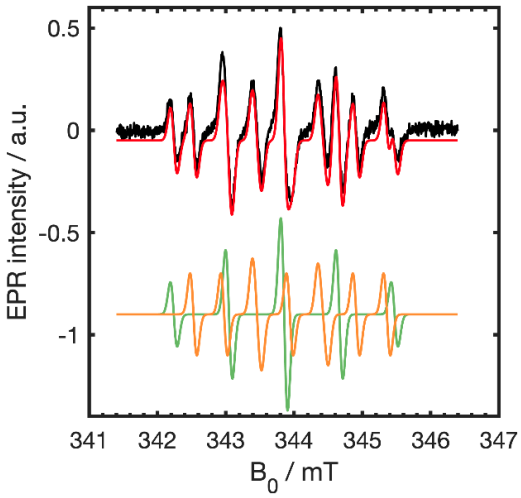

FIGURE C.8: Illustration of a simulation when a mixture of TMA-PTIO and TMA-PTI is present. The X-band CW-EPR spectrum at room temperature (black) is simulated (red) and consists of the sum of contributions of TMA-PTIO (lime green) and TMA-PTI (gold). The spectrum of pure TMA-PTIO consists of 5 lines which can be simulated using a system with two equivalent ^{14}N nuclei, with the isotropic hyperfine value $A = 22.69$ MHz and a g-factor of 2.0082. The spectrum of TMA-PTI consists of 7 lines and can be simulated using two inequivalent ^{14}N nuclei with inequivalent hyperfine values 12.63 and 27.17 MHz and a g-factor of 2.0077.

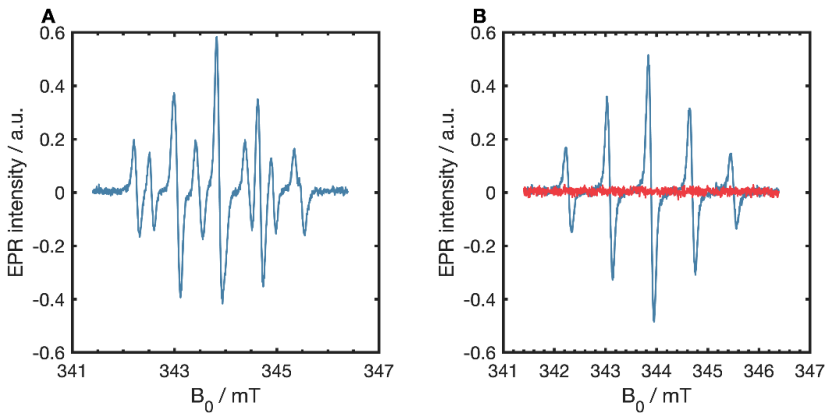

FIGURE C.9: Panel A shows the room temperature X-band CW-EPR spectrum of 25 µM TMA-PTIO when an excess of NONOate is added at pH 7.5. The appearance of the EPR signal of TMA-PTI shows the effectiveness of TMA-PTIO as an NO spin trap. Panel B shows that 10 µM *Ma*Pgb without addition of $NaNO_2$ (2.5× molar excess, blue), does not lead to TMA-PTI formation, and that *Ma*Pgb itself without TMA-PTIO (red) does not contribute to the total signal intensity at room temperature.

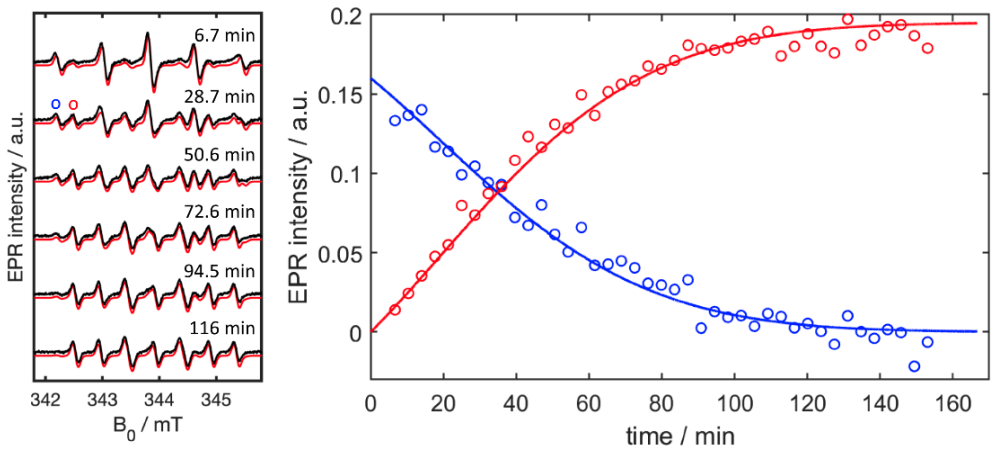

FIGURE C.10: Left: the room temperature X-band CW-EPR spectra (black) and corresponding simulations (red) of 25 µM TMA-PTIO collected over time after addition of 4 mM nitrite. The experiments were performed in a sodium acetate buffer at pH 5. All spectra were collected with a microwave power P=1.5 mW and a modulation amplitude of 0.1 mT. Each simulation consists of a linear combination of the spectra of pure TMA-PTIO and TMA-PTI, respectively. Over time, TMA-PTIO is converted to TMA-PTI. Right: time dependence of the experimental signal intensity of TMA-PTIO (represented by the peak maximum indicated by 'o' (blue) in the right spectrum) and TMA-PTI (represented by the peak maximum 'o' (red) in the right spectrum). The solid lines are simulations considering the model described above.

Fig. C.10 (right) shows the time-dependent conversion of TMA-PTIO to TMA-PTI as it traps nitric oxide that is formed spontaneously in a 4 mM sodium nitrite solution at pH 5. The time dependence can be simulated using a simple model in which the concentration of NO is predicted using the NO formation rate described in [341]:

$$\frac{d[\mathrm{NO}]}{dt} = \frac{K_1[\mathrm{NO_2}^-][\mathrm{HNO_2}]}{[\mathrm{NO_2}^-] + K_\beta}, \tag{C.1}$$

with

$$[\mathrm{HNO_2}] \cong \frac{[\mathrm{H}^+][\mathrm{NO_2}^-]_0}{[\mathrm{H}^+] + K_\alpha}; [\mathrm{NO_2}^-] \cong \frac{K_\alpha[\mathrm{NO_2}^-]_0}{[\mathrm{H}^+] + K_\alpha}. \tag{C.2}$$

The trapping of NO is then described by the simple equation

$$\frac{d[\mathrm{TMA{-}PTIO}]}{dt} = -k_1[\mathrm{TMA{-}PTIO}][NO]. \tag{C.3}$$

The build-up of TMA-PTI evidently follows the decay of TMA-PTIO

$$\frac{d[\mathrm{TMA{-}PTI}]}{dt} = k_1[\mathrm{TMA{-}PTIO}][NO]. \tag{C.4}$$

In order to fit the decay curve in Figure C.10, the initial concentration of NO needed to be taken different from zero, in line with the fact that the nitrite was added from

a concentrated stock solution in which nitrite disproportionation will have been initiated ($[\mathrm{NO}]_0$ = 100-300 µM depending on the batch). The curves in Fig. C.10 are fitted assuming $[\mathrm{NO}]_0$ = 150 (±50) µM and k_1 = 1.3 (±0.2)$\mathrm{M}^{-1}\,\mathrm{s}^{-1}$.

The decay curve (blue circles) can also be fitted satisfactorily with an apparent first-order dependence, with a rate constant 2.4 (± 0.5) $10^{-4}\mathrm{s}^{-1}$. Although this rate constant has no physical meaning it can serve to compare with the apparent first-order reaction constants k_f and k_s observed for the formation of *Ma*Pgb-NO (Table C.4). The time-dependence of the EPR spectra of TMA-PTIO and TMA-PTI in the presence of nitrite and ferric *Ma*Pgb (Figure 6.6 (B)) or ferric Mb (Figure C.11) can be satisfactorily simulated using the same model as introduced above for the case without protein. The only exception is that the build-up of TMA-PTI is now followed by a decay phase in which TMA-PTI is degenerated towards other products. This is introduced in the model assuming

$$\frac{d[\mathrm{TMA{-}PTI}]}{dt} = k_1[\mathrm{TMA{-}PTIO}][\mathrm{NO}] - k_2[TMA - PTI]. \tag{C.5}$$

The curves in Fig. C.11 and Fig. 6.6 (B) can both be satisfactorily fitted assuming $[\mathrm{NO}]_0$ = 300 (± 50) µM, k_1 = 1.3 (± 0.2) $\mathrm{M}^{-1}\,\mathrm{s}^{-1}$ and k_2 = 6.5 10^{-5} (± 1.0 10^{-5}) s^{-1}.

The similarity in the decay parameters indicates that the presence of *Ma*Pgb does not alter significantly the ability of TMA-TPIO to trap NO and hence provides no clear proof of a specific nitrite dismutase activity.

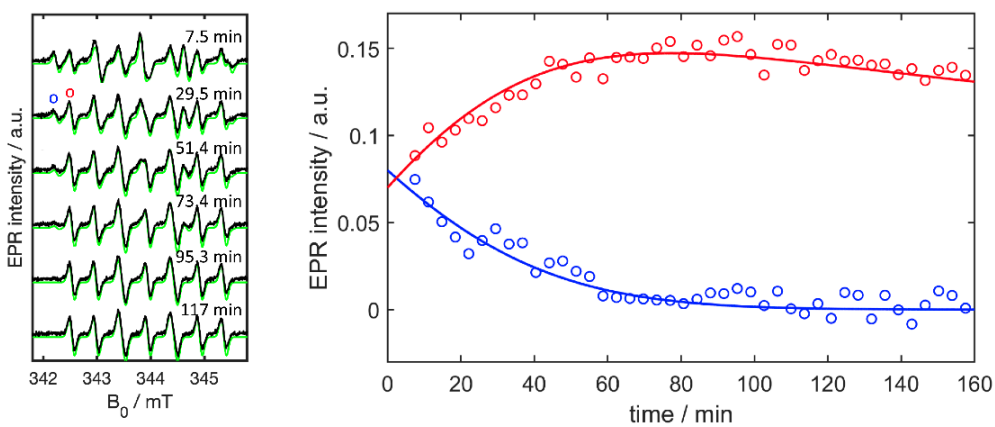

FIGURE C.11: Left: the room temperature X-band CW-EPR spectra (black) and corresponding simulations (green) of 25 µM TMA-PTIO in the presence of 10 µM ferric Mb collected over time after addition of 4 mM nitrite. The experiments were performed in a sodium acetate buffer at pH 5. All spectra were collected with a microwave power P = 1.5 mW and a modulation amplitude of 0.1 mT. Each simulation consists of linear combination of the spectra of pure TMA-PTIO and TMA-PTI, respectively. Over time, TMA-PTIO is converted to TMA-PTI. Right: time dependence of the experimental signal intensity of TMA-PTIO (represented by the peak maximum indicated by 'o' (blue) in the right spectrum) and TMA-PTI (represented by the peak maximum 'o' (red) in the right spectrum). The solid lines are simulations considering the model described below.

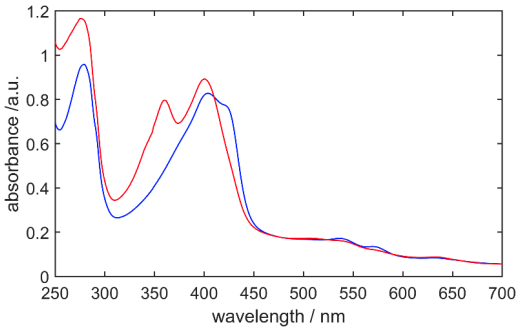

FIGURE C.12: Comparison between the UV/Vis absorption spectrum of ferric *Ma*Pgb at pH 5 (10 µM in heme content) overnight incubated with 1 mM sodium nitrite (blue) and the spectrum measured immediately after addition of (25 µM) TMA-PTIO to the mixture (red).

While an incubation of *Ma*Pgb with nitrite (1:100 ratio) only leads to formation of a limited fraction of *Ma*PgbNO, this protein was rapidly depleted from NO by addition of TMA-PTIO (Fig. C.12). This shows the ability of *Ma*Pgb to exchange NO with TMA-PTIO.

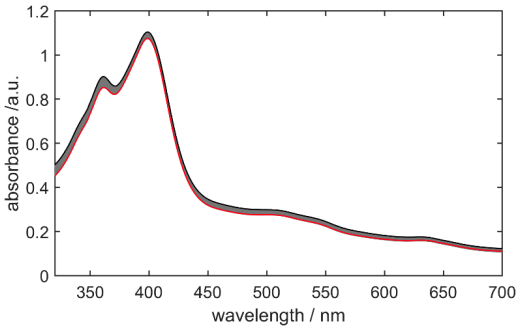

FIGURE C.13: Optical absorption spectra collected over time of *Ma*Pgb (10 µM heme concentration) reacted with 1 mM sodium nitrite in a sodium acetate buffer at pH 5 in presence of 25 µM TMA-PTIO at 20 °C. The black trace shows the absorption spectrum before addition of nitrite, the red trace shows the absorption spectra at the end of the time trace (after 245 minutes).

C.11 Visible absorption and ECD spectrum of Hemin

Hemin was measured in pure water in free form and after incubation with nitrite. In the absorption spectrum a broad positive band with maximum at 392 nm was observed. As expected, no ECD signal was observed, showing that the molecule in solution does not exhibit optical activity. Nitrite was added to the sample in final concentration of 22.4 mM, and new absorption ECD spectra were recorded. A new absorption band at 356 nm was observed corresponding to nitrite, and again no ellipticity was observed. The experiment shows that the ECD signals of ferric *Ma*Pgb treated with nitrite (Fig. 6.3)

can only be ascribed to the heme-ligand complex correctly incorporated in the protein matrix.

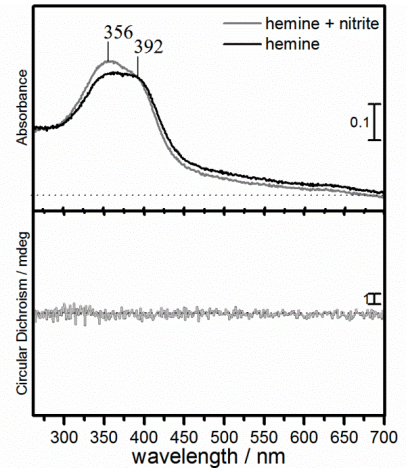

FIGURE C.14: Absorption (top) and ECD (bottom) spectra of hemin in water (black) and complex with 22 µM sodium nitrite (gray) in the spectral range 260-700 nm.

C.12 Heme pocket visualizations of *Ma*Pgb and Mb.

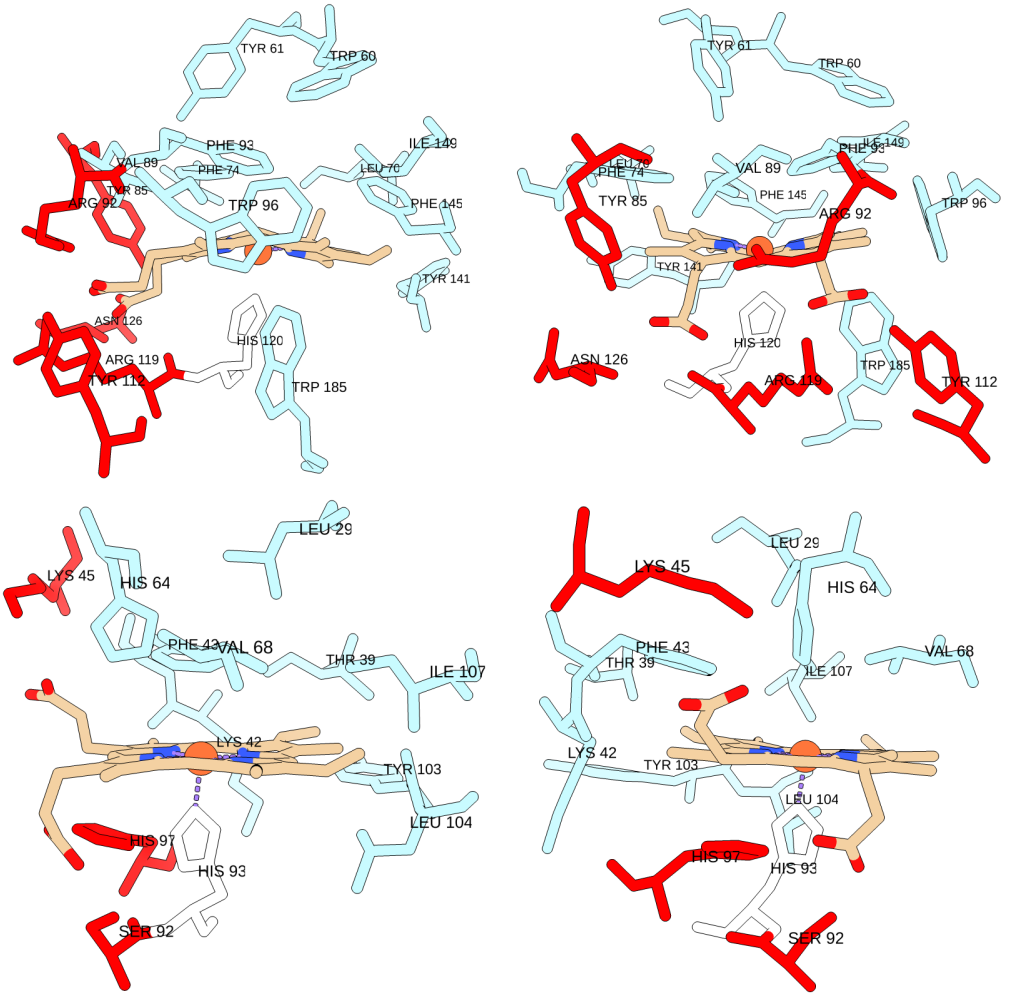

FIGURE C.15: Visualizations of the heme group and pocket of *Ma*Pgb (PDB entry 2VEE; top figures) and Mb (PDB entry 1AZI; bottom figures). The side chains of the residues that interact with the propionate heme side chains are depicted in red, the ones constituting the heme pocket are light blue, and the proximal histidine coordinating the central iron is white.

C.13 Simulation of dependence on nitrite concentration

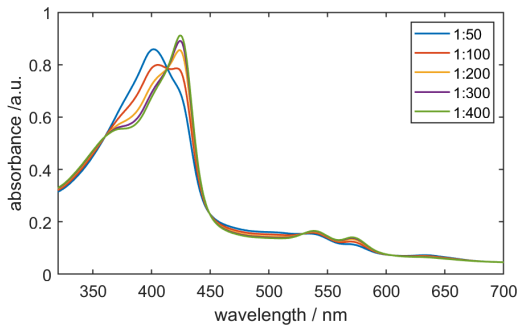

FIGURE C.16: Reconstructed UV/Vis-absorption spectra using weighted percentages of the absorption spectra of ferric *Ma*Pgb and ferric *Ma*PgbNO as described below.

Within the range of nitrite concentrations used in the experiments shown in Fig. 6.3, the concentration of NO formed due to spontaneous disproportionation scales approximately with the nitrite concentration for a fixed pH [341]. Hence, a change of the nitrite concentration by a factor N will also change the NO concentration present after a time t by a factor N. If the observed ferric *Ma*PgbNO is due to simple trapping of NO via

$$\mathrm{MaPgb} + \mathrm{NO} \underset{k_{-1}}{\overset{k_1}{\rightleftharpoons}} \mathrm{MaPgbNO}, \tag{C.6}$$

the relative ratio of [MaPgbNO]/[MaPgb] can be easily written as

$$\frac{[MaPgbNO]}{[\mathrm{MaPgb}]} = k_{eq}[\mathrm{NO}] = \frac{k_1}{k_{-1}}[\mathrm{NO}] = \frac{x}{10-x}, \tag{C.7}$$

with x the concentration of *Ma*PgbNO in µM. Using the UV/Vis-spectra of ferric *Ma*Pgb and *Ma*PgbNO, the ratio $\frac{MaPgbNO}{MaPgb}$ can be determined from the UV-Vis spectrum of *Ma*Pgb incubated with a 100-fold excess of nitrite. When assuming that the NO concentration changes with the same factor as the nitrite concentrations, the spectra of the 50-fold, 200-fold, 300-fold and 400-fold excess cases can then be predicted using the relative contributions of *Ma*Pgb and *Ma*PgbNO determined using the above equation. Fig. C.16 shows the absorption spectra obtained in this way. These absorption spectra match very well with the ones observed in Fig. 6.3, showing that the equilibrium state can be described based on the ligation of only one ligand (presumably NO). This argues against a binding of two nitrite molecules as would be expected for nitrite dismutase.

Appendix D

Supporting information Chapter 7

D.1 UV-Vis absorption spectra of GLB-3 isoforms with H_2O_2 and H_2S

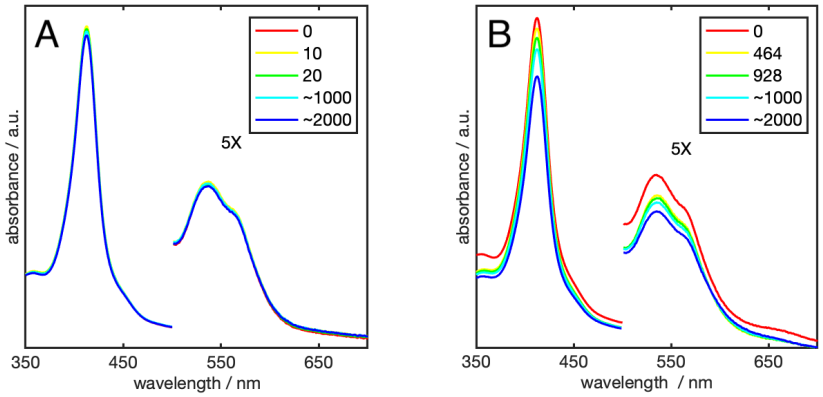

FIGURE D.1: UV-Vis absorption spectra of GLB-3a (A), GLB-3b (B) in the purified Fe(III) state, with various molar excess (amount of excess indicated in the legend) of H_2O_2 (without DTT). The Q bands are magnified by a factor of 5.

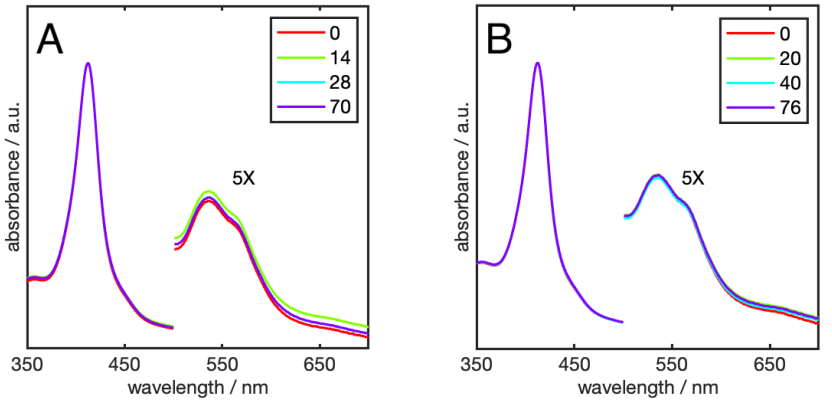

FIGURE D.2: Normalized UV-Vis absorption spectra of GLB-3a (A), GLB-3b (B) in the purified Fe(III) state with various molar excess (amount of excess indicated in the legend) of H_2S (without DTT). The Q bands are magnified by a factor of 5.

D.2 UV-vis enzymatic test reference globins

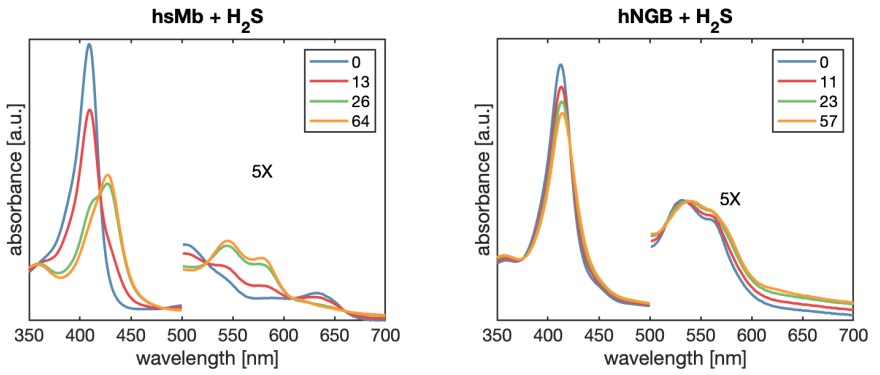

(A) (B)

FIGURE D.3: UV-Vis absorption spectra of hsMb (A) and hNGB (B) in the purified ferric (red), with various molar excess (legend) of H_2S (without DTT). The Q bands are magnified by a factor of 5.

D.3 X-band CW EPR

Species	g_z ±0.02	g_y ±0.03	g_x ±0.04	% ±3%	Axial ligands	Ref.
GLB-3a						
LS1	3.18	2.01	1.37#	30%		[237]
LS2	3.07	2.18	1.36#	40%		[237]
LS3	3.36	1.93	1.01#	30%		[237]
GLB-3a + DTT*					His/His	
LS1	3.17	2.01	1.36 #	32%		[237]
LS2	3.07	2.18	1.35#	48%		[237]
LS3'	3.54	1.93	n.d.	20%		[237]
GLB-3a + DTT**					His/His	
LS1	3.17	2.01	1.38#	41%		[237]
LS2	3.07	2.17	1.36#	59%		[237]
GLB-3b + DTT**					His/His	
LS1	3.16	2.01	1.41#	51%		[237]
LS2	3.07	2.17	1.37#	49%		[237]
GLB-3a C70S					His/His	
LS1	3.15	1.99	1.43#	65%		[237]
LS2	3.07	2.14	1.35#	35%		[237]
GLB-3a C70S + DTT*					His/His	
LS1	3.14	1.97	1.50#	63%		[237]
LS2	3.07	2.18	1.35#	37%		[237]
GLB-3a C70S + DTT**					His/His	
LS1	3.15	1.97	1.48#	59%		[237]
LS2	3.08	2.17	1.32#	41%		[237]
h Ngb					His/His	
LS SH	3.10	2.17	1.30			[300, 93]
LS S-S	3.26	2.06	1.05			[300, 93]
mNgb	3.12	2.15	1.29		His/His	[93]
CYGB	3.20	2.08	1.20		His/His	[93]
GLB-26	3.25	n.d.	n.d.		His/His	[117]
Cyt b5	3.03	2.23	1.43		His/His	[380]
Barley Hb	3.02	2.22	1.48		His/His	[381]
PpcA Cyt	3.24	1.98	1.22		His/His	[382]
heme I						
GLB-3a HE7A					Cys-/His?	
LS4	2.49	2.27	1.88	63%		[237]
LS5	2.41	2.26	1.91	34%		[237]
Ngb HE7A + H2S	2.48	2.29	1.85		H2S/His	[352]
R. sulfidophilum						
SoxAX					Cys-/His	
LS	2.52	2.23	1.84			[366]
LS	2.58	2.30	1.87			[366]
Cyt c M80C	2.56	2.27	1.85		Cys-/His	[383]

TABLE D.1: The principal g-values of GLB-3 and other ferric proteins. EPR parameters of GLB-3 with and without DTT compared to heme proteins, with a histidine or thiolate as an axial ligand, reported to participate in redox reactions, more specific electron transfer. The contribution of each simulated LS form is given. n.d. = not determined, *DTT added prior to EPR measurement, **DTT added right after protein purification, #estimated based on $\sum g_i^2 \approx 16$.

The principal g-values of the LS ferric heme centres found for GLB-3 are typical for $(d_{xy})^2(d_{xz}, d_{yz})^3$ configurations. The LS1 and LS2 complexes of GLB-3 are referred to as normal rhombic or type-II EPR signals. In contrast, the LS3 (and LS3') complex of GLB-3 shows a very high $g_{max} > 3.2$ value, resulting in a large g-anisotropy, making it difficult to observe g_x (g_{min}). This complex is referred to as type-I EPR signals [364]. In line with the UV–Vis data (Fig. 7.3), no signal due to a HS ferric heme center is observed in the EPR spectra of the GLB-3 protein samples.

D.4 The CO rebinding kinetics of GLB-3a and GLB-3b

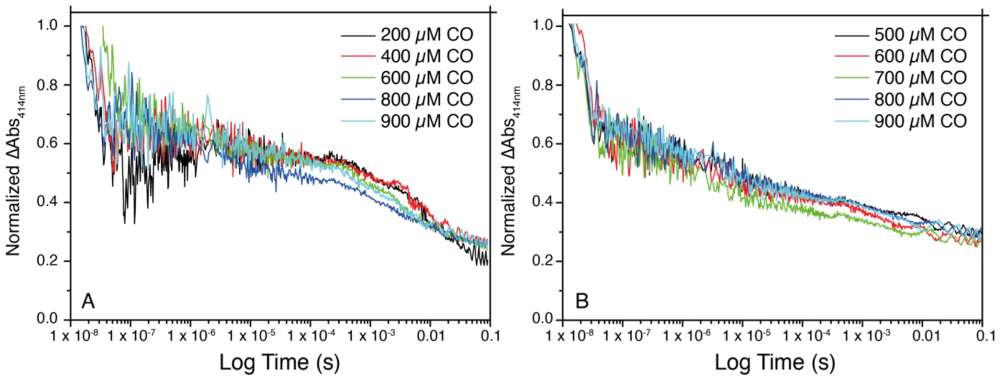

FIGURE D.4: The CO rebinding kinetics curves after flash photolysis at 414 nm of GLB-3a with DTT (A) and GLB-3b with DTT (B). The logarithmic time traces are shown at different CO concentrations. The nonlinear least square fits of the data are shown in red.

D.5 The CO rebinding curves of GLB-3a HE7A

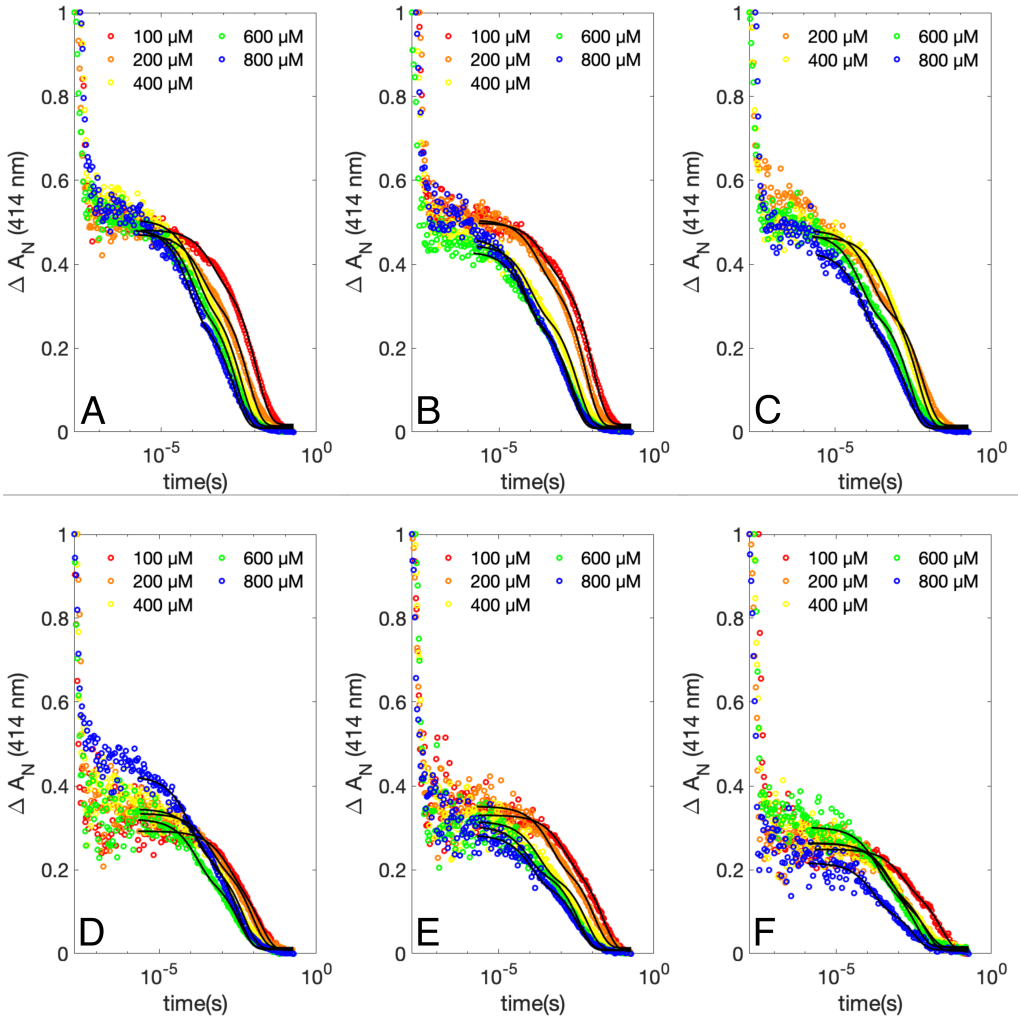

FIGURE D.5: Triplicate of the CO rebinding curves of GLB-3a HE7A (A-C) and GLB-3b HE7A (D-F) after flash photolysis recorded at 414 nm at different CO concentrations (100-800 µM). Continuous lines (black) are nonlinear least-squares fits of the normalized, logarithmic resampled data obtained according to a bi-exponetial model following Eq. 7.2.

D.6 Redox potential

D.6.1 Mediator mixtures

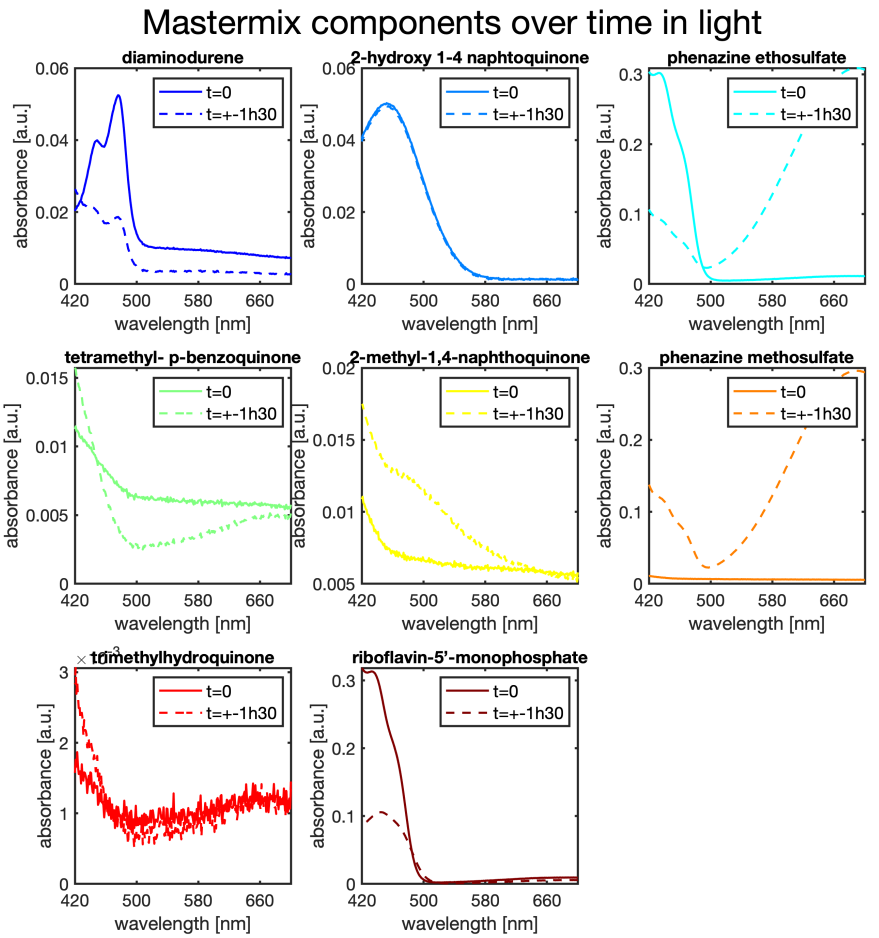

FIGURE D.6: Redox mediators measured after 1 hour and 30 min incubation at room temperature on the lab bench. Diaminodurene changes over time in the Soret region, whereas phenazine ethosulfate and phenazine methosulfate cause problematic changes in the Q-band region.

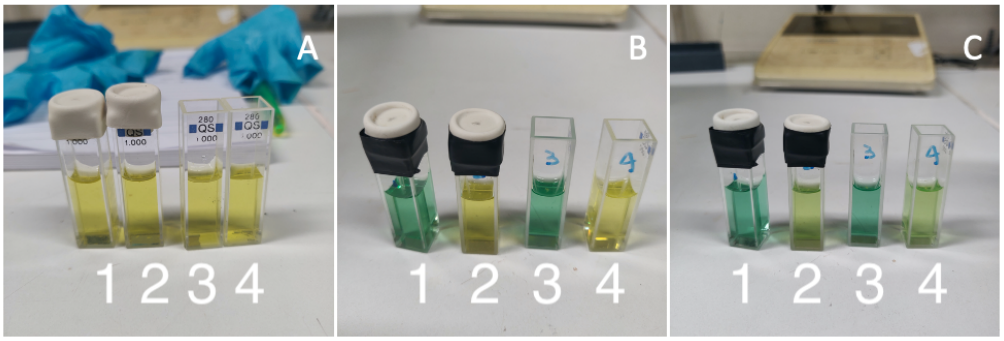

FIGURE D.7: Redox mediator solutions. Panel A: freshly prepared sealed under nitrogen atmosphere (1,2) , and air exposed (3,4). Panel B: 1 and 3 were left on bench, 2 and 4 were kept in dark. Panel C: 2 and 4 from panel B were exposed to light and turned green over time.

D.6.2 Final experiment

The redox potential of WT GLB-3a was measured via potentiometric redox titrations. The change in population from the Fe(III) to the Fe(II) state after each titration with dithionite was monitored through the spectral differences in the absorbance spectra at 530 and 560 nm, and double-checked using the changes in the Soret band (Fig. D.9). The fraction of reduced protein was normalized, plotted against the measured potential vs. SHE, and fitted to the Nernst equation (Fig. D.8). The obtained redox potential E_m is +8 mV ± 19 mV vs. SHE, which falls within the wide range of E_m values reported for heme proteins (Table D.2).

A peculiar feature was observed during the measurements: when approaching the midpoint potential E_m, addition of dithionite leads to the appearance of the spectrum of the reduced ferrous form, which then returned after several minutes to that of the oxidized species until an equilibrium was reached. Past the midpoint potential, the absorption spectra stayed those of the reduced ferrous state and did not change in time for a given potential. This observation may be linked to the fact that the proteins are cysteine rich.

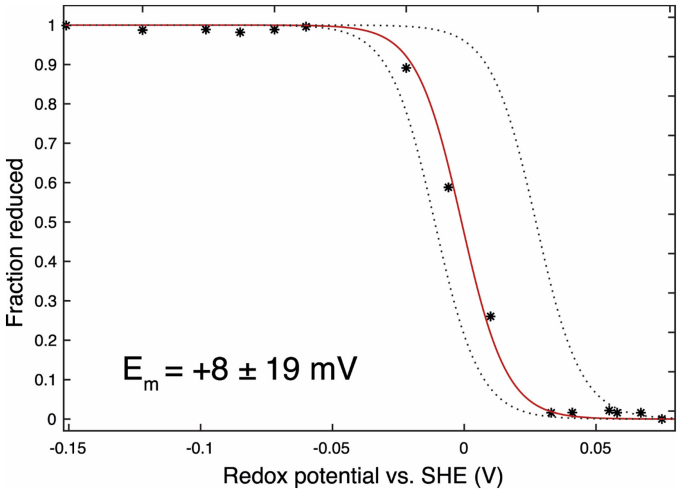

FIGURE D.8: The plot shows the fit of the fraction reduced to the Nernst equation of one data set (solid red line). The measured E_m value is +8 ± 19 mV vs. SHE, which is an average of three experiments. The standard deviation is shown as dashed lines. The titrations were carried out at 25 °C in a mediator mix solution in 100 mM sodium phosphate buffer pH 7.

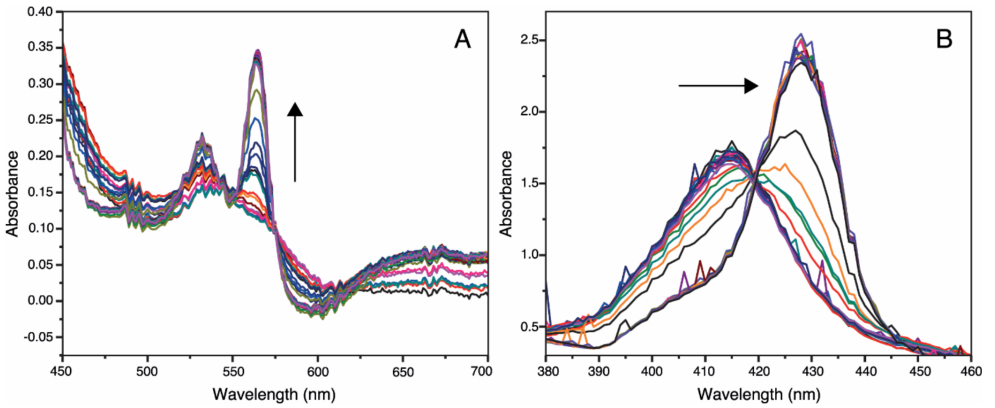

FIGURE D.9: Spectroelectrochemical potentiometric redox titrations of GLB-3a. After each addition of dithionite, an absorbance spectrum of the (A) Q bands and (B) Soret band was recorded each time. Both figures are from two different measurement sets. The arrow indicates the direction of the change in the band(s) when an increasing amount of dithionite was added. The titrations were carried out at 25 °C in a mediator mix solution in 100 mM sodium phosphate buffer pH 7.

Protein	E_m **(mV) vs. SHE**	**Axial ligands**	**Ref.**
hCyt b5	-21	His/His	[384]
Cyt c3	-400	His/His	[375]
Cyt b559	+395	His/His	[385]
Cyt c	+263	Met/His	[386]
HRP	-250	His	[387]
*At*Hb1 and Hb2	-35	His/His	[372]
*At*Hb3	+15	His	[372]
Rice nsHb1	-143	His/His	[388]
Lumbricus Hb	+311	His	[389]
hMb	+50	His	[390]
hNgb*	-136	His/His	[391]
hNgb	-118	His/His	[293]
hCgb	-33	His/His	[392]
Kumaglobin	-400	His/His	[393]
Ce GLB-3a	+8	His/His	[237]
Ce GLB-6	-193	His/His	[148]
Ce GLB-12	0	His/His	[119]
Ce	+30	His/His	[117]

TABLE D.2: The redox potentials (Fe^{2+}/Fe^{3+} couple) of various heme proteins. The redox potential of GLB-3a compared with various hexa- and pentacoordinated heme proteins. * = mutated surface Cys, *At* = *Arabidopsis thaliana*, ns = non-symbiotic.

Appendix E

Scientific Curriculum vitae

Niels Van Brempt

Curriculum Vitae

Address: Wehntalerstrasse 374
8046 Zürich, Switzerland
+417 82 65 21 26
niels.vanbrempt@gmail.com
0000-0003-3940-2210
nvbrempt
Nationality: Belgian
Place of Birth: Beveren, Belgium 04/04/1992

Work Experience

04/2021–09/2023 **Scientific Software Developer**, *Mestrelab Research S.L.*, Santiago de Compostela, Spain
- Plugin development for automation workflows in LC/GC-MS and NMR data processing.
- Scripting ECMA/JavaScript.
- UI design, project management.

09/2016–05/2017 **PhD student** , *KU Leuven*, Belgium
- Successful expression, crystallization and structure determination of a nicotinic acetylcholine binding protein.
- X-ray diffraction data collection at the European Synchrotron Radiation Facility (ESRF), Grenoble and Diamond light source, Oxfordshire.
- Ligand-binding kinetics with Surface Plasmon Resonance (SPR, Biacore).

Education

06/2017–09/2023 **PhD in Physics**, *University of Antwerp*, Belgium
Thesis title : "Globins from *Caenorhabditis elegans* and the Protoglobin from *Methanosarcina acetivorans*: a Spectroscopic Investigation" supervised by Prof. Dr. Van Doorslaer and Prof. Dr. Dewilde († 2020).

09/2014–06/2016 **Master in Science - Biophysics and Medical Physics**, *University of Antwerp*, Belgium, **Great distinction**
Thesis title : "Molecular replacement in X-ray Crystallography: Structure Determination of a Cytochrome c Peroxidase Mutant and a Protein R2r1" supervised by Prof. Dr. Pannu (Leiden, NL) and Prof. Dr. Van Doorslaer.

09/2010–09/2014 **Bachelor of Science - Physics**, *University of Antwerp*, Belgium, **Distinction**

Organizing and Teaching

2016–2020 **Supervision**, *University of Antwerp*, Belgium
Co-supervisor of internships and various Bachelor's and Master's theses at the University of Antwerp.

2019 **Teaching**, *University of Antwerp*, Belgium
Tutorial on basic EPR data collection and data simulation during the PARACAT summer school.

2017 **Local organizing**, *Blankenberge*, Belgium
Assisting with the organization of the 16th edition of the Young Belgian Magnetic Resonance Scientists Symposium.

2014 **Tutor**, *University of Antwerp*, Belgium
Teaching and helping underprivileged high school students with physics assignments.

Training

7/02/2018 - 9/2/2019 **COST training school**, *University of Parma*, Parco Area delle Scienze 23/A 43124 Parma, Italy, COST CM1306 "Understanding Movement and Mechanism in Molecular Machines".

2014 - 2015 **Internship for the M.Sc.**, *Janssen*, Turnhoutseweg 30, 2340 Beerse, Belgium, Introduction to various wet-lab techniques: protein expression, SDS-page, western blot, ChIP-seq.

Publications

2023 **Article**, *Hafideddine, Z., Loier, T., Van Brempt, N., De Henau, S., Ching, H. V., Neukermans, S., Defossé, S., Berghmans, H., Sgammato, R., Aerts, R., Hammerschmid, D., Moons, R., Breugelmans, T., Sobott, F., Johannessen, C., Herrebout, W., P. Braeckman, B., Moens, L., Dewilde, S. & Van Doorslaer, S.*, GLB-3: A resilient, cysteine-rich, membrane-tethered globin expressed in the reproductive and nervous system of Caenorhabditis elegans., Journal of Inorganic Biochemistry
238, 112063.

2023 **Article**, *Sgammato, R., Van Brempt, N., Aerts, R., Van Doorslaer, S., Dewilde, S., Herrebout, W., & Johannessen, C.*, Interaction of nitrite with ferric protoglobin from Methanosarcina acetivorans–an interesting model for spectroscopic studies of the haem–ligand interaction., Dalton Transactions
52(10), 2976-2987.

2023 **Article**, *Van Brempt, N., Sgammato, R., Beirinckx, Q., Hammerschmid, D., Sobott, F., Dewilde, S., Moens, L., Herrebout, W., Johannessen, C. & Van Doorslaer, S.*, he effect of pH and nitrite on the haem pocket of GLB-33, a globin-coupled neuronal transmembrane receptor of Caenorhabditis elegans., Biochimica et Biophysica Acta (BBA)-Proteins and Proteomics
1871(4), 140913.

Presentations

24/05/2019 **Oral**, *N. Van Brempt, Q. Beirinckx, R. Sgammato, S. Dewilde and S. Van Doorslaer.*, The interaction between nitrite and the ferric globin domain of GLB-33, a unique chimeric globin in *Caenorhabditis elegans.*, 27th Annual Meeting of the Benelux EPR Society
Delft, the Netherlands.

23/09/2019 **Poster**, *N. Van Brempt, Z. Hafidedinne, S. Defosse, R. Sgammato, D. Hammerschmid, W. Herrebout, C. Johannessen, F. Sobott, S. Dewilde and S. Van Doorslaer.*, Globins in *Caenorhabditis elegans*: A spectroscopic investigation of GLB-3 and GLB-33 and their interaction with small ligands., Faculty of Science Research Day
Antwerp, Belgium.

6-7/12/2018 **Poster**, *N. Van Brempt, R. Sgammato, Dietmar Hammerschmid, S. Dewilde, S. Van Doorslaer.*, Probing nitrite binding with the globin domain of GLB-33, a chimeric globin from *Caenorhabditis elegans.*, 17th edition of the young Belgian magnetic resonance scientists symposium
Spa, Belgium.

3-6/09/2018 **Oral and poster**, *N. Van Brempt, Q. Beirinckx, H. Berghmans, S. Dewilde, S. Van Doorslaer. Nitrite and nitric oxide binding of GLB-33, a unique chimeric globin in Caenorhabditis elegans examined with EPR and UV-vis spectroscopy.*, XXth international Conference on Oxygen Binding and Sensing Proteins,, Barcelona, Spain.

06/06/2018 **Poster**, *N. Van Brempt, Q. Beirinckx, H. Berghmans, S. Dewilde, S. Van Doorslaer.*, Nitrite reductase activity of GLB-33, a unique chimeric globin in *Caenorhabditis elegans* examined with EPR and UV-vis spectroscopy., 26th Annual Meeting of the Benelux EPR Society
Antwerp, Belgium.

8-12/04/2018 **Poster**, *N. Van Brempt, Q. Beirinckx, H. Berghmans, S. Dewilde, S. Van Doorslaer.*, Nitrite reductase activity of GLB-33, a unique chimeric globin in *Caenorhabditis elegans* examined with EPR and UV-vis spectroscopy., 51st Annual International Meeting of the ESR Spectroscopy Group of the Royal Society of Chemistry
London, United Kingdom.

Software and Computer Skills

Programming ECMA/JavaScript, MATLAB®, C++, HTML, CSS, Python

Graphics Chimera, PyMol, CCP4, Inkscape

Documenting Offce, LaTeX

Research Skills

Wet-lab Cloning, PCR, SDS-page, Western blot, gelelectrophoresis, protein over-expression (*E. coli*, *S. frugiperda*) and protein crystallization, chromatography (HPLC, SEC, IEX, Ni-Affinity).

Spectroscopy Electron Paramagnetic Resonance (EPR: CW and pulsed X-band, Pulsed W-band, ENDOR and data simulation (EasySpin[1])), UV-vis absorption, UV-vis fluorescence, Resonance Raman, Electronic Circular Dichroism (ECD), (theory only) Nuclear Magnetic Resonance (NMR).

Others X-ray diffraction, Mass Spectrometry (MS), Isothermal Titration Calorimetry (ITC), Surface Plasmon Resonance (SPR, Biacore), Chromatin Immunoprecipitation Sequencing (ChIP-Seq).

References

Agustín Barba, *Lead programmer*, Mestrelab Research S.L.
agustin@mestrelab.com

Prof. Dr. Sabine Van Doorslaer, *PhD supervisor, P.I. at Theory and Spectroscopy of Molecules and Materials and vice Dean Faculty of Science*, University of Antwerp
sabine.vandoorslaer@uantwerpen.be

[1] Stoll, S., Schweiger, A. *J. Magn. Reson.* 178(1), 42-55 (2006)

Bibliography

[1] Serge N Vinogradov, David Hoogewijs, Xavier Bailly, Raúl Arredondo-Peter, Michel Guertin, Julian Gough, Sylvia Dewilde, Luc Moens, and Jacques R Vanfleteren. Three globin lineages belonging to two structural classes in genomes from the three kingdoms of life. *Proceedings of the National Academy of Sciences*, 102(32):11385–11389, 2005.

[2] Ross Hardison. Hemoglobins from bacteria to man: evolution of different patterns of gene expression. *Journal of Experimental Biology*, 201(8):1099–1117, 1998.

[3] Ross C Hardison. A brief history of hemoglobins: plant, animal, protist, and bacteria. *Proceedings of the National Academy of Sciences of the United States of America*, 93:5675, 1996.

[4] John C Kendrew, Richard E Dickerson, Bror E Strandberg, Roger G Hart, David R Davies, David C Phillips, and VC Shore. Structure of myoglobin: A three-dimensional fourier synthesis at 2 å. resolution. *Nature*, 185(4711):422–427, 1960.

[5] James T Trent and Mark S Hargrove. A ubiquitously expressed human hexacoordinate hemoglobin. *Journal of Biological Chemistry*, 277(22):19538–19545, 2002.

[6] Thorsten Burmester, Bettina Weich, Sigrid Reinhardt, and Thomas Hankeln. A vertebrate globin expressed in the brain. *Nature*, 407(6803):520–523, 2000.

[7] Alessandra Pesce, Marco Nardini, Mario Milani, and Martino Bolognesi. Protein structure in the truncated (2/2) hemoglobin family. *IUBMB life*, 59(8-9):535–541, 2007.

[8] Dietmar Hammerschmid, Francesca Germani, Salvador I Drusin, Charline Fagnen, Claudio D Schuster, David Hoogewijs, Marcelo A Marti, Catherine Venien-Bryan, Luc Moens, Sabine Van Doorslaer, et al. Structural modeling of a novel membrane-bound globin-coupled sensor in geobacter sulfurreducens. *Computational and Structural Biotechnology Journal*, 19:1874–1888, 2021.

[9] Aik-Hong Teh, Jennifer A Saito, Nazalan Najimudin, and Maqsudul Alam. Open and lys–his hexacoordinated closed structures of a globin with swapped proximal and distal sites. *Scientific reports*, 5:11407, 2015.

[10] Anne Puustinen and M Wikström. The heme groups of cytochrome o from escherichia coli. *Proceedings of the National Academy of Sciences*, 88(14):6122–6126, 1991.

[11] Gunhild Layer. Heme biosynthesis in prokaryotes. *Biochimica et Biophysica Acta (BBA)-Molecular Cell Research*, 1868(1):118861, 2021.

[12] Ulrich Ermler, Roman A Siddiqui, Rainer Cramm, and Bärbel Friedrich. Crystal structure of the flavohemoglobin from alcaligenes eutrophus at 1.75 a resolution. *The EMBO journal*, 14(24):6067–6077, 1995.

[13] Hisashi Iwaasa, Takashi Takagi, and Keiji Shikama. Amino acid sequence of yeast hemoglobin: a two-domain structure. *Journal of molecular biology*, 227(3):948–954, 1992.

[14] Shaobin Hou, Tracey Freitas, Randy W Larsen, Mikhail Piatibratov, Victor Sivozhelezov, Amy Yamamoto, Ella A Meleshkevitch, Mike Zimmer, George W Ordal, and Maqsudul Alam. Globin-coupled sensors: a class of heme-containing sensors in archaea and bacteria. *Proceedings of the National Academy of Sciences*, 98(16):9353–9358, 2001.

[15] Roy E Weber and Serge N Vinogradov. Nonvertebrate hemoglobins: functions and molecular adaptations. *Physiological reviews*, 81(2):569–628, 2001.

[16] Anna Keppner, Darko Maric, Miguel Correia, Teng Wei Koay, Ilaria MC Orlando, Serge N Vinogradov, and David Hoogewijs. Lessons from the post-genomic era: Globin diversity beyond oxygen binding and transport. *Redox biology*, 37:101687, 2020.

[17] Serge N. Vinogradov, David Hoogewijs, Xavier Bailly, Raúl Arredondo-Peter, Julian Gough, Sylvia Dewilde, Luc Moens, and Jacques R. Vanfleteren. A phylogenomic profile of globins. *BMC Evolutionary Biology*, 6:1–17, 2006.

[18] Serge N. Vinogradov, David Hoogewijs, Xavier Bailly, Kenji Mizuguchi, Sylvia Dewilde, Luc Moens, and Jacques R. Vanfleteren. A model of globin evolution. *Gene*, 398(1-2 SPEC. ISS.):132–142, 2007.

[19] Serge N Vinogradov, Mariana Tinajero-Trejo, Robert K Poole, and David Hoogewijs. Bacterial and archaeal globins—a revised perspective. *Biochimica et Biophysica Acta (BBA)-Proteins and Proteomics*, 1834(9):1789–1800, 2013.

[20] Serge N Vinogradov, Daniel A Walz, Bill Pohajdak, Luc Moens, Oscar H Kapp, Tomohiko Suzuki, and Clive NA Trotman. Adventitious variability? the amino acid sequences of nonvertebrate globins. *Comparative Biochemistry and Physiology Part B: Comparative Biochemistry*, 106(1):1–26, 1993.

[21] Morris Goodman, Janet Pedwaydon, John Czelusniak, Tomohiko Suzuki, Toshio Gotoh, Luc Moens, Fumio Shishikura, Daniel Walz, and Serge Vinogradov. An evolutionary tree for invertebrate globin sequences. *Journal of molecular evolution*, 27(3):236–249, 1988.

[22] M.L. Blaxter. Nemoglobins: Divergent nematode globins. *Parasitology Today*, 9(10):353 – 360, 1993.

[23] David T Mitchell, Barrie G. Kitto, and Marvin L Hackert. Structural Analysis of Monomeric Hemichrome and Dimeric Cyanomet Hemoglobins fromCaudina arenicola. *J. Mol. Biol.*, 251(3):421–431, 1995.

[24] Austen F. Riggs. Aspects of the origin and evolution of non-vertebrate hemoglobins. *Integr. Comp. Biol.*, 31(3):535–545, 1991.

[25] Sylvia Dewilde, Bettina Ebner, Evi Vinck, Kambiz Gilany, Thomas Hankeln, Thorsten Burmester, Jill Kreiling, Carol Reinisch, Jacques R. Vanfleteren, Laurent Kiger, Michael C. Marden, Christian Hundahl, Angela Fago, Sabine Van Doorslaer, and Luc Moens. The nerve hemoglobin of the bivalve mollusc Spisula solidissima: Molecular cloning, ligand binding studies, and phylogenetic analysis. *J. Biol. Chem.*, 281(9):5364–5372, 2006.

[26] William E Royer Jr, Hitesh Sharma, Kristen Strand, James E Knapp, and Balaji Bhyravbhatla. Lumbricus erythrocruorin at 3.5 å resolution: architecture of a megadalton respiratory complex. *Structure*, 14(7):1167–1177, 2006.

[27] Flávia A Belato, Carlos G Schrago, Christopher J Coates, Kenneth M Halanych, and Elisa M Costa-Paiva. Newly discovered occurrences and gene tree of the extracellular globins and linker chains from the giant hexagonal bilayer hemoglobin in metazoans. *Genome biology and evolution*, 11(3):597–612, 2019.

[28] Thorsten Burmester, Bettina Ebner, Bettina Weich, and Thomas Hankeln. Cytoglobin: a novel globin type ubiquitously expressed invertebrate tissues. *Molecular biology and evolution*, 19(4):416–421, 2002.

[29] Norifumi Kawada, Dan Bach Kristensen, Kinji Asahina, Kazuki Nakatani, Yukiko Minamiyama, Shuichi Seki, and Katsutoshi Yoshizato. Characterization of a stellate cell activation-associated protein (stap) with peroxidase activity found in rat hepatic stellate cells. *Journal of Biological Chemistry*, 276(27):25318–25323, 2001.

[30] Dominik Kugelstadt, Mark Haberkamp, Thomas Hankeln, and Thorsten Burmester. Neuroglobin, cytoglobin, and a novel, eye-specific globin from chicken. *Biochem. Biophys. Res. Commun.*, 325(3):719–725, dec 2004.

[31] Miriam Blank, Jessica Wollberg, Frank Gerlach, Katja Reimann, Anja Roesner, Thomas Hankeln, Angela Fago, Roy E Weber, and Thorsten Burmester. A membrane-bound vertebrate globin. *PloS one*, 6(9), 2011.

[32] Anja Roesner, Christine Fuchs, Thomas Hankeln, and Thorsten Burmester. A globin gene of ancient evolutionary origin in lower vertebrates: Evidence for two distinct globin families in animals. *Mol. Biol. Evol.*, 22(1):12–20, jan 2005.

[33] C Fuchs, T Burmester, and T Hankeln. The amphibian globin gene repertoire as revealed by the xenopus genome. *Cytogenetic and genome research*, 112(3-4):296–306, 2006.

[34] Vidushi S Patel, Steven JB Cooper, Janine E Deakin, Bob Fulton, Tina Graves, Wesley C Warren, Richard K Wilson, and Jennifer AM Graves. Platypus globin genes and flanking loci suggest a new insertional model for beta-globin evolution in birds and mammals. *BMC biology*, 6(1):34, 2008.

[35] Federico G Hoffmann, Jay F Storz, Thomas A Gorr, and Juan C Opazo. Lineage-specific patterns of functional diversification in the α-and β-globin gene families of tetrapod vertebrates. *Molecular biology and evolution*, 27(5):1126–1138, 2010.

[36] David Hoogewijs, Bettina Ebner, Francesca Germani, Federico G Hoffmann, Andrej Fabrizius, Luc Moens, Thorsten Burmester, Sylvia Dewilde, Jay F Storz, Serge N Vinogradov, et al. Androglobin: a chimeric globin in metazoans that is preferentially expressed in mammalian testes. *Molecular biology and evolution*, 29(4):1105–1114, 2012.

[37] T Burmester and T Hankeln. Function and evolution of vertebrate globins. *Acta Physiologica*, 211(3):501–514, 2014.

[38] Thomas Hankeln, Bettina Ebner, Christine Fuchs, Frank Gerlach, Mark Haberkamp, Tilmann L Laufs, Anja Roesner, Marc Schmidt, Bettina Weich, Sylvia Wystub, et al. Neuroglobin and cytoglobin in search of their role in the vertebrate globin family. *Journal of inorganic biochemistry*, 99(1):110–119, 2005.

[39] David A Gell. Structure and function of haemoglobins. *Blood Cells, Molecules, and Diseases*, 70:13–42, 2018.

[40] Jay F Storz. *Hemoglobin: insights into protein structure, function, and evolution*. Oxford University Press, 2018.

[41] Hans Frauenfelder, Benjamin H. McMahon, Robert H. Austin, Kelvin Chu, and John T. Groves. The role of structure, energy landscape, dynamics, and allostery in the enzymatic function of myoglobin. *Proceedings of the National Academy of Sciences*, 98:2370–2374, 2001.

[42] Serge N Vinogradov and Luc Moens. Diversity of globin function: enzymatic, transport, storage, and sensing. *Journal of Biological Chemistry*, 283(14):8773–8777, 2008.

[43] Ruth Pietri, Ruth G León, Laurent Kiger, Michael C Marden, Laura B Granell, Carmen L Cadilla, and Juan López-Garriga. Hemoglobin i from lucina pectinata: a model for distal heme-ligand control. *Biochimica et Biophysica Acta (BBA)-Proteins and Proteomics*, 1764(4):758–765, 2006.

[44] Cacimar Ramos-Alvarez, Byung-Kuk Yoo, Ruth Pietri, Isabelle Lamarre, Jean-Louis Martin, Juan Lopez-Garriga, and Michel Negrerie. Reactivity and dynamics of H_2S, NO, and O_2 interacting with hemoglobins from lucina pectinata. *Biochemistry*, 52(40):7007–7021, 2013.

[45] Alessandra Pesce, Sylvia Dewilde, Marco Nardini, Luc Moens, Paolo Ascenzi, Thomas Hankeln, Thorsten Burmester, and Martino Bolognesi. Human brain neuroglobin structure reveals a distinct mode of controlling oxygen affinity. *Structure*, 11(9):1087–1095, 2003.

[46] Kapuganti J Gupta, Kim H Hebelstrup, Luis AJ Mur, and Abir U Igamberdiev. Plant hemoglobins: important players at the crossroads between oxygen and nitric oxide. *FEBS letters*, 585(24):3843–3849, 2011.

[47] Angela N Hvitved, James T Trent III, Scott A Premer, and Mark S Hargrove. Ligand binding and hexacoordination in synechocystishemoglobin. *Journal of Biological Chemistry*, 276(37):34714–34721, 2001.

[48] Angela Fago, Antony J Mathews, Luc Moens, Sylvia Dewilde, and Thomas Brittain. The reaction of neuroglobin with potential redox protein partners cytochrome b 5 and cytochrome c. *FEBS letters*, 580(20):4884–4888, 2006.

[49] Subhadip Raychaudhuri, Joanna Skommer, Kristen Henty, Nigel Birch, and Thomas Brittain. Neuroglobin protects nerve cells from apoptosis by inhibiting the intrinsic pathway of cell death. *Apoptosis*, 15(4):401–411, 2010.

[50] Luisa B Maia and José J.G. Moura. How biology handles nitrite. *Chemical Reviews*, 114(10):5273–5357, 2014.

[51] Khalid M Naseem. The role of nitric oxide in cardiovascular diseases. *Molecular aspects of medicine*, 26(1-2):33–65, 2005.

[52] Abraham J Susswein, Ayelet Katzoff, Nimrod Miller, and Itay Hurwitz. Nitric oxide and memory. *The Neuroscientist*, 10(2):153–162, 2004.

[53] DC Jenkins, IG Charles, L L_et Thomsen, DW Moss, LS Holmes, SA Baylis, P Rhodes, K Westmore, PC Emson, and S Moncada. Roles of nitric oxide in tumor growth. *Proceedings of the National Academy of Sciences*, 92(10):4392–4396, 1995.

[54] Nicolas Barraud, Daniel J Hassett, Sung-Hei Hwang, Scott A Rice, Staffan Kjelleberg, and Jeremy S Webb. Involvement of nitric oxide in biofilm dispersal of pseudomonas aeruginosa. *Journal of bacteriology*, 188(21):7344–7353, 2006.

[55] Dhruv P Arora, Sajjad Hossain, Yueming Xu, and Elizabeth M Boon. Nitric oxide regulation of bacterial biofilms. *Biochemistry*, 54(24):3717–3728, 2015.

[56] T Sobko, CI Reinders, EÅ Jansson, E Norin, T Midtvedt, and JO Lundberg. Gastrointestinal bacteria generate nitric oxide from nitrate and nitrite. *Nitric Oxide*, 13(4):272–278, 2005.

[57] Cormac T Taylor and Salvador Moncada. Nitric oxide, cytochrome c oxidase, and the cellular response to hypoxia. *Arteriosclerosis, thrombosis, and vascular biology*, 30(4):643–647, 2010.

[58] Namrta Purwar, Jennifer M McGarry, Joshua Kostera, A Andrew Pacheco, and Marius Schmidt. Interaction of nitric oxide with catalase: structural and kinetic analysis. *Biochemistry*, 50(21):4491–4503, 2011.

[59] JESUS G Valenzuela, FA Walker, and JM Ribeiro. A salivary nitrophorin (nitric-oxide-carrying hemoprotein) in the bedbug cimex lectularius. *Journal of Experimental Biology*, 198(7):1519–1526, 1995.

[60] Jesús Tejero and Mark T Gladwin. The globin superfamily: functions in nitric oxide formation and decay. *Biological chemistry*, 395(6):631–639, 2014.

[61] Brian Lima, Michael T Forrester, Douglas T Hess, and Jonathan S Stamler. S-nitrosylation in cardiovascular signaling. *Circulation research*, 106(4):633–646, 2010.

[62] Alejandro Chamizo-Ampudia, Emanuel Sanz-Luque, Angel Llamas, Aurora Galvan, and Emilio Fernandez. Nitrate reductase regulates plant nitric oxide homeostasis. *Trends in Plant Science*, 22(2):163–174, 2017.

[63] Sylvain Jeandroz, Daniel Wipf, Dennis J Stuehr, Lorenzo Lamattina, Michael Melkonian, Zhijian Tian, Ying Zhu, Eric J Carpenter, Gane Ka-Shu Wong, and David Wendehenne. Occurrence, structure, and evolution of nitric oxide synthase–like proteins in the plant kingdom. *Science Signaling*, 9(417):re2–re2, 2016.

[64] Ivan Gusarov, Laurent Gautier, Olga Smolentseva, Ilya Shamovsky, Svetlana Eremina, Alexander Mironov, and Evgeny Nudler. Bacterial nitric oxide extends the lifespan of c. elegans. *Cell*, 152(4):818–830, 2013.

[65] S Bruce King. Nitric oxide production from hydroxyurea. *Free Radical Biology and Medicine*, 37(6):737–744, 2004.

[66] Jinming Huang, Erin M Sommers, Daniel B Kim-Shapiro, and S Bruce King. Horseradish peroxidase catalyzed nitric oxide formation from hydroxyurea. *Journal of the American Chemical Society*, 124(13):3473–3480, 2002.

[67] Wendy K Alderton, Chris E Cooper, and Richard G Knowles. Nitric oxide synthases: structure, function and inhibition. *Biochemical journal*, 357(3):593–615, 2001.

[68] Simon Daff. No synthase: structures and mechanisms. *Nitric oxide*, 23(1):1–11, 2010.

[69] Nigel M Crawford. Mechanisms for nitric oxide synthesis in plants. *Journal of experimental botany*, 57(3):471–478, 2006.

[70] Matthias Totzeck, Ulrike B Hendgen-Cotta, Peter Luedike, Michael Berenbrink, Johann P Klare, Heinz-Juergen Steinhoff, Dominik Semmler, Sruti Shiva, Daryl Williams, Anja Kipar, et al. Nitrite regulates hypoxic vasodilation via myoglobin-dependent nitric oxide generation. *Circulation*, 126(3):325–334, 2012.

[71] Manuel Morgado, Elisa Cairrão, António José Santos-Silva, and Ignacio Verde. Cyclic nucleotide-dependent relaxation pathways in vascular smooth muscle. *Cellular and Molecular Life Sciences*, 69(2):247–266, 2012.

[72] Yingzi Zhao, Paul M Vanhoutte, and Susan WS Leung. Vascular nitric oxide: Beyond enos. *Journal of pharmacological sciences*, 129(2):83–94, 2015.

[73] Zohar Abergel, Arijit Kumar Chatterjee, Binyamin Zuckerman, and Einav Gross. Regulation of neuronal oxygen responses in c. elegans is mediated through interactions between globin 5 and the h-nox domains of soluble guanylate cyclases. *Journal of Neuroscience*, 36(3):963–978, 2016.

[74] Annelie Persson, Einav Gross, Patrick Laurent, Karl Emanuel Busch, Hugo Bretes, and Mario De Bono. Natural variation in a neural globin tunes oxygen sensing in wild Caenorhabditis elegans. *Nature*, 458(7241):1030–1033, 2009.

[75] Sruti Shiva, Zhi Huang, Rozalina Grubina, Junhui Sun, Lorna A Ringwood, Peter H MacArthur, Xiuli Xu, Elizabeth Murphy, Victor M Darley-Usmar, and Mark T Gladwin. Deoxymyoglobin is a nitrite reductase that generates nitric oxide and regulates mitochondrial respiration. *Circulation research*, 100(5):654–661, 2007.

[76] Morten Gjerning Petersen, Sylvia Dewilde, and Angela Fago. Reactions of ferrous neuroglobin and cytoglobin with nitrite under anaerobic conditions. *Journal of inorganic biochemistry*, 102(9):1777–1782, 2008.

[77] Paul R Gardner. Nitric oxide dioxygenase function and mechanism of flavohemoglobin, hemoglobin, myoglobin and their associated reductases. *Journal of inorganic biochemistry*, 99(1):247–266, 2005.

[78] Denisa Hathazi, Sonia Diana Mahuţ, Florina-Violeta Scurtu, Cristina Bischin, Corina Stanciu, Amr Ali Attia, Grigore Damian, and Radu Silaghi-Dumitrescu. Involvement of ferryl in the reaction between nitrite and the oxy forms of globins. *JBIC Journal of Biological Inorganic Chemistry*, 19(7):1233–1239, 2014.

[79] Agnes Keszler, Barbora Piknova, Alan N Schechter, and Neil Hogg. The reaction between nitrite and oxyhemoglobin a mechanistic study. *Journal of Biological Chemistry*, 283(15):9615–9622, 2008.

[80] Hiroaki Kosaka, Kazuhiko Imaizumi, and Itiro Tyuma. Mechanism of autocatalytic oxidation of oxyhemoglobin by nitrite an intermediate detected by electron spin resonance. *Biochimica et Biophysica Acta (BBA)-Protein Structure and Molecular Enzymology*, 702(2):237–241, 1982.

[81] Michael P Doyle, James G Herman, and Russell L Dykstra. Autocatalytic oxidation of hemoglobin induced by nitrite: activation and chemical inhibition. *Journal of free radicals in biology & medicine*, 1(2):145–153, 1985.

[82] Daniel B Kim-Shapiro, Mark T Gladwin, Rakesh P Patel, and Neil Hogg. The reaction between nitrite and hemoglobin: the role of nitrite in hemoglobin-mediated hypoxic vasodilation. *Journal of inorganic biochemistry*, 99(1):237–246, 2005.

[83] William J Wallace and Winslow S Caughey. Mechanism for the autoxidation of hemoglobin by phenols, nitrite and "oxidant" drugs. peroxide formation by one electron donation to bound dioxygen. *Biochemical and biophysical research communications*, 62(3):561–567, 1975.

[84] Hiroaki Kosaka, Kazuhiko Imaizumi, Kiyohiro Imai, and Itiro Tyuma. Stoichiometry of the reaction of oxyhemoglobin with nitrite. *Biochimica et Biophysica Acta (BBA)-Protein Structure*, 581(1):184–188, 1979.

[85] Radu Silaghi-Dumitrescu, Dimitri A Svistunenko, Daniela Cioloboc, Cristina Bischin, Florina Scurtu, and Chris E Cooper. Nitrite binding to globins: linkage isomerism, epr silence and reductive chemistry. *Nitric Oxide*, 42:32–39, 2014.

[86] James WA Allen, Christopher W Higham, Richard S Zajicek, Nicholas J Watmough, and Stuart J Ferguson. A novel, kinetically stable, catalytically active, all-ferric, nitrite-bound complex of paracoccus pantotrophus cytochrome cd1. *Biochemical Journal*, 366(3):883–888, 2002.

[87] Edmund P Day, Jim Peterson, Jacques J Bonvoisin, Lawrence J Young, James O Wilkerson, and Lewis M Siegel. Magnetization of the sulfite and nitrite complexes of oxidized sulfite and nitrite reductases: Epr silent spin s= 1/2 states. *Biochemistry*, 27(6):2126–2132, 1988.

[88] Alexandra Lambrou and Eftychia Pinakoulaki. Resonance raman detection of the myoglobin nitrito heme fe-on= o/2-nitrovinyl species: implications for helix e-helix f interactions. *Physical chemistry chemical physics: PCCP*, 17(5):3841–3849, 2015.

[89] David E. Schwab, Jonathan S. Stamler, and David J. Singel. EPR spectroscopy of nitrite complexes of methemoglobin. *Inorg. Chem.*, 49(14):6330–6337, 2010.

[90] Mikio Hoshino, Masahiro Maeda, Reiko Konishi, Hiroshi Seki, and Peter C Ford. Studies on the reaction mechanism for reductive nitrosylation of ferrihemoproteins in buffer solutions. *Journal of the American Chemical Society*, 118(24):5702–5707, 1996.

[91] Luciana Capece, Leonardo Boechi, Laura L. Perissinotti, Pau Arroyo-Mañez, Damián E. Bikiel, Giulietta Smulevich, Marcelo A. Marti, and Dario A. Estrin. Small ligand-globin interactions: Reviewing lessons derived from computer simulation. *Biochim. Biophys. Acta - Proteins Proteomics*, 1834(9):1722–1738, 2013.

[92] Sabine Van Doorslaer, Sylvia Dewilde, Laurent Kiger, Sergiu V. Nistor, Etienne Goovaerts, Michael C. Marden, and Luc Moens. Nitric oxide binding properties of neuroglobin: A characterization by EPR and flash photolysis. *J. Biol. Chem.*, 278(7):4919–4925, 2003.

[93] Evi Vinck, Sabine Van Doorslaer, Sylvia Dewilde, and Luc Moens. Structural change of the heme pocket due to disulfide bridge formation is significantly larger for neuroglobin than for cytoglobin. *Journal of the American Chemical Society*, 126(14):4516–4517, 2004.

[94] Alessandra Pesce, Liesbet Thijs, Marco Nardini, Filip Desmet, Lorenza Sisinni, Louise Gourlay, Alessandro Bolli, Massimiliano Coletta, Sabine Van Doorslaer, Xuehua Wan, et al. Hise11 and hisf8 provide bis-histidyl heme hexa-coordination in the globin domain of geobacter sulfurreducens globin-coupled sensor. *Journal of molecular biology*, 386(1):246–260, 2009.

[95] A Iulia Ioanitescu, Sylvia Dewilde, Laurent Kiger, Michael C Marden, Luc Moens, and Sabine Van Doorslaer. Characterization of nonsymbiotic tomato hemoglobin. *Biophysical journal*, 89(4):2628–2639, 2005.

[96] Sabine Van Doorslaer. Understanding heme proteins with hyperfine spectroscopy. *Journal of Magnetic Resonance*, 280:79–88, 2017.

[97] Jun Yi, Leonard M Thomas, Faik N Musayev, Martin K Safo, and George B Richter-Addo. Crystallographic trapping of heme loss intermediates during the nitrite-induced degradation of human hemoglobin. *Biochemistry*, 50(39):8323–8332, 2011.

[98] Androulla Ioannou, Alexandra Lambrou, Vangelis Daskalakis, and Eftychia Pinakoulaki. Nitrite coordination in myoglobin. *Journal of inorganic biochemistry*, 166:49–54, 2017.

[99] Laureano L Bondoc and R Timkovich. Structural characterization of nitrimyoglobin. *Journal of Biological Chemistry*, 264(11):6134–6145, 1989.

[100] Jay B Fox Jr and JS Thomson. The formation of green heme pigments from metmyoglobin and methemoglobin by the action of nitrite. *Biochemistry*, 3(9):1323–1328, 1964.

[101] Joaquín Navascués, Carmen Pérez-Rontomé, Marina Gay, Manuel Marcos, Fei Yang, F Ann Walker, Alain Desbois, Joaquín Abián, and Manuel Becana. Leghemoglobin green derivatives with nitrated hemes evidence production of highly reactive nitrogen species during aging of legume nodules. *Proceedings of the National Academy of Sciences*, 109(7):2660–2665, 2012.

[102] Mary Grace I Galinato, Robert S Fogle III, Amanda Stetz, and Jhenny F Galan. Modulating the nitrite reductase activity of globins by varying the heme substituents: Utilizing myoglobin as a model system. *Journal of inorganic biochemistry*, 154:7–20, 2016.

[103] Radu Silaghi-Dumitrescu. Linkage isomerism in nitrite reduction by cytochrome cd1 nitrite reductase. *Inorg. Chem.*, 43(12):3715–3718, 2004.

[104] Radu Silaghi-Dumitrescu. Linkage isomerism in nitrite reduction by cytochrome cd 1 nitrite reductase. *Inorganic chemistry*, 43(12):3715–3718, 2004.

[105] Irina V Novozhilova, Philip Coppens, Jonghyuk Lee, George B Richter-Addo, and Kimberly A Bagley. Experimental and density functional theoretical investigations of linkage isomerism in six-coordinate {FeNO} 6 iron porphyrins with axial nitrosyl and nitro ligands. *Journal of the American Chemical Society*, 128(6):2093–2104, 2006.

[106] Nan Xu, Jun Yi, and George B Richter-Addo. Linkage isomerization in heme-nox compounds: Understanding no, nitrite, and hyponitrite interactions with iron porphyrins. *Inorganic chemistry*, 49(14):6253–6266, 2010.

[107] Chunmao He, Hideaki Ogata, and Wolfgang Lubitz. Elucidation of the heme active site electronic structure affecting the unprecedented nitrite dismutase activity of the ferriheme b proteins, the nitrophorins. *Chemical science*, 7(8):5332–5340, 2016.

[108] Jun Yi, Martin K Safo, and George B Richter-Addo. The nitrite anion binds to human hemoglobin via the uncommon o-nitrito mode. *Biochemistry*, 47(32):8247–8249, 2008.

[109] Jun Yi, Julie Heinecke, Hui Tan, Peter C Ford, and George B Richter-Addo. The distal pocket histidine residue in horse heart myoglobin directs the o-binding mode of nitrite to the heme iron. *Journal of the American Chemical Society*, 131(50):18119–18128, 2009.

[110] David Hoogewijs, Eva Geuens, Sylvia Dewilde, Luc Moens, Andy Vierstraete, Serge Vinogradov, and Jacques M. Vanfleteren. Genome-wide analysis of the globin gene family of C. elegans. *IUBMB Life*, 56(11-12):697–702, 2004.

[111] David Hoogewijs, Eva Geuens, Sylvia Dewilde, Andy Vierstraete, Luc Moens, Serge Vinogradov, and Jacques R Vanfleteren. Wide diversity in structure and expression profiles among members of the caenorhabditis elegans globin protein family. *BMC genomics*, 8(1):356, 2007.

[112] David Hoogewijs, Sasha De Henau, Sylvia Dewilde, Luc Moens, Marjolein Couvreur, Gaetan Borgonie, Serge N. Vinogradov, Scott W. Roy, and Jacques R. Vanfleteren. The Caenorhabditis globin gene family reveals extensive nematode-specific radiation and diversification. *BMC Evolutionary Biology*, 8(1):1–13, 2008.

[113] Eva Geuens, David Hoogewijs, Evi Vinck, Sabine Van Doorslaer, Jacques Vanfleteren, Luc Moens, and Sylvia Dewilde. Two distinct functional globin classes in Caenorhabditis elegans. *Biophys. J.*, 96(3):557a, feb 2009.

[114] Eva Geuens, David Hoogewijs, Marco Nardini, Evi Vinck, Alessandra Pesce, Laurent Kiger, Angela Fago, Lesley Tilleman, Sasha De Henau, Michael C Marden, et al. Globin-like proteins in caenorhabditis elegans: in vivo localization, ligand binding and structural properties. *BMC biochemistry*, 11(1):1–15, 2010.

[115] Lesley Tilleman, Francesca Germani, Sasha De Henau, Eva Geuens, David Hoogewijs, Bart P. Braeckman, Jacques R. Vanfleteren, Luc Moens, and Sylvia Dewilde. Globins in Caenorhabditis elegans. *IUBMB Life*, 63(3):166–174, 2011.

[116] Laurent Kiger, Lesley Tilleman, Eva Geuens, David Hoogewijs, Christophe Lechauve, Luc Moens, Sylvia Dewilde, and Michael C Marden. Electron transfer function versus oxygen delivery: a comparative study for several hexacoordinated globins across the animal kingdom. *PLoS One*, 6(6):e20478, 2011.

[117] Lesley Tilleman, Sasha de Henau, Martje Pauwels, Nora Nagy, Isabel Pintelon, Bart P. Braeckman, Karolien de Wael, Sabine van Doorslaer, Dirk Adriaensen, Jean Pierre Timmermans, Luc Moens, and Sylvia Dewilde. An N-Myristoylated Globin with a Redox-Sensing Function That Regulates the Defecation Cycle in Caenorhabditis elegans. *PLoS One*, 7(12):1–9, 2012.

[118] Lesley Tilleman, Francesca Germani, Sasha De Henau, Signe Helbo, Filip Desmet, Herald Berghmans, Sabine Van Doorslaer, David Hoogewijs, Liliane Schoofs, Bart P. Braeckman, Luc Moens, Angela Fago, and Sylvia Dewilde. A globin domain in a neuronal transmembrane receptor of Caenorhabditis elegans and Ascaris suum: Molecular modeling and functional properties. *J. Biol. Chem.*, 290:10336–10352, 2015.

[119] Sasha De Henau, Lesley Tilleman, Matthew Vangheel, Evi Luyckx, Stanislav Trashin, Martje Pauwels, Francesca Germani, Caroline Vlaeminck, Jacques R. Vanfleteren, Wim Bert, Alessandra Pesce, Marco Nardini, Martino Bolognesi, Karolien De Wael, Luc Moens, Sylvia Dewilde, and Bart P. Braeckman. A redox signalling globin is essential for reproduction in Caenorhabditis elegans. *Nat. Commun.*, 6:1–14, 2015.

[120] Sydney Brenner. The genetics of caenorhabditis elegans. *Genetics*, 77(1):71–94, 1974.

[121] H Robert Horvitz and John E Sulston. Isolation and genetic characterization of cell-lineage mutants of the nematode caenorhabditis elegans. *Genetics*, 96(2):435–454, 1980.

[122] M. Chalfie, Y. Tu, G. Euskirchen, W.W. Ward, and D.C. Prasher. Green fluorescent protein as a marker for gene expression. *Science*, 263(5148):802–805, 1994. cited By 5159.

[123] Andrew Fire, SiQun Xu, Mary K Montgomery, Steven A Kostas, Samuel E Driver, and Craig C Mello. Potent and specific genetic interference by double-stranded rna in caenorhabditis elegans. *nature*, 391(6669):806–811, 1998.

[124] Brenner S Wood Wb. The nematode caenorhabditis elegans. *Cold Spring Harbor Laboratory*, 1(988):1091–1105, 1988.

[125] John G White, Eileen Southgate, J Nichol Thomson, and Sydney Brenner. The structure of the nervous system of the nematode caenorhabditis elegans. *Philos Trans R Soc Lond B Biol Sci*, 314(1165):1–340, 1986.

[126] Lav R Varshney, Beth L Chen, Eric Paniagua, David H Hall, and Dmitri B Chklovskii. Structural properties of the caenorhabditis elegans neuronal network. *PLoS computational biology*, 7(2):e1001066, 2011.

[127] C. elegans Sequencing Consortium*. Genome sequence of the nematode c. elegans: a platform for investigating biology. *Science*, 282(5396):2012–2018, 1998.

[128] Javier Apfeld and Scott Alper. What can we learn about human disease from the nematode C. Elegans? *Methods Mol. Biol.*, 1706:53–75, 2018.

[129] Z.F. Altun, L.A. Herndon, C.A. Wolkow, C. Crocker, R. Lints, and D.H. Hall. Wormatlas. `http://www.wormatlas.org`, 2002. (ed.s) 2002-2023.

[130] M. L. Blaxter. Nemoglobins: Divergent nematode globins. *Parasitol. Today*, 9(10):353–360, 1993.

[131] V Adducco. The red substance of eustrongylus gigas. *Arch Ital Biol*, 11:52–69, 1889.

[132] AH Burr, R Schiefke, and G Bollerup. Properties of a hemoglobin from the chromatrope of the nematode mermis nigrescens. *Biochimica et Biophysica Acta (BBA)-Protein Structure*, 405(2):404–411, 1975.

[133] Andrew P Kloek, Jian Yang, F Scott Mathews, Carl Frieden, and Daniel E Goldberg. The tyrosine b10 hydroxyl is crucial for oxygen avidity of ascaris hemoglobin. *Journal of Biological Chemistry*, 269(4):2377–2379, 1994.

[134] Jiang Yang, AP Kloek, Daniel E Goldberg, and F Scott Mathews. The structure of ascaris hemoglobin domain i at 2.2 a resolution: molecular features of oxygen avidity. *Proceedings of the National Academy of Sciences*, 92(10):4224–4228, 1995.

[135] Dena M Minning, Andrew J Gow, Joseph Bonaventura, Rod Braun, Mark Dewhirst, Daniel E Goldberg, and Jonathan S Stamler. Ascaris haemoglobin is a nitric oxide-activated 'deoxygenase'. *Nature*, 401(6752):497–502, 1999.

[136] Daniel E Goldberg. Oxygen-avid hemoglobin of ascaris. *Chemical reviews*, 99(12):3371–3378, 1999.

[137] J Sulston, Z Du, K Thomas, R Wilson, L Hillier, R Staden, N Halloran, P Green, J Thierry-Mieg, L Qiu, et al. The c. elegans genome sequencing project: a beginning. *Nature*, 356(6364):37–41, 1992.

[138] Mary Rossillo and Niels Ringstad. Development of specialized sensory neurons engages a nuclear receptor required for functional plasticity. *Genes & Development*, 34(23-24):1666–1679, 2020.

[139] Oscar H Kapp, Luc Moens, Jaak Vanfleteren, Clive NA Trotman, Tomohiko Suzuki, and Serge N Vinogradov. Alignment of 700 globin sequences: extent of amino acid substitution and its correlation with variation in volume. *Protein Science*, 4(10):2179–2190, 1995.

[140] Sarah B Pierce, Michael Costa, Robert Wisotzkey, Sharmila Devadhar, Sheila A Homburger, Andrew R Buchman, Kimberly C Ferguson, Jonathan Heller, Darren M Platt, Amy A Pasquinelli, et al. Regulation of daf-2 receptor signaling by human insulin and ins-1, a member of the unusually large and diverse c. elegans insulin gene family. *Genes & development*, 15(6):672–686, 2001.

[141] Frank Möhrlen, Harald Hutter, and Robert Zwilling. The astacin protein family in caenorhabditis elegans. *European journal of biochemistry*, 270(24):4909–4920, 2003.

[142] Thorsten Burmester and Thomas Hankeln. The respiratory proteins of insects. *Journal of insect physiology*, 53(4):285–294, 2007.

[143] Federico G Hoffmann, Juan C Opazo, David Hoogewijs, Thomas Hankeln, Bettina Ebner, Serge N Vinogradov, Xavier Bailly, and Jay F Storz. Evolution of the globin gene family in deuterostomes: lineage-specific patterns of diversification and attrition. *Molecular biology and evolution*, 29(7):1735–1745, 2012.

[144] Ana B Christensen, Joseph L Herman, Maurice R Elphick, Kord M Kober, Daniel Janies, Gregorio Linchangco, Dean C Semmens, Xavier Bailly, Serge N Vinogradov, and David Hoogewijs. Phylogeny of echinoderm hemoglobins. *PLoS One*, 10(8):e0129668, 2015.

[145] Patrick T McGrath, Matthew V Rockman, Manuel Zimmer, Heeun Jang, Evan Z Macosko, Leonid Kruglyak, and Cornelia I Bargmann. Quantitative mapping of a digenic behavioral trait implicates globin variation in c. elegans sensory behaviors. *Neuron*, 61(5):692–699, 2009.

[146] Jesse M Gray, David S Karow, Hang Lu, Andy J Chang, Jennifer S Chang, Ronald E Ellis, Michael A Marletta, and Cornelia I Bargmann. Oxygen sensation and social feeding mediated by a c. elegans guanylate cyclase homologue. *Nature*, 430(6997):317–322, 2004.

[147] Andy J Chang, Nikolas Chronis, David S Karow, Michael A Marletta, and Cornelia I Bargmann. A distributed chemosensory circuit for oxygen preference in c. elegans. *PLoS Biol*, 4(9):e274, 2006.

[148] Jungjoo Yoon, Mark A Herzik Jr, Michael B Winter, Rosalie Tran, Charles Olea Jr, and Michael A Marletta. Structure and properties of a bis-histidyl ligated globin from caenorhabditis elegans. *Biochemistry*, 49(27):5662–5670, 2010.

[149] Changhong Ren, Yuan Li, Rongrong Han, Dawen Gao, Weiguang Li, Jinping Shi, David Hoogewijs, Bart P. Braeckman, Sasha De Henau, Yiming Lu, Wubin Qu, Yan Gao, Yonghong Wu, Zhihui Li, Huqi Liu, Zhaoyan Wang, and Chenggang Zhang. GLB-13 is associated with oxidative stress resistance in caenorhabditis elegans. *IUBMB Life*, 65(5):423–434, 2013.

[150] Paul Sternberg. *WormBase : Nematode Information Resource*, 2020 (accessed October 27, 2020).

[151] Benny HH Cheung, Merav Cohen, Candida Rogers, Onder Albayram, and Mario De Bono. Experience-dependent modulation of c. elegans behavior by ambient oxygen. *Current Biology*, 15(10):905–917, 2005.

[152] Yang Zhang. I-tasser server for protein 3d structure prediction. *BMC bioinformatics*, 9(1):40, 2008.

[153] John Jumper, Richard Evans, Alexander Pritzel, Tim Green, Michael Figurnov, Olaf Ronneberger, Kathryn Tunyasuvunakool, Russ Bates, Augustin Žídek, Anna Potapenko, et al. Highly accurate protein structure prediction with alphafold. *Nature*, 596(7873):583–589, 2021.

[154] Mihaly Varadi, Stephen Anyango, Mandar Deshpande, Sreenath Nair, Cindy Natassia, Galabina Yordanova, David Yuan, Oana Stroe, Gemma Wood, Agata Laydon, et al. Alphafold protein structure database: massively expanding the structural coverage of protein-sequence space with high-accuracy models. *Nucleic acids research*, 50(D1):D439–D444, 2022.

[155] Patrick C Mahon, Kiichi Hirota, and Gregg L Semenza. Fih-1: a novel protein that interacts with hif-1α and vhl to mediate repression of hif-1 transcriptional activity. *Genes & development*, 15(20):2675–2686, 2001.

[156] David Barford. The role of cysteine residues as redox-sensitive regulatory switches. *Current opinion in structural biology*, 14(6):679–686, 2004.

[157] James G Ferry. Methanosarcina acetivorans: a model for mechanistic understanding of aceticlastic and reverse methanogenesis. *Frontiers in Microbiology*, 11:1806, 2020.

[158] Arnulf Kletzin. General characteristics and important model organisms. *Archaea: molecular and cellular biology*, pages 14–92, 2007.

[159] Ricardo Jasso-Chávez, M Geovanni Santiago-Martínez, Elizabeth Lira-Silva, Erika Pineda, Armando Zepeda-Rodríguez, Javier Belmont-Díaz, Rusely Encalada, Emma Saavedra, and Rafael Moreno-Sánchez. Air-adapted methanosarcina acetivorans shows high methane production and develops resistance against oxygen stress. *PLoS One*, 10(2):e0117331, 2015.

[160] Tracey Allen K. Freitas, Shaobin Hou, and Maqsudul Alam. The diversity of globin-coupled sensors. *FEBS Letters*, 552(2-3):99–104, 2003.

[161] Tracey Allen K. Freitas, Shaobin Hou, Elhadji M Dioum, Jennifer A Saito, James Newhouse, Gonzalo Gonzalez, Marie Alda Gilles-Gonzalez, and Maqsudul Alam. Ancestral hemoglobins in Archaea. *Proc. Natl. Acad. Sci. U. S. A.*, 101(17):6675–6680, 2004.

[162] Tracey Allen K Freitas, Jennifer A Saito, Xuehua Wan, Shaobin Hou, and Maqsudul Alam. *Protoglobin and globin-coupled sensors*. Elsevier, 2008.

[163] Alessandra Pesce, Martino Bolognesi, and Marco Nardini. Protoglobin: Structure and ligand-binding properties. In *Adv. Microb. Physiol.*, volume 63, pages 79–96. Academic Press, jan 2013.

[164] Paolo Ascenzi, Loris Leboffe, Alessandra Pesce, Chiara Ciaccio, Diego Sbardella, Martino Bolognesi, and Massimo Coletta. Nitrite-reductase and peroxynitrite isomerization activities of methanosarcina acetivorans protoglobin. *PLoS One*, 9(5), 2014.

[165] Sabine Van Doorslaer, Martje van den Bosch, Lesley Tilleman, and Sylvia Dewilde. Epr analysis of imidazole binding to methanosarcina acetivorans protoglobin. *Appl. Magn. Reson.*, 46(4):421–433, 2015.

[166] Lesley Tilleman, Stefania Abbruzzetti, Chiara Ciaccio, Giampiero De Sanctis, Marco Nardini, Alessandra Pesce, Filip Desmet, Luc Moens, Sabine Va Doorslaer, Stefano Bruno, Martino Bolognesi, Paolo Ascenzi, Massimo Coletta, Cristiano Viappiani, and Sylvia Dewilde. Structural bases for the regulation of CO binding in the archaeal protoglobin from Methanosarcina acetivorans. *PLoS One*, 10(6), jun 2015.

[167] Roberta Sgammato. *Ligand binding in haem-containing proteins: a chiroptical study*. PhD thesis, Universiteit Antwerpen, 2020.

[168] A. Pesce. Crystal structure of archeal protoglobin: Novel ligand diffusion paths to the heme. *Nuovo Cim. della Soc. Ital. di Fis. C*, 31(4):539–546, 2008.

[169] Marco Nardini, Alessandra Pesce, Liesbet Thijs, Jennifer A Saito, Sylvia Dewilde, Maqsudul Alam, Paolo Ascenzi, Massimiliano Coletta, Chiara Ciaccio, Luc Moens, Martino Bolognesi, and Roma Tre. Archaeal protoglobin structure indicates new ligand diffusion paths and modulation of haem-reactivity. *EMBO Rep.*, 9:157–163, 2008.

[170] Sabine Van Doorslaer, Lesley Tilleman, Ben Verrept, Filip Desmet, Sara Maurelli, Florin Trandafir, Luc Moens, and Sylvia Dewilde. Marked difference in the electronic structure of cyanide-ligated ferric protoglobins and myoglobin due to heme ruffling. *Inorg. Chem.*, 51(16):8834–8841, 2012.

[171] Chiara Ciaccio, Alessandra Pesce, Grazia R. Tundo, Lesley Tilleman, Laura Bertolacci, Sylvia Dewilde, Luc Moens, Paolo Ascenzi, Martino Bolognesi, Marco Nardini, and Massimo Coletta. Functional and structural roles of the N-terminal extension in Methanosarcina acetivorans protoglobin. *Biochimica et Biophysica Acta - Proteins and Proteomics*, 1834(9):1813–1823, 2013.

[172] Damián E Bikiel, Flavio Forti, Leonardo Boechi, Marco Nardini, F Javier Luque, Marcelo A Martí, and Darío A Estrin. Role of heme distortion on oxygen affinity in heme proteins: The protoglobin case. *J. Phys. Chem. B*, 114(25):8536–8543, 2010.

[173] Mehmet Can, Giorgio Zoppellaro, K. Kristoffer Andersson, and Kara L. Bren. Modulation of ligand-field parameters by heme ruffling in cytochromes c revealed by epr spectroscopy. *Inorg. Chem.*, 50(23):12018–12024, 2011.

[174] Flavio Forti, Leonardo Boechi, Damian Bikiel, Marcelo A Martí, Marco Nardini, Martino Bolognesi, Cristiano Viappiani, Darío Estrin, and F Javier Luque. Ligand Migration in Methanosarcina acetivorans Protoglobin: Effects of Ligand Binding and Dimeric Assembly. *J. Phys. Chem. B*, 115:13771–13780, 2011.

[175] M Bolognesi, E Cannillo, P Ascenzi, GM Giacometti, A Merli, and M Brunori. Reactivity of ferric aplysia and sperm whale myoglobins towards imidazole: X-ray and binding study. *Journal of molecular biology*, 158(2):305–315, 1982.

[176] S Abbruzzetti, L Tilleman, S Bruno, C Viappiani, and F Desmet. Ligation Tunes Protein Reactivity in an Ancient Haemoglobin: Kinetic Evidence for an Allosteric Mechanism in Methanosarcina acetivorans Protoglobin. *PLoS One*, 7(3):33614, 2012.

[177] Alessandra Pesce, Lesley Tilleman, Joke Donné, Elisa Aste, Paolo Ascenzi, Chiara Ciaccio, Massimo Coletta, Luc Moens, Cristiano Viappiani, Sylvia Dewilde, Martino Bolognesi, and Marco Nardini. Structure and Haem-Distal Site Plasticity in Methanosarcina acetivorans Protoglobin. *PLoS One*, 8(6), 2013.

[178] Paolo Ascenzi, Alessandra Pesce, Marco Nardini, Martino Bolognesi, Chiara Ciaccio, Massimo Coletta, and Sylvia Dewilde. Reductive nitrosylation of Methanosarcina acetivorans protoglobin: A comparative study. *Biochem. Biophys. Res. Commun.*, 430(4):1301–1305, 2013.

[179] Kazuyoshi Murata and Matthias Wolf. Cryo-electron microscopy for structural analysis of dynamic biological macromolecules. *Biochimica et Biophysica Acta (BBA)-General Subjects*, 1862(2):324–334, 2018.

[180] Andrew W Senior, Richard Evans, John Jumper, James Kirkpatrick, Laurent Sifre, Tim Green, Chongli Qin, Augustin Žídek, Alexander WR Nelson, Alex Bridgland, et al. Improved protein structure prediction using potentials from deep learning. *Nature*, 577(7792):706–710, 2020.

[181] Martin Gouterman. Study of the effects of substitution on the absorption spectra of porphin. *The Journal of Chemical Physics*, 30(5):1139–1161, 1959.

[182] Martin Gouterman. Spectra of porphyrins. *Journal of Molecular Spectroscopy*, 6:138–163, 1961.

[183] Mercedes Rubio, Björn O Roos, Luis Serrano-Andrés, and Manuela Merchán. Theoretical study of the electronic spectrum of magnesium-porphyrin. *The Journal of chemical physics*, 110(15):7202–7209, 1999.

[184] Alsoph H Corwin, Arthur B Chivvis, Robert W Poor, David G Whitten, and Earl Wayne Baker. Porphyrin studies. xxxvii. the interpretation of porphyrin and metalloporphyrin spectra. *Journal of the American Chemical Society*, 90(24):6577–6583, 1968.

[185] Jamal Uddin. *Macro to nano spectroscopy*. BoD–Books on Demand, 2012.

[186] Rita Giovannetti. The use of spectrophotometry uv-vis for the study of porphyrins. *Macro to nano spectroscopy*, 1:87–108, 2012.

[187] Robert W Woody. The exciton model and the circular dichroism of polypeptides. *Monatshefte für Chemie/Chemical Monthly*, 136(3):347–366, 2005.

[188] Francesco Simone Ruggeri, Johnny Habchi, Andrea Cerreta, and Giovanni Dietler. Afm-based single molecule techniques: unraveling the amyloid pathogenic species. *Current pharmaceutical design*, 22(26):3950–3970, 2016.

[189] Roberta Sgammato, Wouter Herrebout, and Christian Johannessen. Resonance Raman optical activity of the imidazole–Myoglobin complex: Titrating enhancement. *Journal of Raman Spectroscopy*, 50(12):1905–1913, 2019.

[190] Sharon M. Kelly, Thomas J. Jess, and Nicholas C. Price. How to study proteins by circular dichroism. *Biochim. Biophys. Acta - Proteins Proteomics*, 1751(2):119–139, 2005.

[191] Tino Krell, Malcolm J Horsburgh, Alan Cooper, Sharon M Kelly, and John R Coggins. Localization of the active site of type ii dehydroquinases: Identification of a common arginine-containing motif in the two classes of dehydroquinases. *Journal of Biological Chemistry*, 271(40):24492–24497, 1996.

[192] Masako Nagai, Yukifumi Nagai, Yayoi Aki, Kiyohiro Imai, Yoshinao Wada, Shigenori Nagatomo, and Yasuhiko Yamamoto. Effect of reversed heme orientation on circular dichroism and cooperative oxygen binding of human adult hemoglobin. *Biochemistry*, 47(2):517–525, 2008.

[193] Alberto Boffi, Jonathan B. Wittenberg, and Emilia Chiancone. Circular dichroism spectroscopy of Lucina I hemoglobin. *FEBS Letters*, 411(2-3):335–338, 1997.

[194] Ewen Smith and Geoffrey Dent. *Modern Raman spectroscopy: a practical approach*. John Wiley & Sons, 2019.

[195] Robin JH Clark and Trevor J Dines. Theory of the resonance electronic raman effect. *Molecular Physics*, 45(6):1153–1162, 1982.

[196] Thomas G Spiro and Thomas C Strekas. Resonance raman spectra of heme proteins. effects of oxidation and spin state. *Journal of the American Chemical Society*, 96(2):338–345, 1974.

[197] Songzhou Hu, Kevin M Smith, and Thomas G Spiro. Assignment of protoheme resonance raman spectrum by heme labeling in myoglobin. *Journal of the American Chemical Society*, 118(50):12638–12646, 1996.

[198] Hartmut Michel, J Behr, A Harrenga, and Aimo Kannt. Cytochrome c oxidase: structure and spectroscopy. *Annual review of biophysics and biomolecular structure*, 27(1):329–356, 1998.

[199] Giulietta Smulevich, Alessandro Feis, and Barry D Howes. Fifteen years of raman spectroscopy of engineered heme containing peroxidases: what have we learned? *Accounts of chemical research*, 38(5):433–440, 2005.

[200] E Zavoisky. Spin-magnetic resonance in paramagnetics. *J Phys USSR*, 9:211–245, 1945.

[201] Marina Bennati and Thomas F Prisner. New developments in high field electron paramagnetic resonance with applications in structural biology. *Reports on Progress in Physics*, 68(2):411, 2005.

[202] Karsten Holldack and Alexander Schnegg. Thz electron paramagnetic resonance/thz spectroscopy at bessy ii. *Journal of large-scale research facilities JLSRF*, 2:51, 2016.

[203] Daniella Goldfarb and Stefan Stoll. *EPR spectroscopy: fundamentals and methods*. John Wiley & Sons, 2018.

[204] Arthur Schweiger and Gunnar Jeschke. *Principles of pulse electron paramagnetic resonance*. Oxford University Press on Demand, 2001.

[205] Sabine Van Doorslaer. Hyperfine spectroscopy: ESEEM. *eMagRes*, 6(1):51–70, 2017.

[206] L_G Rowan, EL Hahn, and WB Mims. Electron-spin-echo envelope modulation. *Physical Review*, 137(1A):A61, 1965.

[207] P Höfer, A Grupp, H Nebenführ, and M Mehring. Hyperfine sublevel correlation (hyscore) spectroscopy: a 2d esr investigation of the squaric acid radical. *Chemical physics letters*, 132(3):279–282, 1986.

[208] JJ Shane, P Höfer, EJ Reijerse, and E De Boer. Hyperfine sublevel correlation spectroscopy (hyscore) of disordered solids. *Journal of Magnetic Resonance (1969)*, 99(3):596–604, 1992.

[209] Claudius Gemperle and Arthur Schweiger. Pulsed electron-nuclear double resonance methodology. *Chemical reviews*, 91(7):1481–1505, 1991.

[210] Marina Brustolon and Elio Giamello. *Electron Paramagnetic Resonance: A Practitioners Toolkit*. John Wiley & Sons, 2009.

[211] ER Davies. A new pulse endor technique. *Physics Letters A*, 47(1):1–2, 1974.

[212] Stefan Stoll and Arthur Schweiger. Easyspin, a comprehensive software package for spectral simulation and analysis in epr. *Journal of magnetic resonance*, 178(1):42–55, 2006.

[213] CPS Taylor. The epr of low spin heme complexes relation of the τ2g hole model to the directional properties of the g tensor, and a new method for calculating the ligand field parameters. *Biochimica et Biophysica Acta (BBA)-Protein Structure*, 491(1):137–148, 1977.

[214] WE Blumberg and J Peisach. Low—spin compounds of heme proteins. ACS Publications, 1971.

[215] JE Bennett, DJE Ingram, P George, and J Stanley Griffith. Paramagnetic resonance absorption of ferrihaemoglobin and ferrimyoglobin derivatives. *Nature*, 176(4478):394–394, 1955.

[216] J Peisach, WE Blumberg, S Ogawa, EA Rachmilewitz, and R Oltzik. The effects of protein conformation on the heme symmetry in high spin ferric heme proteins as studied by electron paramagnetic resonance. *Journal of Biological Chemistry*, 246(10):3342–3355, 1971.

[217] Sabine Van Doorslaer and Bert Cuypers. Electron paramagnetic resonance of globin proteins–a successful match between spectroscopic development and protein research. *Molecular Physics*, 116(3):287–309, 2018.

[218] Jeffrey Harmer, George Mitrikas, and Arthur Schweiger. Advanced pulse epr methods for the characterization of metalloproteins. In *High resolution EPR: Applications to metalloenzymes and metals in medicine*, pages 13–61. Springer, 2009.

[219] Inés García-Rubio, Jesús I Martínez, Rafael Picorel, Inmaculada Yruela, and Pablo J Alonso. Hyscore spectroscopy in the cytochrome b 559 of the photosystem ii reaction center. *Journal of the American Chemical Society*, 125(51):15846–15854, 2003.

[220] E Vinck, S Van Doorslaer, S Dewilde, G Mitrikas, A Schweiger, and L Moens. Analyzing heme proteins using epr techniques: the heme-pocket structure of ferric mouse neuroglobin. *JBIC Journal of Biological Inorganic Chemistry*, 11(4):467–475, 2006.

[221] Sergey Milikisiyants, Ruchira Chatterjee, Amanda Weyers, Ashley Meenaghan, Christopher Coates, and KV Lakshmi. Ligand environment of the s2 state of photosystem ii: A study of the hyperfine interactions of the tetranuclear manganese cluster by 2d 14n hyscore spectroscopy. *The Journal of Physical Chemistry B*, 114(33):10905–10911, 2010.

[222] Albert JR Heck. Native mass spectrometry: a bridge between interactomics and structural biology. *Nature methods*, 5(11):927–933, 2008.

[223] Kristina Lorenzen and Esther van Duijn. Native mass spectrometry as a tool in structural biology. *Current protocols in protein science*, 62(1):17–12, 2010.

[224] Robert HH van den Heuvel and Albert JR Heck. Native protein mass spectrometry: from intact oligomers to functional machineries. *Current opinion in chemical biology*, 8(5):519–526, 2004.

[225] Ruedi Aebersold and Matthias Mann. Mass spectrometry-based proteomics. *Nature*, 422(6928):198–207, 2003.

[226] Aneika C Leney and Albert JR Heck. Native mass spectrometry: what is in the name? *Journal of the American Society for Mass Spectrometry*, 28(1):5–13, 2016.

[227] Brandon T Ruotolo and Carol V Robinson. Aspects of native proteins are retained in vacuum. *Current opinion in chemical biology*, 10(5):402–408, 2006.

[228] J. Fernandez De La Mora. Electrospray ionization of large multiply charged species proceeds via Dole's charged residue mechanism. *Anal. Chim. Acta*, 406(1):93–104, 2000.

[229] Rita K Upmacis, David P Hajjar, Brian T Chait, and Urooj A Mirza. Direct observation of nitrosylated heme in myoglobin and hemoglobin by electrospray ionization mass spectrometry. *Journal of the American Chemical Society*, 119(43):10424–10429, 1997.

[230] Djemel Hamdane, Laurent Kiger, Sylvia Dewilde, Brian N Green, Alessandra Pesce, Julien Uzan, Thorsten Burmester, Thomas Hankeln, Martino Bolognesi, Luc Moens, et al. The redox state of the cell regulates the ligand binding affinity of human neuroglobin and cytoglobin. *Journal of Biological Chemistry*, 278(51):51713–51721, 2003.

[231] Suk-Joon Hyung, Carol V Robinson, and Brandon T Ruotolo. Gas-phase unfolding and disassembly reveals stability differences in ligand-bound multiprotein complexes. *Chemistry & biology*, 16(4):382–390, 2009.

[232] Frank Sobott, Margaret G McCammon, and Carol V Robinson. Gas-phase dissociation pathways of a tetrameric protein complex. *International Journal of Mass Spectrometry*, 230(2-3):193–200, dec 2003.

[233] Ronald Pethig and Jonathan AR Price. The influence of electrostatic interactions on the activity of lysozyme. *International Journal of Quantum Chemistry*, 30(S13):39–51, 1986.

[234] Niels Van Brempt, Roberta Sgammato, Quinten Beirinckx, Dietmar Hammerschmid, Frank Sobott, Sylvia Dewilde, Luc Moens, Wouter Herrebout, Christian Johannessen, and Sabine Van Doorslaer. The effect of ph and nitrite on the haem pocket of glb-33, a globin-coupled neuronal transmembrane receptor of caenorhabditis elegans. *Biochimica et Biophysica Acta (BBA) - Proteins and Proteomics*, 1871(4):140913, 2023.

[235] Alessandra Pesce, Martino Bolognesi, Alessio Bocedi, Paolo Ascenzi, Sylvia Dewilde, Luc Moens, Thomas Hankeln, and Thorsten Burmester. Neuroglobin and cytoglobin. *EMBO reports*, 3(12):1146–1151, 2002.

[236] Henri Wajcman, Laurent Kiger, and Michael C Marden. Structure and function evolution in the superfamily of globins. *Comptes rendus biologies*, 332(2-3):273–282, 2009.

[237] Zainab Hafideddine, Tim Loier, Niels Van Brempt, Sasha De Henau, HY Vincent Ching, Sander Neukermans, Saskia Defossé, Herald Berghmans, Roberta Sgammato, Roy Aerts, et al. Glb-3: A resilient, cysteine-rich, membrane-tethered globin expressed in the reproductive and nervous system of caenorhabditis elegans. *Journal of Inorganic Biochemistry*, 238:112063, 2023.

[238] Francesco P. Nicoletti, Enrica Droghetti, Barry D. Howes, Juan P. Bustamante, Alessandra Bonamore, Natascia Sciamanna, Darío A. Estrin, Alessandro Feis, Alberto Boffi, and Giulietta Smulevich. H-bonding networks of the distal residues and water molecules in the active site of Thermobifida fusca hemoglobin. *Biochim. Biophys. Acta - Proteins Proteomics*, 1834(9):1901–1909, 2013.

[239] J Qin, U Pande, G N La Mar, F Ascoli, P Ascenzi, F Cutruzzola, C Travaglini-Allocatelli, and M Brunori. 1H NMR study of the dynamics of the pH modulation of axial coordination in Aplysia limacina (Val(E7)) and sperm whale double mutant His(E7)– >Val,Thr(E10)–>Arg metmyoglobin. *J Biol Chem*, 268(32):24012–24021, 1993.

[240] Mark T Gladwin, Alan N Schechter, Daniel B Kim-Shapiro, Rakesh P Patel, Neil Hogg, Sruti Shiva, Richard O Cannon, Malte Kelm, David A Wink, Michael Graham Espey, et al. The emerging biology of the nitrite anion. *Nature chemical biology*, 1(6):308–314, 2005.

[241] Nicoletta Castiglione, Serena Rinaldo, Giorgio Giardina, Valentina Stelitano, and Francesca Cutruzzola. Nitrite and nitrite reductases: from molecular mechanisms to significance in human health and disease. *Antioxidants & redox signaling*, 17(4):684–716, 2012.

[242] Kenyatta Cosby, Kristine S Partovi, Jack H Crawford, Rakesh P Patel, Christopher D Reiter, Sabrina Martyr, Benjamin K Yang, Myron A Waclawiw, Gloria Zalos, Xiuli Xu, et al. Nitrite reduction to nitric oxide by deoxyhemoglobin vasodilates the human circulation. *Nature medicine*, 9(12):1498–1505, 2003.

[243] Jon W. Jacklet. Nitric oxide signaling in invertebrates. *Invertebr. Neurosci.*, 3(1):1–14, 1997.

[244] Ulrike Kreutzer and Thomas Jue. Role of myoglobin as a scavenger of cellular no in myocardium. *American Journal of Physiology-Heart and Circulatory Physiology*, 286(3):H985–H991, 2004.

[245] Mark T Gladwin and Daniel B Kim-Shapiro. The functional nitrite reductase activity of the heme-globins. *Blood*, 112(7):2636–2647, 2008.

[246] Douglas D Thomas, Katrina M Miranda, Carol A Colton, Deborah Citrin, Michael Graham Espey, and David A Wink. Heme proteins and nitric oxide (no): the neglected, eloquent chemistry in no redox signaling and regulation. *Antioxidants and Redox Signaling*, 5(3):307–317, 2003.

[247] Androulla Ioannou, Alexandra Lambrou, Vangelis Daskalakis, and Eftychia Pinakoulaki. Coupling of helix ef motion with the o-nitrito and 2-nitrovinyl coordination in myoglobin. *Biophysical Chemistry*, 221:10–16, 2017.

[248] Ilenia Serra, Daniel Schmidt, Vera Pfanzagl, Georg Mlynek, Stefan Hofbauer, Kristina Djinović-Carugo, Paul G Furtmüller, Inés García-Rubio, Sabine Van Doorslaer, and Christian Obinger. Impact of the dynamics of the catalytic arginine on nitrite and chlorite binding by dimeric chlorite dismutase. *Journal of Inorganic Biochemistry*, 227:111689, 2022.

[249] Edmund P. Day, Jim Peterson, Jacques J. Bonvoisin, Lawrence J. Young, James O. Wilkerson, and Lewis M. Siegel. Magnetization of the Sulfite and Nitrite Complexes of Oxidized Sulfite and Nitrite Reductases: EPR Silent Spin S = 1/2 States. *Biochemistry*, 27(6):2126–2132, 1988.

[250] Thomas G Spiro, Giulietta Smulevich, and Chang Su. Probing protein structure and dynamics with resonance raman spectroscopy: cytochrome c peroxidase and hemoglobin. *Biochemistry*, 29(19):4497–4508, 1990.

[251] Sylvia Dewilde, Kirsten Mees, Laurent Kiger, Christophe Lechauve, Michael C Marden, Alessandra Pesce, Martino Bolognesi, and Luc Moens. Expression, purification, and crystallization of neuro- and cytoglobin. In *Methods in enzymology*, volume 436, pages 341–357. Elsevier, 2008.

[252] Paul HC Eilers. A perfect smoother. *Analytical chemistry*, 75(14):3631–3636, 2003.

[253] Jun Yi, Julie Heinecke, Hui Tan, Peter C. Ford, and George B. Richter-Addo. The distal pocket histidine residue in horse heart myoglobin directs the O-binding mode of nitrite to the heme iron. *J. Am. Chem. Soc.*, 131(50):18119–18128, 2009.

[254] Masako Nagai, Chika Kobayashi, Yukifumi Nagai, Kiyohiro Imai, Naoki Mizusawa, Hiroshi Sakurai, Saburo Neya, Megumi Kayanuma, Mitsuo Shoji, and Shigenori Nagatomo. Involvement of propionate side chains of the heme in circular dichroism of myoglobin: experimental and theoretical analyses. *The Journal of Physical Chemistry B*, 119(4):1275–1287, 2015.

[255] Masako Nagai, Yukifumi Nagai, Kiyohiro Imai, and Saburo Neya. Circular dichroism of hemoglobin and myoglobin. *Chirality*, 26(9):438–442, 2014.

[256] Reinhard Schweitzer-Stenner. Cytochrome c: a multifunctional protein combining conformational rigidity with flexibility. *New Journal of Science*, 2014, 2014.

[257] Tong-Jian Shen, Nancy T Ho, Virgil Simplaceanu, Ming Zou, Brian N Green, Ming F Tam, and Chien Ho. Production of unmodified human adult hemoglobin in escherichia coli. *Proceedings of the National Academy of Sciences*, 90(17):8108–8112, 1993.

[258] Alessandro Feis, Barry D Howes, Lisa Milazzo, Daniela Coppola, and Giulietta Smulevich. Structural determinants of ligand binding in truncated hemoglobins: Resonance raman spectroscopy of the native states and their carbon monoxide and hydroxide complexes. *Biopolymers*, 109(10):e23114, 2018.

[259] Alessandro Feis, Mario P Marzocchi, Mauro Paoli, and Giulietta Smulevich. Spin state and axial ligand bonding in the hydroxide complexes of metmyoglobin, methemoglobin, and horseradish peroxidase at room and low temperatures. *Biochemistry*, 33(15):4577–4583, 1994.

[260] Francesco P Nicoletti, Juan P Bustamante, Enrica Droghetti, Barry D Howes, Maria Fittipaldi, Alessandra Bonamore, Paola Baiocco, Alessandro Feis, Alberto Boffi, Dario A Estrin, et al. Interplay of the h-bond donor–acceptor role of the distal residues in hydroxyl ligand stabilization of thermobifida fusca truncated hemoglobin. *Biochemistry*, 53(51):8021–8030, 2014.

[261] Charles P Scholes, Roger A Isaacson, and George Feher. Determination of the zero-field splitting of fe3+ in heme proteins from the temperature dependence of the spin-lattice relaxation rate. *Biochimica et Biophysica Acta (BBA)-General Subjects*, 244(1):206–210, 1971.

[262] David W Kraus and JB Wittenberg. Hemoglobins of the lucina pectinata/bacteria symbiosis. i. molecular properties, kinetics and equilibria of reactions with ligands. *Journal of Biological Chemistry*, 265(27):16043–16053, 1990.

[263] Dimitri A Svistunenko, Brandon J Reeder, Mieebi M Wankasi, Radu-Lucian Silaghi-Dumitrescu, Chris E Cooper, Serena Rinaldo, Francesca Cutruzzolà, and Michael T Wilson. Reaction of aplysia limacina metmyoglobin with hydrogen peroxide. *Dalton Transactions*, (8):840–850, 2007.

[264] Dillon B. Nye, Eric A. Johnson, Melissa H. Mai, and Juliette T.J. Lecomte. Replacement of the heme axial lysine as a test of conformational adaptability in the truncated hemoglobin THB1. *J. Inorg. Biochem.*, 201(September):110824, 2019.

[265] Zach N. Nilsson, Brian L. Mandella, Kakali Sen, Demet Kekilli, Michael A. Hough, Pierre Moënne-Loccoz, Richard W. Strange, and Colin R. Andrew. Distinguishing Nitro vs Nitrito Coordination in Cytochrome c Using Vibrational Spectroscopy and Density Functional Theory. *Inorg. Chem.*, 56(21):13205–13213, 2017.

[266] Bing Wang, Yelu Shi, Jesús Tejero, Samantha M Powell, Leonard M Thomas, Mark T Gladwin, Sruti Shiva, Yong Zhang, and George B Richter-Addo. Nitrosyl myoglobins and their nitrite precursors: Crystal structural and quantum mechanics and molecular mechanics theoretical investigations of preferred fe–no ligand orientations in myoglobin distal pockets. *Biochemistry*, 57(32):4788–4802, 2018.

[267] Wilford Tse, Nathan Whitmore, Myles R Cheesman, and Nicholas J Watmough. Influence of the heme distal pocket on nitrite binding orientation and reactivity in sperm whale myoglobin. *Biochemical Journal*, 478(4):927–942, 2021.

[268] Peter L Hagedoorn, Daniel C De Geus, and Wilfred R Hagen. Spectroscopic characterization and ligand-binding properties of chlorite dismutase from the chlorate respiring bacterial strain gr-1. *European journal of biochemistry*, 269(19):4905–4911, 2002.

[269] Helena Hernández and Carol V Robinson. Determining the stoichiometry and interactions of macromolecular assemblies from mass spectrometry. *Nature protocols*, 2(3):715–726, 2007.

[270] Joseph Gault, Joseph AC Donlan, Idlir Liko, Jonathan TS Hopper, Kallol Gupta, Nicholas G Housden, Weston B Struwe, Michael T Marty, Todd Mize, Cherine Bechara, et al. High-resolution mass spectrometry of small molecules bound to membrane proteins. *Nature methods*, 13(4):333–336, 2016.

[271] Frank Sobott, Margaret G McCammon, Helena Hernández, and Carol V Robinson. The flight of macromolecular complexes in a mass spectrometer. *Philosophical Transactions of the Royal Society A: Mathematical, Physical and Engineering Sciences*, 363(1827):379–391, 2005.

[272] Jonathan TS Hopper and Neil J Oldham. Collision induced unfolding of protein ions in the gas phase studied by ion mobility-mass spectrometry: the effect of ligand binding on conformational stability. *Journal of the American Society for Mass Spectrometry*, 20(10):1851–1858, 2009.

[273] A Konijnenberg, A Butterer, and F Sobott. Native ion mobility-mass spectrometry and related methods in structural biology. *Biochimica et Biophysica Acta (BBA)-Proteins and Proteomics*, 1834(6):1239–1256, 2013.

[274] Bradley I. Goetz, Howard W. Shields, Swati Basu, Pamela Wang, S. Bruce King, Neil Hogg, Mark T. Gladwin, and Daniel B. Kim-Shapiro. An electron paramagnetic resonance study of the affinity of nitrite for methemoglobin. *Nitric Oxide - Biol. Chem.*, 22(2):149–154, 2010.

[275] PP Schmidt, R Kappl, and J Hüttermann. On the mode of hexacoordinated no-binding to myo- and hemoglobin: Variable-temperature epr studies at multiple microwave frequencies. *Applied Magnetic Resonance*, 21(3):423–440, 2001.

[276] Eliane Wajnberg, Marilia P Linhares, Léa J El-Jaick, and George Bemski. Nitrosyl hemoglobin: Epr components at low temperatures. *European biophysics journal*, 21(1):57–61, 1992.

[277] Florin Trandafir, Sabine Van Doorslaer, Sylvia Dewilde, and Luc Moens. Temperature dependence of no binding modes in human neuroglobin. *Biochimica et Biophysica Acta (BBA)-Proteins and Proteomics*, 1702(2):153–161, 2004.

[278] Randall H Morse and SI Chan. Electron paramagnetic resonance studies of nitrosyl ferrous heme complexes. determination of an equilibrium between two conformations. *Journal of Biological Chemistry*, 255(16):7876–7882, 1980.

[279] Irina I Vlasova, Vladimir A Tyurin, Alexandr A Kapralov, Igor V Kurnikov, Anatoly N Osipov, Maxim V Potapovich, Detcho A Stoyanovsky, and Valerian E Kagan. Nitric oxide inhibits peroxidase activity of cytochrome c· cardiolipin complex and blocks cardiolipin oxidation. *Journal of Biological Chemistry*, 281(21):14554–14562, 2006.

[280] Marina Radoul, Mahesh Sundararajan, Alexey Potapov, Christoph Riplinger, Frank Neese, and Daniella Goldfarb. Revisiting the nitrosyl complex of myoglobin by high-field pulse EPR spectroscopy and quantum mechanical calculations. *Phys. Chem. Chem. Phys.*, 12(26):7276–7289, 2010.

[281] Daniel Schmidt, Ilenia Serra, Georg Mlynek, Vera Pfanzagl, Stefan Hofbauer, Paul G Furtmüller, Kristina Djinović-Carugo, Sabine Van Doorslaer, and Christian Obinger. Arresting the catalytic arginine in chlorite dismutases: impact on heme coordination, thermal stability, and catalysis. *Biochemistry*, 60(8):621–634, 2021.

[282] Giorgio M Giacometti, Alvaro Da Ros, Eraldo Antonini, and Maurizio Brunori. Equilibrium and kinetics of the reaction of aplysia myoglobin with azide. *Biochemistry*, 14(8):1584–1588, 1975.

[283] Jun Qin, Gerd N La Mar, Franca Ascoli, Martino Bolognesi, and Maurizio Brunori. Solution 1h nuclear magnetic resonance determination of hydrogen bonding of the e10 (66) arg side-chain to the bound ligand in aplysia cyano-met myoglobin. *Journal of molecular biology*, 224(4):891–897, 1992.

[284] Carlo Travaglini Allocatelli, Francesca Cutruzzola, Andrea Brancaccio, Maurizio Brunori, Jun Qin, and Gerd N La Mar. Structural and functional characterization of sperm whale myoglobin mutants: role of arginine (e10) in ligand stabilization. *Biochemistry*, 32(23):6041–6049, 1993.

[285] Denis L Rousseau, Yuan-chin Ching, Maurizio Brunori, and Giorgio M Giacometti. Axial coordination of ferric aplysia myoglobin. *Journal of Biological Chemistry*, 264(14):7878–7881, 1989.

[286] Myles Richard Cheesman, Colin Greenwood, and Andrew J Thomson. Magnetic circular dichroism of hemoproteins. In *Advances in Inorganic Chemistry*, volume 36, pages 201–255. Elsevier, 1991.

[287] Mahesh Sundararajan and Frank Neese. Distal Histidine Modulates the Unusual O-Binding of Nitrite to Myoglobin: Evidence from the Quantum Chemical Analysis of EPR Parameters. *Inorg. Chem.*, 54(15):7209–7217, 2015.

[288] Yutaka Orii and Masayuki Morita. Measurement of the ph of frozen buffer solutions by using ph indicators. *The Journal of Biochemistry*, 81(1):163–168, 1977.

[289] Vijay S Sharma, TG Traylor, Robert Gardiner, and H Mizukami. Reaction of nitric oxide with heme proteins and model compounds of hemoglobin. *Biochemistry*, 26(13):3837–3843, 1987.

[290] Lei-Bin Wu, Hong Yuan, Shu-Qin Gao, Yong You, Chang-Ming Nie, Ge-Bo Wen, Ying-Wu Lin, and Xiangshi Tan. Regulating the nitrite reductase activity of myoglobin by redesigning the heme active center. *Nitric oxide*, 57:21–29, 2016.

[291] Donald Bashford, Cyrus Chothia, and Arthur M Lesk. Determinants of a protein fold: Unique features of the globin amino acid sequences. *Journal of molecular biology*, 196(1):199–216, 1987.

[292] Francesca Germani, Alessandra Pesce, Andrea Venturini, Luc Moens, Martino Bolognesi, Sylvia Dewilde, and Marco Nardini. High resolution crystal structures of the Cerebratulus lacteus mini-Hb in the unligated and carbomonoxy states. *Int. J. Mol. Sci.*, 13(7):8025–8037, jun 2012.

[293] Jesús Tejero, Courtney E Sparacino-Watkins, Venkata Ragireddy, Sheila Frizzell, and Mark T Gladwin. Exploring the mechanisms of the reductase activity of neuroglobin by site-directed mutagenesis of the heme distal pocket. *Biochemistry*, 54(3):722–733, 2015.

[294] A. M. Tyryshkin, S. A. Dikanov, E. J. Reijerse, C. Burgard, and J. Hüttermann. Characterization of bimodal coordination structure in nitrosyl heme complexes through hyperfine couplings with pyrrole and protein nitrogens. *J. Am. Chem. Soc.*, 121(14):3396–3406, 1999.

[295] Sergei A. Dikanov and Yuri Tsvetkov. *Electron Spin Echo Envelope (ESEEM) Modulation.* CRC Press, Boca Raton, 1992.

[296] Max F Perutz, John V Kilmartin, Kyoshi Nagai, Attila Szabo, and Sanford R Simon. Influence of globin structures on the state of the heme. iv. ferrous low spin derivatives. *Biochemistry*, 15(2):378–387, 1976.

[297] Ryo Nakajima and Isao Yamazaki. The conversion of horseradish peroxidase c to a verdohemoprotein by a hydroperoxide derived enzymatically from indole-3-acetic acid and by m-nitroperoxybenzoic acid. *Journal of Biological Chemistry*, 255(5):2067–2071, 1980.

[298] Mark S Hargrove, Anthony J Wilkinson, and John S Olson. Structural factors governing hemin dissociation from metmyoglobin. *Biochemistry*, 35(35):11300–11309, 1996.

[299] Sylvia Dewilde, Laurent Kiger, Thorsten Burmester, Thomas Hankeln, Veronique Baudin-Creuza, Tony Aerts, Michael C Marden, Roland Caubergs, and Luc Moens. Biochemical characterization and ligand binding properties of neuroglobin, a novel member of the globin family. *Journal of Biological Chemistry*, 276(42):38949–38955, 2001.

[300] SV Nistor, E Goovaerts, S Van Doorslaer, S Dewilde, and L Moens. Epr-spectroscopic evidence of a dominant his–feiii–his coordination in ferric neuroglobin. *Chemical physics letters*, 361(5-6):355–361, 2002.

[301] Masao Nakamura and Shingo Nakamura. Conversion of metmyoglobin to no myoglobin in the presence of nitrite and reductants. *Biochimica et Biophysica Acta (BBA)-General Subjects*, 1289(3):329–335, 1996.

[302] K-P Dinse. Pulsed endor. ch. 17. In *Advanced EPR*. 1989.

[303] Roman Davydov, Robert L Osborne, Sun Hee Kim, John H Dawson, and Brian M Hoffman. Epr and endor studies of cryoreduced compounds ii of peroxidases and myoglobin. proton-coupled electron transfer and protonation status of ferryl hemes. *Biochemistry*, 47(18):5147–5155, 2008.

[304] Marco Flores, Eliane Wajnberg, and George Bemski. Temperature dependence of q-band electron paramagnetic resonance spectra of nitrosyl heme proteins. *Biophysical journal*, 73(6):3225–3229, 1997.

[305] Ignez Caracelli, Nilce C Meirelles, Marcel Tabak, Oswaldo Baffa Filho, and Otaciro R Nascimento. An esr study of nitrosyl-aplysia brasiliana myoglobin and nitrosyl annelidae glossoscolex paulistus erythrocruorin. *Biochimica et Biophysica Acta (BBA)-Protein Structure and Molecular Enzymology*, 955(3):315–320, 1988.

[306] Marina Radoul, Dmytro Bykov, Serena Rinaldo, Francesca Cutruzzola, Frank Neese, and Daniella Goldfarb. Dynamic hydrogen-bonding network in the distal pocket of the nitrosyl complex of pseudomonas aeruginosa cd1 nitrite reductase. *Journal of the American Chemical Society*, 133(9):3043–3055, 2011.

[307] F Trandafir, P Heerdt, M Fittipaldi, E Vinck, S Dewilde, L Moens, and S Van Doorslaer. Studying high-spin ferric heme proteins by pulsed epr spectroscopy: Analysis of the ferric form of the e7q mutant of human neuroglobin. *Applied Magnetic Resonance*, 31:553–572, 2007.

[308] Tadayuki Uno, Daisuke Ryu, Hiroko Tsutsumi, Yoshikazu Tomisugi, Yoshinobu Ishikawa, Anthony J Wilkinson, Hideaki Sato, and Takashi Hayashi. Residues in the distal heme pocket of neuroglobin: implications for the multiple ligand binding steps. *Journal of Biological Chemistry*, 279(7):5886–5893, 2004.

[309] Roberta Sgammato, Niels Van Brempt, Roy Aerts, Sabine Van Doorslaer, Sylvia Dewilde, Wouter Herrebout, and Christian Johannessen. Interaction of nitrite with ferric protoglobin from methanosarcina acetivorans – an interesting model for spectroscopic studies of the haem–ligand interaction. *Dalton Trans.*, 52:2976–2987, 2023.

[310] Tracey Allen K. Freitas, Jennifer A. Saito, Shaobin Hou, and Maqsudul Alam. Globin-coupled sensors, protoglobins, and the last universal common ancestor. *J. Inorg. Biochem.*, 99(1):23–33, 2005.

[311] Alessandra Pesce, Lesley Tilleman, Sylvia Dewilde, Paolo Ascenzi, Massimo Coletta, Chiara Ciaccio, Stefano Bruno, Luc Moens, Martino Bolognesi, and Marco Nardini. Structural heterogeneity and ligand gating in ferric methanosarcina acetivorans protoglobin mutants. *IUBMB Life*, 63(5):287–294, 2011.

[312] Mahesh Sundararajan and Frank Neese. Detailed qm/mm study of the electron paramagnetic resonance parameters of nitrosyl myoglobin. *Journal of chemical theory and computation*, 8(2):563–574, 2012.

[313] Haitao Li, Craig Hemann, Tamer M Abdelghany, Mohamed A El-Mahdy, and Jay L Zweier. Characterization of the mechanism and magnitude of cytoglobin-mediated nitrite reduction and nitric oxide generation under anaerobic conditions. *Journal of Biological Chemistry*, 287(43):36623–36633, 2012.

[314] H Detlef Klüber and Ralf Conrad. Effects of nitrate, nitrite, no and n2o on methanogenesis and other redox processes in anoxic rice field soil. *FEMS Microbiology Ecology*, 25(3):301–318, 1998.

[315] Lukasz P. Kozlowski. IPC - Isoelectric Point Calculator. *Biology Direct*, 11(1):1–16, 2016.

[316] Hans FM Boelens, Paul HC Eilers, and Thomas Hankemeier. Sign constraints improve the detection of differences between complex spectral data sets: Lc- ir as an example. *Analytical chemistry*, 77(24):7998–8007, 2005.

[317] Giulietta Smulevich. Understanding heme cavity structure of peroxidases: comparison of electronic absorption and resonance raman spectra with crystallographic results. *Biospectroscopy*, 4(S5):S3–S17, 1998.

[318] Enrica Droghetti, Barry D Howes, Alessandro Feis, Paola Dominici, Maria Fittipaldi, and Giulietta Smulevich. The quantum mechanically mixed-spin state in a non-symbiotic plant hemoglobin: The effect of distal mutation on ahb1 from arabidopsis thaliana. *Journal of inorganic biochemistry*, 101(11-12):1812–1819, 2007.

[319] Martin M Maltempo. Magnetic state of an unusual bacterial heme protein. *The Journal of Chemical Physics*, 61(7):2540–2547, 1974.

[320] M Abe, T Kitagawa, and Y Kyogoku. Resonance raman spectra of octaethylporphyrinato-ni (ii) and meso-deuterated and 15n substituted derivatives. ii. a normal coordinate analysis. *The Journal of Chemical Physics*, 69(10):4526–4534, 1978.

[321] TG Spiro and XY Li. Biological applications of raman spectroscopy, vol. 3, resonance raman spectra of hemes and metalloporphyrins. *Kapitel*, 1:1–37, 1988.

[322] Charles Weiss, Hiroshi Kobayashi, and Martin Gouterman. Spectra of porphyrins. Part III. Self-consistent molecular orbital calculations of porphyrin and related ring systems. *Journal of Molecular Spectroscopy*, 16(2):415–450, 1965.

[323] Alexandra Lambrou and Eftychia Pinakoulaki. Resonance Raman detection of the myoglobin nitrito heme Fe-O-N=O/2-nitrovinyl species: Implications for helix E-helix F interactions. *Phys. Chem. Chem. Phys.*, 17(5):3841–3849, 2015.

[324] Androulla Ioannou and Eftychia Pinakoulaki. Resonance raman detection of the heme fe (ii)-no/2-nitrovinyl species in myoglobin. *Journal of Molecular Structure*, 1152:257–260, 2018.

[325] Bih-Show Lou, Jennifer K Snyder, Paul Marshall, Jinn-Shyan Wang, Gang Wu, Richard J Kulmacz, Ah-Lim Tsai, and Jianling Wang. Resonance raman studies indicate a unique heme active site in prostaglandin h synthase. *Biochemistry*, 39(40):12424–12434, 2000.

[326] Estelle M Maes, F Ann Walker, William R Montfort, and Roman S Czernuszewicz. Resonance raman spectroscopic study of nitrophorin 1, a nitric oxide-binding heme protein from rhodnius p rolixus, and its nitrosyl and cyano adducts. *Journal of the American Chemical Society*, 123(47):11664–11672, 2001.

[327] Chunmao He and Markus Knipp. Formation of nitric oxide from nitrite by the ferriheme b protein nitrophorin 7. *J. Am. Chem. Soc.*, 131(34):12042–12043, 2009.

[328] Christian Johannessen and Salim Abdali. Surface enhanced raman optical activity as an ultra sensitive tool for ligand binding analysis. *Spectroscopy*, 21(3):143–149, 2007.

[329] Bayden R Wood, Mehdi Asghari-Khiavi, Elena Bailo, Don McNaughton, and Volker Deckert. Detection of nano-oxidation sites on the surface of hemoglobin crystals using tip-enhanced raman scattering. *Nano letters*, 12(3):1555–1560, 2012.

[330] Lorna Ashton, Victoria L Brewster, Elon Correa, and Royston Goodacre. Detection of glycosylation and iron-binding protein modifications using raman spectroscopy. *Analyst*, 142(5):808–814, 2017.

[331] Bayden R Wood and Don McNaughton. Raman excitation wavelength investigation of single red blood cells in vivo. *Journal of Raman Spectroscopy*, 33(7):517–523, 2002.

[332] Anatoli Ianoul, Thomas Coleman, and Sanford A Asher. Uv resonance raman spectroscopic detection of nitrate and nitrite in wastewater treatment processes. *Analytical chemistry*, 74(6):1458–1461, 2002.

[333] Alberto Boffi, Jonathan B Wittenberg, and Emilia Chiancone. Circular dichroism spectroscopy of lucina i hemoglobin. *FEBS letters*, 411(2-3):335–338, 1997.

[334] Anatoly N. Osipov, Nikolai V. Gorbunov, Billy W. Day, Nabil M. Elsayed, and Valerian E. Kagan. Electron spin resonance and mass spectral analysis of interactions of ferrylhemoglobin and ferrylmyoglobin with nitric oxide. *Methods in Enzymology*, 268:193–203, 1996.

[335] Barry D Howes, Christine B Schiødt, Karen G Welinder, Mario P Marzocchi, Jian-Guo Ma, Jun Zhang, John A Shelnutt, and Giulietta Smulevich. The quantum mixed-spin heme state of barley peroxidase: a paradigm for class iii peroxidases. *Biophysical journal*, 77(1):478–492, 1999.

[336] W Robert Scheidt and Christopher A Reed. Spin-state/stereochemical relationships in iron porphyrins: implications for the hemoproteins. *Chemical Reviews*, 81(6):543–555, 1981.

[337] Ru-Jen Cheng, Ping-Yu Chen, Pong-Ren Gau, Chun-Chia Chen, and Shie-Ming Peng. Control of spin state by ring conformation of iron (iii) porphyrins. a novel model for the quantum-mixed intermediate spin state of ferric cytochrome c 'from photosynthetic bacteria. *Journal of the American Chemical Society*, 119(10):2563–2569, 1997.

[338] Robert W Woody and Ming-Chu Hsu. Origin of the heme cotton effects in myoglobin and hemoglobin. *Journal of the American Chemical Society*, 93(14):3515–3525, 1971.

[339] Chunmao He, Barry D. Howes, Giulietta Smulevich, Sigrun Rumpel, Edward J. Reijerse, Wolfgang Lubitz, Nicholas Cox, and Markus Knipp. Nitrite dismutase reaction mechanism: Kinetic and spectroscopic investigation of the interaction between nitrophorin and nitrite. *J. Am. Chem. Soc.*, 137(12):4141–4150, 2015.

[340] Chunmao He, Hideaki Ogata, and Markus Knipp. Formation of the complex of nitrite with the ferriheme b β-barrel proteins nitrophorin 4 and nitrophorin 7. *Biochemistry*, 49(28):5841–5851, 2010.

[341] Alexandre Samouilov, Periannan Kuppusamy, and Jay L. Zweier. Evaluation of the magnitude and rate of nitric oxide production from nitrite in biological systems. *Archives of Biochemistry and Biophysics*, 357(1):1–7, 1998.

[342] Yuji Kaneko, Masao Yuda, Takayoshi Iio, Tomohiko Murase, and Yasuo Chinzei. Kinetic analysis on nitric oxide binding of recombinant Prolixin-S, a nitric oxide transport protein from the blood-sucking bug, Rhodnius prolixus. *Biochimica et Biophysica Acta - Protein Structure and Molecular Enzymology*, 1431(2):492–499, 1999.

[343] Jon O. Lundberg, Eddie Weitzberg, and Mark T. Gladwin. The nitrate-nitrite-nitric oxide pathway in physiology and therapeutics. *Nature Reviews Drug Discovery*, 7(2):156–167, feb 2008.

[344] Antonello Merlino, Barry D Howes, Guido di Prisco, Cinzia Verde, Giulietta Smulevich, Lelio Mazzarella, and Alessandro Vergara. Occurrence and formation of endogenous histidine hexa-coordination in cold-adapted hemoglobins. *IUBMB life*, 63(5):295–303, 2011.

[345] Daniele De Sanctis, Sylvia Dewilde, Alessandra Pesce, Luc Moens, Paolo Ascenzi, Thomas Hankeln, Thorsten Burmester, and Martino Bolognesi. Crystal structure of cytoglobin: the fourth globin type discovered in man displays heme hexa-coordination. *Journal of molecular biology*, 336(4):917–927, 2004.

[346] Mark S Hargrove, Eric Allen Brucker, Boguslaw Stec, Gautam Sarath, Raúl Arredondo-Peter, Robert V Klucas, John S Olson, and George N Phillips Jr. Crystal structure of a nonsymbiotic plant hemoglobin. *Structure*, 8(9):1005–1014, 2000.

[347] Daniele De Sanctis, Sylvia Dewilde, Clemens Vonrhein, Alessandra Pesce, Luc Moens, Paolo Ascenzi, Thomas Hankeln, Thorsten Burmester, Marco Ponassi, Marco Nardini, et al. Bishistidyl heme hexacoordination, a key structural property in drosophila melanogaster hemoglobin. *Journal of Biological Chemistry*, 280(29):27222–27229, 2005.

[348] Kevin Nys, Bert Cuypers, Herald Berghmans, Dietmar Hammerschmid, Luc Moens, Sylvia Dewilde, and Sabine Van Doorslaer. Surprising differences in the respiratory protein of insects: A spectroscopic study of haemoglobin from the european honeybee and the malaria mosquito. *Biochimica et Biophysica Acta (BBA) - Proteins and Proteomics*, 1868(6):140413, 2020.

[349] Julie A Hoy, Suman Kundu, James T Trent, S Ramaswamy, and Mark S Hargrove. The crystal structure of synechocystis hemoglobin with a covalent heme linkage. *Journal of Biological Chemistry*, 279(16):16535–16542, 2004.

[350] Daniele De Sanctis, Alessandra Pesce, Marco Nardini, Martino Bolognesi, Alessio Bocedi, and Paolo Ascenzi. Structure-function relationships in the growing hexa-coordinate hemoglobin subfamily. *IUBMB life*, 56(11-12):643–651, 2004.

[351] Theodore R Weiland, Suman Kundu, James T Trent, Julie A Hoy, and Mark S Hargrove. Bis-histidyl hexacoordination in hemoglobins facilitates heme reduction kinetics. *Journal of the American Chemical Society*, 126(38):11930–11935, 2004.

[352] Markus Ruetz, Jacques Kumutima, Brianne E Lewis, Milos R Filipovic, Nicolai Lehnert, Timothy L Stemmler, and Ruma Banerjee. A distal ligand mutes the interaction of hydrogen sulfide with human neuroglobin. *Journal of Biological Chemistry*, 292(16):6512–6528, 2017.

[353] Hazel M Girvan and Andrew W Munro. Heme sensor proteins. *Journal of Biological Chemistry*, 288(19):13194–13203, 2013.

[354] Seiji Watanabe, Nozomu Takahashi, Hiroyuki Uchida, and Keisuke Wakasugi. Human neuroglobin functions as an oxidative stress-responsive sensor for neuroprotection. *Journal of Biological Chemistry*, 287(36):30128–30138, 2012.

[355] Thorsten Burmester and Thomas Hankeln. What is the function of neuroglobin? *Journal of Experimental Biology*, 212(10):1423–1428, 2009.

[356] Kwang Woo Hwang, Manoj Raje, Kyung-Jin Kim, Benjamin C Stark, Kanak L Dikshit, Dale A Webster, et al. Vitreoscilla hemoglobin: intracellular localization and binding to membranes. *Journal of Biological Chemistry*, 276(27):24781–24789, 2001.

[357] Chong Liu, Yuan He, and Zengyi Chang. Truncated hemoglobin o of mycobacterium tuberculosis: the oligomeric state change and the interaction with membrane components. *Biochemical and biophysical research communications*, 316(4):1163–1172, 2004.

[358] Beyhan Ertas, Laurent Kiger, Miriam Blank, Michael C Marden, and Thorsten Burmester. A membrane-bound hemoglobin from gills of the green shore crab carcinus maenas. *Journal of Biological Chemistry*, 286(5):3185–3193, 2011.

[359] Nozomu Takahashi, Seiji Watanabe, and Keisuke Wakasugi. Crucial roles of glu60 in human neuroglobin as a guanine nucleotide dissociation inhibitor and neuroprotective agent. *PLoS One*, 8(12):e83698, 2013.

[360] Akira Hayashi, Tomokazu Suzuki, and Masateru Shin. An enzymic reduction system for metmyoglobin and methemoglobin, and its application to functional studies of oxygen carriers. *Biochimica et Biophysica Acta (BBA)-Protein Structure*, 310(2):309–316, 1973.

[361] E Antonini and M Brunori. *Hemoglobin and Myoglobin in Their Recation with Ligands*. Neuberger, A. and Tatum, E. L, eds, Amsterdam, 1971.

[362] CJ Wallace and I Clark-Lewis. Functional role of heme ligation in cytochrome c. effects of replacement of methionine 80 with natural and non-natural residues by semisynthesis. *Journal of Biological Chemistry*, 267(6):3852–3861, 1992.

[363] Birgitte Jensen and Angela Fago. Reactions of ferric hemoglobin and myoglobin with hydrogen sulfide under physiological conditions. *Journal of Inorganic Biochemistry*, 182:133–140, 2018.

[364] F Ann Walker. Magnetic spectroscopic (epr, eseem, mössbauer, mcd and nmr) studies of low-spin ferriheme centers and their corresponding heme proteins. *Coordination Chemistry Reviews*, 185:471–534, 1999.

[365] Nitin Kumar Bisht, Stefania Abbruzzetti, Sheetal Uppal, Stefano Bruno, Francesca Spyrakis, Andrea Mozzarelli, Cristiano Viappiani, and Suman Kundu. Ligand migration and hexacoordination in type 1 non-symbiotic rice hemoglobin. *Biochimica et Biophysica Acta (BBA)-Proteins and Proteomics*, 1814(8):1042–1053, 2011.

[366] Myles R Cheesman, Phillip J Little, and Ben C Berks. Novel heme ligation in ac-type cytochrome involved in thiosulfate oxidation: Epr and mcd of soxax from rhodovulum sulfidophilum. *Biochemistry*, 40(35):10562–10569, 2001.

[367] Benoit J Smagghe, Gautam Sarath, Emily Ross, Jean-louis Hilbert, and Mark S Hargrove. Slow ligand binding kinetics dominate ferrous hexacoordinate hemoglobin reactivities and reveal differences between plants and other species. *Biochemistry*, 45(2):561–570, 2006.

[368] Laura Calvo-Begueria, Bert Cuypers, Sabine Van Doorslaer, Stefania Abbruzzetti, Stefano Bruno, Herald Berghmans, Sylvia Dewilde, Javier Ramos, Cristiano Viappiani, and Manuel Becana. Characterization of the heme pocket structure and ligand binding kinetics of non-symbiotic hemoglobins from the model legume lotus japonicus. *Frontiers in Plant Science*, 8:407, 2017.

[369] Mark S Hargrove. Ligand binding with stopped-flow rapid mixing. *Protein-Ligand Interactions: Methods and Applications*, pages 323–341, 2005.

[370] P Leslie Dutton. [23] redox potentiometry: Determination of midpoint potentials of oxidation-reduction components of biological electron-transfer systems. In *Methods in enzymology*, volume 54, pages 411–435. Elsevier, 1978.

[371] George S Wilson. [22] determination of oxidation-reduction potentials. In *Methods in enzymology*, volume 54, pages 396–410. Elsevier, 1978.

[372] Augustin C Mot, Cristina Puscas, Patricia Miclea, Galaba Naumova-Letia, Sorin Dorneanu, Dorina Podar, Nico Dissmeyer, and Radu Silaghi-Dumitrescu. Redox control and autoxidation of class 1, 2 and 3 phytoglobins from arabidopsis thaliana. *Scientific reports*, 8(1):1–13, 2018.

[373] F Ann Walker. The heme environment of mouse neuroglobin: histidine imidazole plane orientations obtained from solution nmr and epr spectroscopy as compared with x-ray crystallography. *JBIC Journal of Biological Inorganic Chemistry*, 11:391–397, 2006.

[374] Alexander N Morozov, James P Roach, Margarita Kotzer, and David C Chatfield. A possible mechanism for redox control of human neuroglobin activity. *Journal of Chemical Information and Modeling*, 54(7):1997–2003, 2014.

[375] Julia M Shifman, Brian R Gibney, R Eryl Sharp, and P Leslie Dutton. Heme redox potential control in de novo designed four-α-helix bundle proteins. *Biochemistry*, 39(48):14813–14821, 2000.

[376] N Nagahara. Intermolecular disulfide bond to modulate protein function as a redox-sensing switch. *Amino acids*, 41:59–72, 2011.

[377] Min Wang, Jian Gao, Pavel Müller, and Bernd Giese. Electron transfer in peptides with cysteine and methionine as relay amino acids. *Angewandte Chemie International Edition*, 48(23):4232–4234, 2009.

[378] Jin Meng, Ling Fu, Keke Liu, Caiping Tian, Ziyun Wu, Youngeun Jung, Renan B Ferreira, Kate S Carroll, T Keith Blackwell, and Jing Yang. Global profiling of distinct cysteine redox forms reveals wide-ranging redox regulation in c. elegans. *Nature communications*, 12(1):1415, 2021.

[379] Thomas G Spiro. Resonance raman spectroscopy as a probe of heme protein structure and dynamics. In *Advances in protein chemistry*, volume 37, pages 111–159. Elsevier, 1985.

[380] R Bois-Poltoratsky and A Ehrenberg. Magnetic and spectrophotometric investigations of cytochrome b5. *European Journal of Biochemistry*, 2(3):361–365, 1967.

[381] Tapan Kanti Das, H Caroline Lee, Stephen MG Duff, Robert D Hill, Jack Peisach, Denis L Rousseau, Beatrice A Wittenberg, and Jonathan B Wittenberg. The heme environment in barley hemoglobin. *Journal of Biological Chemistry*, 274(7):4207–4212, 1999.

[382] Nina Ponomarenko, Jens Niklas, P Raj Pokkuluri, Oleg Poluektov, and David M Tiede. Electron paramagnetic resonance characterization of the triheme cytochrome from geobacter sulfurreducens. *Biochemistry*, 57(11):1722–1732, 2018.

[383] Paul MA Gadsby and Andrew J Thomson. Assignment of the axial ligands of ferric ion in low-spin hemoproteins by near-infrared magnetic circular dichroism and electron paramagnetic resonance spectroscopy. *Journal of the American Chemical Society*, 112(13):5003–5011, 1990.

[384] Tomomi Aono, Yoichi Sakamoto, Masahiro Miura, Fusako Takeuchi, Hiroshi Hori, and Motonari Tsubaki. Direct electrochemical analyses of human cytochromes b5 with a mutated heme pocket showed a good correlation between their midpoint and half wave potentials. *Journal of Biomedical Science*, 17(1):1–15, 2010.

[385] P Horton, J Whitmarsh, and WA Cramer. On the specific site of action of 3-(3, 4-dichlorophenyl)-1, 1-dimethylurea in chloroplasts: inhibition of a dark acid-induced decrease in midpoint potential of cytochrome b-559. *Archives of biochemistry and biophysics*, 176(2):519–524, 1976.

[386] Gianantonio Battistuzzi, Marco Borsari, James A Cowan, Antonio Ranieri, and Marco Sola. Control of cytochrome c redox potential: axial ligation and protein environment effects. *Journal of the American Chemical Society*, 124(19):5315–5324, 2002.

[387] Hirokazu Yamada, Ryu Makino, and Isao Yamazaki. Effects of 2, 4-substituents of deuteroheme upon redox potentials of horseradish peroxidases. *Archives of biochemistry and biophysics*, 169(1):344–353, 1975.

[388] Smita Kakar, Federico G Hoffman, Jay F Storz, Marian Fabian, and Mark S Hargrove. Structure and reactivity of hexacoordinate hemoglobins. *Biophysical chemistry*, 152(1-3):1–14, 2010.

[389] Scott C Dorman, Clare F Kenny, Lee Miller, Rhoda Elison Hirsch, and John P Harrington. Role of redox potential of hemoglobin-based oxygen carriers on methemoglobin reduction by plasma components. *Artificial Cells, Blood Substitutes, and Biotechnology*, 30(1):39–51, 2002.

[390] Shin-ichi Adachi, Shingo Nagano, Yoshihito Watanabe, Koichiro Ishimori, and Isao Morishima. Alteration of human myoglobin proximal histidine to cysteine or tyrosine by site-directed mutagenesis: characterization and their catalytic activities. *Biochemical and biophysical research communications*, 180(1):138–144, 1991.

[391] Stanislav Trashin, Mats De Jong, Evi Luyckx, Sylvia Dewilde, and Karolien De Wael. Electrochemical evidence for neuroglobin activity on no at physiological concentrations. *Journal of Biological Chemistry*, 291(36):18959–18966, 2016.

[392] Bert Cuypers, Stijn Vermeylen, Dietmar Hammerschmid, Stanislav Trashin, Vanoushe Rahemi, Albert Konijnenberg, Amy De Schutter, C-H Christina Cheng, Daniela Giordano, Cinzia Verde, et al. Antarctic fish versus human cytoglobins–the same but yet so different. *Journal of inorganic biochemistry*, 173:66–78, 2017.

[393] Kazuo Kobayashi, JeeEun Kim, Yohta Fukuda, Takahiro Kozawa, and Tsuyoshi Inoue. Fast autooxidation of a bis-histidyl-ligated globin from the anhydrobiotic tardigrade, ramazzottius varieornatus, by molecular oxygen. *The journal of biochemistry*, 169(6):663–673, 2021.